Finite Element Modelling and Simulation for a 'Smart' Tyre

by

Wayne Hall

A thesis submitted in partial fulfilment of the requirements for the degree of Doctor of Philosophy in Engineering

School of Engineering, University of Warwick

January 2003

To Angie and Patrick

Contents

List of Figures

List of Tables

Acknowledgments

I would like to acknowledge the support provided by colleagues at Dunlop Tyres Limited and Ove Arup & Partners. A special mention must be given to Mr. Nigel Nock (Dunlop Tyres) and Dr. Brian Walker (Ove Arup & Partners) for their advice on the Finite Element (FE) modelling work, and also Mr. Mike Beeson and Dr. Kim Hardy (Dunlop Tyres) for providing technical information in relation to the experimental aspects of the research. The financial assistance provided by the Engineering and Physical Sciences Research Council (research grant GR/M86835) is also acknowledged.

I would like to thank my supervisors Dr. J. Toby Mottram and Dr. R. Peter Jones for their help and encouragement. The guidance they have given me is much appreciated and has no doubt been of the highest professional standard. I would also like to thank my colleague Mr. Daniel Dennehy for his assistance with the tyre experiments and for the numerous stimulating conversations and discussions. The help and direction provided by other research colleagues at the University of Warwick is also recognised.

Finally, I would like to thank my family and friends for their support during the writing of this thesis. To my beloved wife Angie and son Patrick, I extend my most grateful appreciation. Their continuous support and encouragement has made this thesis possible.

Declaration

The research presented in this thesis is original work carried out by the author. Aspects of the work have also been discussed in the following publications:

W. HALL, J. T. Mottram, D. J. Dennehy and R. P. Jones, 'Characterisation of the Contact Patch Behaviour of an Automobile Tyre by Physical Testing,' *International Journal of Vehicle Design* (submitted June 2002).

G. J. Tomka, S. Eaton, J. Milne, W. HALL, R. P. Jones and J. T. Mottram, 'Foresight Vehicle: Smarter Tires using Advance Sensors for Improved Safety,' *SAE 2002 World Congress*, Paper 2002-01-1871, Arlington, Virginia, USA, June 2002.

J. T. Mottram, W. HALL and R. P. Jones, 'Finite Element Modelling and Simulation for a Smart Tire,' *Tire Technology Expo 2002*, Hamburg, Germany, February 2002.

W. HALL, R. P. Jones and J. T. Mottram, 'Modelling of an Automobile Tyre using LS-DYNA3D,' *Third European LS-DYNA Conference*, Paris, France, June 2001.

W. HALL, R. P. Jones, J. T. Mottram, N. Nock and K. Hardy, 'Finite Element Simulation of a Vertically Loaded Automobile Tyre,' *IoM International Rubber Conference*, Birmingham, United Kingdom, June 2001, pp. 536-545.

Summary

This thesis presents an initial Finite Element (FE) based modelling investigation aimed at supporting the development of 'smart' tyre or intelligent tyre technologies. Physical tests carried out with a stationary (non-rolling) and rolling experimental tyre are used to enhance understanding of tyre behaviour in the contact patch and validate the modelling methodology. Simulation results with the explicit FE package LS-DYNA are then used to characterise the internal stresses and strains at several positions in the tyre tread.

Two separate FE models are developed to simulate the stationary and rolling tyre behaviour at the macroscopic level. The models differ only with respect to the mesh density in the circumferential direction, the mesh through the cross section is identical. The complex tyre structure is represented as a rubber and reinforced rubber composite, and the mesh specification and the material descriptions used in the models are discussed. The structural behaviour of the stationary experimental tyre under normal load is simulated. The inflation of the tyre, the wheel fit and the normal loading against the horizontal surface are represented. Simulation results are also presented when a subsequent longitudinal or lateral load is applied to the stationary tyre. These analyses were conducted to determine the longitudinal and lateral tyre stiffnesses, respectively.

The predicted normal load-deflection characteristics and contact patch dimensions (length and width) are compared with a reasonable degree of success to those obtained in the full-scale physical tests. The longitudinal and lateral simulations also appear to give realistic tyre stiffnesses. The contact patch dimensions give a good trend-wise agreement, but the length and width are greater than the experimental measurements. A parametric study is carried out and this disparity is related to a deficiency in the performance of the contact algorithms. It is concluded that it not straightforward to accurately predict contact patch behaviour, and therefore the internal transient stresses and strains in a rolling tyre in absolute terms. However, the good trend-wise agreement suggests that the modelling methodology should be capable of predicting internal transient responses which are related to the 'actual' deformations in the contact region.

To simulate the rolling tyre behaviour on flat bed and drum surfaces, consideration is given to the inflation of the tyre, the wheel fit, the normal loading and the rotation of the tyre. Numerical instabilities are found to occur and these are related to imperfections inherent in version 950d of the code. This version was, at the time, the most up to date release. The current release is version 960 and it does not contain many of the imperfections in the earlier version. Thus, the flat bed simulation is repeated using the current version. The predicted contact patch stresses are presented and a reasonable correlation is achieved with the experimental data. The internal stresses and strains are then characterised at a number of selected positions in the tread region. These stresses and strains are discussed in context with the development of smart tyre technologies and are useful as a guide to the most appropriate location for an in-tyre sensor (or sensors).

Notation

Italic Symbols

A	area of contacted segment
B	stiffness factor
C	shape factor; Mooney-Rivlin elastic constant (e.g. C_1, C_2)
C_s	longitudinal tyre stiffness
C_α	cornering tyre stiffness
d	depth; maximum diagonal
d_c	decay coefficient
D	peak factor
E	curvature factor
f_s	penalty stiffness factor
F	resultant force (e.g. F_x, F_y, F_z)
$F_{y\alpha}$	cornering force
$F_{y\gamma}$	camber thrust
G	shear modulus
l	contact patch half length
L	length
m	degrees of freedom
M	moment (e.g. M_x, M_y, M_z)
N	number of
k	penalty stiffness
K	bulk modulus
p	pressure
r_e	tyre effective rolling radius

R	specific gas constant
s	slip ratio
S	offset (e.g. S_h, S_v)
t	time
T	temperature
u, v, w	displacement components in x-, y- and z-directions, respectively
V	forward velocity; volume
V_{rel}	relative velocity
w	contact patch width
W	strain energy function
x, y, z	Cartesian coordinate system; tyre axis system

Greek Symbols

α	slip angle
δ	shear distortion
ε	direct strain (e.g. ε_x, ε_y, ε_x)
ϕ	diameter
Δt	time step size
$\overline{\Delta t}$	average time step size
γ	camber angle; shear strain
λ	extension ratio (e.g. λ_1, λ_2, λ_3)
μ	friction coefficient (e.g. μ_p, μ_s)
σ	direct stress (e.g. σ_x, σ_y, σ_x)
τ	shear stress (e.g. τ_{xy}, τ_{yz}, τ_{zx})
ω	natural frequency

Subscripts and Superscripts

c	cord
e	element; effective

ex	external
f	friction
h	horizontal
i	label for nodes
in	internal
max	maximum
n	nominal
n	normal direction or step number
p	peak
s	sliding
t	true
v	vertical
x, *y*, *z*	Cartesian coordinates; tyre axes
1 , *2* , *3*	principal coordinates

Mathematical Symbols

[ ]	square matrix
{ }	vector, or column matrix
{δ}	global displacement vector
$\{\dot{\delta}\}$	velocity vector
$\{\ddot{\delta}\}$	acceleration vector
$\{\delta^e\}$	element displacement vector
{F}	global force vector
$\{\mathbf{F}_{ex}\}$	external force vector
$\{\mathbf{F}_{in}\}$	internal force vector
$\{\mathbf{F}^e\}$	element force vector
[K]	global/system stiffness matrix
$[\mathbf{K}^e]$	element stiffness matrix
[M]	global/system mass matrix
$[\mathbf{M}^e]$	global/system mass matrix

Chapter 1 Introduction

In recent years, there has been a significant increase in the number of vehicles on the nation's roads. An increase of nearly 4 million vehicles has been observed since 1990 [1] and road traffic is expected to reach 35 million vehicles by the year 2025 [2], a further increase of about 10 million vehicles. The relationship between road accidents and traffic flow has been investigated by Dickerson *et al.* [3] and the accident-flow relationship is seen to substantially increase at high traffic flows. The increase in vehicles and their habitual use is causing the nation's roads to become busier and, thus, more hazardous.

Although the level of traffic congestion has increased, accident statistics published by the Government indicate an improvement in road safety. The statistics show the number of deaths to be nearly half the total of 30 years previously and indicate a considerable reduction in the number of serious injuries. In contrast, the total number of casualties (deaths, serious and slight injuries) has not fallen greatly over the same period - only 12 % since 1967 [1]. Many factors have contributed to the shift from fatal and serious injuries to slight injuries. These factors include compulsory seat belt usage and better highway engineering. A significant contribution has also been made in the area of vehicle safety design were numerous primary and secondary safety features have been introduced. Primary and secondary safety features are defined as vehicle engineering aspects which "as far as possible reduce the risk of an accident", and structural and design features that "reduce the consequences of accidents", respectively [4]. Primary safety features such as vehicle dynamics control systems, including Anti-lock Braking Systems (ABS) and traction control or Anti-Spin Regulation (ASR) are now standard on many vehicles. Airbags and deformable 'crush zones' that dissipate the energy in the event of an impact are also now standard and are examples of secondary safety features.

To sustain the improvement, further road safety measures need to be introduced to cope with the predicted increase in levels of traffic congestion. The Government is committed

to road safety issues and has published a safety strategy [5]. This strategy impacts on vehicle manufacturers because vehicle safety design is considered as a potential area for continuous improvement. Since the greatest progress can be made in accident prevention, the development of new vehicle dynamics control systems is essential. Tyres play the most crucial role in the support of vehicle dynamics and therefore one approach favoured by tyre technologists is to integrate sensor systems into tyres to monitor the contact patch forces [6, 7]. Thus, the 'smart' tyre concept may soon become a reality.

1.1 Automobile Tyres

Apart from gravitational and aerodynamic forces, all other forces which affect the motion of a ground vehicle are generated at the interface between the tyre and the ground, known as the contact patch. These longitudinal, lateral and vertical forces (see Figure 1.1) are the resultant of normal and shear stresses which arise in the contact patch area [8]. They are transmitted through the tyre structure to the vehicle via the wheel. An overturning moment, a rolling resistance moment and an aligning moment also exist when an offset in the forces occurs relative to the centre of the contact patch.

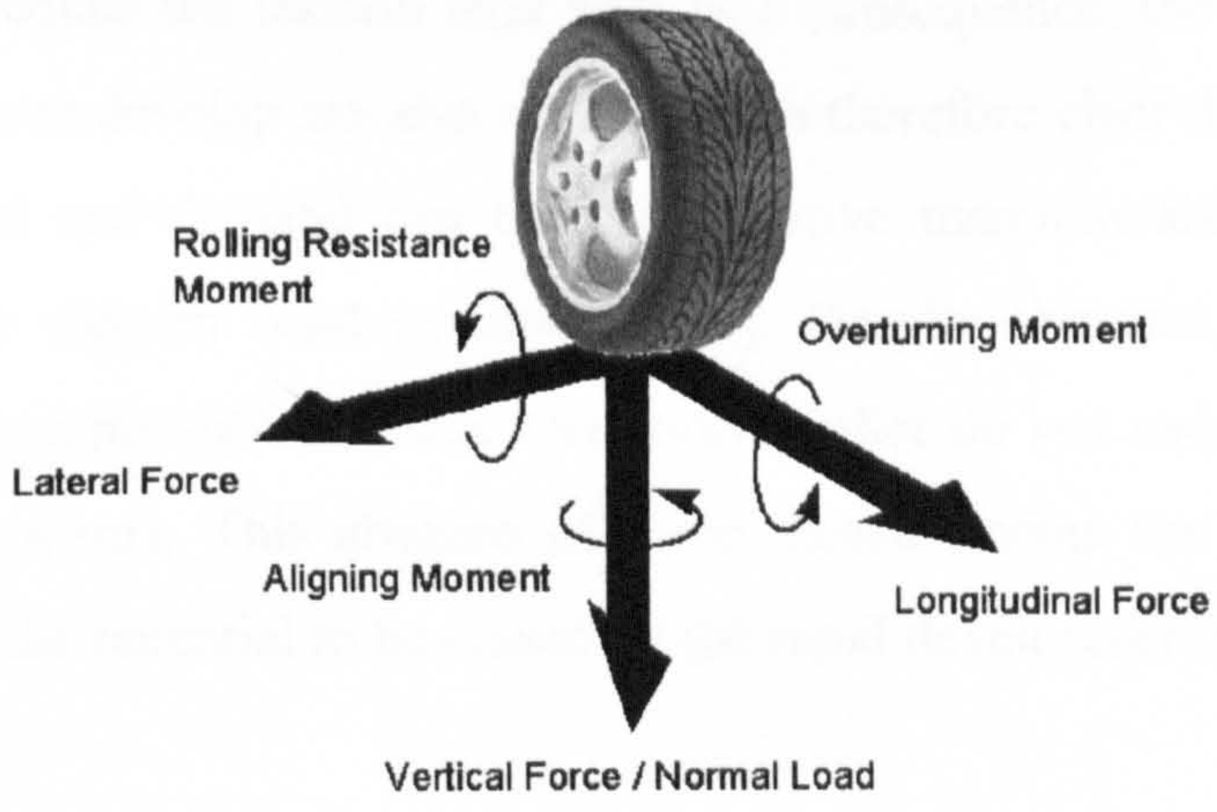

Figure 1.1 Tyre forces and moments

It should be noted that there is a limit to the longitudinal and lateral forces that a rolling tyre can develop. This limit is determined by the vertical force (normal load) and the friction coefficient μ between the tyre and the ground surface. The normal load is governed by the weight of the vehicle and, thus, at a given load, the friction condition determines the maximum contact patch forces [9], and therefore the manoeuvres a

vehicle can undertake. The friction condition and the interdependence of the longitudinal and lateral forces is described by the 'friction ellipse' [10]. This is shown in Figure 1.2.

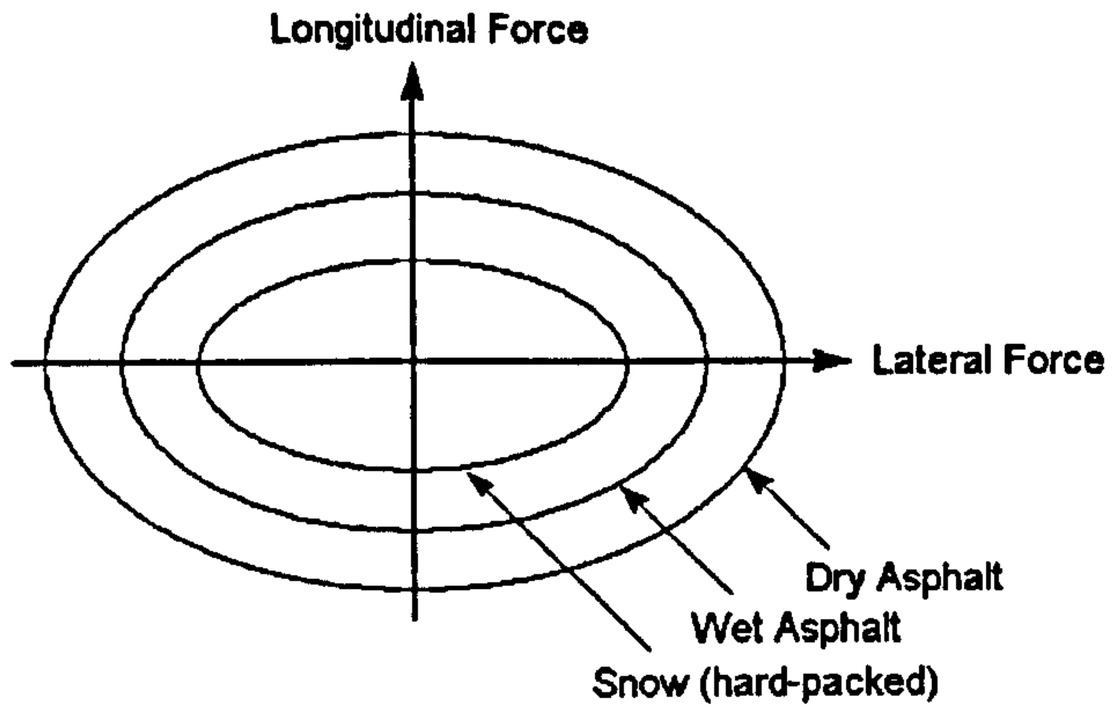

Figure 1.2 The 'friction ellipse' concept

The friction ellipse identifies the friction limit for a tyre. The friction can be used to develop a longitudinal force for acceleration/braking, a lateral force for cornering/lane change manoeuvers, or a combination of the two, but in no case can the vector total of the two exceed the limit [8]. The longitudinal and lateral forces may develop in either a positive or negative direction. Adverse driving conditions such as on wet, snowy and icy roads substantially reduce the friction limit and, as a consequence, the longitudinal and lateral forces which can develop are also reduced. It is therefore clear that knowledge of the friction potential and demand can help to improve manoeuvrability and thereby vehicle safety under slippery road conditions [11]. Despite this fact, current vehicle dynamics controls systems such as those mentioned earlier do not make use of contact patch force measurements. This absence of force measurements for future dynamics control systems has the potential to be erased by the rapid developments in 'smart' tyres.

1.2 'Smart' Tyres

The concept of 'smart' tyres or intelligent tyre technologies involves the instrumentation of a tyre by a sensor device embedded in the structure. The sensor device is used to measure the tyre stresses, strains or deformations and the sensor outputs are then related to the contact patch forces. Previous work on in-tyre sensor technology has been concentrated at Darmstadt University of Technology and the tyre manufacturer

Continental. The early work at Darmstadt [13, 14] used a Hall-effect sensor to detect three-dimensional movements of a tread embedded magnet. Continental have developed a SideWall Torsion (SWT) sensor [15] that provides an estimate of the longitudinal and lateral forces in the contact patch by monitoring the magnetic field generated by alternate north-south poles embedded in the tyre. A recent collaboration between Continental and Darmstadt [16] has also resulted in the integration of wireless Surface Acoustic Wave (SAW) sensors to measure internal stresses in the tread. The smart tyre concept is not a new idea but the technology is yet to advance into the mainstream [12].

1.3 Thesis Motivation

The work reported in this thesis was carried out as part of the Foresight Vehicle Link project 'Smarter Tyres using Advanced Sensors for Improved Safety' (STASIS). The long-term aim of the STASIS project is to establish in-tyre sensor system technology for monitoring tyre behaviour in road vehicles. The project originally involved a consortium consisting of Dunlop Tyres Limited, QinetiQ (formerly DERA), Avonwood Developments Limited, Ove Arup & Partners, Rover Group, and the University of Warwick. It should be noted, however, that due to unforeseen circumstances Dunlop Tyres withdrew support from the project in December 2000 and, as a consequence, the project has been continued without input from a tyre manufacturer. The research reported herein is the author's (University of Warwick's) contribution to the project.

Smart tyre technologies have the potential to provide information on a vehicle's state via sensors in each tyre. To provide the most direct information, the sensors need to be embedded local to the contact patch and the influence of the tyre behaviour on the sensor outputs needs to be realised. It appears to date that little research effort has been expended on investigation of contact patch behaviour [9] and therefore the magnitude and frequency of the corresponding internal stresses, strains and deformations are not fully understood. Thus, the most appropriate position for the in-tyre sensors is still not known. The sensors must survive in operation and their position is therefore depend on the transient stresses and strains they will experience. It is therefore clear that in order to support the development of sensor systems it is necessary to gain a greater understanding of tyre behaviour local to the contact region. The work reported in this thesis aims to provide an initial investigation of the complex internal stresses and strains

via numerical modelling. The numerical results emerging from the application of the modelling methodology could then be used to identify the optimal location for a sensor (or sensors) and the transfer function between the contact stresses and sensor outputs.

To satisfy the research aim, Finite Element (FE) based structural analysis techniques are used to simulate the stationary (non-rolling) and rolling behaviour of an experimental tyre. Only advanced FE based modelling can provide simulations at the desired macroscopic level but such simulations are only as good as the FE program, and the way in which it is employed. Thus, a major aspect of the work presented in the thesis is model validation. Physical tests carried out with the experimental tyre are used to enhance understanding of tyre behaviour in the contact patch and validate the modelling methodology. Simulation results with the explicit software package LS-DYNA [17] are then used to characterise the internal stresses and strains at several positions in the tread.

1.4 Thesis Outline

This chapter has highlighted the importance of tyres in vehicle safety design and has also introduced the smart tyre concept and discussed some relevant work in this area. Chapter 2 reviews the tyre research literature relevant to this study. It describes the modern automobile tyre structure and the forces and moments exerted on it. The chapter discusses previous work carried out to characterise tyre behaviour in the contact patch and then remarks on the related attempts to simulate this behaviour using simple models. An overview of complex FE tyre models is also presented and the implicit and explicit FE approaches are briefly discussed. The chapter highlights the lack of knowledge about local tyre behaviour in the contact region and the absence of existing FE tyre models to simulate this behaviour. Thus, the chapter establishes the motivation behind the thesis.

Chapters 3 describes an experimental investigation which aims to characterise tyre behaviour in the contact patch with reference to the author's need to validate advanced FE simulations. Physical tests are carried out with a stationary (non-rolling) and rolling experimental tyre. The stationary experiments are conducted on a load-deflection machine and the rolling tyre experiments on flat bed and rolling drum machines, each instrumented with a tri-axial stress transducer. Load-deflection characteristics and contact patch dimensions are presented for the non-rolling tyre. Many plots giving the

normal pressure and shear stress distributions under free-rolling and cornering (slip and camber angle) conditions are presented for a high friction surface, and a comparison is made between the contact patch behaviour when the tyre is rolled on the horizontal (at 0.18 km/h) and drum (10 to 50 km/h) surfaces. The investigation therefore characterises the contact patch behaviour of the experimental tyre and, by doing so, also contributes novel experimental measurements that correspond to 'actual' tyre contact deformations.

Chapter 4 describes two state-of-the-art FE tyre models developed to simulate stationary and rolling tyre behaviour. The models are developed for analysis by the explicit solver LS-DYNA [17]. They depict the complex structure of the experimental tyre as a rubber and reinforced rubber composite. The mesh specification and material descriptions used in the development of the models are discussed, and consideration is given to the difficult issue of modelling contact and friction. The chapter also discusses salient features of the solution algorithms used in the code. The aim of the chapter is to present a modelling methodology which is capable of predicting tyre behaviour in the contact patch and the internal stresses and strains a sensor will experience in operation.

In Chapter 5, the structural behaviour of the experimental tyre during the stationary experiments is simulated using LS-DYNA version 950d. This version was, at the time, the most up to date release. The inflation of the tyre, the wheel fit and the normal loading against a rigid horizontal surface are considered. It should be noted that the simulation is representative of the full-scale tests. A parametric study is presented which characterises the sensitivity of the analysis results to changes in the mesh density of the tyre and surface, and to variations in the elastic properties of the 'tyre' components. The chapter also presents simulation results obtained at several inflation pressures and when a subsequent quasi-static longitudinal or lateral load is applied to the tyre. The aim of the chapter is therefore to validate the modelling methodology for non-rolling behaviour.

In Chapter 6, rolling tyre behaviour on the flat bed and rolling drum machines is simulated. Consideration is given to the inflation of the tyre, the wheel fit, the normal loading and the rotation of the tyre. Numerical problems are observed in these simulations and the problems are related to imperfections inherent in version 950d of the code. Thus, the flat bed simulation is repeated using the current release, version 960. Inconsistencies in the simulation results obtained using the two version are found and

these are discussed in relation to the earlier model validation work carried out with version 950d. The predicted contact stresses are then compared with a reasonable degree of success to those found by full-scale physical testing, and the internal stresses and strains are characterised at a several positions in the tread. These stresses and strains are discussed in context with the development of smart or intelligent tyre technologies.

The final chapter of this thesis, Chapter 7, summarises the work carried out by the author. Each of the individual chapters are reviewed in turn and the salient points are highlighted. The main conclusions are presented and the work is discussed in context with to the research aim. Finally, some recommendations are given for further work.

Chapter 2 Automobile Tyres, Tyre Behaviour and Modelling

2.1 Introduction

Apart from gravitational and aerodynamic forces, all actions which affect the motion of ground vehicles are generated at the tyre/ground contact patch. Thus, it has been said that the "critical control forces (and moments) that determine how a vehicle turns, brakes and accelerates are developed in four contact patches no bigger than a man's hand [1]." As previously discussed in Chapter 1, these forces and moments are the resultant of normal and shear stresses which arise in the contact patch area. They are transmitted through the tyre structure to the vehicle via the wheel. It is therefore clear that a thorough understanding of a tyre's structure and behaviour, particularly the contact patch stresses and their relationship to the internal tyre deformations, and resultant forces and moments is essential for the development of smart tyre technologies.

This chapter presents an overview of the tyre research literature. Primarily, it discusses the behaviour of modern radial-ply tyres but the characteristics of bias-ply tyres are also considered. This is because much of the previous research has been conducted on this type of construction. Finite Element (FE) based modelling provides the best opportunity to simulate the internal deformations, so a review of FE tyre models is given, and the implicit and explicit methods are briefly described. The attempts to model tyres using simple empirical and semi-empirical models are also mentioned. The chapter highlights the lack of knowledge about contact patch behaviour and the absence of existing models to simulate this behaviour. By doing so, it establishes the motivation behind the thesis.

2.2 Tyre Construction

Two basic tyre constructions are commonly used; radial-ply and bias-ply tyres, as shown in Figure 2.1. Bias-ply tyres were exclusively used in the automotive industry until the

advantages of radial-ply tyres was recognised in the 1960's. Since then, radial-ply tyres have gradually displaced bias-ply tyres on passenger cars and have been the standard for a number of years. The use of radial-ply tyres on trucks, however, initially lagged that on passenger cars, such that (even as recently as) in the early 1990's both radial- and bias-ply tyres experienced approximately equal use [8]. Today, radial-ply tyres are also standard on trucks [18]. Bias-belted tyres were briefly employed as a cross between the radial- and bias-ply constructions during the transition period but are now rarely used.

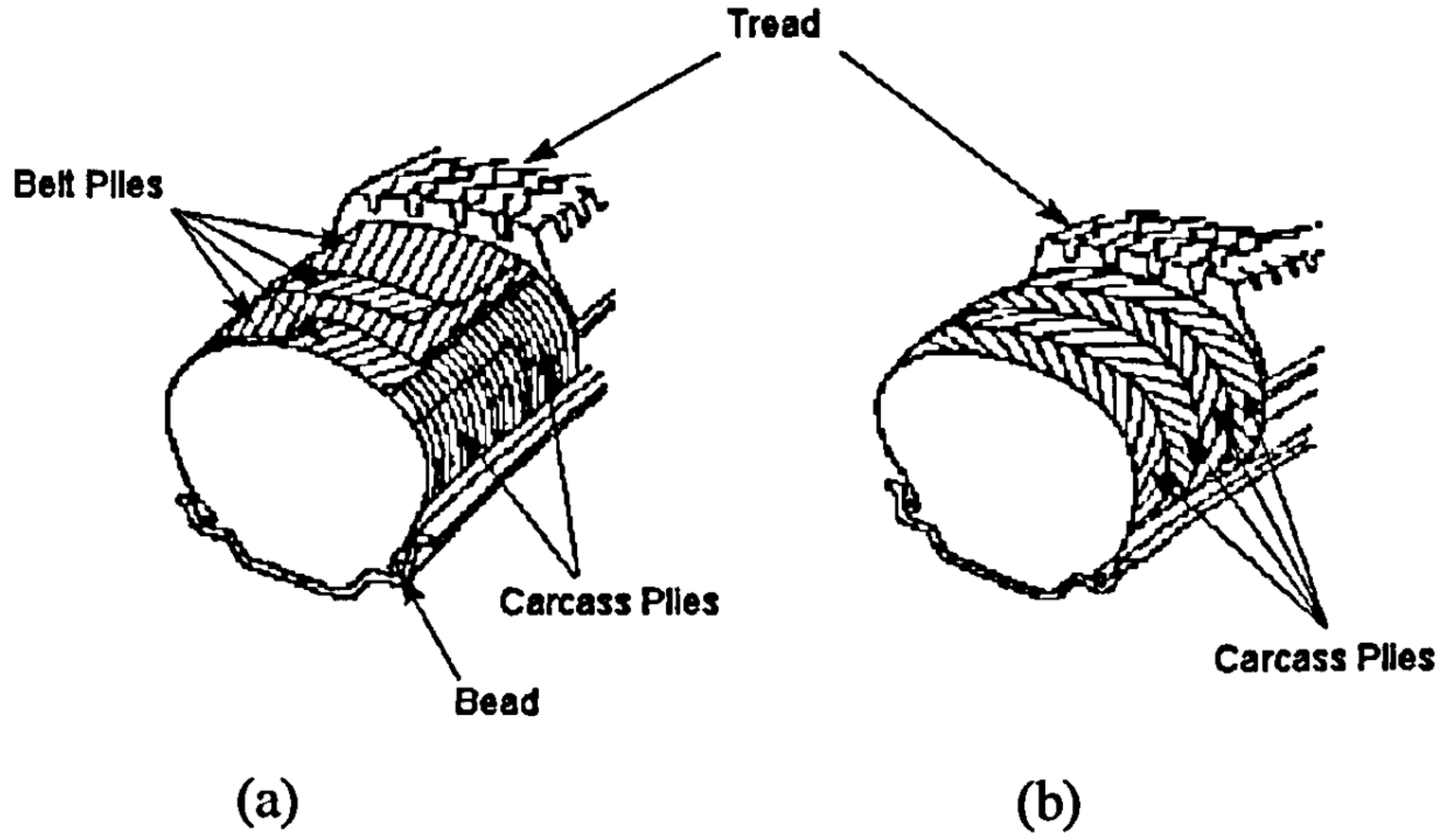

Figure 2.1 Tyre construction: (a) radial-ply tyre; (b) bias-ply tyre [18]

The radial-ply construction is characterised by the carcass plies (cords usually of a synthetic material embedded in a rubber matrix) which extend radially from one bead to the other, i.e. at 90 degrees to the tyre circumference. The beads form a foundation for the carcass plies, and anchor the tyre to the wheel. The construction provides a soft ride but little directional stability. Directional stability is supplied by the belt (cords of steel or other high-strength materials embedded in a rubber matrix) that runs circumferentially around the tyre. The cords in the belt are usually orientated at approximately 20 degrees to the tyre circumference. The belt stiffens the tread region, keeping the tread in contact with the ground. For passenger car tyres, usually there are two carcass plies of synthetic cords, such as nylon, rayon or polyester, and the belt comprises two plies of steel cords and two plies of synthetic cords, such as nylon or rayon. For truck tyres, usually there is one carcass ply of steel cords, and four plies of steel cords in the belt [8, 18, 19].

In a bias-ply tyre the carcass comprises two or more plies which extend diagonally from one bead to the other with the cords orientated at an angle between 35 and 40 degrees

to the tyre circumference. The cords in adjacent plies run in opposite directions. Thus, the cords overlap in a diamond (criss-cross) pattern. In operation, the orientation of the cords causes the carcass plies to flex and rub. This flexing action produces a wiping motion between the tyre tread and ground surface during rolling which is one of the main cause of higher tyre wear and higher rolling resistance in bias-ply tyres [18, 19].

2.3 Sizes and Load Rating

Tyre sizes are commonly specified by two dimensions; the section width given in millimeters for radial-ply tyres, and the wheel rim diameter given in inches. The load-carrying capacity (rated load) is primarily dependent upon the tyre size. The outer diameter of the tyre, which is independently variable from the wheel rim diameter, is usually identified by the aspect ratio. This aspect ratio is the ratio between the section height and the section width and is usually expressed as a percentage. The terminology is shown in Figure 2.2. The type and construction of the tyre are identified by letters; P denotes a passenger car tyre and LT a light truck, R, B and D indicate radial-ply, bias-belted and bias-ply constructions, respectively. For example, a P195/65R15 identifies a passenger car tyre having a section width of 195 mm and an aspect ratio of 65 percent. The tyre has a radial-ply construction and is mounted on a 15 inch diameter wheel rim.

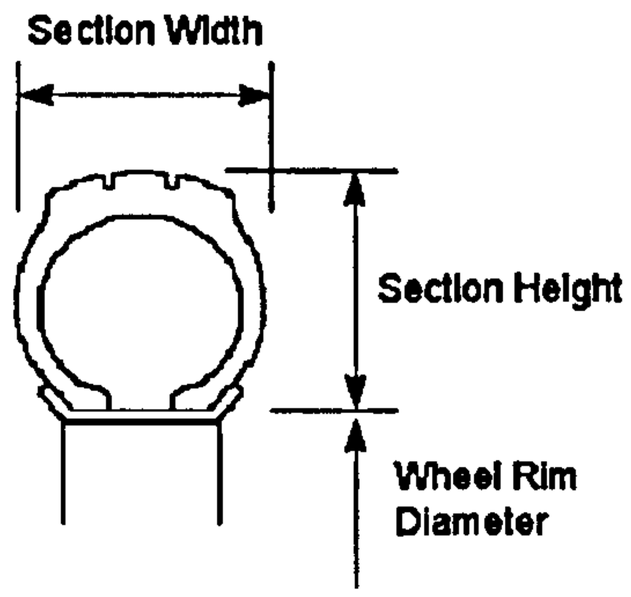

Figure 2.2 Tyre terminology

2.4 Forces and Moments

To describe the forces and moments exerted on a tyre, it is necessary to define an axis system. Figure 2.3 shows the tyre axis system recommended by the Society of Automotive Engineers (SAE). The origin of the axis is at the centre of the contact patch.

The *x*-axis, known as longitudinal axis, is the intersection of the wheel plane and the ground plane with the positive direction forward. The *z*-axis or vertical axis is perpendicular to the ground plane with the positive direction downward. The *y*-axis or lateral axis is in the ground plane and is directed to make the axis system right-handed.

The longitudinal force F_x is the force in the *x*-direction exerted on the tyre by the ground. The force in the *y*-direction is referred to as the cornering force $F_{y\alpha}$ when caused by the slip angle α only, camber thrust $F_{y\gamma}$ when caused by the camber angle γ only, or more generally the lateral force F_y. Slip angle is the angle formed between the direction of travel of the wheel and the line of intersection of the wheel plane and ground plane. Camber angle is the angle formed between the *xz*-plane and the wheel plane. The normal load (or the vertical force) F_z is the force in the vertical direction. The overturning moment M_x, the rolling resistance moment M_y and the aligning moment M_z are moments about the longitudinal, lateral and vertical axes, respectively.

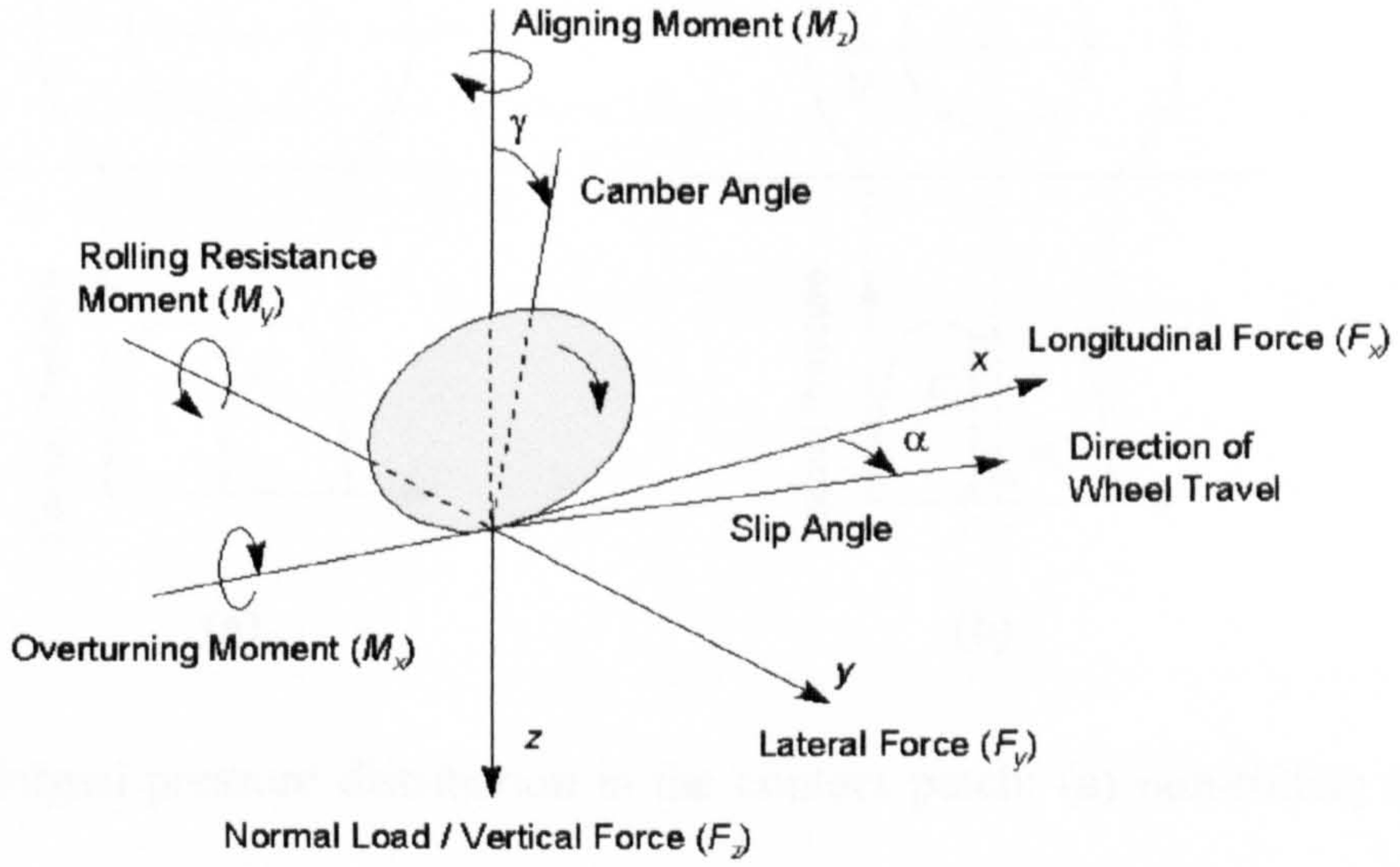

Figure 2.3 Tyre axis system and nomenclature [20]

As mentioned, the forces and moments are the resultant of normal and shear stresses distributed in the contact patch. Normal stresses σ_z arise as the inflation pressure acts through the tyre onto the ground, shear stresses (τ_{xz} and τ_{yz}) arise due to friction coupling between the tyre tread and the ground surface. There are two primary mechanisms responsible for friction coupling; surface adhesion and hysteresis [21].

Surface adhesion is the result of molecular bonding, hysteresis is the energy loss as the tyre deforms during rolling [22] and is the main cause of rolling resistance in tyres [18].

2.5 Rolling Resistance

The pressure distribution in the contact patch is not uniform (as was assumed to be the case for many years [23]) it varies in both the longitudinal and lateral directions. In a rolling tyre, the pressure distribution is also not symmetrical about the lateral axis. This is shown in Figure 2.4 and also in the experimental results presented in Chapter 3. The pressure at the front of the contact patch is slightly greater than at the rear. This is because a longitudinal force, referred to as the rolling resistance, exists in the contact patch. The pressure distribution is shifted in the direction of rolling (to the left) to maintain equilibrium. This characteristic is discussed in a number of text books [8, 18].

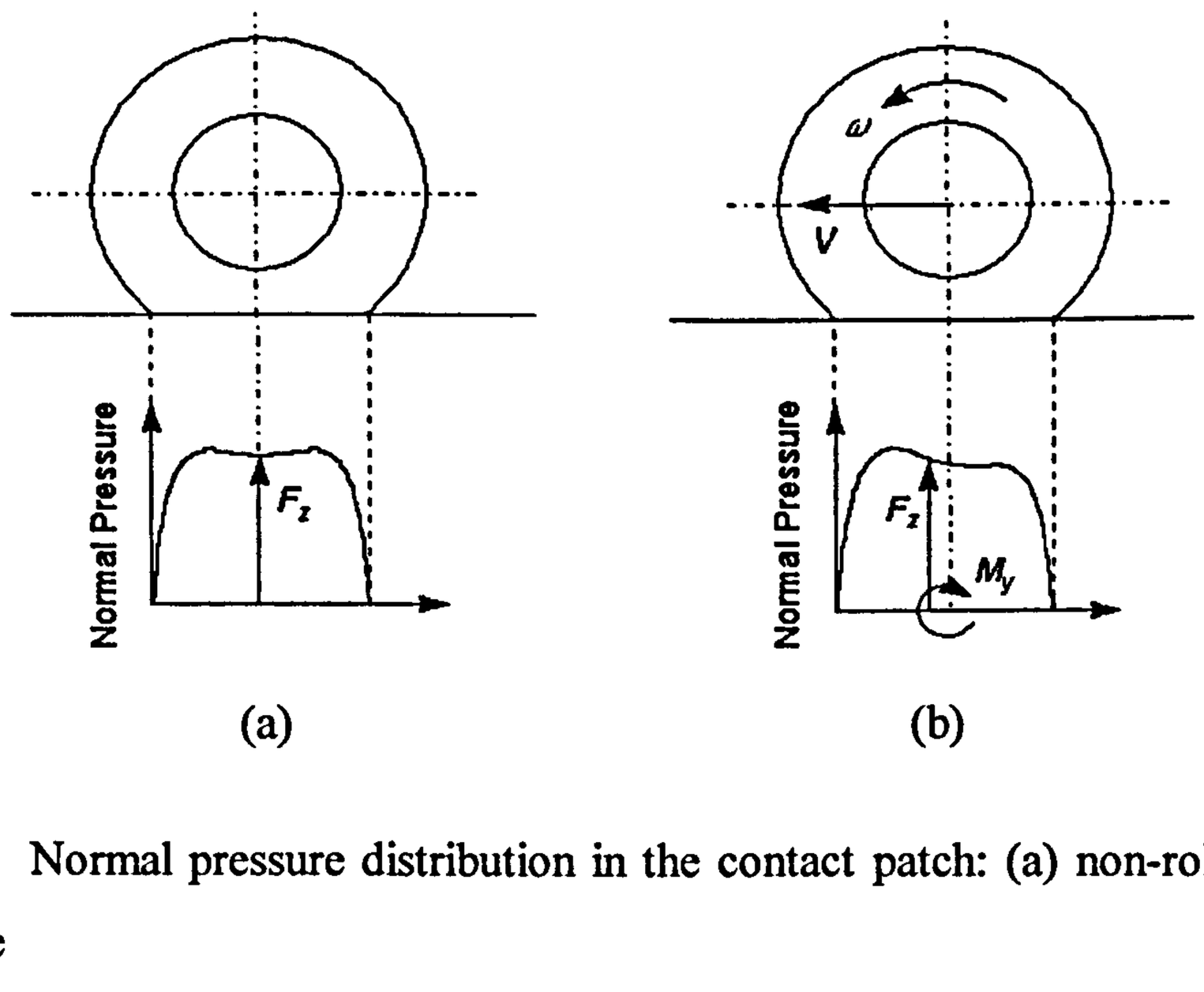

Figure 2.4 Normal pressure distribution in the contact patch: (a) non-rolling tyre; (b) rolling tyre

Numerous papers have been published that discuss the various factors which influence the rolling resistance of tyres [24-26]. These factors include the tyre construction and materials, surface condition, inflation pressure and speed. The rolling resistance coefficient for a range of radial-ply and bias-ply passenger car tyres (at their rated loads and inflation pressures) with speed is shown in Figure 2.5. The rolling resistance coefficient is ratio of the rolling resistance to the magnitude of the normal load. As mentioned earlier, rolling resistance is higher in bias-ply tyres [19]. An increase in the

tread depth, the thickness of the sidewalls or the number of carcass plies in the structure also tend to increase the rolling resistance. Tyres made of synthetic and butyl rubber compounds also usually have higher rolling resistance than those made of natural rubber.

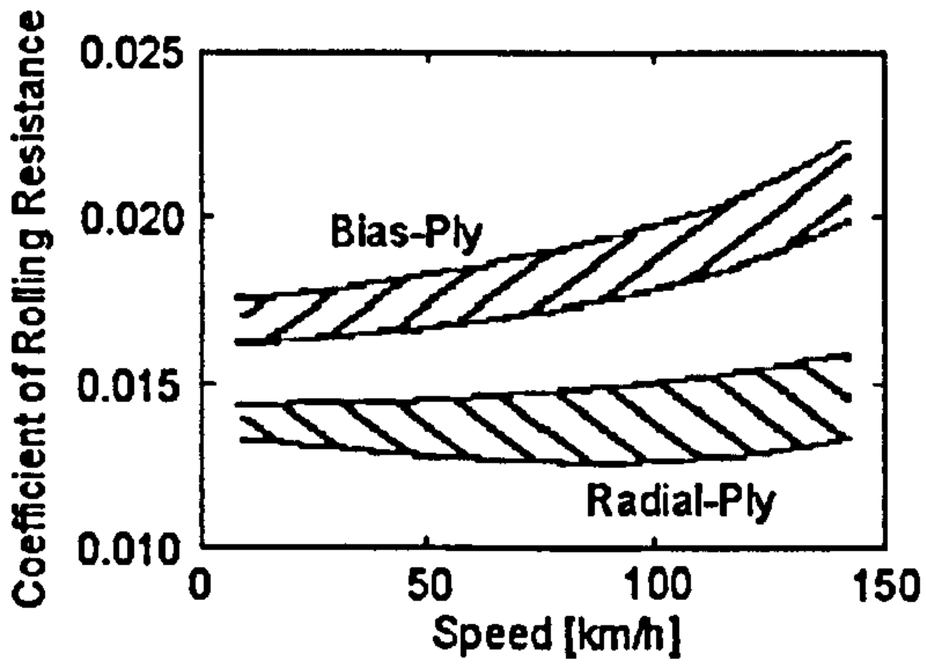

Figure 2.5 Variation in rolling resistance coefficient of bias- and radial-ply passenger car tyres with speed on a smooth ground surface at rated load and inflation pressure [18]

On smooth surfaces the rolling resistance is lower than on rough surfaces. This is shown in research by DeRadd [27] where the author has published experimental results obtained in laboratory and outdoor tests conducted on various road surfaces. The rolling resistance has also been shown to reduce with an increase in tyre inflation pressure [28]. This reduction, however, is found to be more significant in bias- than in radial-ply tyres.

2.6 Tractive Properties

Under acceleration or braking conditions, longitudinal slip is observed in the contact patch as the tyre tread deflects to develop and sustain a friction force, i.e. an acceleration or braking force, respectively. The contact stresses during braking are shown in Figure 2.6. To the author's knowledge, these contact stresses have only been investigated by Novop'skii and Nepomnyashchii [29], and Bode [30]. The work by Novop'skii and Nepomnyashchi could not be located, and the publication by Bode was found to be in German (an English translation was not available). The work of the authors' is, however, reviewed by Browne *et al.* [31]. This review is therefore important because it presents the only available experimental data (in English) on the contact tractive stresses.

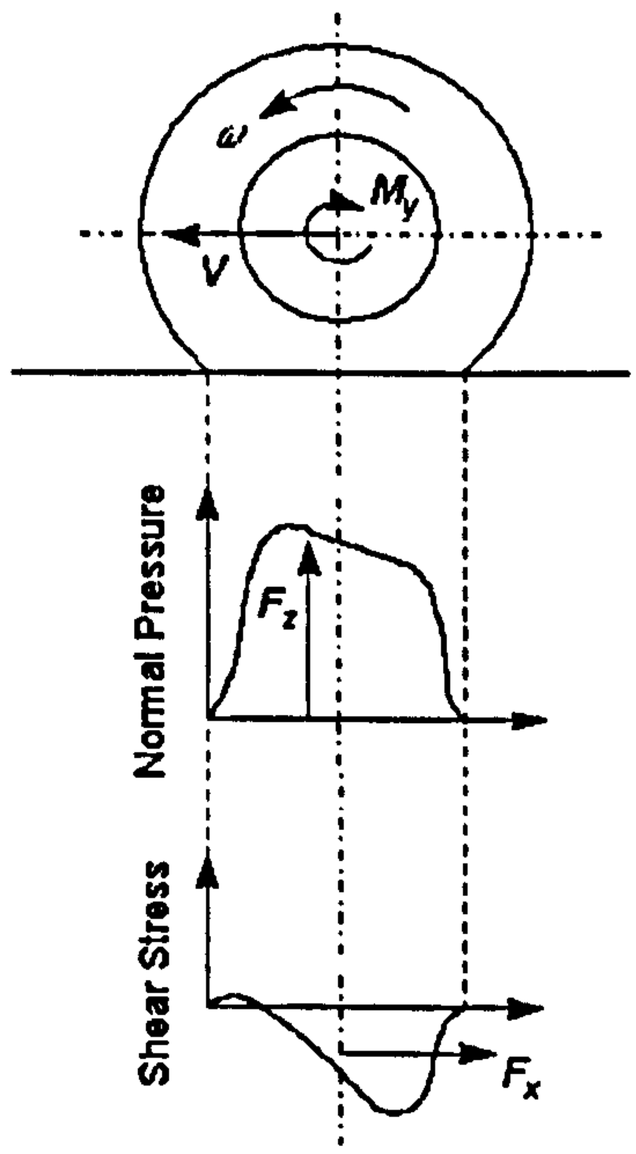

Figure 2.6 Contact patch behaviour during braking [10]

As tread elements enter the contact patch they are deflected in the longitudinal direction. The deflection occurs because the tyre is moving faster than the perimeter of the tyre tread. The deflection and the corresponding longitudinal shear stress build-up as the element moves through the contact patch until the shear stress on the element overcomes the available friction and the element begins to slip (slide) noticeably on the surface. In the sliding region, the deflection and shear stress diminish, reaching zero as the element leaves the contact patch. Integrating the longitudinal shear stresses over the contact patch area yields the longitudinal force. Thus, acceleration and braking forces are generated by producing a difference between the tyre rolling speed and its linear speed of travel. As a consequence, longitudinal slip is produced in the contact patch.

The longitudinal slip s is usually defined non-dimensionally as a ratio of the forward speed [32, 33]. This slip ratio is given by

$$s = 1 - \left(\frac{r_e \omega}{V}\right), \quad V \neq 0 \tag{2.1}$$

where r_e is the tyre effective rolling radius, ω is angular velocity of the wheel, and V is the forward velocity. It should be noted that in Equ.(2.1) the slip ratio is positive during

braking but the longitudinal force is negative according to the SAE tyre axis system shown in Figure 2.3. During acceleration, the ratio is negative but the force is positive.

The braking force developed by the tyre is known to vary with longitudinal slip, as shown in Figure 2.7. A similar curve is produced in acceleration. As the slip increases, the friction force increases along an initial slope which is characterised by the longitudinal stiffness C_s of the tyre. The longitudinal stiffness tends to be low when the tyre is new and has full tread depth, and increases with age, i.e. as the tyre wears.

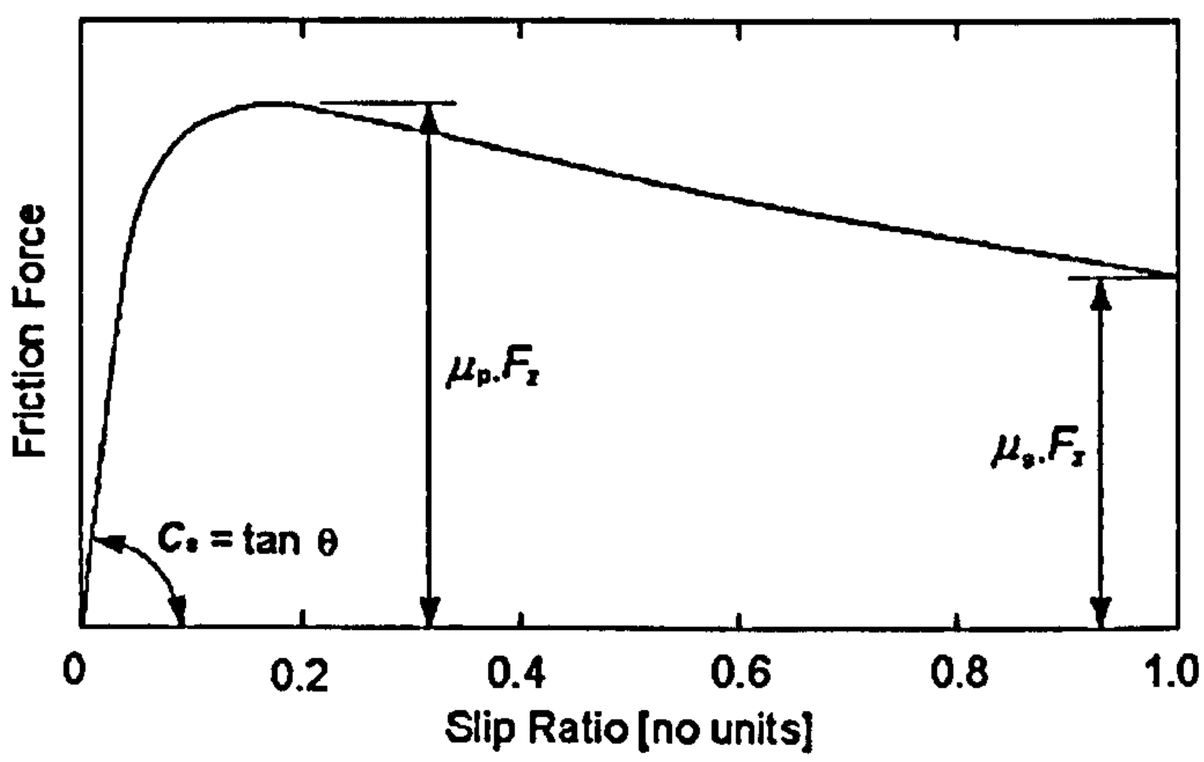

Figure 2.7 Variation in friction force with longitudinal slip during braking

The friction force usually reaches a maximum when the slip ratio is between 0.1 and 0.2 [33, 34]. Beyond the peak value, the friction force reduces as the sliding region at the rear of the contact patch extends further forward. At a slip ratio of 1.0 the sliding region has extended the entire length of the contact patch and the wheel is said to be locked.

The friction force is characterised at the peak and sliding conditions by the friction coefficients μ_p and μ_s, respectively. These peak and sliding coefficients are the ratio of the friction forces to the magnitude of the normal load. They are influenced by a number of factors including the ground surface and its condition, the normal load, the inflation pressure and the forward speed. Typical peak and sliding coefficients for a variety of surfaces are shown in Table 2.1. The grip (surface adhesion) is provided when the tyre tread deforms around microscopic asperities in the surface [35]. Rain, ice and snow fill these asperities and reduce tyre grip and therefore the friction coefficients. In the work conducted by Ervin [36] it is shown that increasing the normal load decreases the friction coefficients; at the rated load of the tyre, the peak and sliding coefficients

decrease by about 0.01 for a 10 percent increase in the magnitude of the normal load. On dry ground surfaces, the friction coefficients are known to be slightly affected by the inflation pressure. On wet surfaces, an increase in the inflation pressure significantly increases both coefficients [8]. In work by Dugoff and Brown [37], a significant decrease in the peak and sliding coefficients is shown to occur as the speed increases.

Surface	Peak coefficient μ_p	Sliding coefficient μ_s
Asphalt and concrete (dry)	0.8-0.9	0.75
Asphalt (wet)	0.5-0.7	0.45-0.6
Concrete (wet)	0.8	0.7
Gravel	0.6	0.55
Earth road (dry)	0.68	0.65
Earth road (wet)	0.55	0.4-0.5
Snow (hard-packed)	0.2	0.15
Ice	0.1	0.07

Table 2.1 Typical tyre/ground friction coefficients for a range of surfaces [18]

Anti-lock Braking Systems (ABS) mentioned in Chapter 1 monitor wheel motion during braking manoeuvers. Sensors detect excessive wheel deceleration and the slip ratio is estimated from this information [9]. The braking system maintains the slip ratio near the peak of the friction-slip curve and does not allow the wheels to lockup. Thus, with ABS the dominant tyre performance parameter is the peak friction coefficient. As a consequence, the braking distances are greatly decreased, reducing the likelihood of an impact with a vehicle or obstacle in front during braking. Similarly, the peak coefficient is of primary importance when traction control or Anti-Spin Regulation (ASR) is employed. By monitoring excessive accelerations, the acceleration or hill-climbing performance of a vehicle is optimised. Such systems are, as previously mentioned, important to vehicle dynamics control but they do not measure contact patch forces.

2.7 Cornering Characteristics

The lateral forces required during cornering (or lane change maneuvers) are created by lateral slip (slip angle), lateral inclination (camber angle), or a combination of the two.

2.7.1 Slip Angle

When a slip angle is applied to a rolling tyre, tread elements are deflected in the lateral direction as they progress through the contact patch, as shown in Figure 2.8 [8]. The deflection and corresponding shear stress increases as the element moves through the contact patch until the shear stress on the element overcomes the available friction and sliding occurs. This local behaviour has been investigated by Gough [38], and Lippmann and Oblizajek [39]; no other research into the contact stresses could be found. Integration of the lateral shear stresses over the contact patch yields the cornering force which is generated towards the rear of the contact patch, at a distance from the centre of the contact patch which is usually referred to as the pneumatic trail. At the centre of the contact patch, the cornering force and an aligning moment exist. The magnitude of the aligning moment is equal to the cornering force multiplied by the pneumatic trail.

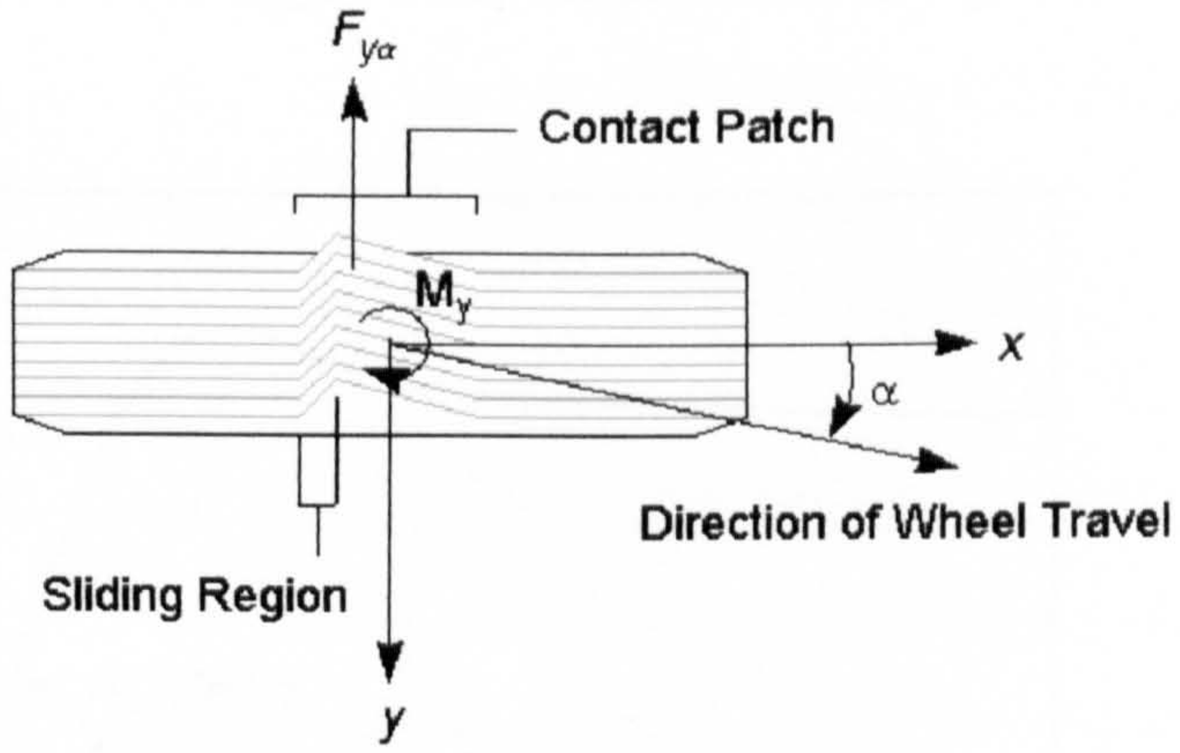

Figure 2.8 Tread deflection in contact patch at a slip angle [8]

The development of the cornering force is not instantaneous, it lags the applied slip angle as the tyre sidewalls deflect in the lateral direction [38, 40]. The cornering force usually takes approximately one revolution of the tyre to reach the steady-state condition [41]; the distance required to reach the steady-state usually being referred to as the relaxation length. A typical cornering force response to a step change in the applied slip angle is shown in Figure 2.9. Evidently, the time lag depends on the speed of rotation of the tyre. For a passenger car travelling at a speed of 50 km/h, the time lag will be around 0.1 second, which is imperceptible to many motorists. The effect, however, may be noticed by 'expert' drivers as a lag or sluggishness in turning response.

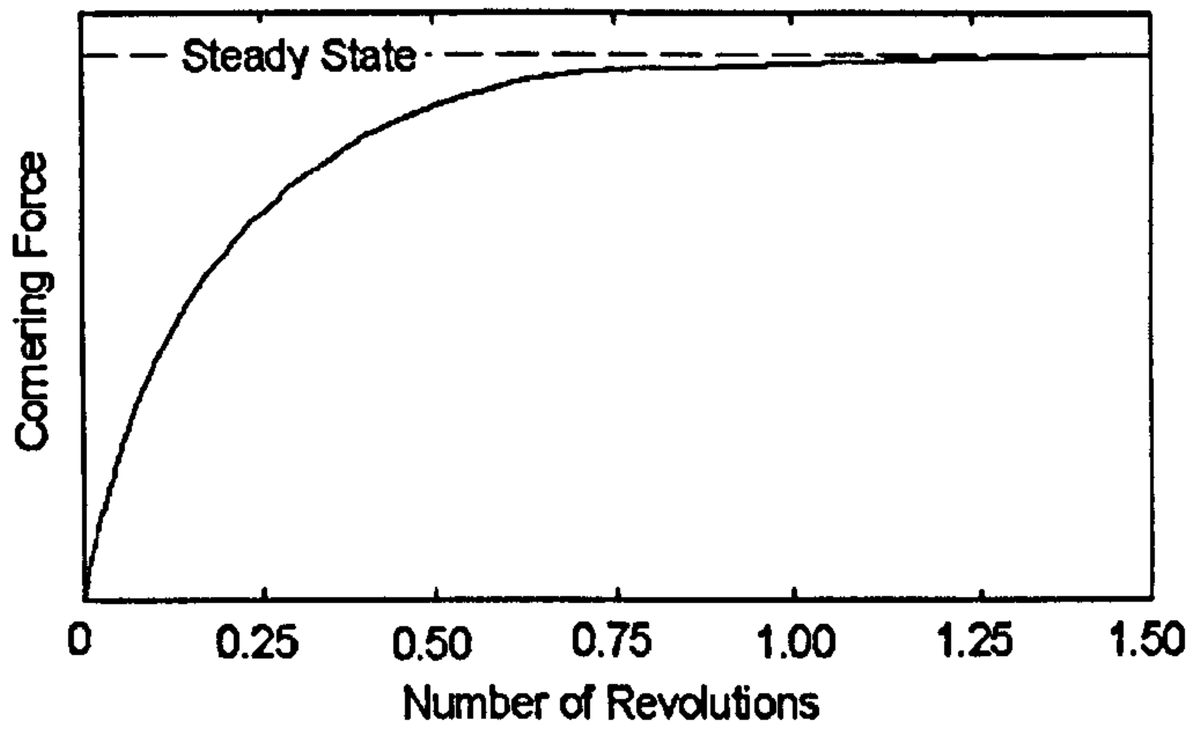

Figure 2.9 Cornering force response to a step change in the applied slip angle [8]

The global cornering properties of tyres have been studied extensively [19, 22, 31], and are usually characterised in the steady-state condition. The general relationship between the slip angle and the cornering force is shown in Figure 2.10. It should be noted that when the slip angle is positive the cornering force is negative according to the tyre axis system shown in Figure 2.3. A negative slip angle results in a positive cornering force.

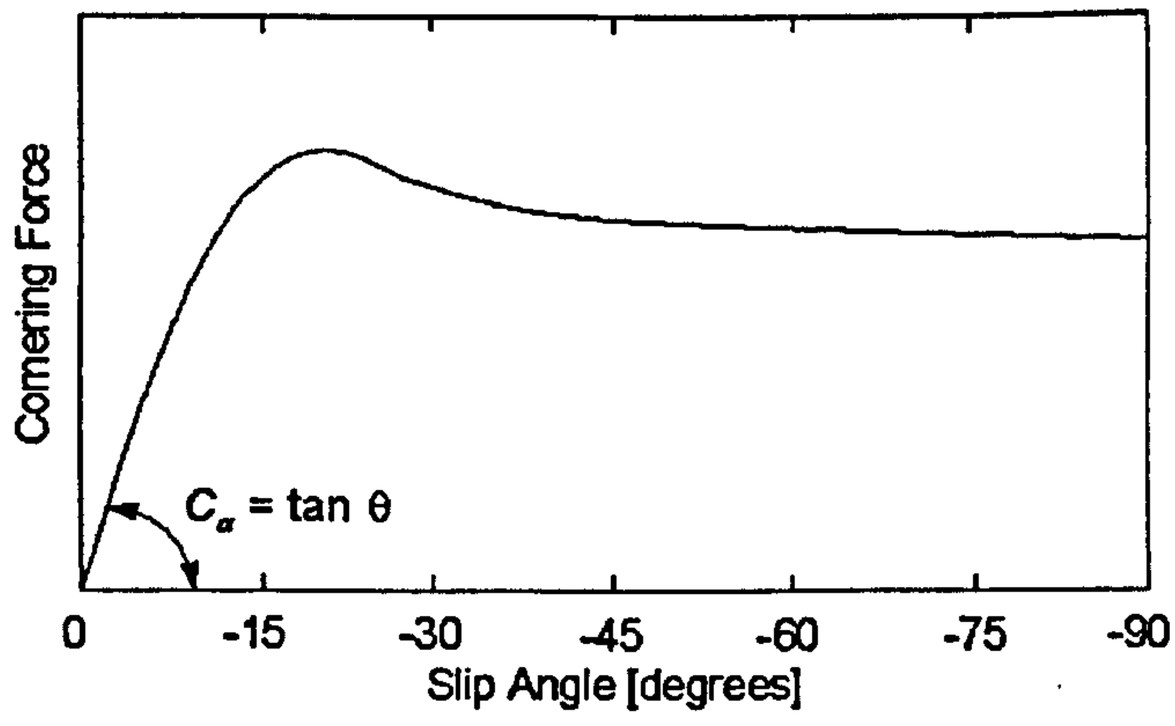

Figure 2.10 Variation in cornering force with slip angle [8] (note negative slip angles)

The cornering force increases with slip angle along an initial slope which is characterised by the cornering stiffness C_α of the tyre. The cornering stiffness is given by

$$C_\alpha = -\left(\frac{dF_{y\alpha}}{d\alpha}\right)\Bigg|_{\alpha=0} \tag{2.2}$$

The cornering stiffness is defined as the negative of the slope, and is therefore positive.

The maximum cornering force, which is equal to the peak coefficient of friction multiplied by the normal load, usually occurs when the slip angle is between 15 and 25 degrees [8, 18]. Beyond the peak value, the cornering force diminishes as the sliding region grows in the contact patch. At a 90 degree slip angle (beyond normal operating conditions and corresponding to a vehicle sliding sideways without forward motion), the cornering force is equal to the sliding friction coefficient multiplied by the normal load.

The cornering stiffness of a tyre is dependent on a number of factors, most notably the normal load and inflation pressure. The effect of normal load on the cornering stiffness and cornering coefficient is discussed in a number of text books [8, 18] and also in work by Chu [42]. The cornering coefficient is the ratio of the cornering stiffness to the magnitude of the normal load. It should be noted that the cornering stiffness increases to a maximum near the rated load of the tyre [8]. This increase in stiffness is not proportional to the increase in magnitude of the normal load and, as a consequence, the cornering coefficient decreases as the magnitude of the normal load is increased. The cornering stiffness of a tyre also increases with an increase in the inflation pressure but the increase tends to be less significant than that observed with normal load [18]. This is shown in the papers by Nordeen and Cortese [22], and also Collier and Warchol [28].

Segel [43] has studied the relationship between the aligning moment (sometimes referred to as the aligning torque) and slip angle for a bias- and radial-ply truck tyre at various normal loads. Initially, the aligning moment increases with an increase in slip angle. The moment reaches a maximum at a particular slip angle and then decreases with a further increase in slip angle. It should be noted that the maximum aligning moment does not usually occur when the cornering force is at a maximum [38]. This is mainly because the sliding of tread elements at the rear of the contact patch causes the point of application of the cornering force to shift forward. At very high slip angles the sliding region can advance forward such a distance that the aligning moment can become negative [8, 44].

2.7.2 Camber Angle

When a camber angle is applied to a tyre, a camber thrust $F_{y\gamma}$ develops orientated in the direction the tyre is inclined. This is shown in Figure 2.11. This camber thrust is generated because the axis of rotation of the tyre is not parallel to the ground, but the

tyre is constrained to move in a straight-line. The thrust acts in front of the wheel centre and an aligning moment is also produced. The aligning moment due to camber angle for a bias-ply tyre is typically of the order of 10 percent of the magnitude produced in response to an equivalent slip angle, and the value is even less for a radial-ply tyre [8].

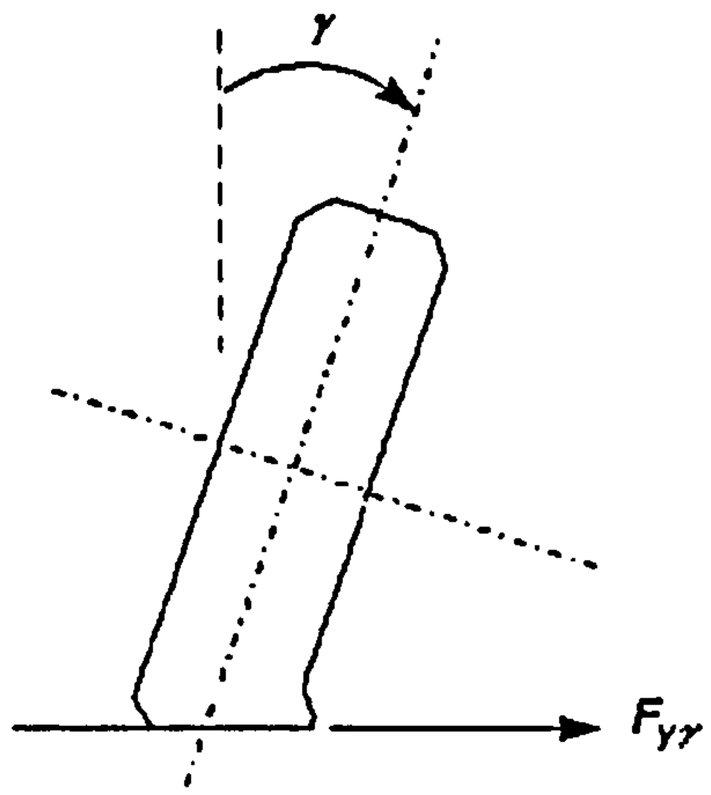

Figure 2.11 Behaviour of a cambered tyre

The relationship between camber thrust and camber angle is discussed in reference [22], and is characterised by a parameter referred to as the camber stiffness C_γ, given by

$$C_\gamma = \left(\frac{dF_{y\gamma}}{d\gamma} \right) \Bigg|_{\gamma = 0} \tag{2.3}$$

The camber stiffness is typically between 10 and 20 percent of the cornering stiffness. Similar to the cornering stiffness, the normal load and inflation pressure have an influence on the camber stiffness. The camber stiffness increases with an increase in the magnitude of the normal load [22]. This is shown in work by Segel [43] who considered the variation of stiffness with normal load for three truck tyres. An increase in the stiffness is also observed for bias-ply tyres with an increase in inflation pressure. Radial-ply tyres, however, are much less sensitive to changes in the inflation pressure [36].

2.7.3 Conicity and Ply Steer

It is interesting to note that, due to "non-symmetries [10]" in the tyre construction, such as conicity and ply steer, a lateral force usually develops even at zero slip and camber

angles. Conicity is usually caused by an asymmetrical offset in the position of the belts during fabrication. The tyre has a bias towards a conical shape and, as a consequence, will want to follow an arc centred about the apex of the cone. This is shown in Figure 2.12. The tyre is restrained to maintain a straight-line during rolling and, thus, a lateral force develops. The lateral force does not change direction with reverse rotation.

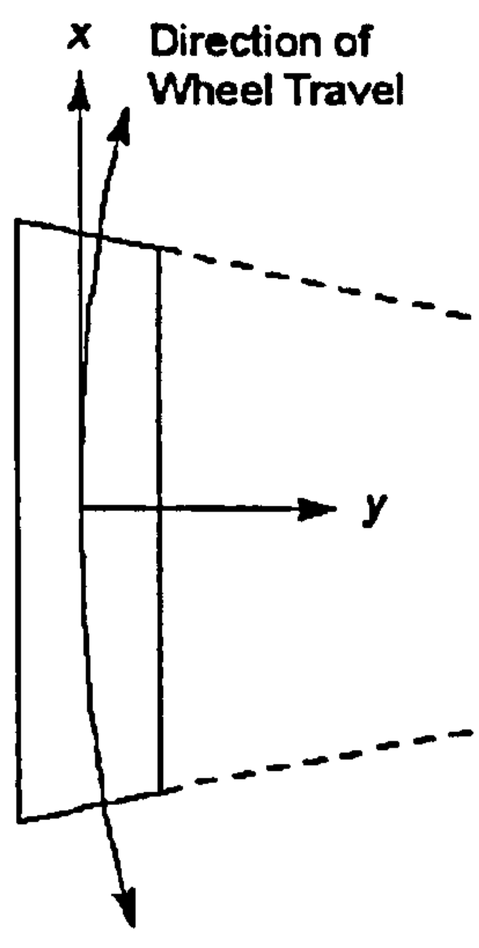

Figure 2.12 Conicity in an automobile tyre

Ply steer arises due to the orientation of the cords in the belts, and is generally a larger effect than conicity. During free-rolling, the tyre will steer from its intended straight-line course. A lateral force develops when the tyre is constrained to roll in a straight-line and this force changes direction with reverse rotation. To minimise the effect of ply steer, the cords in successive layers of the belt are orientated at opposite angles (see Section 2.2).

2.8 Combined Braking and Cornering

When longitudinal and lateral slip are applied simultaneously to a tyre, both the longitudinal and lateral forces differ considerably from the values obtained under independent conditions [8]. Figures 2.13 and 2.14 show the influence of longitudinal slip and slip angle on the braking force and lateral force, respectively. These measurements were taken from the text book by Milliken and Milliken [10]. They show that applying a slip angle usually reduces the braking force at a constant longitudinal slip. Similarly, applying a longitudinal slip usually reduces the lateral force at a constant slip angle. The relationship between the braking and lateral forces under various slip conditions has

been investigated by many researchers [33, 45] and it can be shown that the friction ellipse concept introduced in Chapter 1 is realised by enveloping the resultant curves.

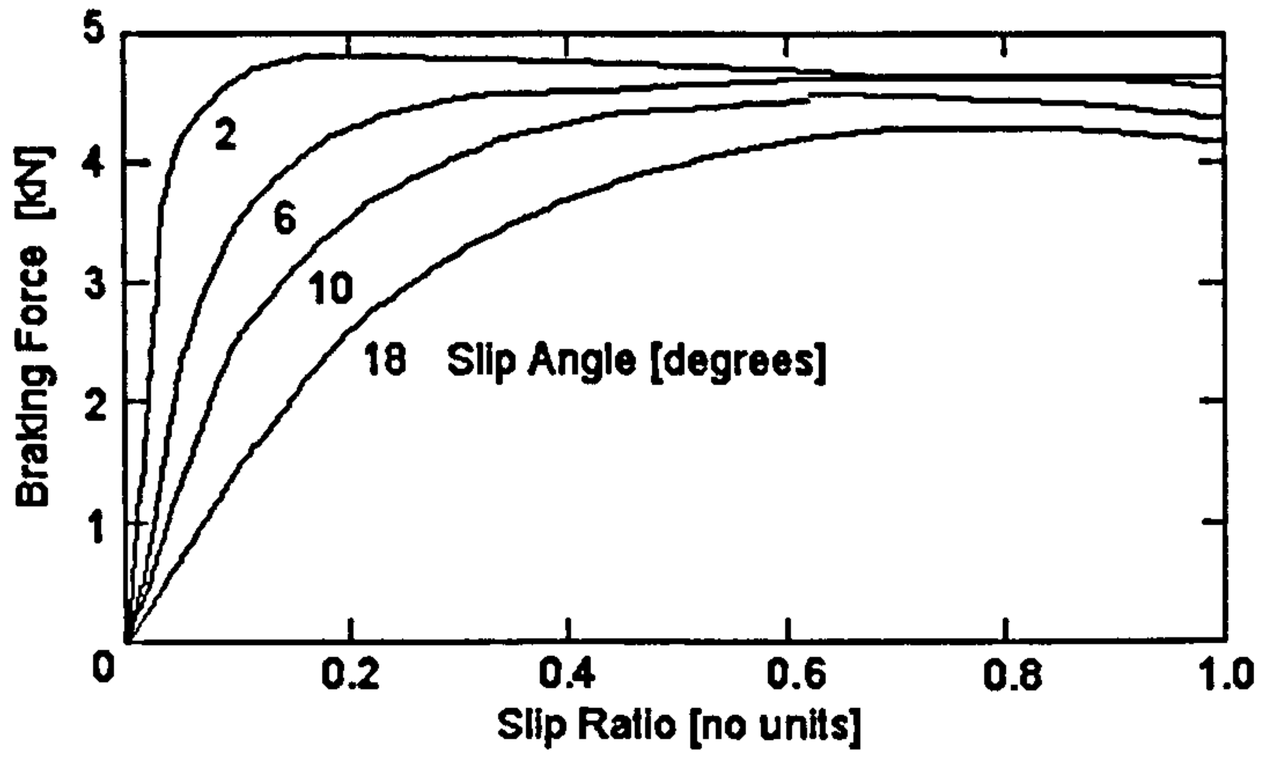

Figure 2.13 Variation in braking force with longitudinal slip at various slip angles [10]

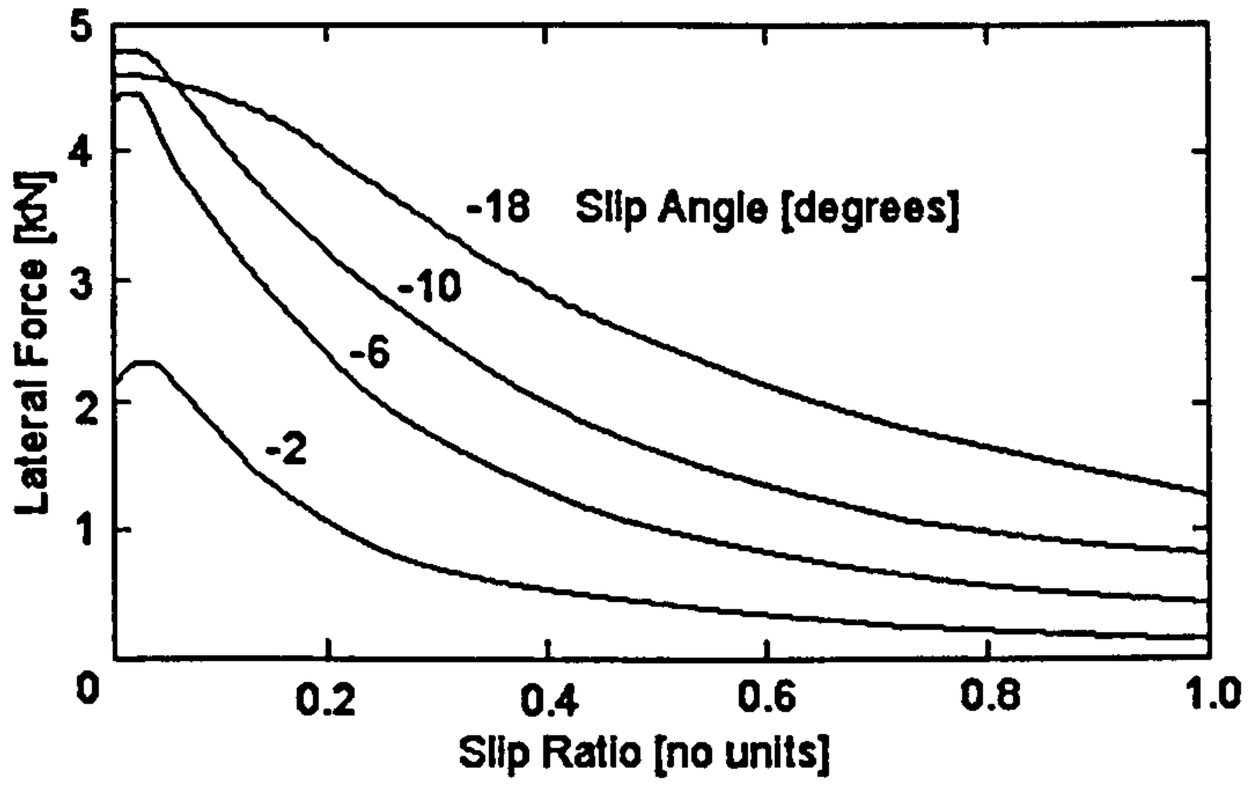

Figure 2.14 Variation in lateral force with longitudinal slip at various slip angles [10]

Based on the experimental observations described above, attempts have been made to formulate simple models to predict the longitudinal and lateral forces as functions of longitudinal slip and slip angle. Two of the most common models are the 'brush model' [33, 45, 46] and the 'magic formula model' [34, 47, 48]. The brush model is a semi-empirical tyre model which derives a relationship between the slip condition and the tyre response based on a limited understanding of both the tyre structure, and the interaction between the tyre and the ground. The magic formula model is an empirical model and determines the complex relationships based on experimental data. A detailed overview of these tyre models and other empirical and semi-empirical models is provided in reference [34]. The text book by Wong [18] also gives some insight into simple models.

2.8.1 Brush Model

The brush model is based on an idealised representation of the tyre local to the contact patch. The model consists of a row of elastic cylinders radially attached to a circular belt. The cylinders represent tread elements and the belt is assumed to deflect only in the vertical direction by applying a normal load. A contact length arises, and in the case of a frictionless contact surface, the cylinders (tread elements) are assumed to be orientated normal to both the ground and the flattened region of the belt. In the presence of friction, the cylinders deflect in the longitudinal and lateral direction when the tyre/wheel deviates from the free-rolling condition. The deflection of the tread elements is established by considering the displacements at both ends of the cylinder. The tractive contact stresses are acceptably assumed to be linearly dependent upon the deflections (when no sliding occurs in the contact patch), and are calculated based on the longitudinal and cornering stiffnesses which are determined from experimental data.

Sliding of the tread elements in the contact patch is introduced when the resultant shear stress exceeds the maximum allowable shear stress τ_{max} determined by the coefficient of friction μ and the normal pressure σ_z. In the landmark paper by Dugoff *et al.* [33], the normal pressure distribution in the contact patch is assumed to be uniform. Although this approximation is not exact, it represents an acceptable estimation for radial-ply tyres except at the edges of the contact patch. The maximum shear stress is given by

$$\tau_{max} = (\tau_{xz}^{\ 2} + \tau_{yz}^{\ 2})^{1/2} = \mu|\sigma_z| = \frac{\mu|F_z|}{2lw} \tag{2.4}$$

where l is the contact patch half length, and w is the contact patch width. It should be noted that this equation is related to the friction ellipse concept previously discussed.

In contrast to Dugoff *et al.* [33], other researchers have assumed different normal pressure distributions. In the models developed by Bernard *et al.* [45] and Francher *et al.* [46], the distribution in the contact patch is assumed to be trapezoidal in form, as shown in Figure 2.15, and is determined by the ratio $a/2l$. A uniform distribution is obtained when the ratio $a/2l$ is equal to zero and a triangle distribution is obtained when $a/2l$ equals 0.5. Bernard *et al.* [45] discuss varying the ratio $a/2l$ and suggest a uniform

distribution for radial-ply tyres and a distribution defined by the ratio $a/2l$ equals 0.25 for bias-ply and bias-belted tyres. Both Zegelaar [41] and Sakai [49] assumed a parabolic distribution. In the author's opinion, a better method would be to use contact stresses obtained by physical testing. However, such data has not been readily available. In Chapter 3, data is presented that could be used with the brush model to improve understanding of the contact patch stresses and their relationship to the global forces.

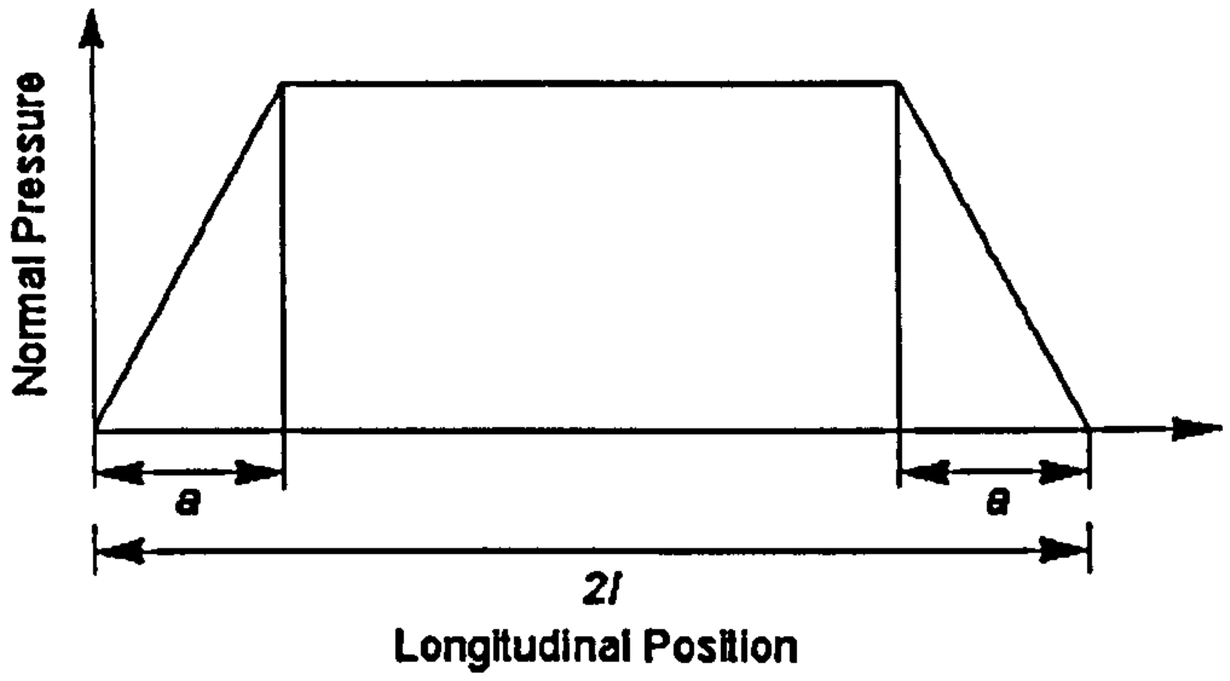

Figure 2.15 Normal pressure distribution [45]

2.8.2 Magic Formula Model

In the general form, the magic formula model [34, 47, 48] is based on the observation that global tyre force and moment characteristics under pure slip conditions (either longitudinal slip or slip angle) appear to be sine curves that have been modified by introducing an arctangent function (see Figures 2.7 and 2.10). The magic formula is

$$y(x) = D\sin(C\arctan\{Bx - E[Bx - \arctan(Bx)]\}) \tag{2.5}$$

where

$$y(x) = Y(X) - S_v$$

and

$$x = X + S_h$$

$Y(X)$ is either the longitudinal force F_x, the lateral force F_y, or the aligning moment M_z, and X is either the longitudinal slip s or slip angle α. The significance of the coefficients B, C, and D, and also the offsets S_h and S_v is shown in Figure 2.16.

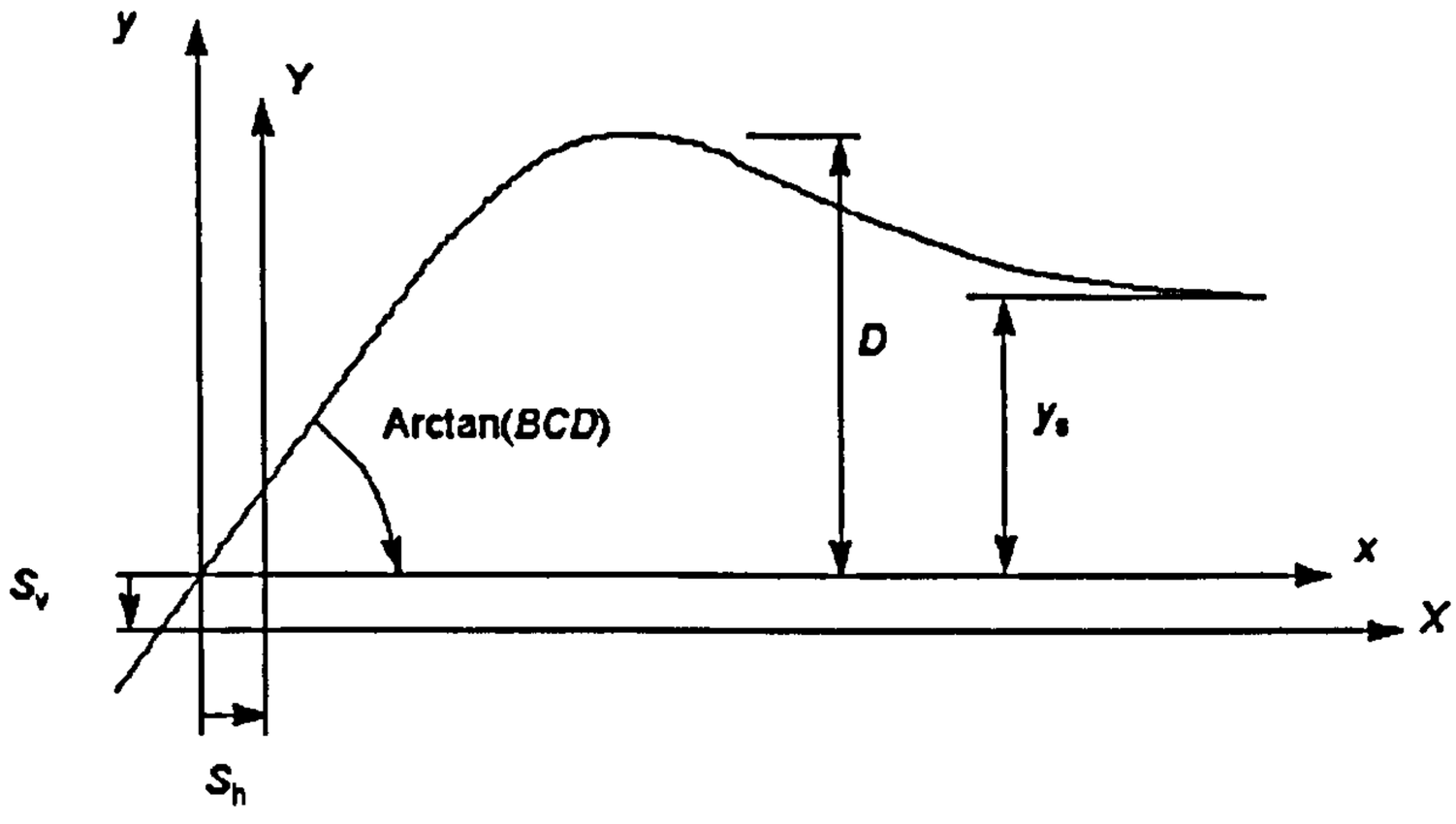

Figure 2.16 Coefficients used in the magic formula tyre model [44]

The coefficient D represents the peak value and the coefficient C determines the shape of the curve. Typical values used for the shape factor C are 1.65, 1.30 and 2.40 for the longitudinal force, lateral force and aligning moment curves, respectively [47]. The coefficients C and D also determine the asymptotic value at large slip angles y_s via

$$y_s = D\sin\left(\frac{\pi C}{2}\right) \tag{2.6}$$

The coefficient B influences the slope of the curve at the origin BCD. As discussed in Sections 2.6 and 2.7, the initial slope of the longitudinal force-slip and lateral force–slip angle curves is characterised by the longitudinal stiffness C_s and the cornering stiffness C_α, respectively. The coefficient E influences the curvature near the peak of the curve and the longitudinal slip or slip angle x_m at which the peak value occurs, and is given by

$$E = \frac{Bx_m - \tan\left(\frac{\pi}{2C}\right)}{Bx_m - \arctan(Bx_m)} \tag{2.7}$$

The offsets S_h and S_v account for rolling resistance (see Section 2.5) in the longitudinal force curve. In the lateral force and aligning moment curves, they account for non-symmetries in the tyre construction, such as conicity and ply steer (Section 2.7.3), and may also be used to represent the offset of the lateral force curve due to camber angle.

To express the dependence of the coefficients B, C, D and E and the offsets S_h and S_v on the normal load, further functions are provided. The numerous constants (more than 30) in these functions are described by Pacejka and Bakker as the "ultimate parameters in the model [47]." These parameters are determined by regression techniques from tyre experimental data and are usually calculated with specific computer software [50, 51].

It is important to reiterate that the magic formula model does not incorporate an understanding of tyre behaviour or the interaction between the tyre and the ground surface, and therefore it has only a limited use in the development of smart tyre technologies. Nevertheless, it is noted that many years' research has been borne out of this formula and its ability to predict tyre characteristics under a wide range of conditions. The formula is routinely used in the automotive industry and was instrumental in the evolution of tyre modelling as a vehicle and tyre development tool.

2.9 Finite Element Models

In parallel with simple models, there has also been a move towards simulating rolling tyres by the Finite Element (FE) method and numerous FE models are presented in the literature. These models have evolved as the software has developed and computational power has increased, and as a consequence, the models vary greatly. Implicit FE software was initially used to simulate tyre behaviour but the complexity of the automobile tyre structure, and limitations associated with the implicit method meant the prediction of dynamic tyre responses was not feasible. Thus, most simulations have been limited to prediction of static behaviour [52-54]. In the early 1970's, Durand and Jankovick [52] and then later (in 1981) Kennedy, Patel and McMinn [53] simulated tyre deformation due to inflation pressure. Trinko [54] attempted to simulate the pressure distribution in the contact patch under normal load but only a reasonable correlation was obtained with experimental data. The author suggests the correlation is related to the mesh specification which was limited by the available computational resource. Similar work has been carried out by other researchers [55, 56] with varying degrees of success.

In recent years, increases in computational power and the development of explicit FE software has made the prediction of dynamic (rolling tyre) behaviour attainable, and work in this area has increased. The work, however, has focused on the prediction of

global tyre behaviour [57-60]. Koa and Muthukrishnan [57] have simulated the global responses of a tyre impacting a cleat and a reasonable correlation was obtained between the dynamic forces at the wheel hub with those obtained experimentally. Further work has also been carried out by Kamoulakos and Koa [58], and Hanley [59]. At selected inflation pressures, Koishi, Kabe and Shiratori [60] have simulated the cornering forces of a radial-ply passenger car tyre. To the author's knowledge no other work has been performed to specifically simulate local tyre behaviour in the contact region. And it is this category of model which is essential to the development of smart tyre technologies.

To develop a FE model, a physical understanding of the tyre structure, particularly the geometry and material properties, is required. The tyre structure is divided into small discrete subregions (elements) joined only at specific points (nodes) on their boundaries to form a mesh. This is shown in Figure 2.17 [61]. The forces are transmitted by the nodes from one element to the next. The elements may be one-, two, or three-dimensional as described in the text book by Mottram and Shaw [62], and the model may consist of a few axisymmetric elements [63] or many thousands of solid and shell/membrane elements [57, 64]. The most frequently used elements are based on the stiffness method and the stresses, strains and displacements are determined by simple displacement functions; the unknown in these functions being the nodal displacements.

2.9.1 Implicit Integration

In traditional implicit integration, the response of an element in the FE mesh is given by

$$\{\mathbf{F}^e\} = [\mathbf{K}^e]\{\delta^e\} \tag{2.8}$$

where $\{\mathbf{F}^e\}$ is the element force vector, $[\mathbf{K}^e]$ is the element stiffness matrix, and $\{\delta^e\}$ is the element displacement vector. It should be noted that for an eight-node solid element, nodal displacements comprise three independent translational displacements. Similarly, three independent forces are assumed to act at each node. These independent forces and displacements are defined based on a Cartesian coordinate system, and have components in the x-, y- and z-directions, such that at node i the nodal displacements are u_i, v_i and w_i, and the nodal forces are F_{xi}, F_{yi} and F_{zi}. The element vectors $\{\mathbf{F}^e\}$

and $\{\delta^e\}$ have twenty four terms (degrees of freedom m) and thus $[\mathbf{K}^e]$ is a 24 by 24 matrix. In a whole structure, the number of degrees of freedom is a combination of all of the element degrees of freedom and are typically in the order of hundreds of thousands.

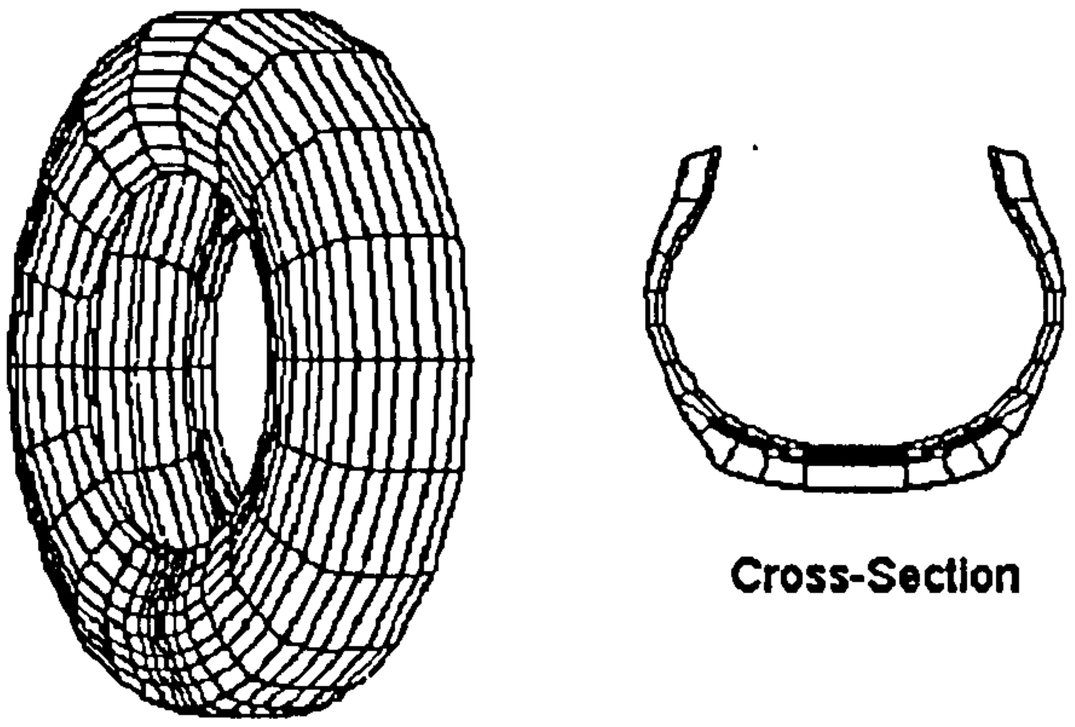

Figure 2.17 Finite element model of a passenger car tyre

In non-linear analysis which is necessary for the simulation of tyre behaviour, the global force vector $\{\mathbf{F}\}$ and stiffness matrix $[\mathbf{K}]$ are non-linearly dependent upon the global displacement vector $\{\delta\}$ and the complexity and computational time is increased. To determine the non-linear response, the force-displacement relationship is usually broken down into a series of linear steps, and a combination of load incrementation and iteration methods are employed to obtain the final solution. A general overview of these methods is provided by Becker [65]. Further details on the algorithms etc. are presented in the text book by Crisfield [66]. The methods are usually automated in the software package and require little or no interaction from the FE analyst. Thus, the accuracy of these numerical methods has a significant influence on the reliability of the simulation results.

Implicit solution methods can also be used to progress simulations in the time domain, but the global equilibrium must first be achieved by iteration before the local element variables are calculated. In contrast, explicit methods calculate local variables directly without the need for global equilibrium calculations. Thus, the explicit method is better suited for predicting highly transient deformations [67]. This is the reason the explicit package LS-DYNA [17] is used for the simulation work herein. The fundamental difference between explicit and implicit time integration methods is demonstrated by

comparison of the solution of Newton's Second Law using each method [68]. Newton's Second Law can be expressed in matrix format (ignoring damping) for FE purposes as

$$[\mathbf{M}]\{\ddot{\delta}\} + [\mathbf{K}]\{\delta\} = \{\mathbf{F}_{ex}\} \tag{2.9}$$

where $[\mathbf{M}]$ is the mass matrix and $\{\ddot{\delta}\}$, and $\{\mathbf{F}_{ex}\}$ are the nodal accelerations and external force vectors, respectively.

In implicit integration, a solution is incremented from step n to step $n+1$ in time. The implicit program iterates to determine Equ.(2.9) is satisfied by the equilibrium of internal forces (left-hand side) with external forces (right-hand side) and the implicit solution is

$$[\mathbf{M}]\{\ddot{\delta}\}_{n+1} + [\mathbf{K}]\{\delta\}_{n+1} = \{\mathbf{F}_{ex}\}_{n+1} \tag{2.10}$$

The time integration is typically calculated using a finite difference method based on average acceleration and, thus, the nodal accelerations and displacements are related via

$$\frac{\{\delta\}_{n+1} - 2\{\delta\}_n + \{\delta\}_{n-1}}{\Delta t^2} = \frac{\{\ddot{\delta}\}_{n+1} + 2\{\ddot{\delta}\}_n + \{\ddot{\delta}\}_{n-1}}{4} \tag{2.11}$$

By substituting Equ.(2.11) into Equ. (2.10), the displacements can be solved directly:

$$\left[\frac{4[\mathbf{M}]}{\Delta t^2} + [\mathbf{K}]\right]\{\delta\}_{n+1} = \{\mathbf{F}_{ex}\}_{n+1} + \frac{4[\mathbf{M}]}{\Delta t^2}(2\{\delta\}_n - \{\delta\}_{n-1}) + [\mathbf{M}](2\{\dot{\delta}\}_n + \{\ddot{\delta}\}_{n-1}) \tag{2.12}$$

where Δt is the time step size. The displacements at step $n+1$ are a function of the displacements and accelerations at the previous time step and, thus, Equ.(2.12) requires the formation of the mass/stiffness matrix terms on the left-hand side before equilibrium calculations can commence. If equilibrium is not achieved, the matrix coefficients need to be recalculated with a different time step at a considerable computational cost.

2.9.2 Explicit Integration

In explicit integration, Equ.(2.9) is first rearranged into the form:

$$[\mathbf{M}]\{\ddot{\delta}\} = \{\mathbf{F}_{ex}\} - [\mathbf{K}]\{\delta\} = \{\mathbf{F}_{ex}\} - \{\mathbf{F}_{in}\} \tag{2.13}$$

where $\{\mathbf{F}_{in}\}$ is the internal nodal force vector and the accelerations can be calculated directly via a diagonal (lumped) mass matrix that is trivial to solve. Thus, the nodal velocities and displacements can then be calculated via the central-difference method as

$$\{\dot{\delta}\}_{n+1/2} = \{\dot{\delta}\}_{n-1/2} + \overline{\Delta t}\,\{\ddot{\delta}\}_n \tag{2.14(a))}$$

$$\{\delta\}_{n+1} = \{\delta\}_n + \Delta t_{n+1}\,\{\dot{\delta}\}_{n+1/2} \tag{2.14(b))}$$

where

$$\overline{\Delta t} = \frac{\Delta t_{n+1} + \Delta t_n}{2}$$

It should be noted that in Equ.(2.14(a)) the velocities are calculated at the half time step position but this is usually trivial because the time step size is small [68]. More significantly is the fact that (for stability of the central-difference method) the time step size is limited by the system frequency ω. The stable time step size can be shown to be

$$\Delta t \leq \frac{2}{\omega} \tag{2.15}$$

Thus, the maximum time step size is governed by the highest system natural frequency. A good estimate of the highest frequency of the system can be obtained by considering the properties of the individual elements in the mesh. This method has a significant computational benefit [68] and is therefore used in explicit software programs. In the program, the time step size for each element is calculated to determine the controlling value. Increasing the mass (via the element mass matrix $[\mathbf{M}^e]$) or reducing

the stiffness (via the element stiffness matrix $[\mathbf{K}^e]$) of the controlling elements increases the stable time step by reducing the highest frequency of the mesh. Obviously, reducing the mass or increasing the stiffness has the opposite effect. An increase in the time step size reduces the computational time, *and visa versa.* This method to reduce simulation time is used by the author in Chapters 5 and 6. In non-linear analysis, there is not a significant increase in computational time because the small time step size effectively allows the development of numerical methods that linearise the non-linear response [67]. A comprehensive description of these methods is provided by Belytschko *et al.* [69].

2.10 Summary

A review of the tyre research literature has been completed. The chapter has described the modern automobile tyre structure and the normal and shear stresses, and resultant forces and moments exerted on it. Previous work carried out to characterise tyre behaviour in the contact patch has been discussed and the related attempts to simulate this behaviour using simple empirical and semi-empirical models have been highlighted. An overview of complex FE tyre models has also been presented and the implicit and explicit methods have been discussed. Thus, the information reported in this chapter is essential to aid understanding of the research methodology and discussions presented in subsequent chapters. The chapter has highlighted the lack of knowledge about local tyre behaviour in the contact patch and the absence of existing tyre models to simulate this behaviour. By doing so, the chapter has established the motivation behind this thesis.

Chapter 3 Experimental Work to Characterise Tyre Behaviour in the Contact Patch

3.1 Introduction

Numerous papers exist which present simple models that predict resultant forces and moments in a rolling tyre. As discussed in Section 2.8, the models may be broadly categorised into two groups; empirical models, notably the 'magic formula model' [34, 47, 48], and semi-empirical models such as the 'brush model' [33, 45, 46]. Empirical models derive a relationship between the an input condition and the tyre response using experimental data. Semi-empirical models combine experimental data with a limited understanding of the tyre structure and the interaction between the tyre and the ground, but in doing so, imply the nature of the contact normal and shear stress distributions.

In parallel with these simplified treatments there has also been a move towards simulating rolling tyres by the Finite Element (FE) method (see Section 2.9). Although FE tyre models have the potential to show internal structural deformations local to the contact patch, the models have tended to be used to simulate global tyre behaviour [57, 59, 60]. Advanced simulations of rolling tyres are important to the tyre industry since if contact patch stresses could be continually measured in each of the tyres under motion, that tyre could become a key sensor in future vehicle control technology [7, 70]. To assess the performance of such models, there is a need to have physical test data that corresponds to 'actual' contact deformations. Thus, the purpose of this chapter is to enhance understanding of tyre behaviour in the contact patch with reference to the author's need to validate FE simulations. The investigation also contributes essential new physical test data that could be used by tyre technologists and/or vehicle dynamic analysts to evaluate the assumed contact stresses in existing semi-empirical models.

3.2 Experimental Tyre

A P195/65 R15 automobile tyre mounted on a standard wheel with a 5.5J rim contour was provided by Dunlop Tyres Limited for the purpose of the investigation. The same experimental tyre was also used in the related project carried out by Dennehy [9]. A labelled and dimensioned sketch of the tyre cross-section is shown in Figure 3.1.

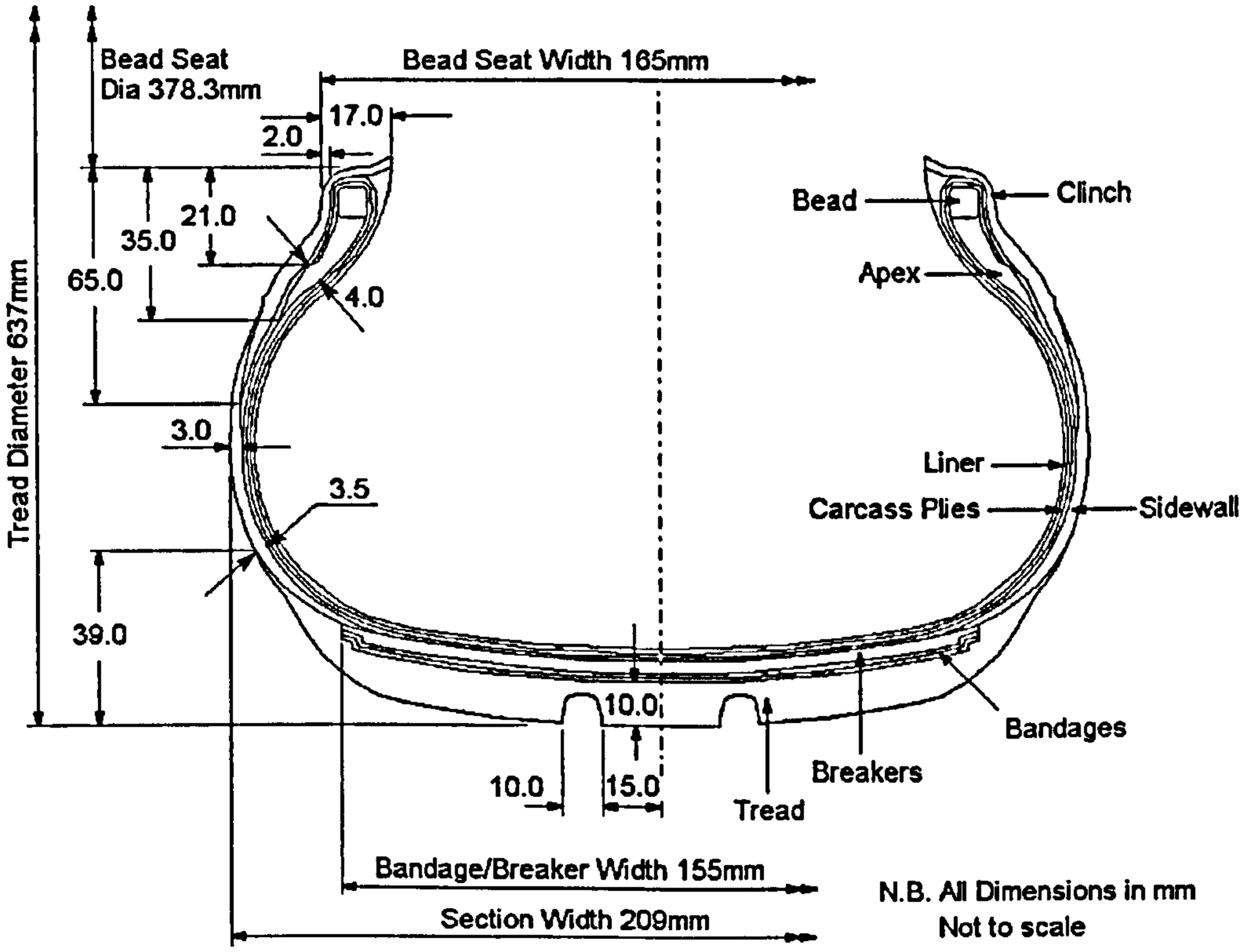

Figure 3.1 Experimental tyre cross-section

The construction of the experimental tyre was considered to be typical of a radial-ply passenger car tyre (see Section 2.2) and consisted of a number of rubber components (tread, sidewall, liner, apex and clinch), and a number of reinforced rubber composites (bead, carcass plies and belt). The carcass comprises two plies of nylon cords orientated at 90 degrees to the tyre circumference and the belt comprises two plies of steel cords known as breakers, and two plies of nylon cords referred to in this thesis as bandages. This terminology is common in the tyre industry. The steel cords in the belt are orientated at approximately 20 degrees to the tyre circumference and the nylon cords are oriented circumferentially around the tyre. The tyre has a simple plain tread consisting of two circumferential grooves. This tread pattern was selected to eliminate the complex

but small scale local effects which are caused by modern tread designs. The grooves were cut in the experimental tyre to represent the approximate ratio of contacting to non-contacting patch area, the 'land/sea ratio', observed in a typical automobile tyre.

3.3 Testing Equipment

The stationary (non-rolling) behaviour of the experimental tyre was investigated using a load-deflection machine and the rolling behaviour using flat bed and rolling drum tyre testing machines at the research laboratories of Dunlop Tyres Ltd., Birmingham, UK.

3.3.1 Load-Deflection Machine

The load-deflection machine shown in Figure 3.2 is used to measure the structural behaviour of a stationary tyre under normal load. The machine consists of two adjustable carriages running on rails, and a rigid glass plate against which the tyre is loaded. The specimen is mounted on a wheel unit and subjected to quasi-statical loading. The rear carriage contains an electrically operated loading system which allows normal loads to 50 kN to be applied. The position of the carriage is set by means of four pegs which fit into holes to give a coarse adjustment to enable a range of tyre sizes to be tested. The second carriage contains the load cell and the unit to which the tyre/wheel is attached. The glass plate can also be adjusted to give camber angles between ± 45 degrees.

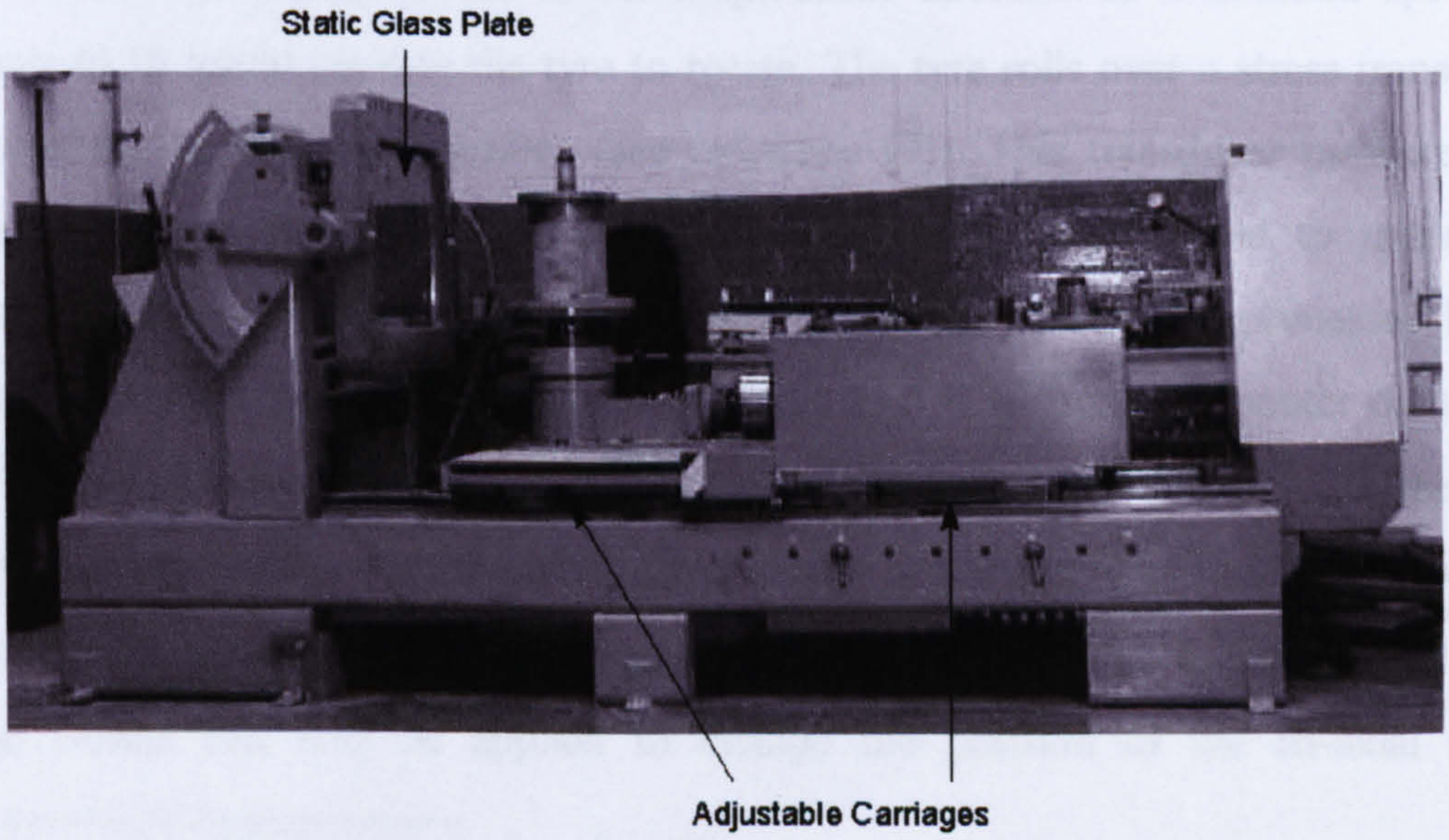

Figure 3.2 Load-deflection machine

3.3.2 Flat Bed Tyre Testing Machine

The rolling tyre experiments on the flat bed tyre testing machine were carried out by a colleague at the University of Warwick [9] with the assistance of the author. The flat bed tyre testing machine is shown in Figure 3.3. It should be noted that the physical testing data has not previously been analysed in the detail presented in this thesis.

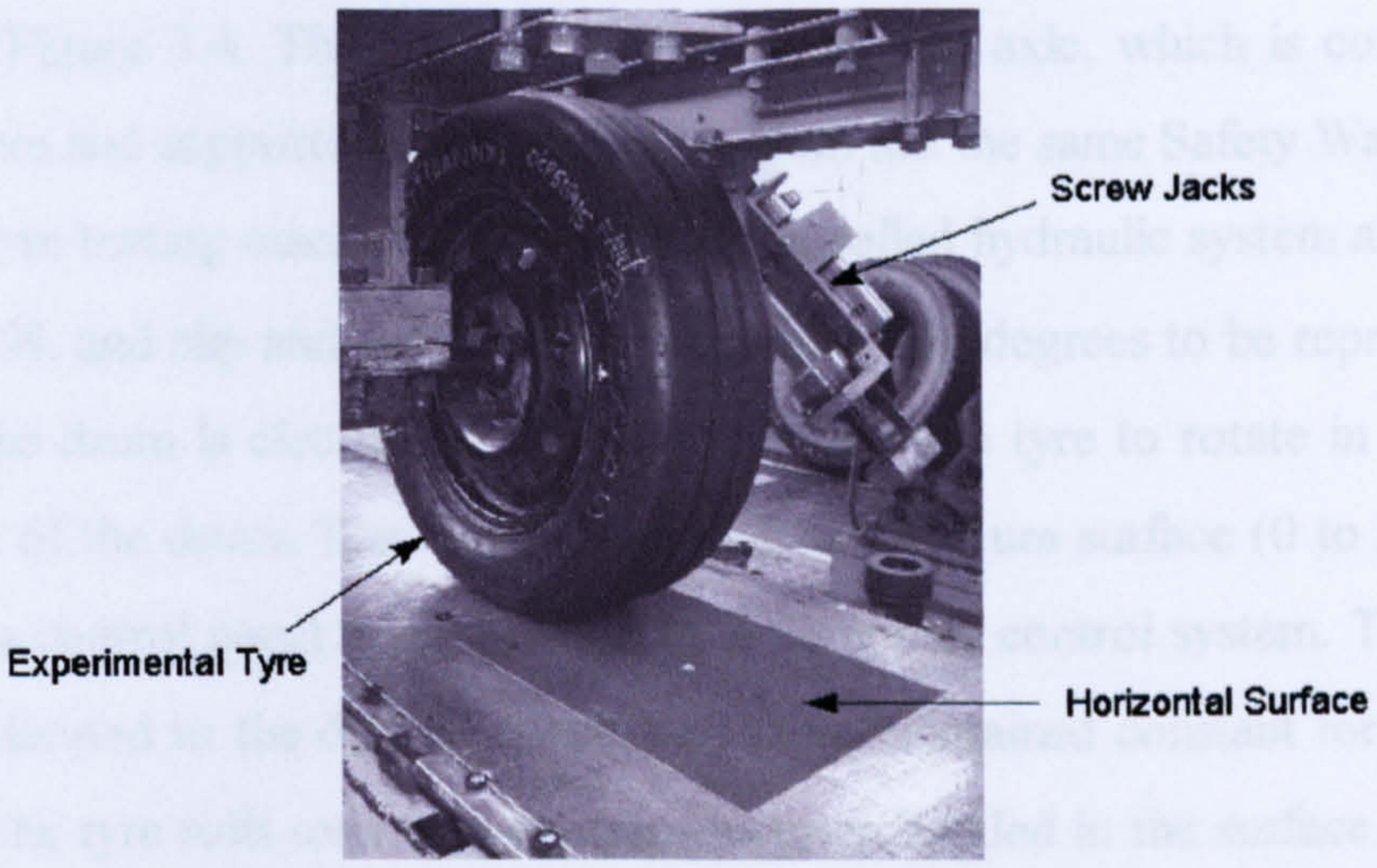

Figure 3.3 Experimental set-up on the flat bed tyre testing machine [9]

The flat bed tyre testing machine is used to roll a tyre at a low-speed over a 1.83 m long horizontal surface. On top of the steel flat bed there is a thin surface layer of Safety Walk[1], a coarse glasspaper material. The tyre is normally loaded against the surface which is then electrically driven in the longitudinal direction at a constant speed of 0.05 m/s (0.18 km/h) causing the tyre to rotate. The tyre rolls over a stress transducer embedded in the horizontal surface (see reference [9]). This transducer measures the normal and shear stresses at the surface, and is regularly calibrated to ensure its accuracy. The measurements are sampled at a frequency of 100 Hz, processed by an adjoining computer and then stored electronically in ASCII-format computer data files. These files are loaded into MATLAB [71] for analysis and visualisation. Adjustment on a number of electrically operated screw jacks allows normal loads to 35 kN, and slip and camber angles between ±15 and ±25 degrees, respectively, to be applied to the tyre. Lateral offsets can also be applied to change the position of the tri-axial stress

[1] Trade mark of 3M United Kingdom PLC (http://www.3m.com)

transducer relative to the tyre's centre-line. A program executed on the adjoining computer is used to calculate the screw jack settings for the required normal load, lateral offset, and slip and camber angles. The jack settings are then applied manually.

3.3.3 Rolling Drum Tyre Testing Machine

The rolling drum tyre testing machine is used to roll a tyre on a 2.39 m diameter drum, as shown in Figure 3.4. The tyre is mounted on a stub axle, which is connected to a frame structure and supported to ground. The drum has the same Safety Walk surface as the flat bed tyre testing machine. A computer controlled hydraulic system allows normal loads to 10 kN, and slip and camber angles between ±14 degrees to be represented. The rotation of the drum is electrically driven and causes the tyre to rotate in the opposite sense to that of the drum. The tangential speed of the drum surface (0 to 230 km/h) is selected via a control panel and regulated by a computer control system. The drum and tyre are accelerated to the desired speed, and then maintained constant for the duration of the test. The tyre rolls over a stress transducer embedded in the surface of the drum. This transducer is similar in construction and operation to that on the flat bed tyre testing machine. The normal and shear stresses are sampled at a constant frequency of 1024 Hz, processed by an adjoining computer and then stored electronically in ASCII-format computer data files. MATLAB [71] is again used for analysis and visualisation.

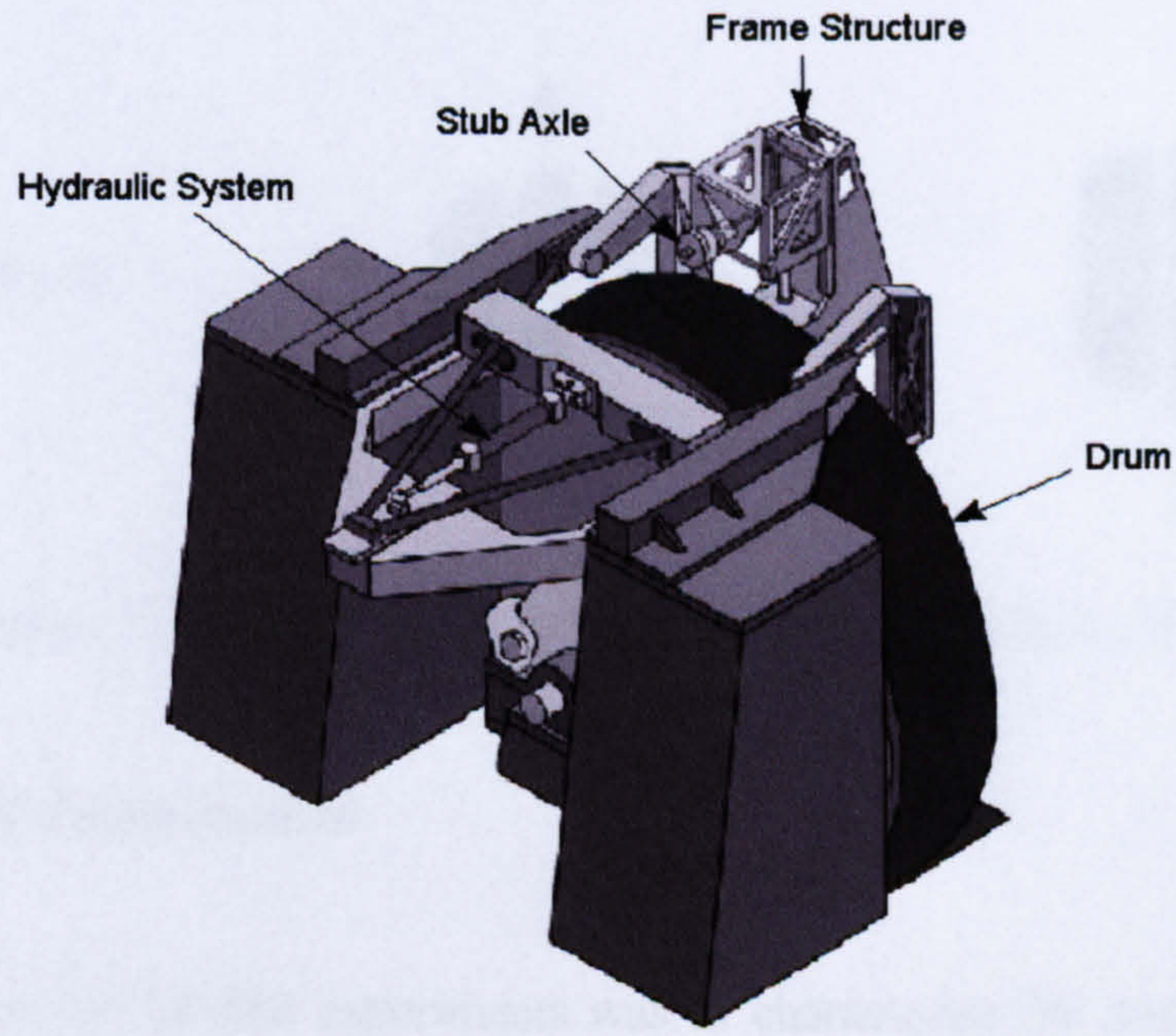

Figure 3.4 Sketch of rolling drum tyre testing machine

3.4 Tyre Experiments

The experiments carried out on the load-deflection machine are referred to here as the stationary experiments. Those carried out on the flat bed and rolling drum tyre testing machine are referred to as the flat bed and drum experiments, respectively. It should be noted that, in all the experiments, the inflation pressure of the tyre was kept constant at 200 kPa (29 psi). This is because the inflation pressure is known to influence tyre characteristics (see Sections 2.5 and 2.7). To ensure a meaningful comparison between the flat bed and drum experiments, similar environmental conditions were also observed.

3.4.1 Stationary Experiments

The stationary experiments were conducted to determine the vertical stiffness and the growth of the contact patch under normal load. Experiments were conducted at normal loads between 1 kN and 5 kN, in increments of 1 kN. The tyre's surface was coated in carbon black and a sheet of card was fixed to the glass plate. A print of the contact patch was produced at each normal load. The contact patch prints at 1, 3 and 5 kN are shown in Figure 3.5. The contact patch dimensions were measured from these prints using a mm ruler. The contact length was measured at the lateral centre of the tyre (see Figure 3.1) and the width was measured at the longitudinal centre, i.e. along the *y*-axis.

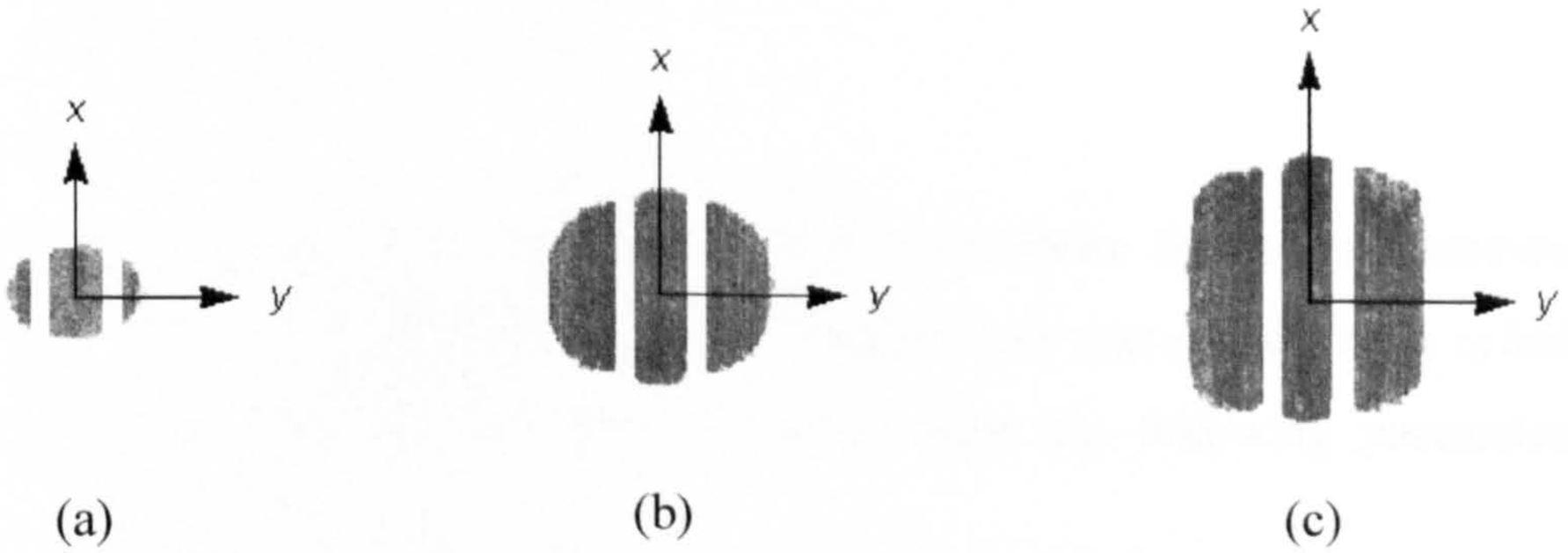

(a) (b) (c)

Figure 3.5 Contact patch prints: (a) 1 kN; (b) 3 kN; (c) 5 kN

3.4.2 Flat Bed Experiments

The objective of the flat bed experiments was to characterise the normal pressure and shear stress distributions in the contact patch when the experimental tyre was rolled on a

horizontal surface. The contact patch behaviour was investigated under free-rolling and cornering conditions (see Section 2.5 and 2.7), and the experiments were conducted with the following parameters as independent variables:

- normal loads between 1 kN and 5 kN, in increments of 1 kN;
- slip angles to 2 degrees, in 0.5 degree intervals; and
- camber angles to 6 degrees, in 2 degree intervals.

During the slip and camber angle experiments, the normal load was kept constant at 3 kN. This value was selected based on the assumption that the weight of a typical saloon car is 12 kN (i.e. 3 kN per wheel). A constant normal load was applied because the tyre/ground friction coefficients and cornering characteristics are known to be influenced by normal load. This has previously been mentioned in Sections 2.6 and 2.7.

To compensate for conicity and ply steer effects, a slip angle correction was applied to the experimental tyre. The correction was approximately -0.4 degrees and the application of a slip angle was additional to this correction. Thus, an experiment conducted at zero slip angle was actually performed at a slip angle of -0.4 degrees and at a slip angle of 1 degree the test was performed at 0.6 degrees etc. [9]. The slip angle correction ensured that the tyre was in the free-rolling condition, i.e. the lateral force exerted on the tyre was about zero when zero slip and camber angles were applied.

3.4.3 Rolling Drum Experiments

The rolling drum experiments were conducted to characterise the normal pressure and shear stress distributions in the contact patch when the tyre was rolled over a cylindrical surface. The drum experiments were conducted with the following parameters as independent variables:

- normal loads between 1 kN and 5 kN, in increments of 1 kN;
- speeds between 10 km/h and 50 km/h, in increments of 10 km/h;
- slip angles to 4 degrees, in 1 degree increments; and
- camber angles to 4 degrees, in 1 degree increments.

It should be noted that the slip angle correction described in relation to the flat bed experiments was again applied. The normal load exerted on the experimental tyre during

the speed, slip and camber angle experiments was also again kept constant at 3 kN.

3.5 Results and Discussion: Stationary Experiments

The load-deflection characteristics of the experimental tyre are shown in Figure 3.6. In the figure, the normal load is given in kN and the deflection in mm. The load was measured by the load cell on the rear carriage. This load cell was calibrated to comply with the requirements of Dunlop Tyres Ltd. in-house procedures in accordance with IS0 9001. An approximately linearly relationship is observed between the load and deflection. This relationship is typical and has been confirmed by others researches [35, 72]. The stiffness of the experimental tyre is estimated to be approximately 180 kN/m.

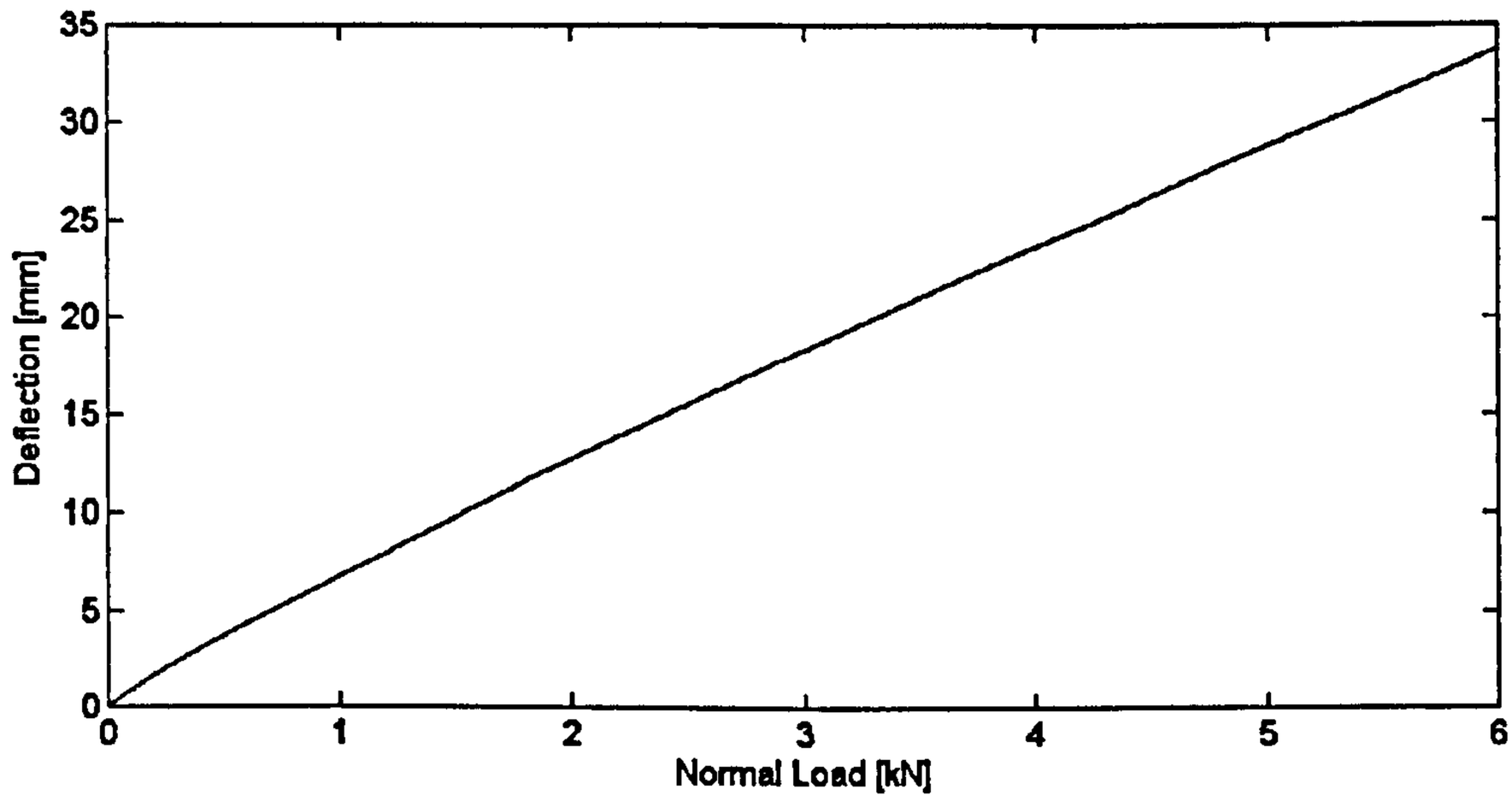

Figure 3.6 Measured normal load-deflection characteristics

As an undeflected tyre is inflated, it takes up an equilibrium shape. This inflated shape causes tension in the cords of the carcass plies and belt (casing cords), and in the cords of the bead, referred to as the bead coil. To carry a normal load, the tyre deforms and a contact region develops at the interface between the tyre and ground surface. The growth of this contact patch in the experimental tyre is shown in Figure 3.7. The inflation pressure acts through the tyre and onto the surface. As the normal load increases, the contact patch becomes longer and wider and changes from an oval shape to a rectangular one. This has been shown for the experimental tyre in Figure 3.5. The tension in the casing cords in the contact region is determined by the tension in the cords

in the deformed 'free' regions (adjacent to the contact region) not the inflation pressure. In the deformed free regions there is a reduction in the curvature and, as a consequence, the tension in the cords is reduced. However, the tension in the bead coil is maintained by the load transmitted from the wheel to the tyre. In effect, "the wheel rim hangs in the bead coil which in turn hangs in the tyre walls away from the deflected region [72]."

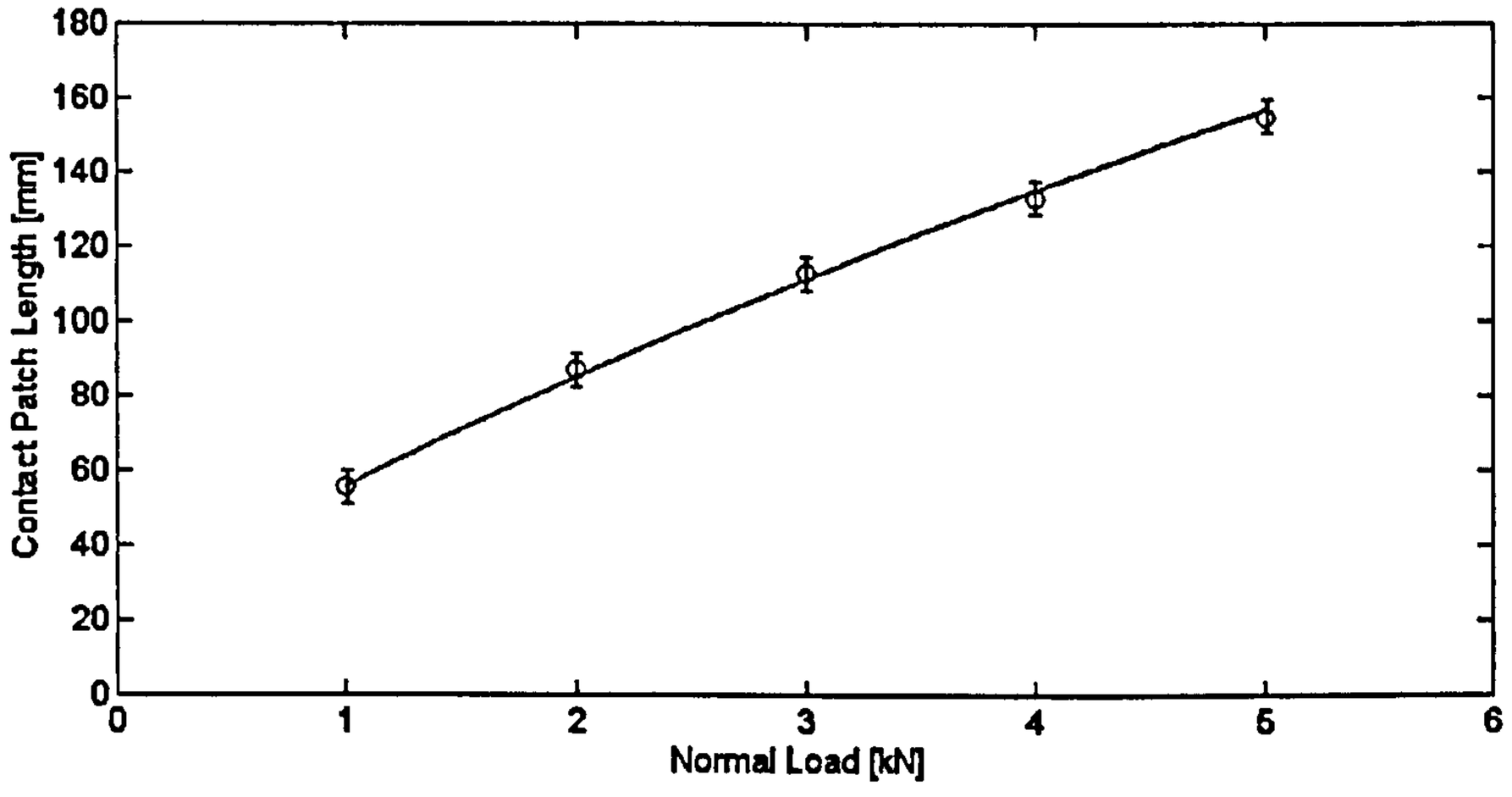

(a)

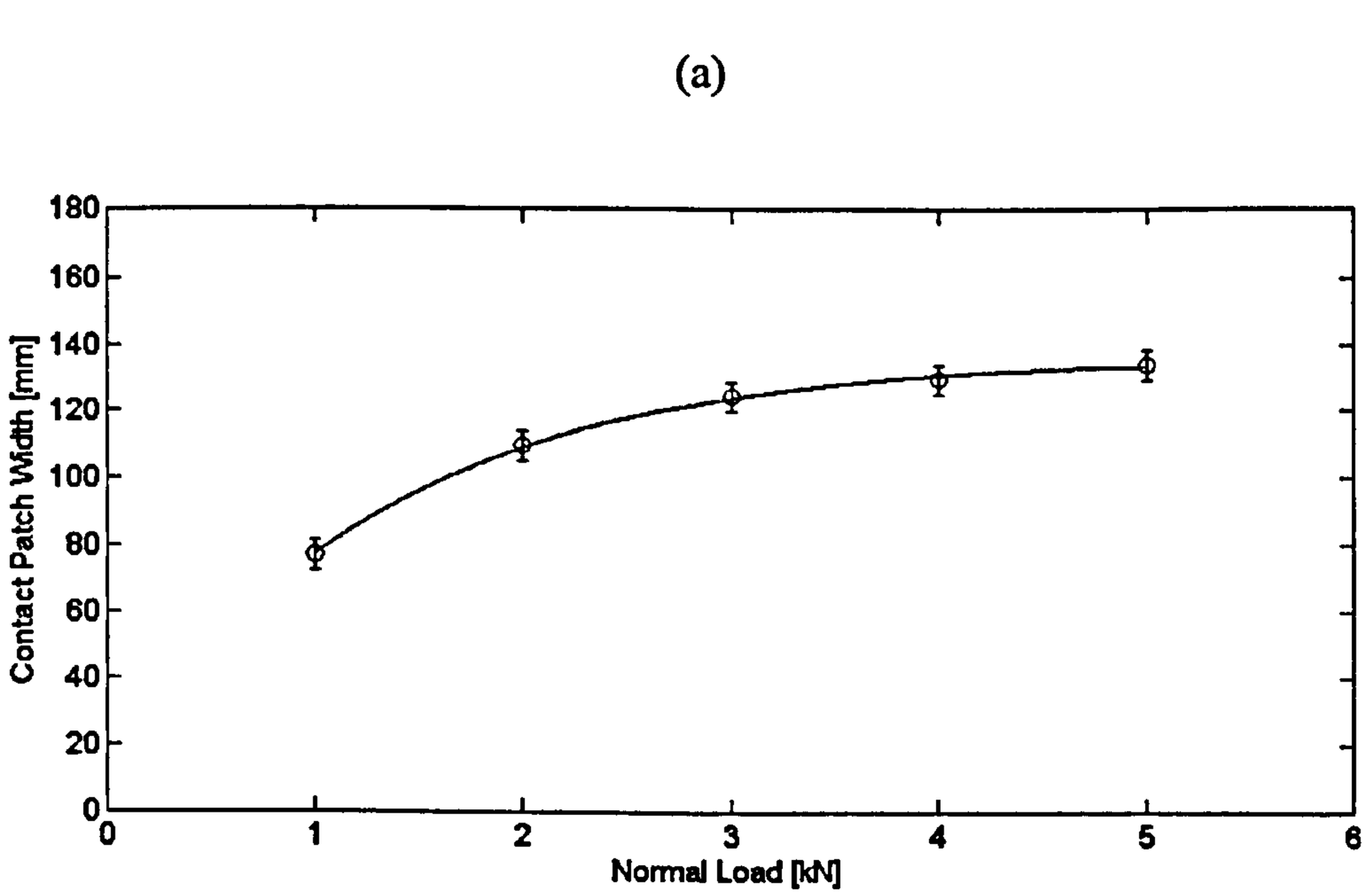

(b)

Figure 3.7 Measured contact patch dimensions with normal load: (a) length; (b) width

To provide a meaningful comparison, the contact patch dimensions (length and width) are presented on identical axes. The experimental measurements are represented by the circular points and a line of 'best-fit' is also included. The possible errors are

represented with 'error bars'. The normal load is equal to the inflation pressure multiplied by the contact area plus a small contribution due to the tyre structure [72]. Since the inflation pressure remains approximately constant, the contact patch area and, hence, the contact length and width grow as the load increases. An approximately linear relationship between load and contact patch length, and a non-linear relationship between load and contact patch width are observed (for loads between 1 kN and 5 kN). The rate of increase of the contact patch width reduces as the normal load is increased.

3.6 Results and Discussion: Flat Bed Experiments

In Figures 3.8, 3.10 and 3.11, and Figures 3.12 to 3.15, plots are presented for the stress distributions measured using the transducers in the flat bed and rolling drum testing machines, respectively. The two transducers were again calibrated to comply with the requirements of Dunlop Tyres Ltd. in-house procedures in accordance with IS0 9001. The components measured are the normal pressure, and the longitudinal and lateral shear stresses. The normal engineering sign convention is used [73] and the units for stress are kPa. To provide a basis for a meaningful comparison (as was the case for the contact patch length and width), the normal pressure and shear stress ranges are identical in each of the figures. It should be noted that the stress values are those measured by the stress transducer as the contacting tread element progresses through the contact patch. These normal pressure and shear stress measurements are assumed to be the same as the instantaneous stresses in the contact patch. In what follows the contact patch starts on the left-side of the plot and the first part of the stress distribution is referred to as the 'front'. The contacting element progresses through the contact patch from left to right. The 'rear' of the contact patch is the region where the contact is gradually lost. The region between the front and the rear is referred to as the 'centre'.

It is recognised by the tyre industry that no measurements should be taken from a rolling tyre until it has revolved approximately one revolution. This relaxation distance (see Figure 2.9) for the experimental tyre is approximately 1.8 m. The ordinates in Figures 3.8, 3.10 and 3.11, and Figures 3.12 to 3.15 give the distance travelled by the tyre and are different on the two tyre testing machines. In the case of the flat bed tyre testing machine, the distance is limited by the travel of the horizontal surface. This limit is approximately 0.9 revolutions of the tyre. The same restriction does not apply to the

rolling drum tyre testing machine and the tyre was therefore allowed to roll significantly further than the relaxation distance. For the stress distributions shown in Figures 3.8, 3.10 and 3.11, and Figures 3.12 to 3.15, the distance represented by the plots is 0.2 m.

The presence of the Safety Walk surface provides a high friction contact which is believed necessary to obtain shear stress measurements that are comparable to how contact and friction is modelled by FE simulation. In the related work by Dennehy [9], a series of tests with the flat bed tyre testing machine has been conducted and the contacting surface was either steel or 'highly' greased steel. It is the author's opinion that with these two surface conditions, the stress transducer output was adversely affect by slippage (low friction). Thus, simulation of these results was considered unfeasible.

3.6.1 Free-Rolling Characteristics

The normal pressure and shear stress distributions in the contact patch at normal loads between 1 kN and 5 kN are shown in Figure 3.8. These measurements were obtained along the length of the contact patch at the lateral centre of the tyre (see Figure 3.1). As discussed in Section 3.4.2, a slip angle correction was applied to the experimental tyre.

The normal pressure at the front of the contact patch is shown in Figure 3.8(a) to be slightly greater than that at the rear. This characteristic has been previously discussed in Section 2.5. The distribution is not symmetrical because a longitudinal force, usually referred to as the rolling resistance, exists in the contact patch. This rolling resistance is also evident in Figure 3.8(b) where the magnitude of the longitudinal shear stresses at the rear of the contact patch are greater than those at the front. As discussed, the rolling resistance will change on different surfaces, and with various tyre constructions and sizes. This point is worthy of consideration if the normal and shear contact stress distributions presented in this thesis are to be used (herein or by others) to validate advanced FE models or evaluate the assumed contact stresses in semi-empirical models.

As a tread element enters the contact patch, the normal pressure (Figure 3.8(a)) exerted on the horizontal surface rapidly increases to a maximum, and then steadily reduces as the element progresses through the contact patch. The maximum pressure in Figure 3.8(a) does not change with normal load and it is approximately 320 kPa. This

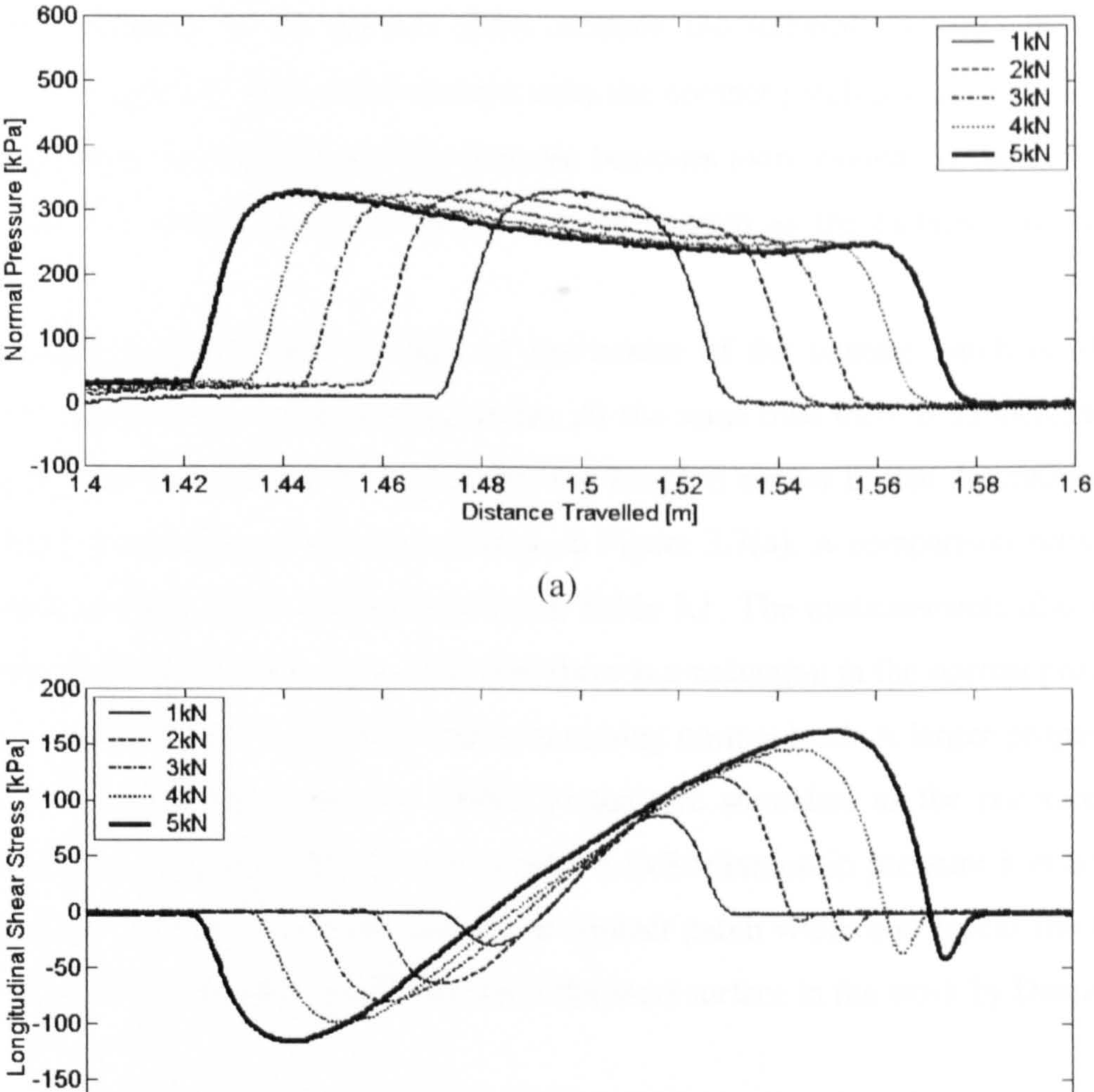

(a)

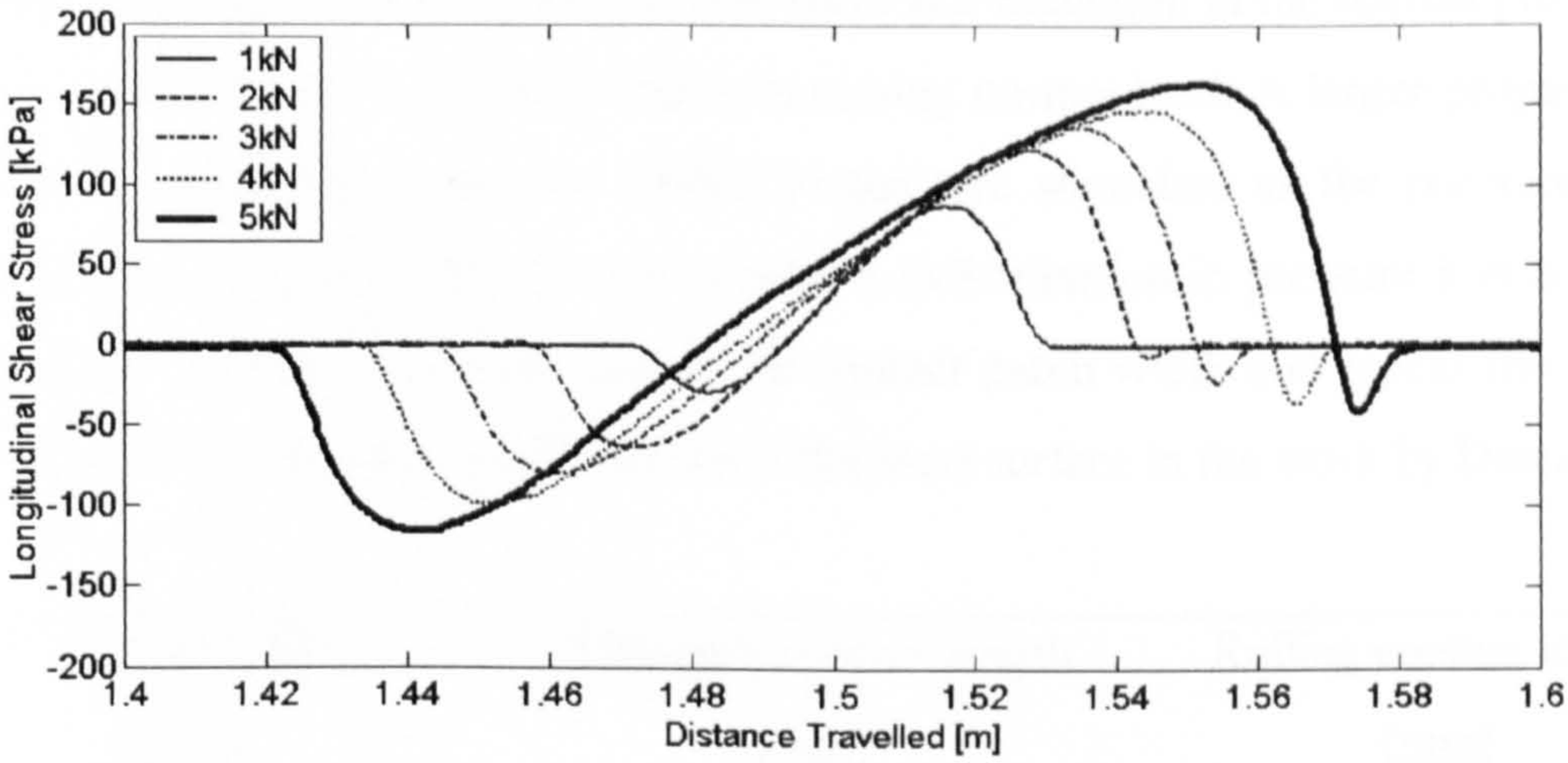

(b)

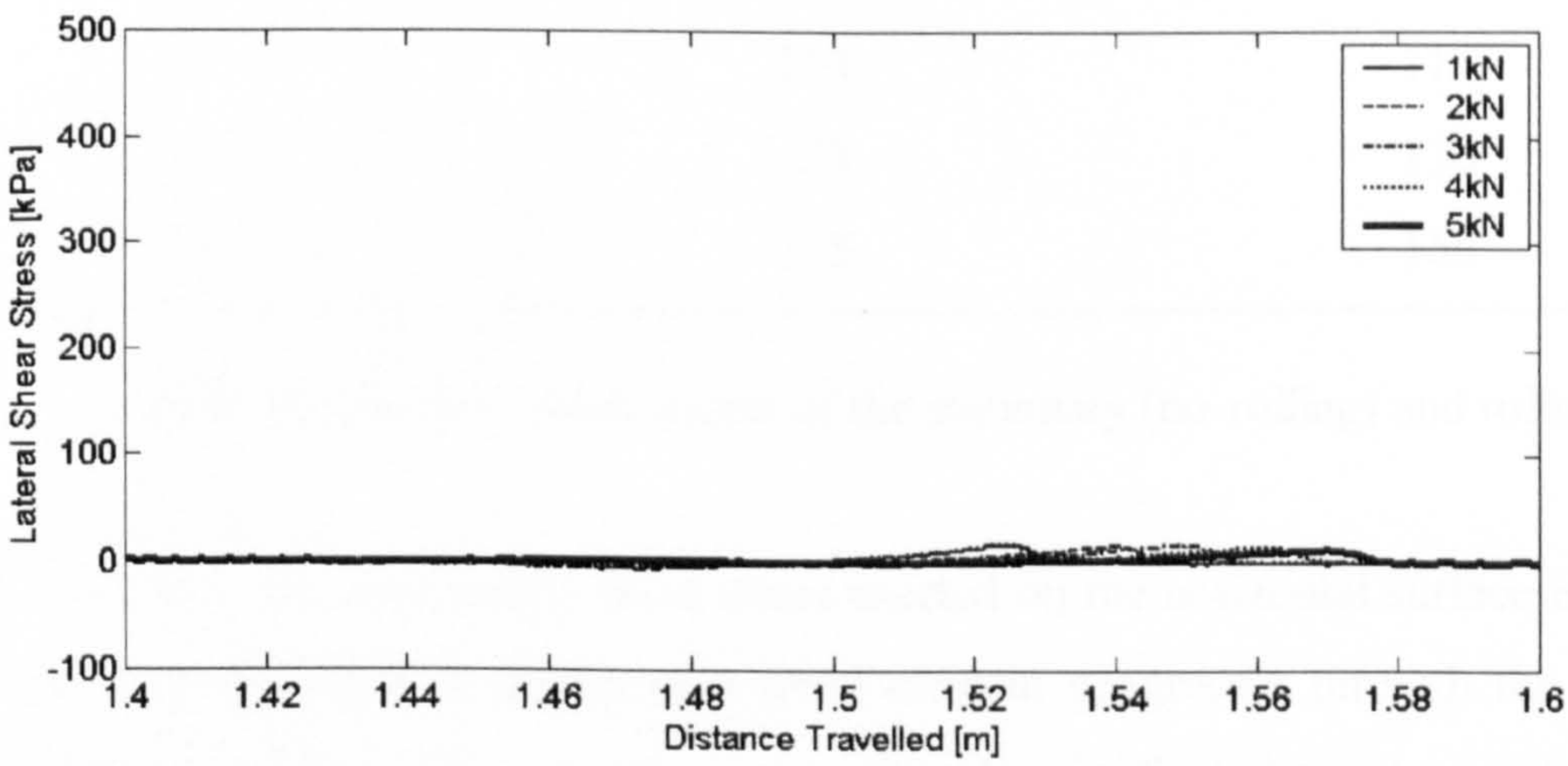

(c)

Figure 3.8 Measured contact stress distributions with normal load on a horizontal (flat) surface: (a) normal pressure; (b) longitudinal shear stress; (c) lateral shear stress

exceeds the tyre inflation pressure by a factor of 1.6. DeBeer [23] suggests the maximum pressure in the contact patch exceeds the inflation pressure by a factor between 1.5 and 2.0. Before the element exits the contact patch a slight increase in the normal pressure is observed and this increase becomes more evident as the normal load increases. The normal pressure rapidly reduces to zero as the element exits contact.

A reduction in the normal pressure at the centre of the contact patch is observed (Figure 3.8(a)) as the normal load increases. At the same time there is an increase in the contact length from about 0.06 to 0.16 m. The length is similar to that determined under stationary (non-rolling) condition as shown in Figure 3.7(a). A comparison between the static and rolling contact lengths is given in Table 3.1. The measurements also confirm the observation by Browne *et al.* [31] that there is a reduction in the normal pressure as the tyre centre 'buckles' upwards under increasing normal load. A larger proportion of the pressure distribution must be shifted to the tyre shoulders as the pressure at the lateral centre reduces [9, 23]. To verify such a redistribution in pressure it is necessary to move the transducer laterally across the contact patch width and repeat the flat bed experiments. This has been confirmed for a flat steel surface in the work by Dennehy [9].

Normal load [kN]	Stationary contact length [mm]	Rolling contact length [mm]
1	56	59
2	87	88
3	113	114
4	133	136
5	155	156

Table 3.1 Measured contact patch length of the stationary (no-rolling) and rolling tyre

In Figure 3.8(b), the longitudinal shear stress exerted on the horizontal surface is shown to follow a sinusoidal-style sweep as a tread element progresses through the contact patch. The magnitude of the negative and positive longitudinal shear stresses increases as the normal load increases. At a normal load of 5 kN, the maxima are -120 and 165 kPa, respectively. These characteristics are mentioned by Dennehy *et al.* [74], but the longitudinal (x-) axis is incorrectly identified as the lateral (y-) axis, and *vice versa*.

This highlights the lack of knowledge of contact patch behaviour and gives additional support to the motivation behind the thesis. The increase in the magnitude of the shear stresses at the rear compared to those at the front is also evident but is not discussed.

The sinusoidal-style sweep in the longitudinal shear stresses shown in Figure 3.8(b) develops because the radius at the perimeter of the tyre tread changes [10] as shown in Figure 3.9. As a tread element enters contact, the tangential velocity decreases as the radius reduces and a negative longitudinal shear stress is exerted on the horizontal surface; a positive shear stress must be exerted on the tyre. A positive shear stress develops on the surface at the rear as the tyre radius recovers. A small kink in the longitudinal shear stress is usually observed at the trailing edge of the contact patch and is more evident as the magnitude of the normal load increases. This kink is also shown in the work published by Lippmann and Oblizajek [39] and by Seitz and Hussman [75]. It is stated in the paper by Browne *et al.* [31] that no clear explanation for the behaviour is at hand. However, in a more recent paper by Lippmann [76] the kink is related to 'slippage' in the contact patch. The author believes this explanation to be correct.

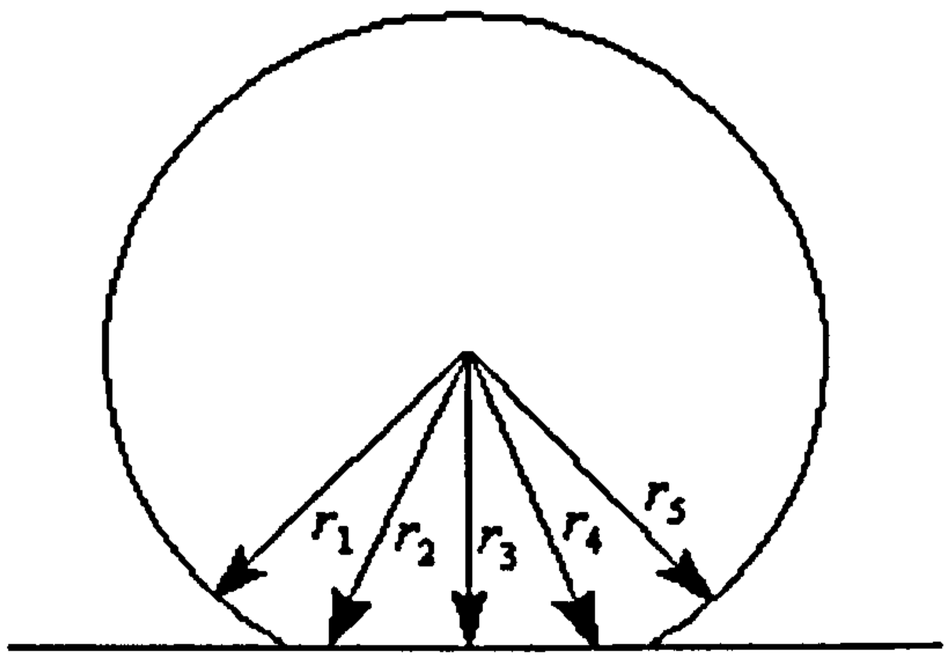

Figure 3.9 Radius change at the perimeter of the tyre tread; $r1 > r2 > r3 < r4 < r5$

The lateral shear stresses (Figure 3.8(c)) are small in comparison to the longitudinal shear stresses. This is to be expected since the slip angle correction was applied to the tyre. If the slip angle correction was exact, the lateral shear stresses would be zero; conicity and ply steer effects would be negligible. Evidently this is not the case but the lateral shear stresses are not considered significant and, thus, are not discussed further.

3.6.2 Cornering Characteristics and Slip Angle

The normal pressure and shear stress distributions in the contact patch under slip angle (α) variations to 2 degrees (in increments of 0.5 degrees) are shown in Figure 3.10. Further measurements at higher slip angles (up to 4 degrees) were also taken but the data was found to exhibit obvious errors and thus, the contact stresses are not presented herein. These errors were due to a problem associated with the stress transducer. The normal load exerted on the tyre during the slip angle tests was 3 kN and the applied slip angle was additional to the slip angle correction. It should be noted that by applying a slip angle, the orientation of the tyre axes (x-, y-) changes relative to the fixed transducer axes. A cross-coupling effect occurs, and the longitudinal (x-) and lateral (y-) shear stresses need to be resolved [9]. At small slip angles (<10 degrees), the cross-coupling effect is not significant, and its presence was neglected. This is shown in Appendix A.

In Figure 3.10(a), a reduction (maximum 15 percent) in the normal pressure exerted on the Safety Walk surface is shown to occur as the slip angle increases. A slight reduction in the contact patch length is also evident. These characteristics are probably related to tread distortion occurring under slip angle conditions. A reduction of up to 30 percent is observed in the longitudinal shear stresses (Figure 3.10(b)) at the rear of the contact patch as the slip angle increases. A much smaller reduction occurs at the front where the stress is lower. These reductions are related to the friction ellipse concept described in Section 1.1. The friction ellipse assumes that the friction limit for a tyre is determined by the coefficient of friction and the normal load, and that the friction can be used to develop a longitudinal force, a lateral force or a combination of the two. Since the longitudinal and lateral resultant forces are related to the longitudinal and lateral shear stress distributions, the friction limit determines the shear stress that can develop. The available friction is dominated by the lateral shear stresses in Figure 3.10(c). As Figure 3.10(b) shows, an accompanying reduction in the longitudinal shear stresses follows.

In Figure 3.10(c), the lateral shear stress exerted on the surface is shown to increase approximately linearly as a tread element progresses through the contact patch. This is a common assumption in physical models [33, 45, 46]. The element enters the contact patch and remains in the original position of contact with the surface. The longitudinal axis (direction of heading) differs from the direction of travel and the element is

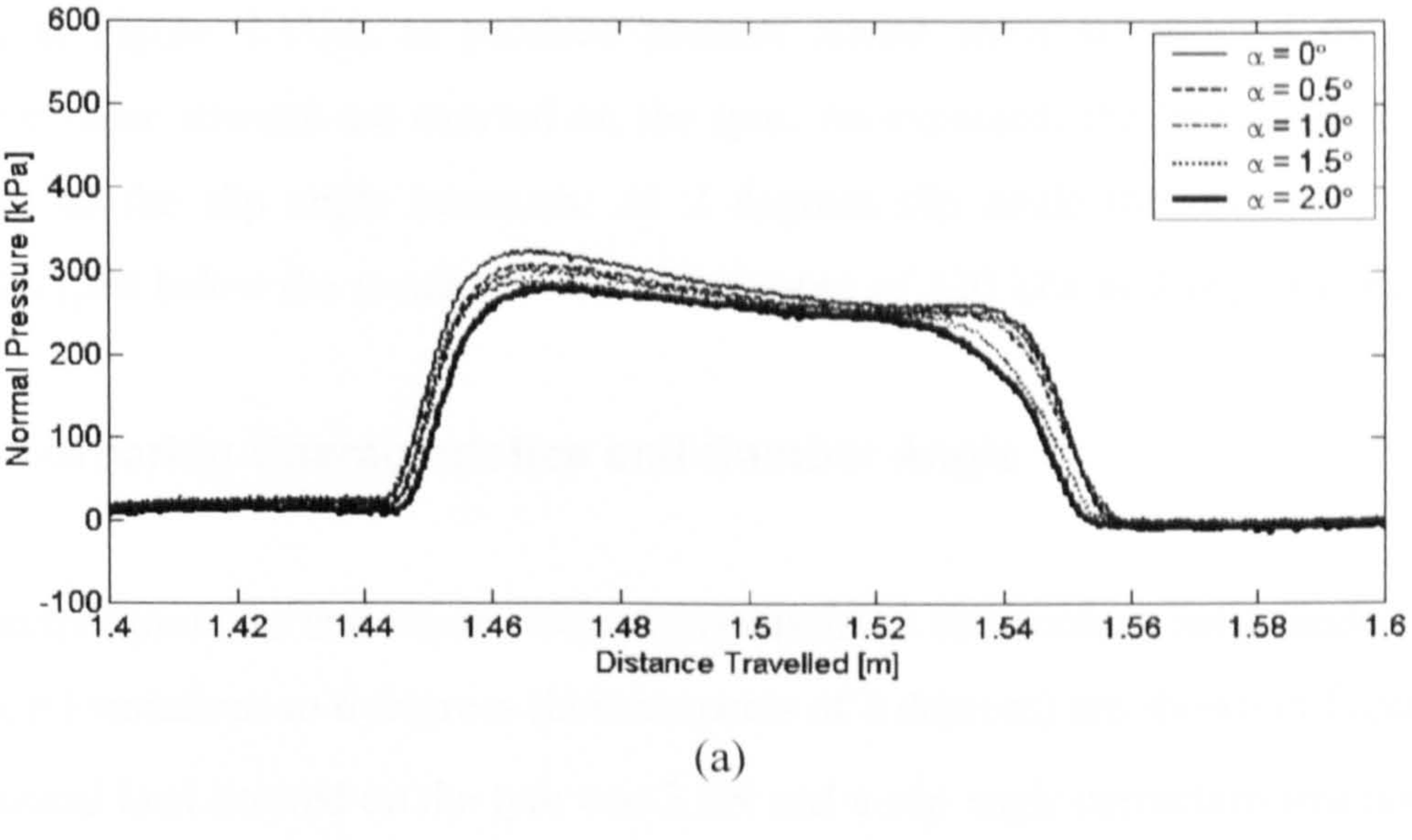

(a)

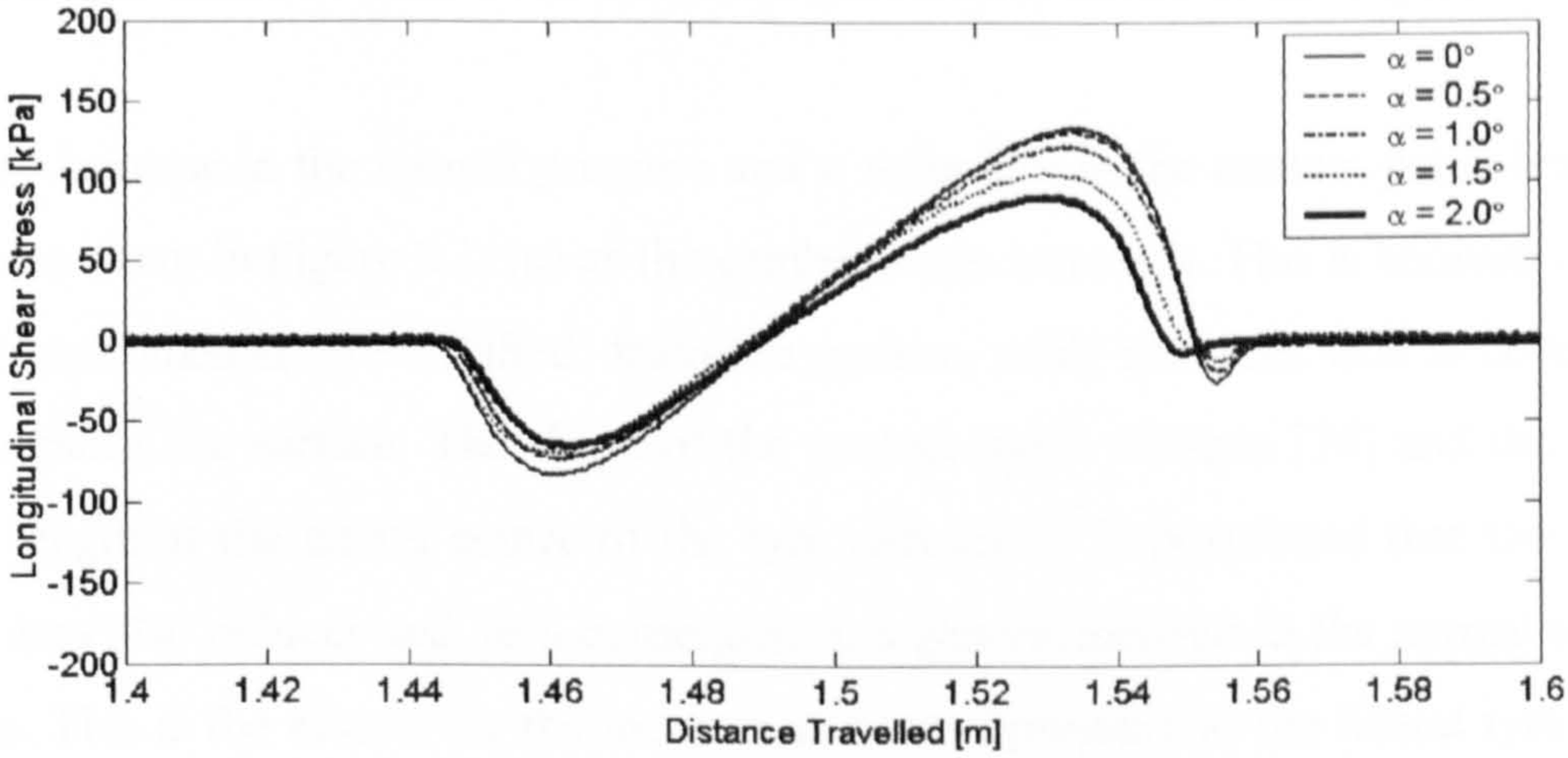

(b)

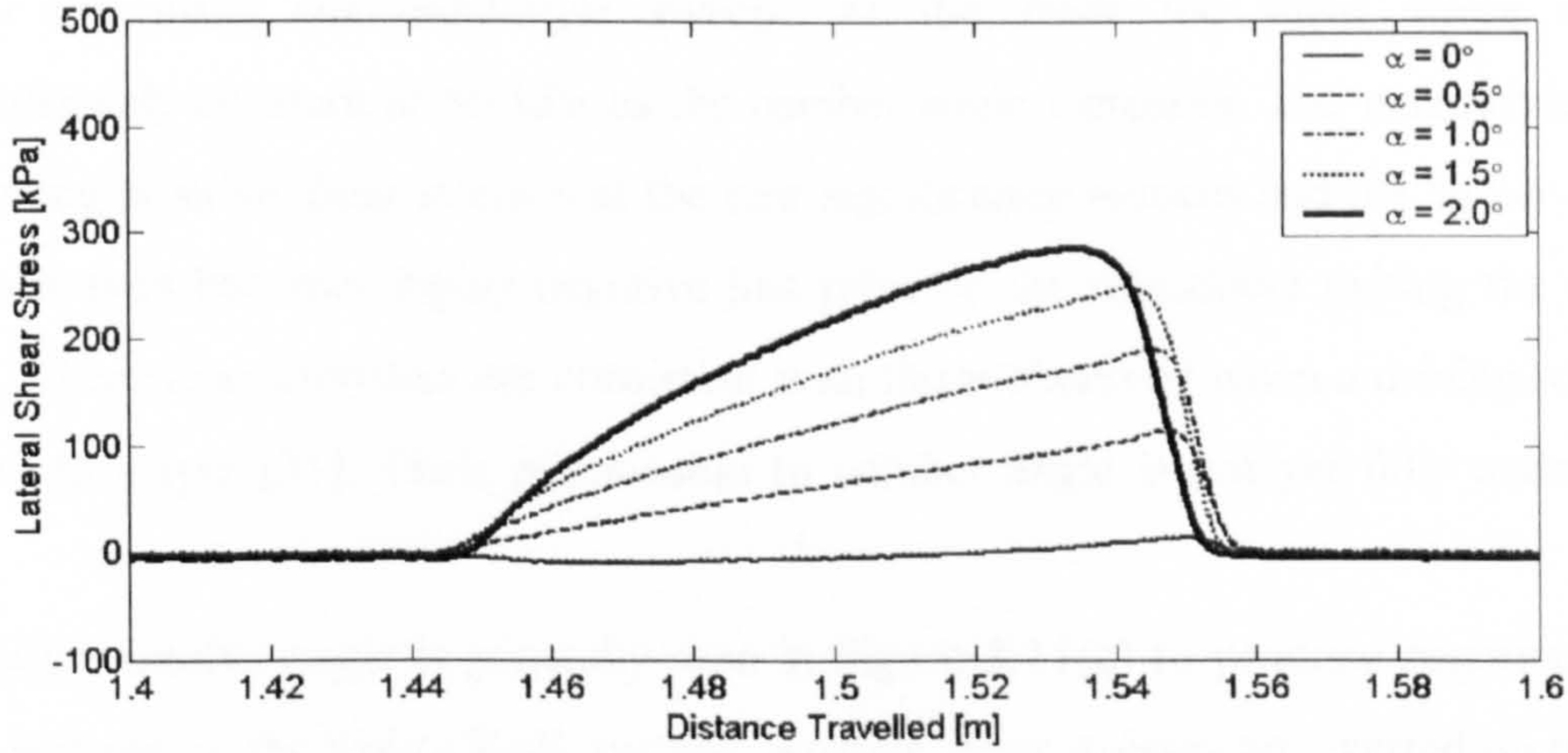

(c)

Figure 3.10 Measured contact stress distributions with slip angle on a horizontal (flat) surface: (a) normal pressure; (b) longitudinal shear stress; (c) lateral shear stress

deflected laterally. This has been discussed in Section 2.7.1. A positive slip angle is shown in Figure 3.11(c) to produce positive lateral shear stresses on the surface; negative shear stresses are exerted on the tyre. As expected, the lateral shear stresses increase as the slip angle increases. At 2 degrees slip angle the maximum stress is 290 kPa (just below the maximum normal pressure of 320 kPa at 0 degrees slip angle).

3.6.3 Cornering Characteristics and Camber Angle

The normal pressure and shear stress distributions in the contact patch under camber angle (γ) variations to 6 degrees (in increments of 2 degrees) are shown in Figure 3.11. The normal load exerted on the tyre was 3 kN and a slip angle correction was applied to the tyre. The measurements were obtained at the lateral centre of the experimental tyre.

A small increase in the normal pressure and a reduction in the contact patch length are shown to occur in Figure 3.11(a) as the camber angle increases. This is because one side of the experimental tyre is 'lifted' from the surface, while the other side is compressed more against the surface. The shape of the contact patch changes [74] and the contact patch length at the lateral centre of the tyre reduces. It is postulated that the contact patch area also reduces and, as a consequence, a general increase in the normal pressure occurs. This is the reason for the increase in normal pressure at the lateral tyre centre.

In Figure 3.11(b), the longitudinal shear stress on the surface is generally shown to follow the usual sinusoidal-style sweep. At the front the shear stress remains approximately constant at 80 kPa as the camber angle increases. The magnitude of the recovering positive shear stresses at the rear significantly reduces and for higher camber angles it even becomes highly negative just prior to the transducer exiting the contact patch. These characteristics are consistent with those observed when a driving torque is applied to a tyre [31]. Their relationship to camber angle is not yet fully understood.

A positive camber angle is generally seen in Figure 3.11(c) to produce negative lateral shear stresses on the Safety Walk surface; positive shear stresses are exerted on the tyre. The magnitude of the lateral shear stresses are significantly lower (< 100 kPa) than those obtained under the equivalent slip angle conditions (see Figure 3.10(c)). This is because the camber stiffness of the tyre is significantly less than that of the cornering stiffness.

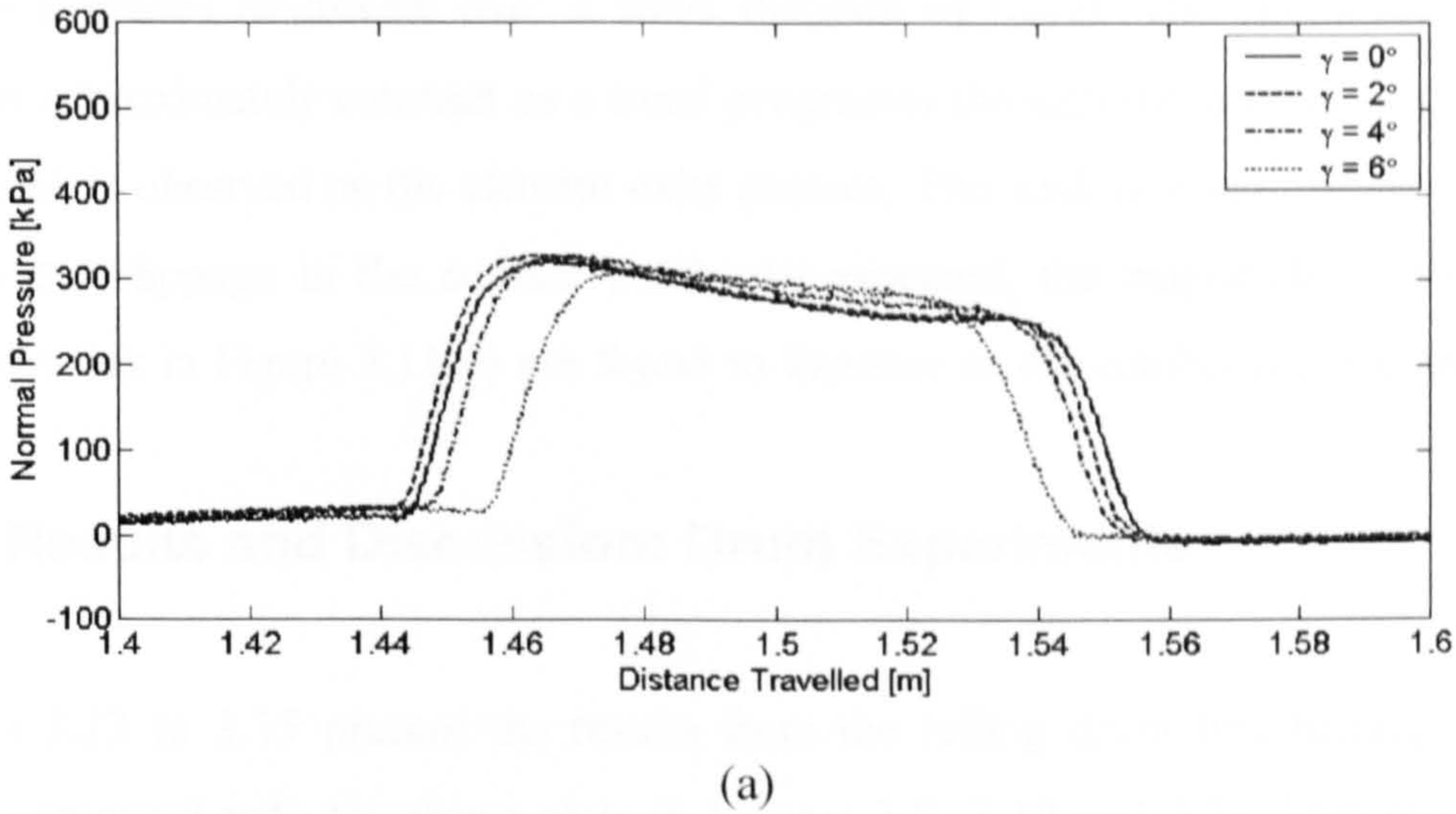

(a)

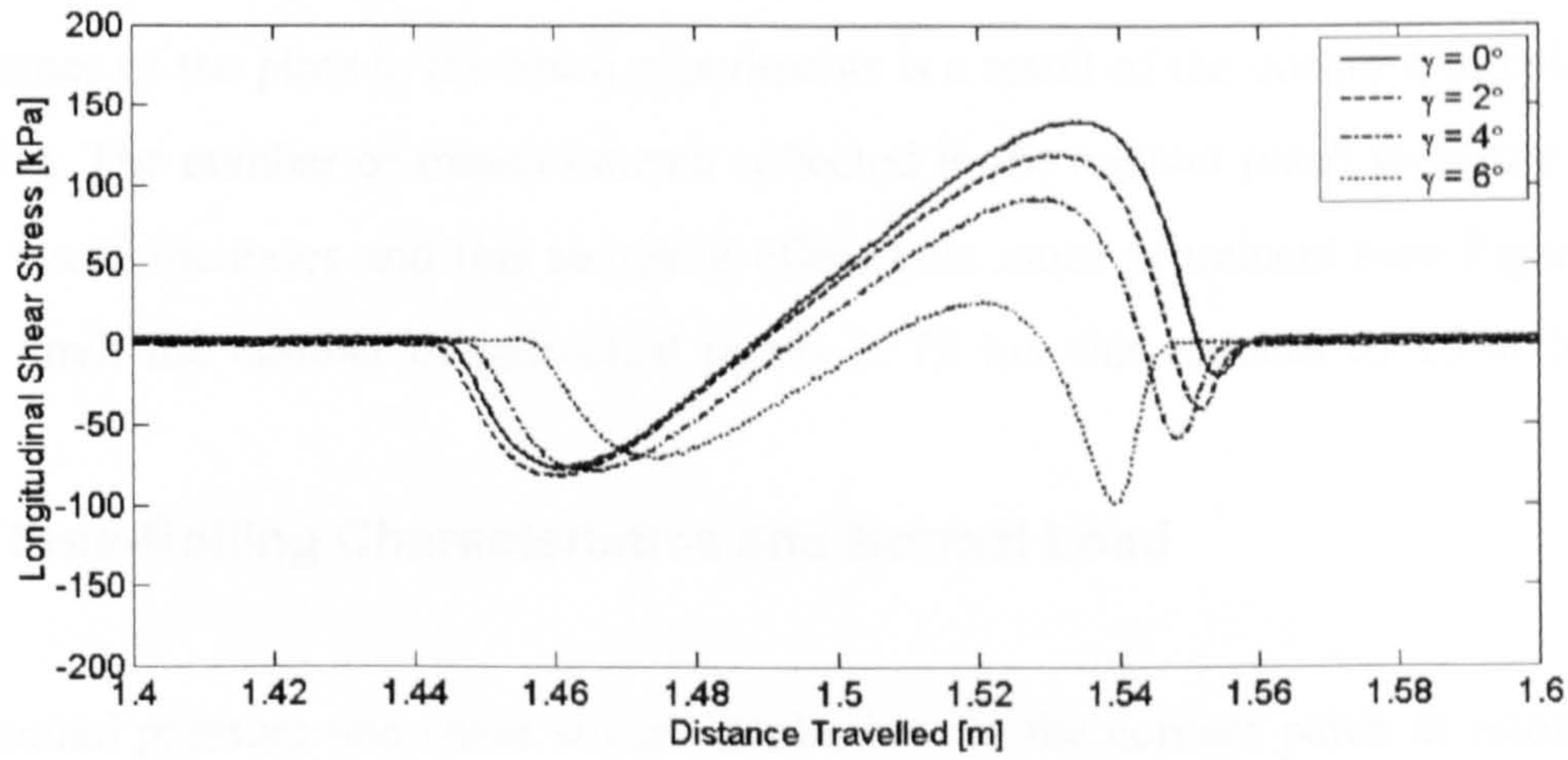

(b)

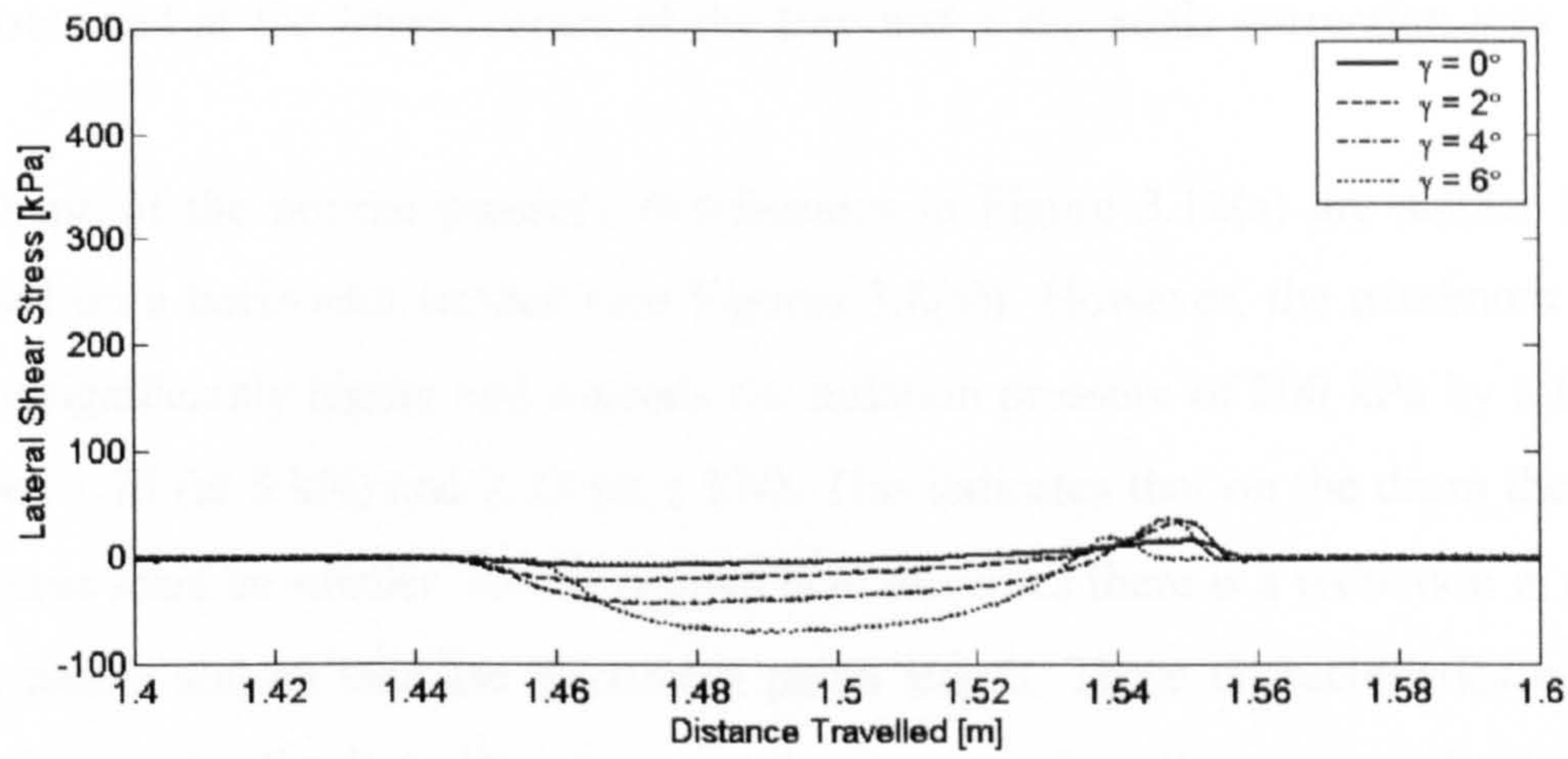

(c)

Figure 3.11 Measured contact stress distributions with camber angle on a horizontal (flat) surface: (a) normal pressure; (b) longitudinal shear stress; (c) lateral shear stress

As a tread element enters contact the lateral shear stress exerted on the horizontal surface increases negatively over a short distance of travel. The lateral shear stress remains approximately constant as a tread progresses through the contact patch, until a small kink is observed as the element exits contact. This kink is again understood to be due to the slippage in the contact patch. As expected, the magnitude of the lateral shear stresses in Figure 3.11(c) are found to increase as the camber angle is increased.

3.7 Results and Discussion: Drum Experiments

Figures 3.12 to 3.15 present the results from the rolling drum tyre testing machine. When compared with the stress plots in Figures 3.8, 3.10 and 3.11 from the flat bed machine it is straightforward to see similarities and differences. The discontinuous appearance of the plots in the drum experiments is a result of the constant sample rate of 1024 Hz. The number of measurements collected in the contact patch therefore reduces as the speed increases and this sampling effect gets more prominent (see Figure 3.13). At 10 km/h the number of individual points is 75 but this reduces to 15 at 50 km/h.

3.7.1 Free-Rolling Characteristics and Normal Load

The normal pressure and shear stress distributions in the contact patch at normal loads between 1 kN and 5 kN (in increments of 1 kN) are shown in Figure 3.12. The tangential speed of the drum and tyre (no relative slip) was 20 km/h. Measurements were obtained at the lateral centre of the tyre and a slip angle correction was applied.

The shape of the normal pressure distributions in Figure 3.12(a) are similar to those obtained on a horizontal surface (see Figures 3.8(a)). However, the maximum value is usually significantly higher and exceeds the inflation pressure of 200 kPa by a factor of between 1.75 (at 5 kN) and 2.25 (at 1 kN). This indicates that on the drum the contact patch area must be smaller. As the normal load increases there is a reduction in pressure at the centre and an increase in contact patch length. These characteristics were also observed on the flat bed. However, on the drum surface the stress reduction at the centre is more significant. This is due to the tyre buckling phenomenon being magnified by the drum surface. As a tread element exits the contact patch the normal pressure is shown to slightly oscillate before returning to the zero state. It is believed that such

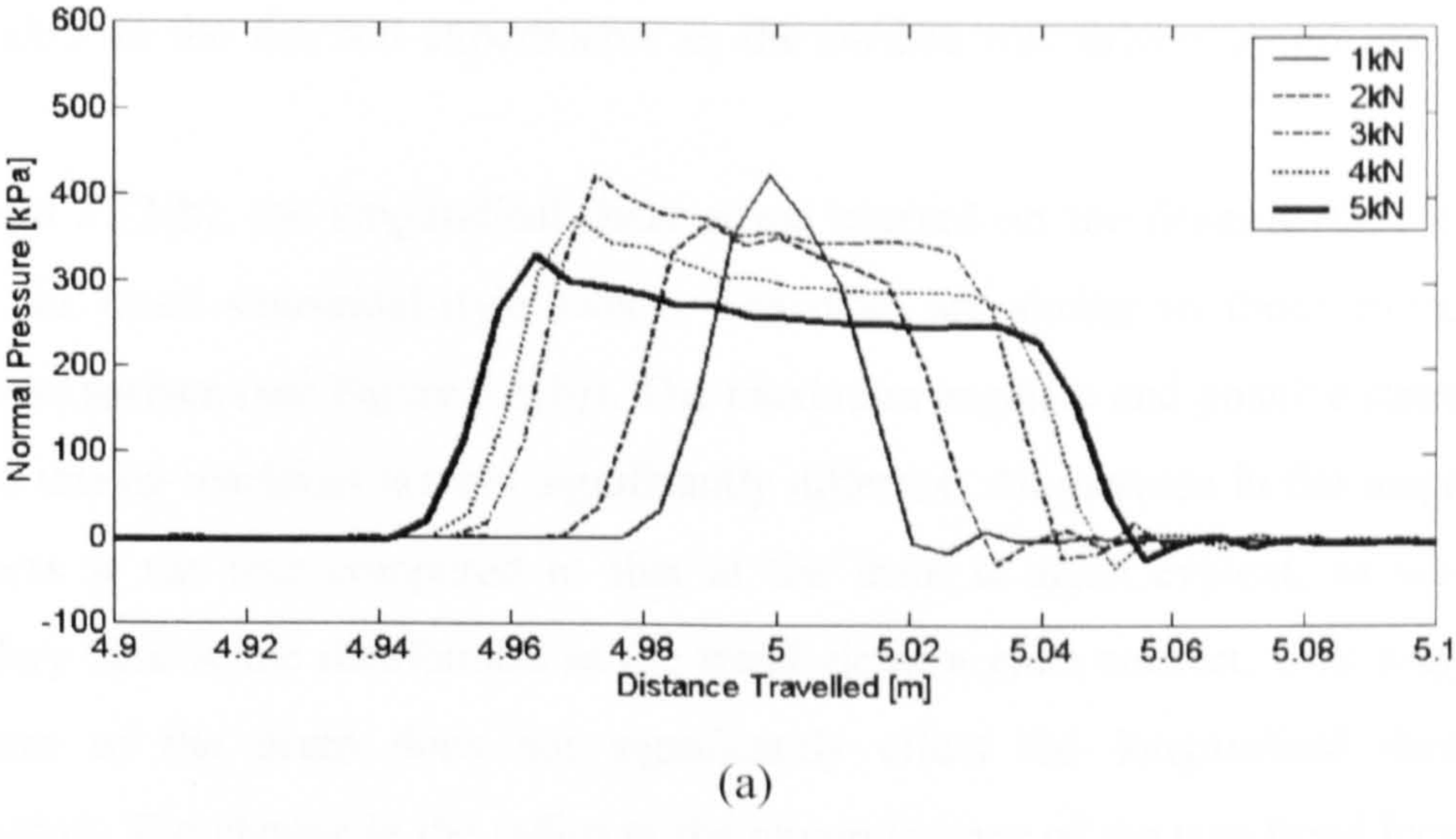

(a)

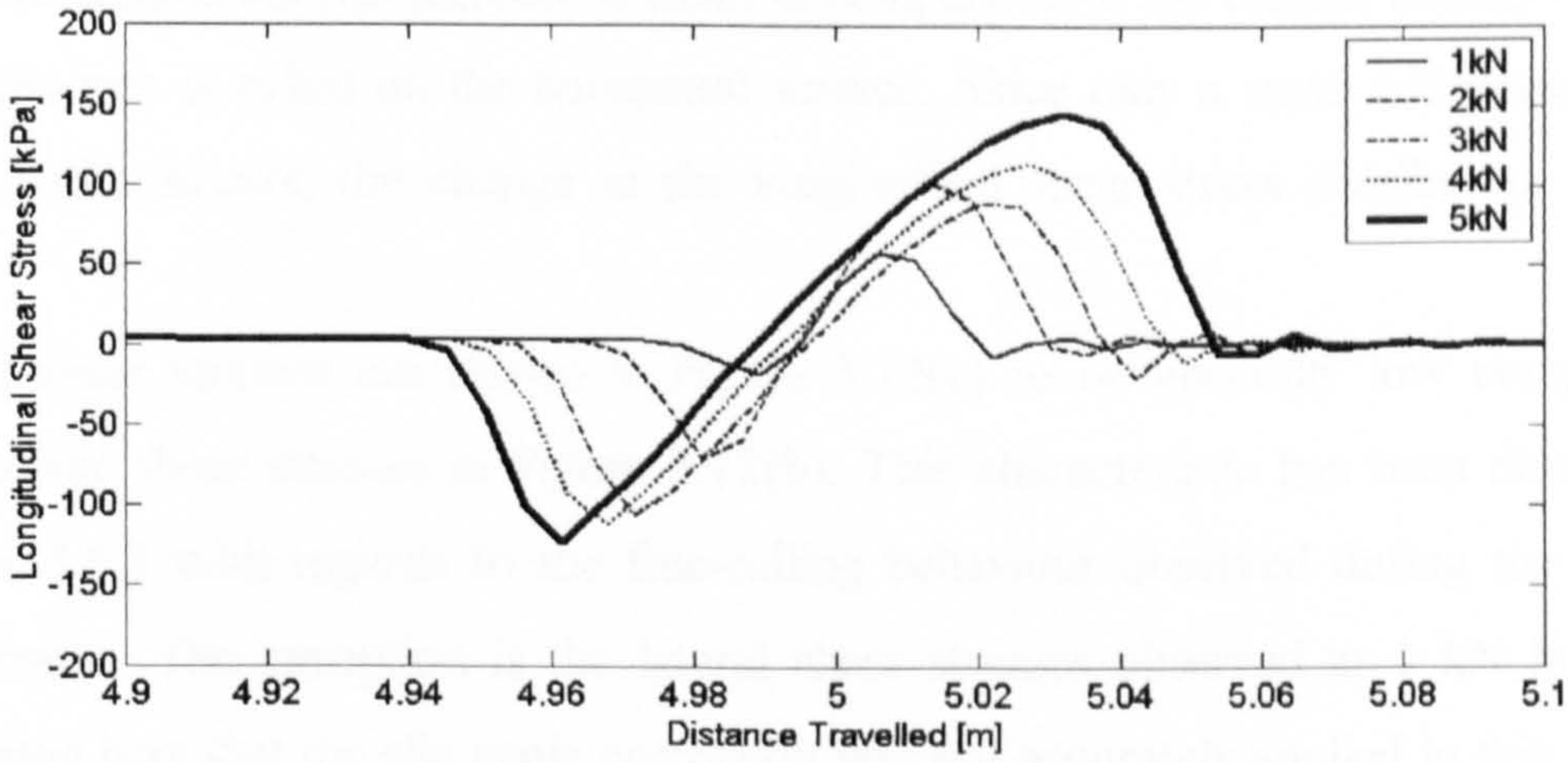

(b)

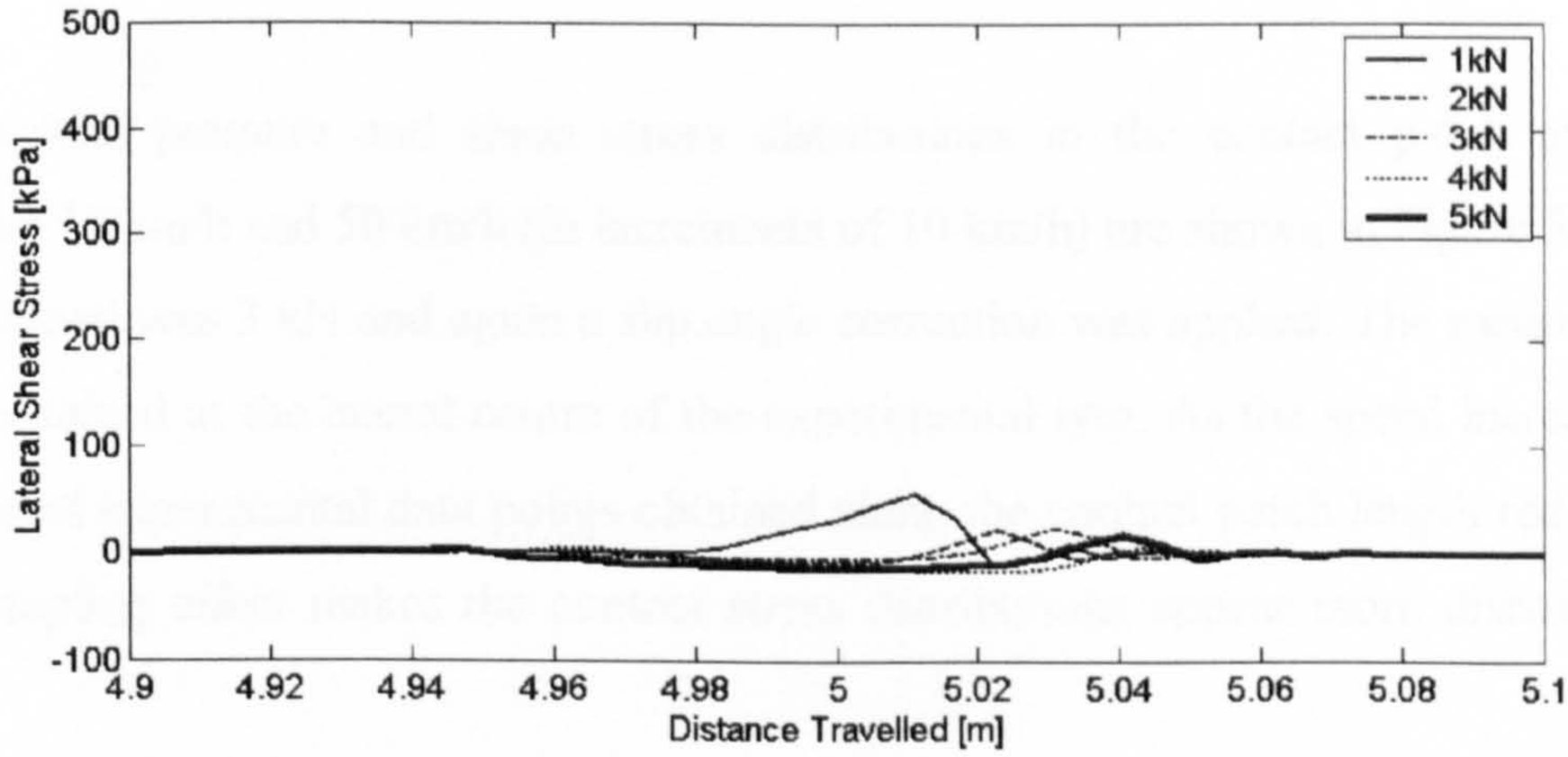

(c)

Figure 3.12 Measured contact stress distributions with normal load on a cylindrical (drum) surface: (a) normal pressure; (b) longitudinal shear stress; (c) lateral shear stress

secondary oscillation is a dynamic response of the stress transducer. This oscillation is not evident in the flat bed experiments as the surface was driven at too low a speed.

In Figure 3.12(b), the longitudinal shear stress exerted on the drum surface is seen to follow the usual sinusoidal-style sweep. The plots are similar to those found on the horizontal surface (see Figure 3.8(b)). The maximum negative and positive stresses from the two testing machines are not significantly different. An increase in the magnitude of the stress at the rear compared to that at the front is again evident, as well as the secondary kink in the distribution as the tread element exits contact. This suggests the curvature of the drum does not significantly effect the longitudinal shear stress distribution. The change in the radius at the circumference of the tyre tread increases on the drum surface but this increase is small in comparison to the change already exhibited when the tyre is rolled on the horizontal surface. Since only a small additional change in the radius occurs, the change in the longitudinal shear stress distribution is small.

Lateral shear stresses are shown in Figure 3.12(c) to be generally low compared to longitudinal shear stresses in Figure 3.12(b). This characteristic has been discussed in Section 3.6.1 with regards to the free-rolling behaviour observed during the flat bed experiments. The exception is the lateral shear stresses observed at 1 kN load. It is postulated here that the slip angle correction was not accurately applied in this instance.

3.7.2 Free-Rolling Characteristics and Speed

The normal pressure and shear stress distributions in the contact patch at speeds between 10 km/h and 50 km/h (in increments of 10 km/h) are shown in Figure 3.13. The normal load was 3 kN and again a slip angle correction was applied. The measurements were obtained at the lateral centre of the experimental tyre. As the speed increases, the number of experimental data points obtained along the contact patch length reduces and this sampling effect makes the contact stress distributions appear more discontinuous.

A significant change in the normal pressures is observed in Figure 3.13(a) at the different speeds. No logical trend is evident, with the ascending order for maximum stresses shown to be 20, 50, 30, 10 and 40 km/h; at speeds of 10, 30 and 50 km/h the stress peaks at about 500 kPa. A change in the longitudinal shear stresses is also evident in

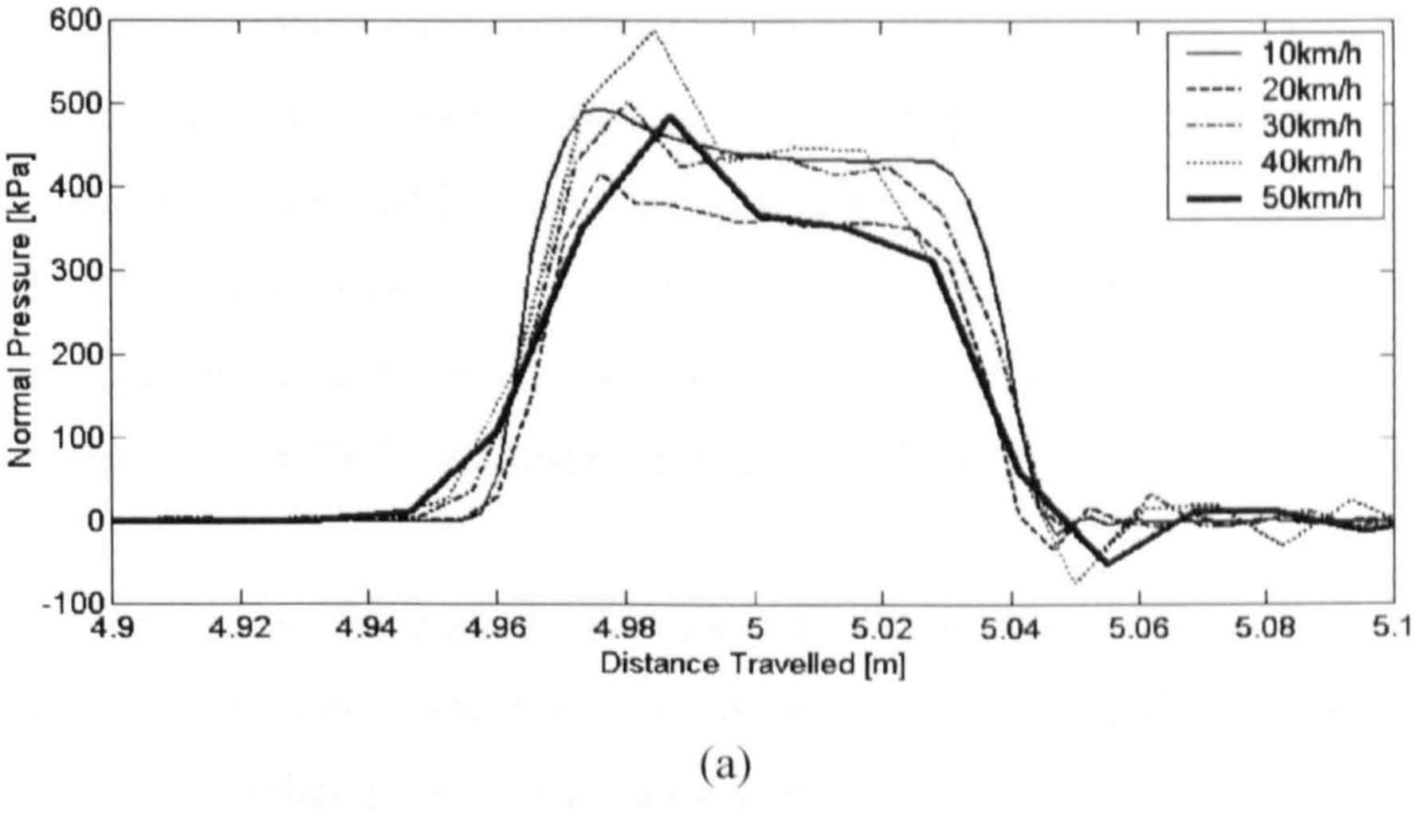

(a)

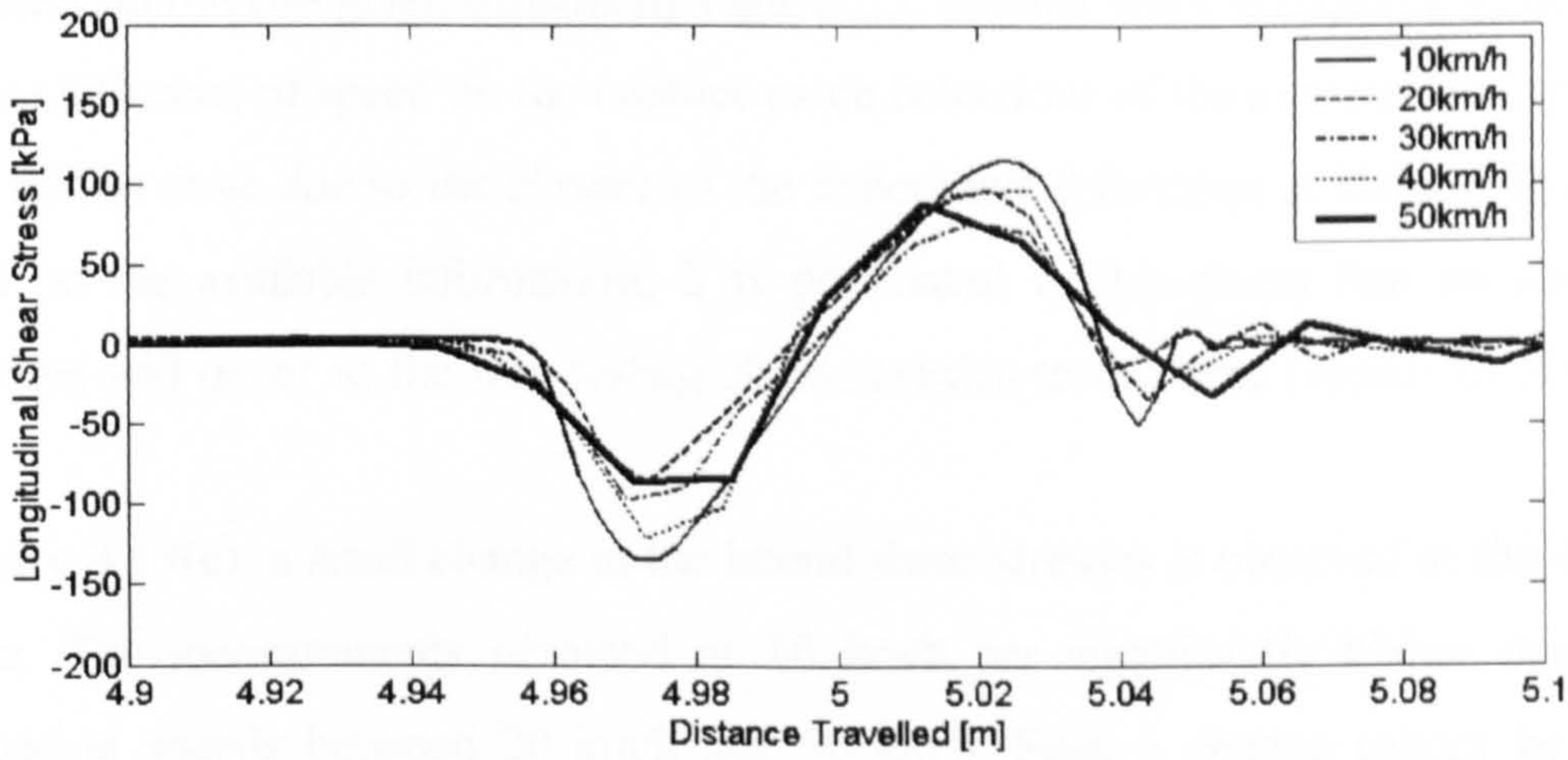

(b)

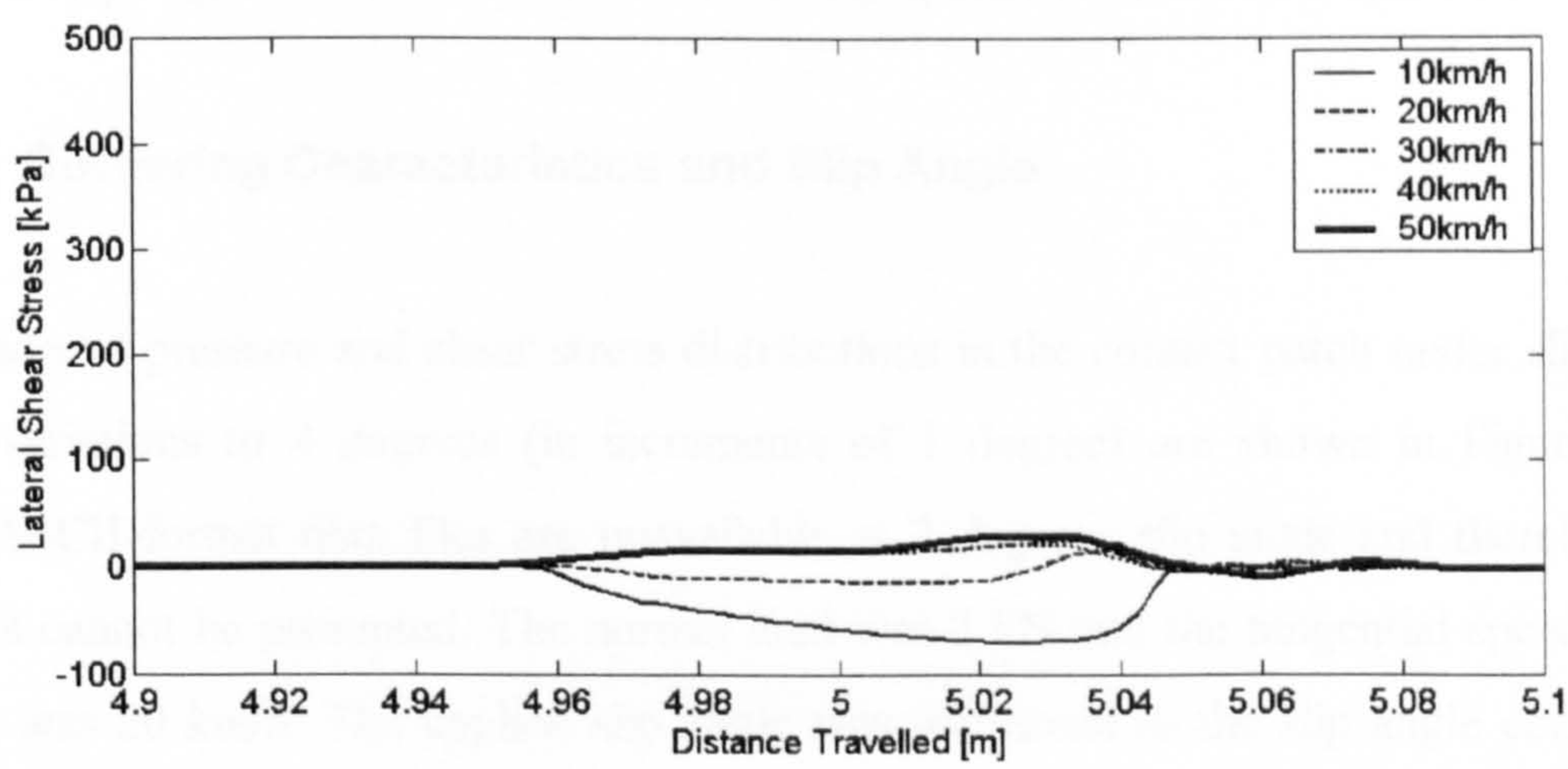

(c)

Figure 3.13 Measured contact stress distributions with forward speed on a cylindrical (drum) surface: (a) normal pressure; (b) longitudinal shear stress; (c) lateral shear stress

Figure 3.13(b), but again there appears to be no discernible pattern to this change. A number of investigations by other researchers has examined the effects of speed [31] but these studies have mostly been carried out using bias-ply tyres. Generally, the results suggest an increase in speed causes an increase in the normal pressure at the front of the contact patch and a decrease at the rear. Since such a change in the pressure distribution is caused by an increase in the rolling resistance (as discussed in Section 3.6.1), there must be an increase in the longitudinal shear stress towards the rear of the contact patch.

This type of change in the contact stress distributions is not confirmed by the measurements plotted in Figure 3.13 or in the work by Seitz and Hussmann [75] where the authors suggest that no effect will be evident for radial-ply tyres up to approximately 130 km/h, an opinion given support by Figure 2.5. Further work is required to determine the true influence of speed on the contact patch behaviour of the experimental tyre. This could not be done due to the closure of the experimental facilities at Dunlop Tyres Ltd. Based on the available information, it is postulated in this thesis that no noticeable difference will occur in the free-rolling characteristics tested here (speeds to 50 km/h).

In Figure 3.13(c), a small change in the lateral shear stresses is observed at the different speeds. The measurements obtained at 10 km/h are significantly higher than those obtained at speeds between 20 km/h and 50 km/h. Such a change cannot be related to the physical behaviour of the experimental tyre and, thus, it is again postulated that the slip angle correction was not accurately applied at the lowest speed of 10 km/h.

3.7.3 Cornering Characteristics and Slip Angle

The normal pressure and shear stress distributions in the contact patch under slip angle (α) variations to 4 degrees (in increments of 1 degree) are shown in Figure 3.14. The ASCII-format data files are unavailable at 2 degrees slip angle and therefore the results cannot be presented. The normal load was 3 kN and the tangential speed of the drum was 20 km/h. The applied slip angle was additional to the slip angle correction.

In Figure 3.14(a), the normal pressure distribution is shown to differ considerably with slip angle from that obtained using the flat bed machine (see Figures 3.10(a)). The pressure is much higher with the maximum about 1.5 times that recorded on the

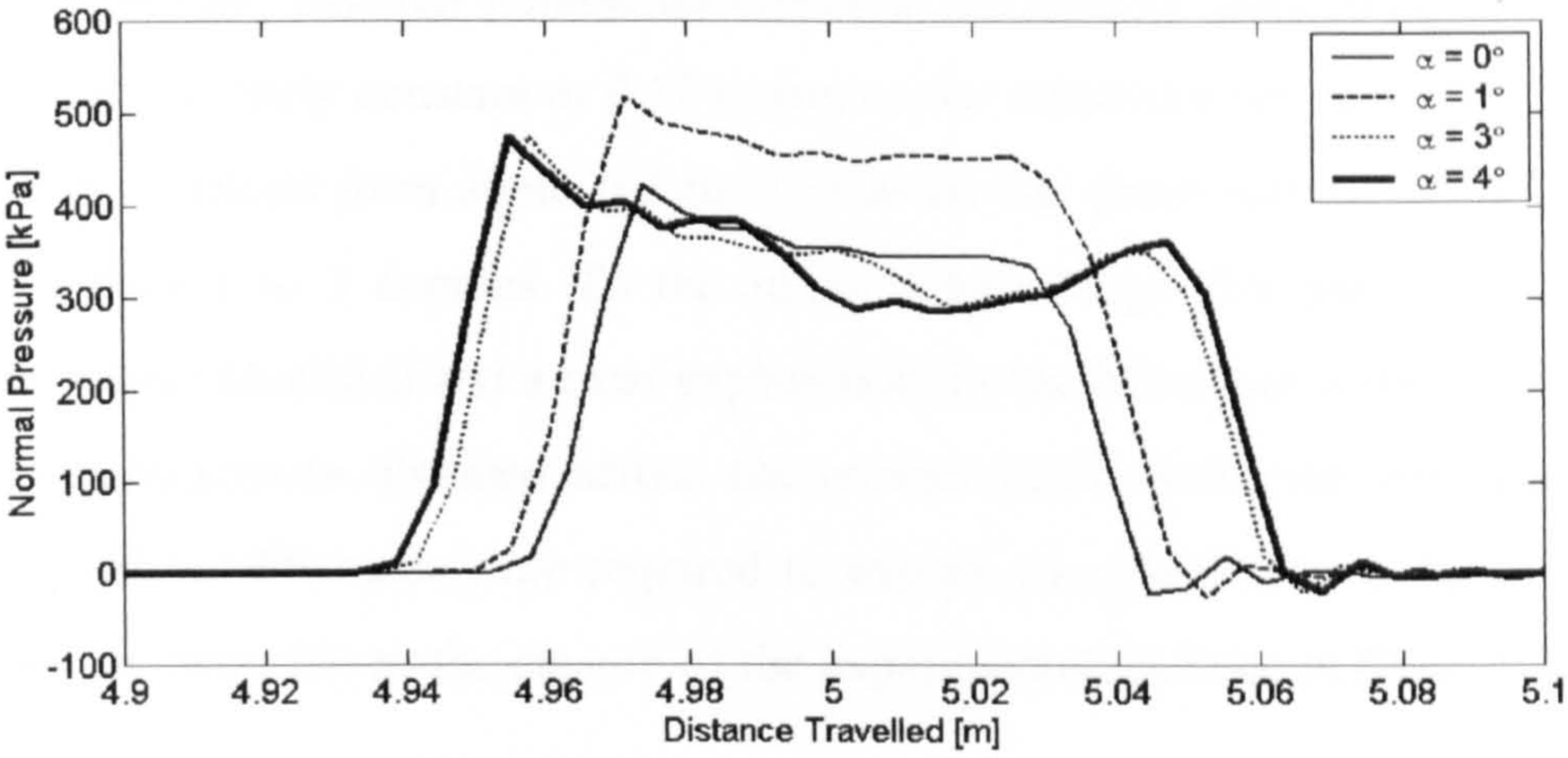

(a)

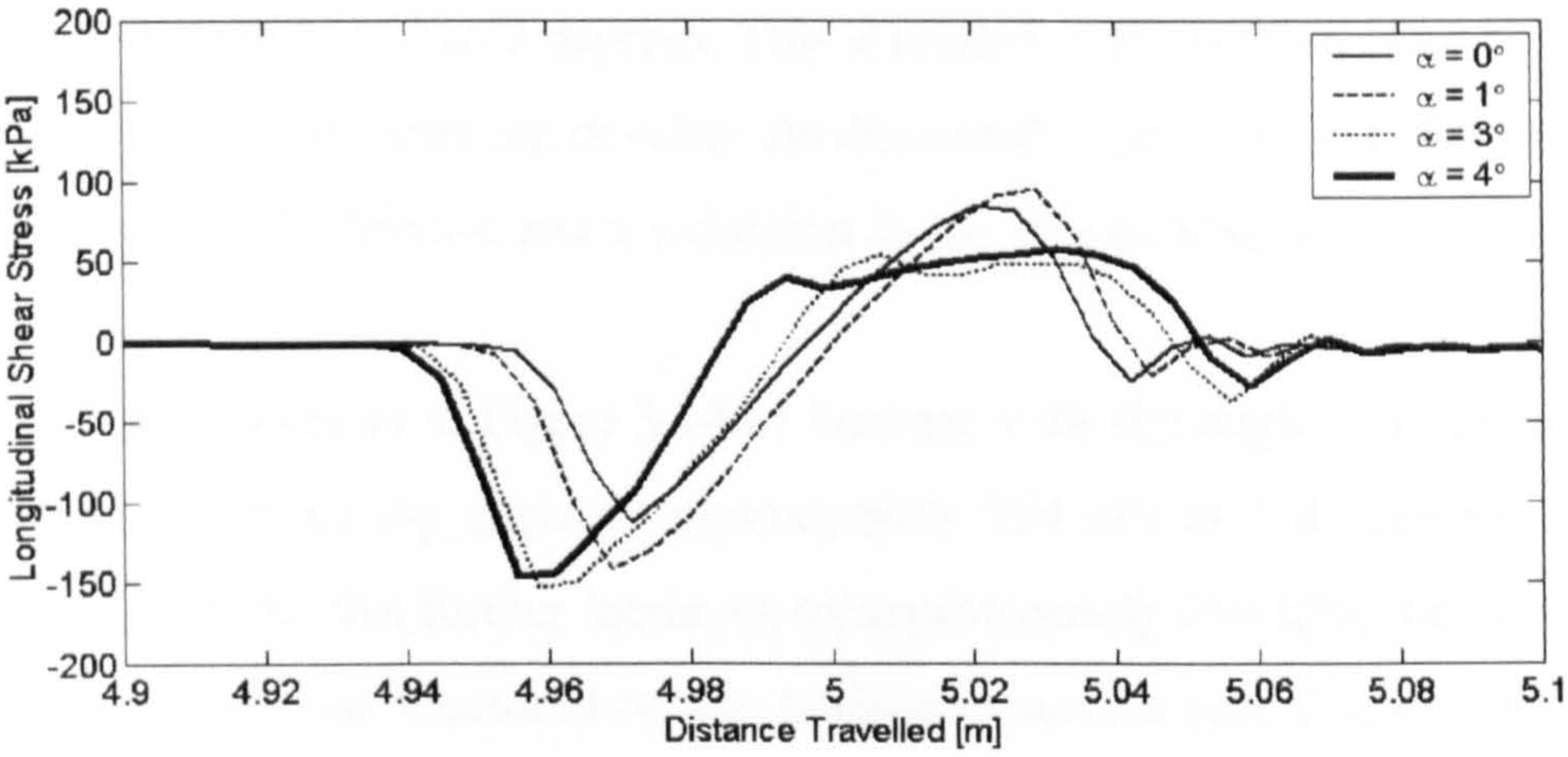

(b)

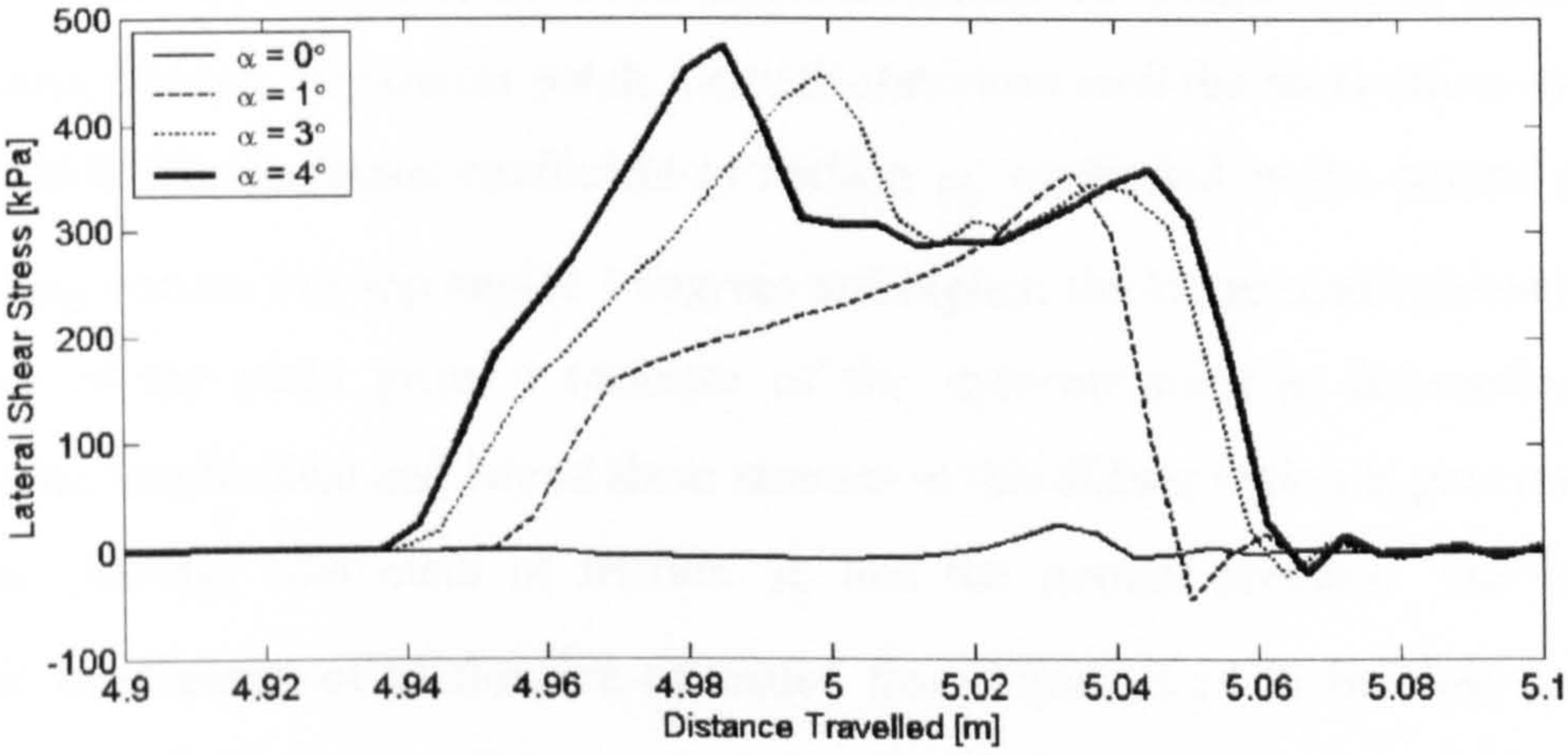

(c)

Figure 3.14 Measured contact stress distributions with slip angle on a cylindrical (drum) surface: (a) normal pressure; (b) longitudinal shear stress; (c) lateral shear stress

horizontal surface. Another notable difference is the contact patch length. On the flat bed surface it is fairly constant at 0.11 m (up to the maximum slip angle of 2 degrees). The length increases from about 0.1 to 0.13 m on the drum surface as the slip angle increases from 1 to 3 degrees. To the author's knowledge this phenomenon has not previously been identified and a clear explanation for the behaviour is not at hand. Thus, further measurements obtained across the contact patch width (or simulation results from a validated FE model) are required to explain the phenomenon. Again the work could not be done due to the closure of the experimental facilities at Dunlop Tyres Ltd.

The longitudinal shear stresses shown in Figure 3.14(b) again follow a sinusoidal-style sweep. A significant reduction in the stresses is shown to occur towards the rear as the slip angle increases from 1 to 3 degrees. This is related to the friction ellipse limiting the maximum shear stresses that can develop. As discussed in Section 3.6.1, the lateral shear stresses dominate the friction and a reduction in the longitudinal shear stresses occurs.

The lateral shear stresses in Figure 3.14(c) increase with slip angle from approximately 0 kPa at zero degrees slip angle to approximately 350 kPa at 1 degree slip angle. At 4 degrees slip angle, this further increases to approximately 450 kPa. These values are much higher than those measured on the horizontal surface (see Figure 3.10(c)) at an equivalent slip angle. At a slip angle of 1 degree the difference is greater than three times. A smaller contact patch area on the cylindrical surface is one possible reason for the difference. On the drum, the shear stress increases more rapidly as a tread element progresses through the contact patch. Growth continues until the shear stress overcomes the available friction (static coefficient of friction μ_p multiplied by the normal pressure) and sliding occurs. For slip angles 3 degrees and higher, the lower stress plateau towards the rear of the plots gives a measure of the dynamic friction. Interaction of the developing longitudinal and lateral shear stresses in this sliding region is governed by the dynamic (sliding) coefficient of friction μ_s and the normal pressure. The static and dynamic coefficients of friction are estimated from Figure 3.14 to be close to 1.2 and 1.0, respectively. It is reasonably assumed that the friction coefficients are the same at all positions across the contact patch. This is the consistent with the approach adopted in semi-empirical tyre models [33, 45, 46]. It should be noted that these friction coefficients are significantly higher than those observed on typical road surfaces (see Table 2.1). The values are relevant to the development of the rolling FE tyre model

discussed in Chapter 4 and to the subsequent rolling tyre simulations using this model.

3.7.4 Cornering Characteristics and Camber Angle

The normal pressure and shear stress distributions in the contact patch with camber angle (γ) variations to 4 degrees (in increments of 1 degree) are shown in Figures 3.15. The normal load exerted on the tyre was 3 kN and the tangential speed of the drum was 20 km/h. The measurements were obtained along the length of the contact patch at the lateral centre of the experimental tyre and a slip angle correction was again applied.

The normal pressure and shear stress characteristics shown in Figure 3.15 are similar to those previously highlighted from the flat bed experiments in Figure 3.11. The exception to this is the distinct reduction in the normal pressures at non-zero camber angles. Figure 3.15(a) shows that the reduction is approximately constant with camber angles 1 degree and higher. The author cannot offer an explanation for this observation based on the physical behaviour of the experimental tyre. However, it is known that the measurements at camber angles between 1 and 4 degrees were not taken on the same day as the 0 degree results; they were taken much later. Thus, it is postulated here that the stress transducer was not in calibration when the normal pressure measurements at camber angles between 1 and 4 degrees were obtained. Calibration was the responsibility of Dunlop Tyres Ltd. and was beyond the control of the author. The author believes that the longitudinal and lateral shear stresses are accurate and representative of the 'actual' tyre behaviour. Only the normal pressure measurements appear to be effected. The shear stress distributions in Figures 3.15(b) and 3.15(c) correlate well with their corresponding distributions from the flat bed experiments in Figures 3.11(b) and 3.11(c), respectively.

3.8 Summary

A comprehensive experimental investigation into the contact patch behaviour of an automobile tyre has been completed. The stationary behaviour of the tyre under normal load, and the behaviour under free-rolling and cornering (slip and camber angle) conditions has been characterised. The load-deflection characteristics and contact patch dimensions of the stationary tyre have been presented, and a reasonably complete picture is given on how the normal and shear stress distributions might change under driving

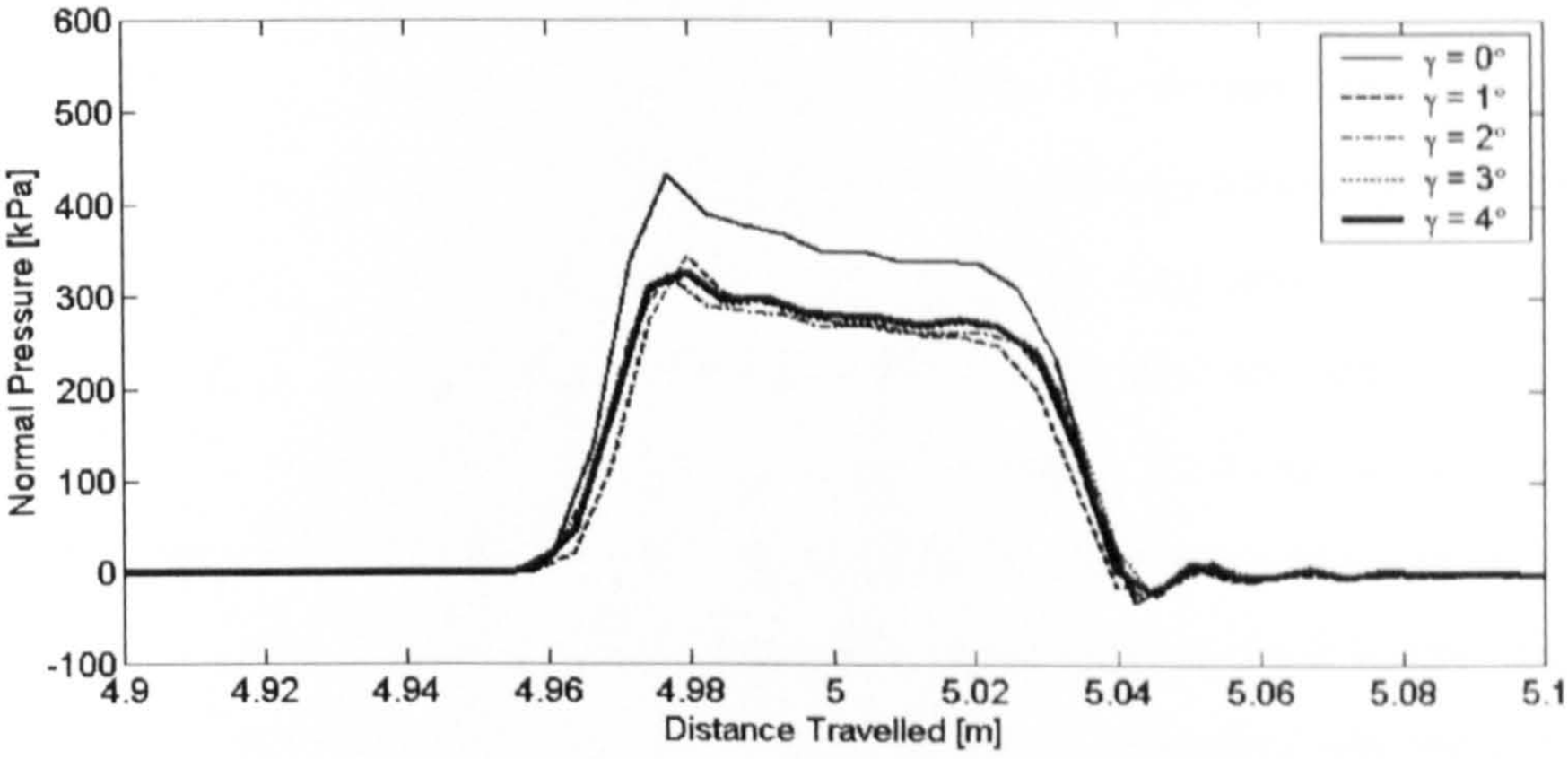

(a)

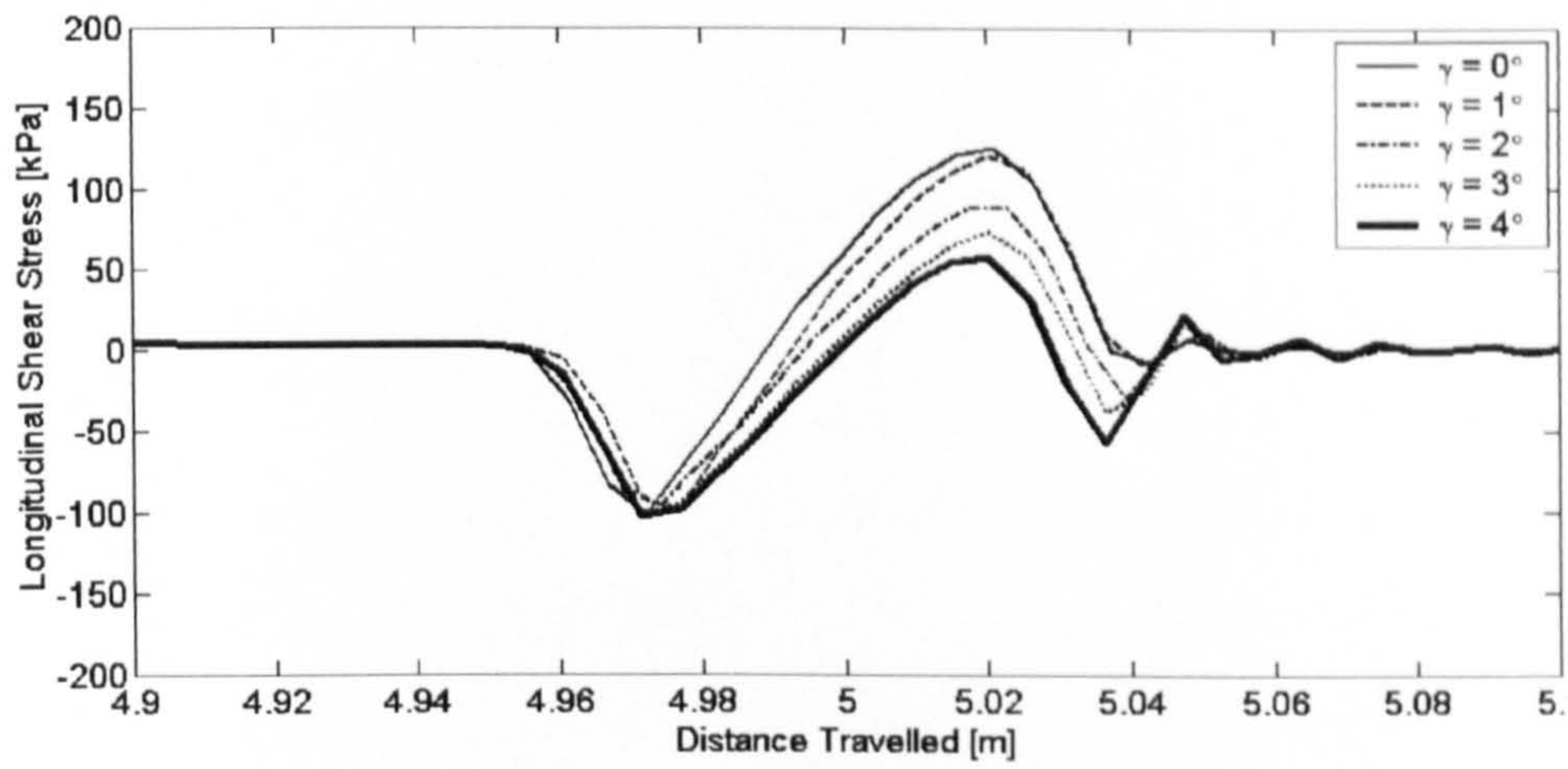

(b)

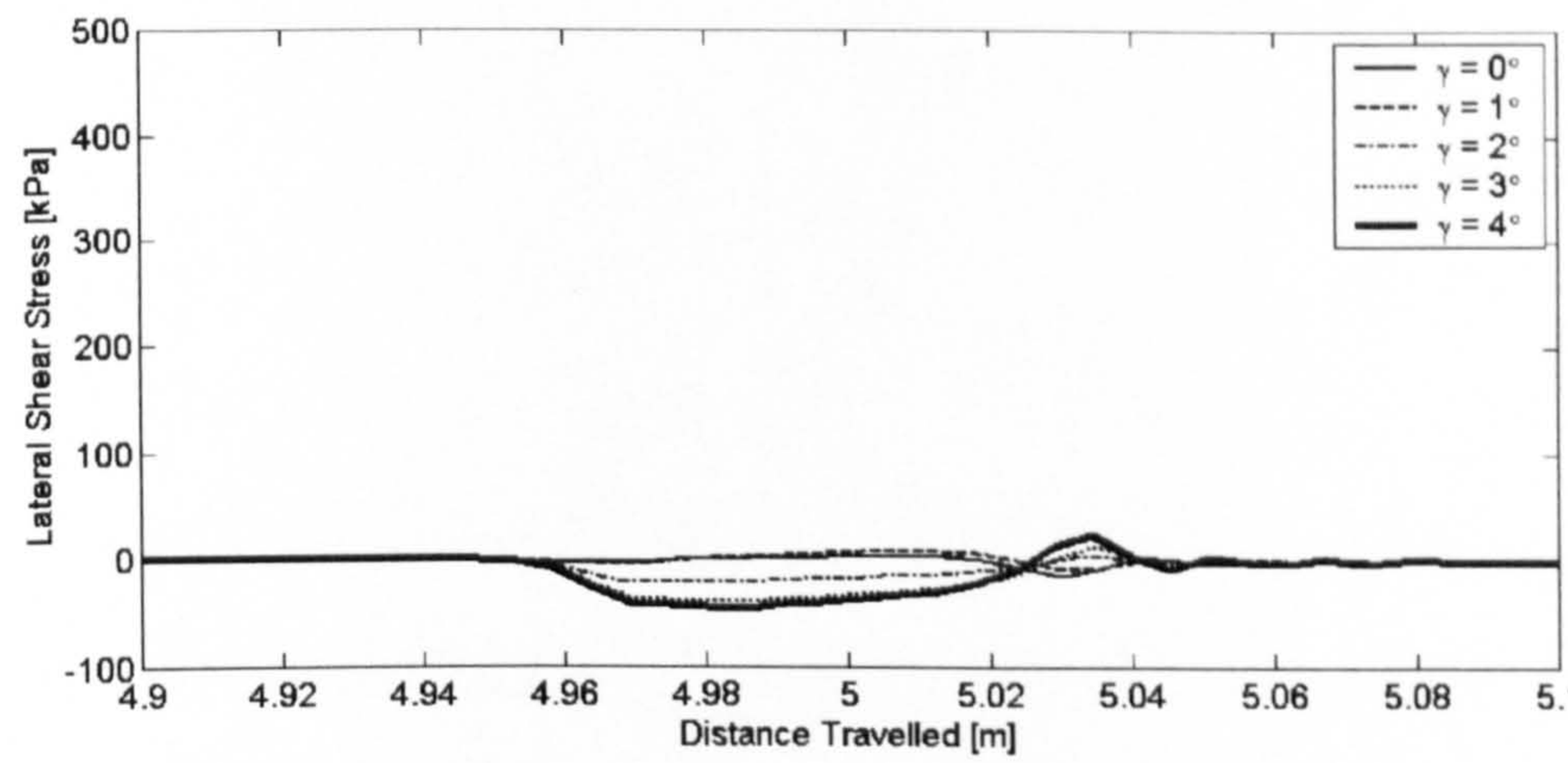

(c)

Figure 3.15 Measured contact stress distributions with camber angle on a cylindrical (drum) surface: (a) normal pressure; (b) longitudinal shear stress; (c) lateral shear stress

conditions. The results have been analysed to provide better understanding of the physical behaviour of tyres in the contact patch. A comparison between stress measurements obtained on a horizontal and a drum surface has also been presented and significant differences between the two surfaces are reported. The measurements presented in this chapter provide a valuable source of physical test data that can be used to evaluate the performance of mathematical models such as those presented in Chapter 4. Simulation results obtained using these models are compared in Chapters 5 and 6 to the stationary and free-rolling physical test data presented in this chapter. The contact patch behaviour during cornering conditions is not used in this thesis but may be used by other researchers to evaluate similar FE tyre models or semi-empirical models.

Chapter 4 Finite Element Models for Simulation of Macroscopic Tyre Behaviour

4.1 Introduction

Finite Element (FE) tyre models presented in the literature vary greatly (see Section 2.9). The mesh may consist of only a few axisymmetric elements [63] or many thousands of solid, membrane/shell and beam elements [57, 64]. This is because the modelling approach depends not only on the requirements of the simulation but also on the available computational resource. To satisfy the aims of the research outlined in Section 1.3, it is necessary to establish a mesh refinement sufficiently adequate to simulate macroscopic tyre behaviour local to the contact patch, but which is not so refined that the computational cost becomes intolerable with currently available computational resources. The material constitutive equations are important since no numerical simulation can reliably predict the structural response when the material property descriptions are incorrect. An acceptable representation of contact and friction is also important to simulate the actual tyre/wheel contact, and the interaction between the tyre and the contacted 'ground' surface. This chapter addresses these important aspects of the FE modelling, and presents two models developed to simulate stationary and rolling tyre behaviour. The chapter also highlights the author's modelling experiences in relation to the explicit solver LS-DYNA [17] and identifies important areas which must be considered by analysts undertaking tyre simulations. It should be noted that, unless otherwise stated, version 950d of the code has been used in this thesis.

4.2 Mesh Generation

Two separate tyre models were developed for analysis using LS-DYNA [17]. HyperMesh [77] was used to generate the LS-DYNA model descriptions. One model was specifically developed to simulate the structural behaviour of the stationary experimental tyre (see Section 3.4.1), while the second model was developed to predict

the rolling tyre response (Sections 3.4.2 and 3.4.3). These models are referred to here as the stationary and rolling models, respectively. The stationary and the rolling meshes are shown in Figures 4.1 and 4.2. The two meshes differ only with respect to the element density in the circumferential direction, the mesh through the cross-section is identical. The models represent the tyre as a complex arrangement of rubber components and reinforced rubber composites. The wheel is considered as a separate entity. Many FE tyre models in the literature [78-80] simply represent the wheel using constraint equations but this approach is only acceptable if the purpose of the model is to simulate behaviour under static or typical driving conditions. During atypical driving conditions, slippage or, in extreme cases, seperation can occur between the tyre and wheel. To enable simulations to be acceptable under atypical loading situations, an independent wheel model is necessary. Thus, the tyre and wheel are modelled separately in this thesis and the tyre/wheel contact (wheel fit) is considered as an additional boundary condition.

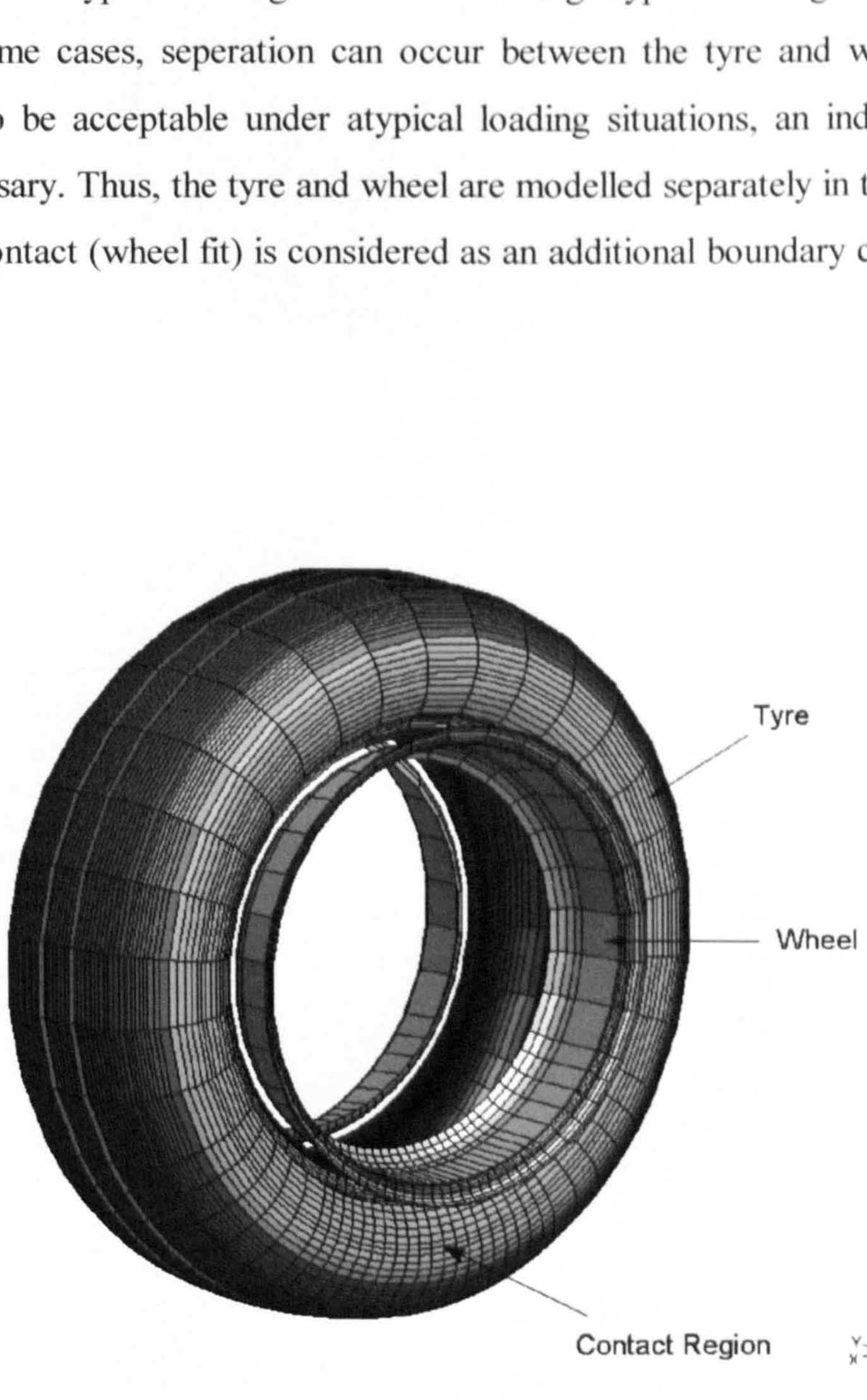

Figure 4.1 Three-dimensional stationary (non-rolling) model

(a)

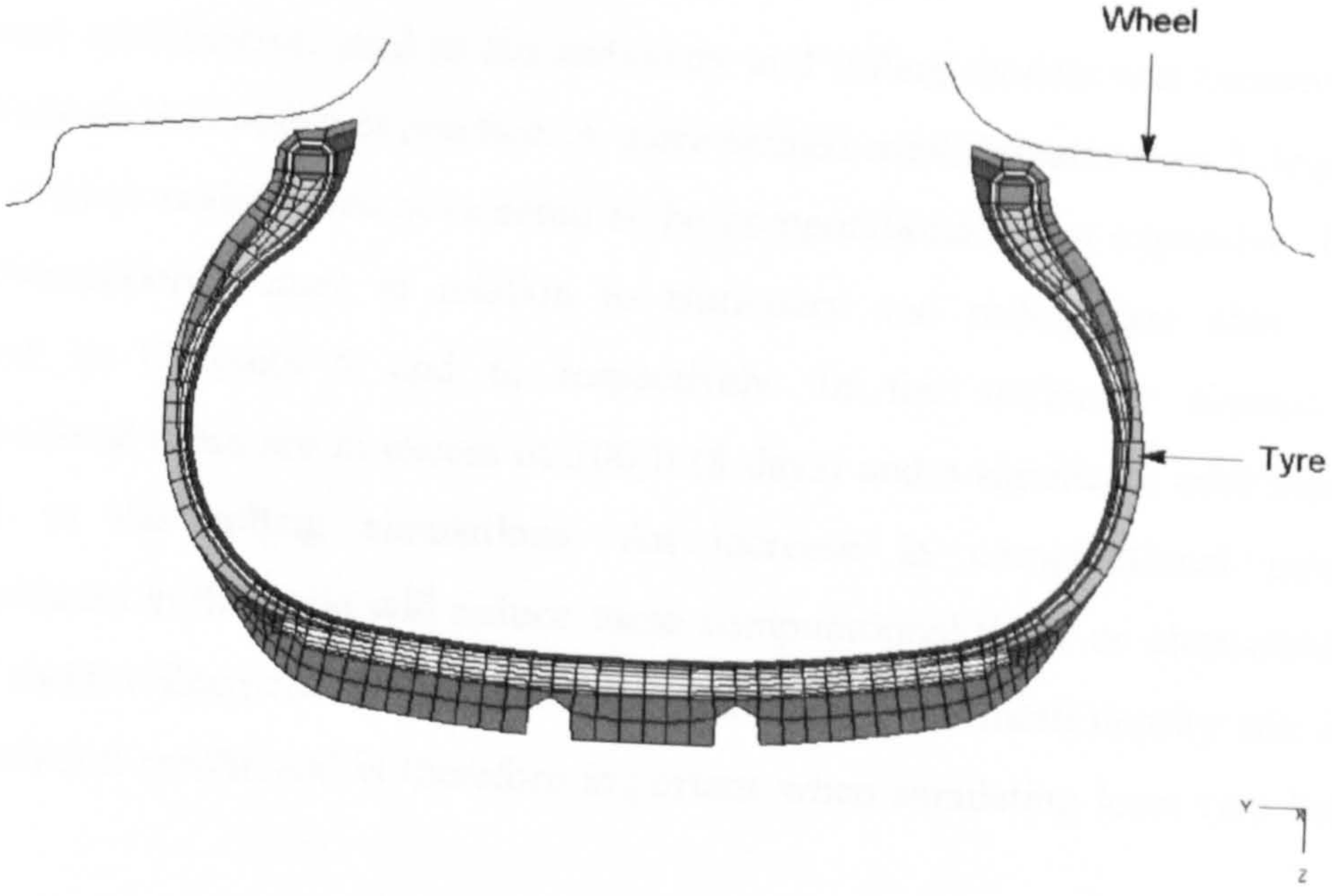

(b)

Figure 4.2 Rolling model: (a) three-dimensional model; (b) cross-section

The stationary model in Figure 4.1 is refined local to the intended contact region and the elements extend every 3 degrees around the circumference. Further from the contact region, the mesh density is reduced and elements extend every 6, and then 12 degrees. Reducing the mesh density reduces the number of nodes and elements in the model and, hence, the computational time. A total of 56,400 solid and membrane elements are used to model the stationary (non-rolling) tyre and 1,400 shell elements to model the wheel.

In Figure 4.2, the rolling model is shown to have a uniform mesh density with elements extending every 3 degrees around the tyre circumference. This mesh specification is essential in a Lagrangian analysis because the region of contact between the 'tyre' and 'ground' continually changes during rolling. In an Eulerian analysis, the mesh specification in Figure 4.1 would be appropriate [69] but to the author's knowledge it is not possible to implement this approach in LS-DYNA [17] for solid mechanics problems, only those in fluid mechanics [81]. In the rolling model there are 135,360 solid and membrane elements in the tyre and 3,360 shell elements in the wheel. As a result of the necessary circumferential mesh refinement there is therefore 2.4 times the number of nodal displacement unknowns (degrees of freedom) in the rolling model.

The mesh specification used in the stationary and rolling models was considered to be the maximum acceptable in practice. A more refined mesh (greater than 3 degrees local to the contact region) was considered to be computationally too expensive. Details of the computational times in relation to stationary and rolling tyre simulations are provided in Chapters 5 and 6, respectively. In the stationary simulations, the computational times are in excess of 200 h (8 days) and a significant additional cost is evident in the rolling simulations. An increase in computational power and improvements in the code will reduce these computational times or alternatively allow greater mesh refinement in the future. It is noted that the mesh density can influence the simulation results and is therefore important when simulating local tyre behaviour.

4.2.1 Tyre Components

To allow separate stresses and strains to be determined in the tyre components, the rubber components (tread, sidewalls, liner, apexes and clinches) and reinforced rubber composites (carcass plies, bandages and breakers) need to be individually represented.

The rubber components are modelled here as deformable continua using linear (constant stress) solid elements [17]. Volume integration is carried out with one-point Gaussian quadrature. A significant cost saving is obtained by using the one-point integration (default) element instead of the fully integrated (8-point) solid element. In simulations conducted with the stationary and rolling models, using the fully integrated elements was found to approximately treble computational time. It should also be noted that one-point integration has another advantage in addition to cost. Fully integrated elements used in plasticity problems and other problems where a material's Poisson's ratio approaches 0.5 (rubber typically has a Poisson's ratio >0.49) can lock-up in constant volume bending modes. This element locking is undesirable and can cause numerical instability.

The biggest disadvantage to one-point integration is the need to control the zero energy modes which arise, known as hourglassing modes (see Figure 4.3). Hourglass modes typically give a zig-zag appearance to a mesh usually referred to as hourglass deformation. Such unwarranted deformation modes can swamp the actual deformation which is sought and, as a consequence, are commonly resisted by viscosity which is automatically calculated in the code. The viscous form of hourglass control is the default in LS-DYNA [17] and is acceptable in most situations. In some situations, however, numerical problems can occur and it is beneficial to select a stiffness method of hourglass control instead of a viscous one. A detailed description of the viscous and stiffness methods of hourglass control is given in the book by Jacob and Goulding [68].

An investigation was conducted by the author to determine the most acceptable control method for the stationary and rolling models. It was found that the viscous methods available in the LS-DYNA code (types 1 to 3) did not adequately control hourglass deformation in the models. This is clearly shown in Figure 4.4 where the default viscous formulation (type 1) has been used with the stationary model. In the figure, the wheel fit and a inflation pressure of 200 kPa are represented. The standard Flanagan-Belytschko stiffness formulation (type 4) also did not perform well. Thus, the author prefers the Flanagan-Belytschko stiffness formulation with exact volume integration (type 5) to control hourglass modes. A stiffness formulation based on the Flanagan-Belytschko formulation is also used in a LS-DYNA tyre model developed by Kao and Muthukrishnan [57] but the type is not clearly specified. This leads the author to believe that for tyre simulations using explicit FE software, such as LS-DYNA [17], a stiffness

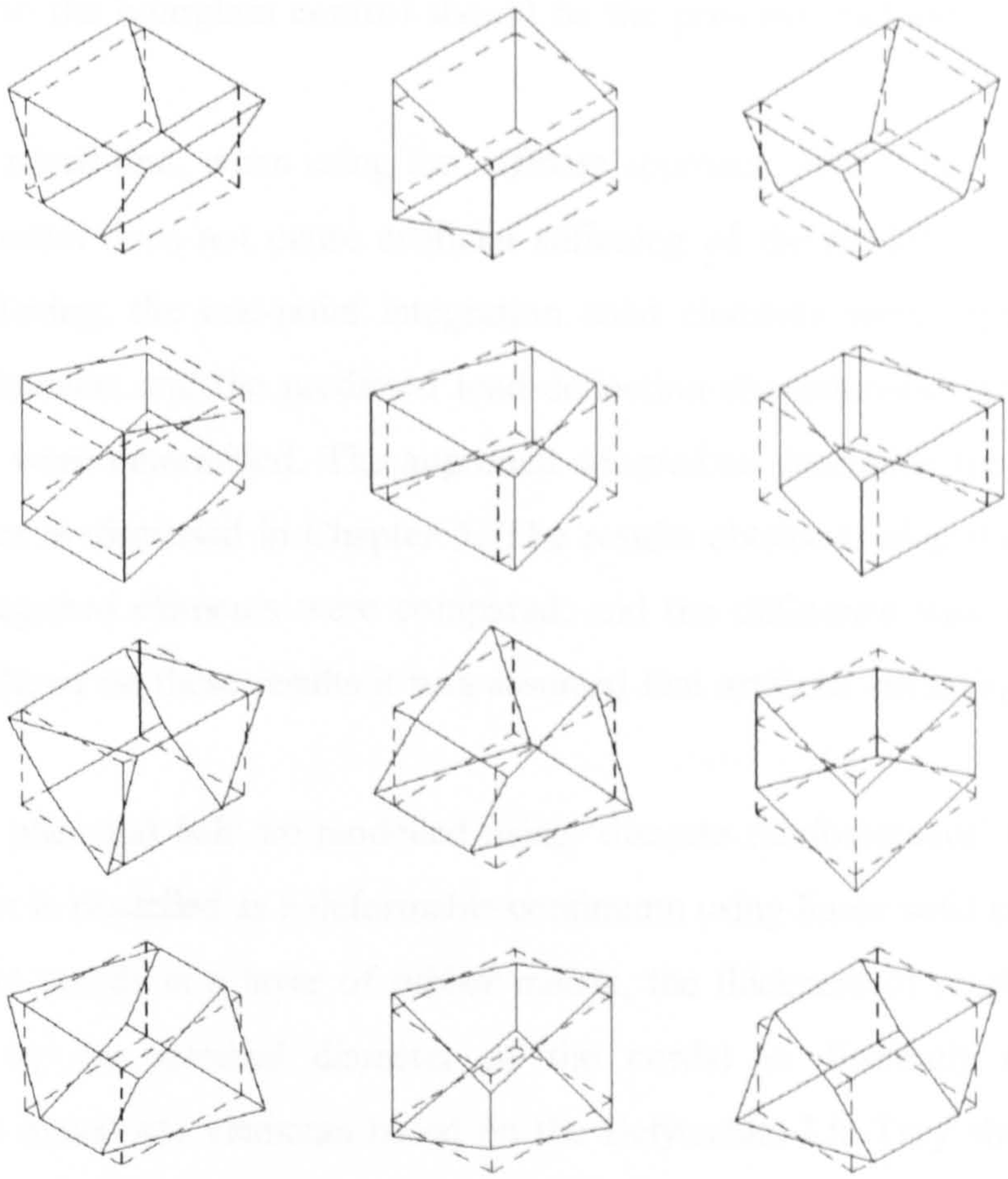

Figure 4.3 Hourglass modes of an eight node element with one integration point [68]

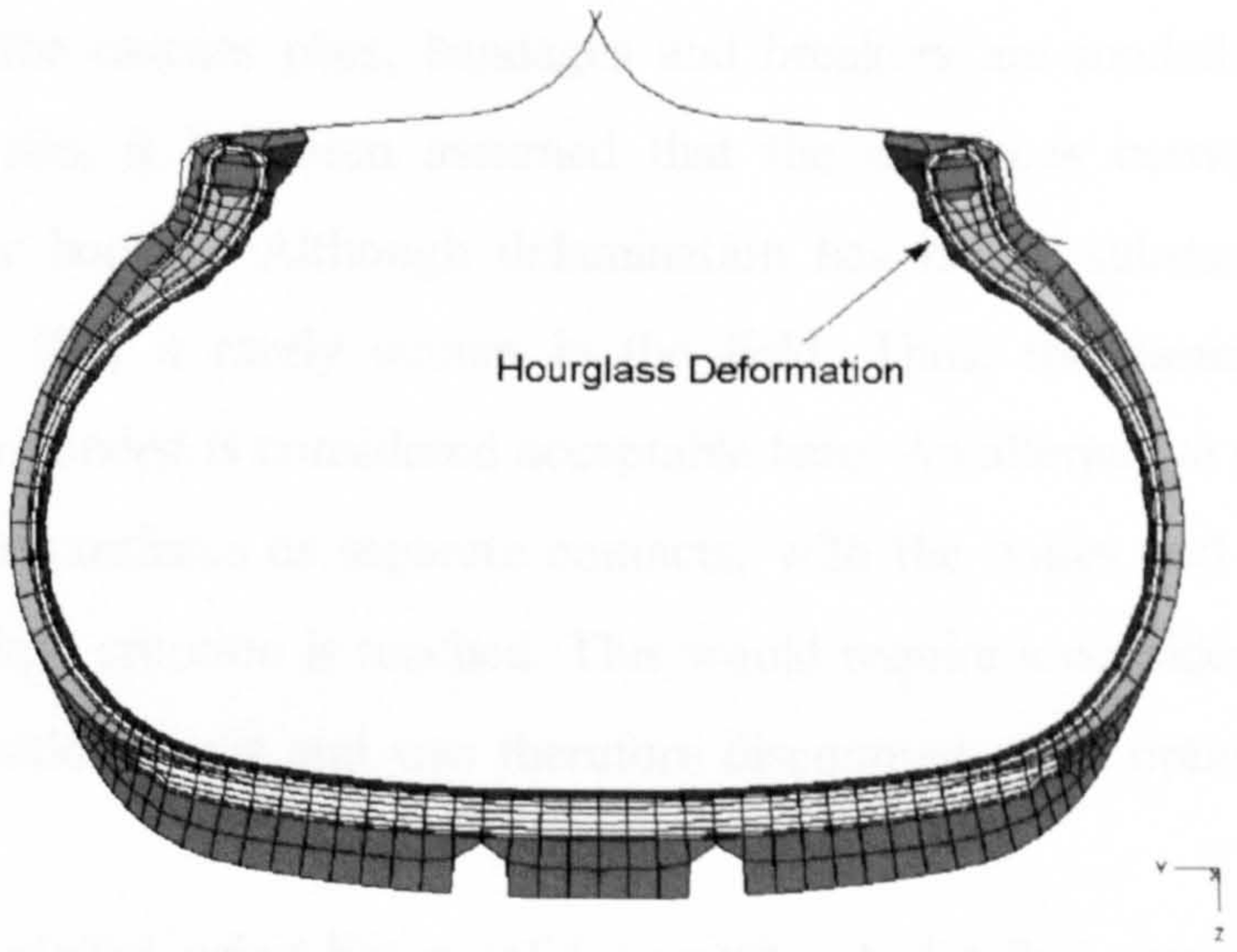

Figure 4.4 Deformation of the 'tyre' cross-section when the default (type 1) viscous hourglass control formulation in LS-DYNA is employed with the stationary model

formulation to the hourglass control should be the principal method for consideration.

It should be noted that, when using the stiffness approach, care is needed to ensure the hourglass control does not cause artificial stiffening of the model [57]. To check for artificial stiffening, the one-point integration solid elements were replaced with fully integrated elements and the predicted load-deflection characteristics of the tyre under normal load were determined. The approach adopted to determine the load-deflection characteristics is discussed in Chapter 5. The results obtained using the one-point and the fully integrated elements were compared, and the difference was found to not be significant. Based on these results it was assumed that artificial stiffening did not occur.

The carcass plies and belt are modelled using 'discrete reinforcement' techniques. The rubber matrix is modelled as a deformable continuum using linear solid elements and the reinforcement (cords in a layer of rubber matrix, the thickness of reinforcement being determined by the nominal diameter of the cords) is discretely modelled using quadrilateral membrane elements based on the Belytschko-Lin-Tsay shell element [82, 83]. The approach allows separate stresses and strains to be obtained in the matrix and reinforcement, but not in individual cords. To predict stresses and strains in individual cords would require each of the cords to be individually represented and would significantly increase the number of elements in the model, and hence computational time. The interfaces between adjacent components and between the matrix and reinforcement of the carcass plies, bandages and breakers are modelled using shared nodes. In doing this, it has been assumed that the interfaces between the various materials are fully bonded. Although delamination has had a substantial amount of attention recently [84] it rarely occurs in the field. Thus, the assumption that the interfaces are fully bonded is considered acceptable here. An alternative approach would be to model these interfaces as separate contacts, with the nodes tied to the adjacent surface until a failure criterion is reached. This would require a considerable amount of additional computational cost and was therefore discounted as an option in this thesis.

The beads are modelled using linear solid elements. A detailed representation of the beads was not considered to be important because they are a significant distance from the area of particular interest, i.e. the contact patch. Only the overall behaviour (usually referred to as the global material behaviour) of the beads is modelled and, as a

consequence, separate stresses and strains may not be obtained in the cords and matrix.

4.2.2 Steel Wheel

The steel wheel is coarsely modelled in two halves using Belytschko-Lin-Tsay shell elements [82, 83]. To allow simulation of the interaction between the tyre and the wheel, these two halves are initially positioned either side of the tyre (see Figure 4.2). Since the steel wheel is much stiffer than the contacting tyre clinch (>100 times) and no stress output is required, it was assumed to be rigid. The rigid material model (model 20) in LS-DYNA [17] is used. This model requires the user to define a modulus of elasticity, which is used in any contact model (see Section 4.7), and also the density which is used to determine the mass of the wheel. A Young's modulus of 200 GPa and a density of 7860 kg/m^3 are assumed in this thesis. These values are representative of bulk steel.

4.3 Material Properties

The tyre consists of a number of material components. Their mechanical properties required as input data to LS-DYNA [17] are given in Tables 4.1 and 4.2. Densities are essential since a dynamic (rolling) analysis requires knowledge of the mass associated with each degree of freedom (see Section 2.9). The density for all rubber compounds are shown in Tables 4.1 and 4.2. To determine densities for the reinforcements, the well known Rule of Mixtures was used with the constituent densities given in Table 4.2 and their calculated volume fractions. The volume fraction of the cords V_c is given by

$$V_c = N \times \frac{(\pi \phi_e^{\,2} / 4)}{\phi_n}, \tag{4.1}$$

where N is the number of cords per unit length, ϕ_n is the nominal diameter of the cords and ϕ_e is the effective diameter. The volume fraction of rubber matrix is $1 - V_c$.

4.4 Rubber Compounds

A material's elastic behaviour is described in terms of its stress/strain relationships. For

Rubber Component	Secant Modulus (100 %) [MPa]	Density [kg/m^3]	Poisson's Ratio [no units]
Tread	1.25	1150	>0.49
Sidewalls	1.07	1120	>0.49
Liner	1.79	1140	>0.49
Apexes	7.13	1180	>0.49
Clinches	3.30	1160	>0.49

Table 4.1 Mechanical property data for rubber components (Dunlop Tyres Limited)

many materials, such as mild steel, these constitutive relationships are assumed to be linear to the elastic limit and a corresponding modulus of elasticity is defined [62]. The tensile stress/strain relationship is non-linear for rubber compounds and therefore a single modulus of elasticity can only refer to a very small portion of the elastic behaviour. The secant modulus is usually quoted (it is the instantaneous modulus at a specific strain value). For rubbers, it is sometimes quoted at strains of 50, 100 and 300 percent [85] but is often given only at the 100 percent strain value. In FE modelling, this is useful only when rubber is highly strained and the results can be approximated in those regions where the strains are much lower. Secant moduli data is therefore not useful to the tyre FE analyst, as internal rubber compound strains are typically less than 10 percent (this value was obtained from FE analyses using the models described here). As a consequence of this, and the reluctance of tyre manufacturers to release property data for their preferred rubber compounds, relevant stress/strain data for FE modelling is not easy to obtain. Thus, methods to approximate the elastic behaviour are needed.

A simple method to characterise the fundamental stress/strain relationships for the rubber compounds in the experimental tyre (see Section 3.2) is used in this thesis. Consideration is given to the five rubber components, and the three rubber matrices associated with the carcass plies, bandages and breakers. The relationships are estimated using experimental data provided by Dunlop Tyres Limited for a typical 'unknown' rubber compound subjected to simple extension. The stress/strain data was obtained in accordance with BS 903: Part A2: 1995 (ISO 37: 1994). The engineering stress against engineering strain data is provided in Appendix B. Consideration is given to strains up to

	Rubber Matrix			Cords						
Reinforced Rubber Composites	Secant Modulus (100 %)	Density	Poisson's Ratio	Elastic Modulus	Density	Poisson's Ratio	Nominal Diameter	Effective Diameter	End Count	Cord Angle
	[MPa]	[kg/m^3]	[no units]	[GPa]	[kg/m^3]	[no units]	[mm]	[mm]	[1/m]	[degrees]
Beads	*	*	*	*	*	*	*	*	*	0
Carcass Plies	3.16	1120	> 0.49	3.36	1170	0.4	0.660	0.552	1050	90
Bandages	≈ 3.16	1120	> 0.49	2.93	1140	0.4	0.660	0.552	1050	0
Breakers	≈ 3.16	1120	> 0.49	*	*	*	0.750	0.560	700	21

N.B. * indicates that the data was not available

Table 4.2 Mechanical property data for reinforced rubber composites (Dunlop Tyres Limited)

50 percent. The secant modulus at 100 percent strain was also provided and was 3.19 MPa. To estimate the stress/strain relationship for the rubber compounds in the experimental tyre, the engineering stresses in Appendix B were scaled based on the specific 100 percent secant modulus listed in Tables 4.1 and 4.2, and that of the unknown tyre compound. This approximation assumes the stress/strain relationships for each of the rubber tyre compounds is similar to that of the unknown compound.

4.5 Mooney-Rivlin Equation

Numerous constitutive models exist in the literature to simulate the elastic behaviour of rubber compounds [86, 87]. Seven different rubber models are available in LS-DYNA [17]. The Mooney-Rivlin equation is commonly used in FE tyre models [57, 88] and it is seen as the industry standard. The model mathematically represents the elastic behaviour in terms of a strain energy function. This strain energy function is based on the acceptable assumption that rubber is incompressible (i.e. $\lambda_1 \lambda_2 \lambda_3 = 1$), since the bulk modulus is several orders of magnitude greater than the shear modulus, and isotropic in the unstrained state. The Mooney-Rivlin strain energy function W is

$$W = C_1(I_1 - 3) + C_2(I_2 - 3) \tag{4.2}$$

where C_1 and C_2 are elastic constants related to the material's shear modulus, and the independent variables I_1 and I_2 are related to the principal extension ratios λ_1, λ_2, and λ_3, by $I_1 = \lambda_1 + \lambda_2 + \lambda_3$ and $I_2 = 1/\lambda_1^2 + 1/\lambda_2^2 + 1/\lambda_3^2$. These extension ratios are related to the engineering strain ε by $\lambda = 1 + \varepsilon$, and the relationships between the principal true stresses σ_1^t, σ_2^t and σ_2^t, and the corresponding strains (Figure 4.5) are

$$\sigma_1^t - \sigma_2^t = 2(\lambda_1^2 - \lambda_2^2)(C_1 + \lambda_3^2 C_2) \tag{4.3(a)}$$

$$\sigma_2^t - \sigma_3^t = 2(\lambda_2^2 - \lambda_3^2)(C_1 + \lambda_1^2 C_2) \tag{4.3(b)}$$

and

$$\sigma_3^t - \sigma_1^t = 2(\lambda_3^2 - \lambda_1^2)(C_1 + \lambda_2^2 C_2) \tag{4.3(c)}$$

Thus, if a rubber compound is subjected to simple extension or uniaxial compression in the λ_1-direction then: $\lambda_1 = \lambda$, $\lambda_2 = \lambda_3 = \lambda^{-1/2}$; the principal true stresses $\sigma_2^t = \sigma_3^t = 0$; and the principal stress σ_1^t can be obtained from Equ. 4.3(a). Equs. 4.3(b) and 4.3(c) are used when extension is in the λ_2 - and λ_3 -directions, respectively. The true stress is

$$\sigma_1^t = 2(\lambda^2 - 1/\lambda)(C_1 + C_2/\lambda) \tag{4.4}$$

and the engineering stress σ_1 (force per unstrained cross-sectional area) is given by

$$\sigma_1 = 2(\lambda - 1/\lambda^2)(C_1 + C_2/\lambda) \tag{4.5}$$

It should be noted that for the case of simple extension $\lambda > 1$ (see Figure 4.6(a)), while for uniaxial compression $\lambda < 1$. Thus, a positive stress is obtained in tension and a negative stress in compression. This is consistent with standard sign convention [73].

If the same compound is subjected to simple shear as shown in Figure 4.6(b): $\lambda_1 = \lambda$; $\lambda_2 = 1$; and $\lambda_3 = 1/\lambda$. The shear strain $\gamma = \lambda - 1/\lambda = \tan\phi$ and the shear stress τ_{xy} is

$$\tau_{xy} = 2(C_1 + C_2)\gamma \tag{4.6}$$

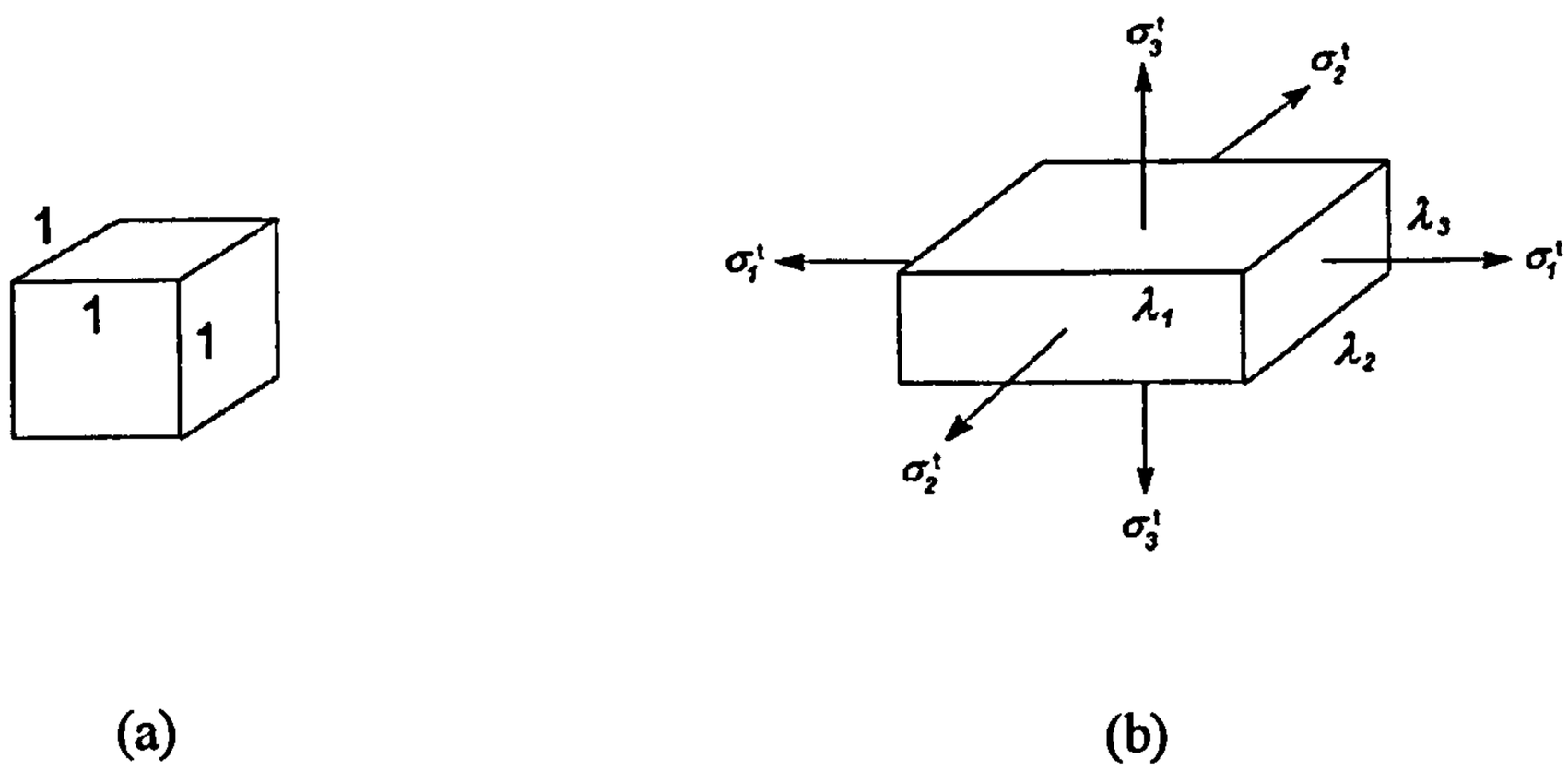

(a) (b)

Figure 4.5 Pure homogeneous strain: (a) unstrained state; (b) strained state

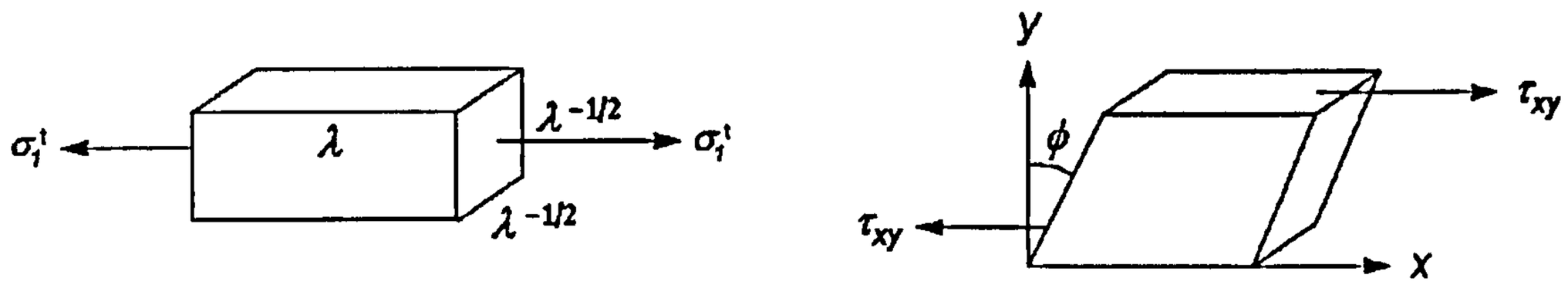

(a) (b)

Figure 4.6 Particular types of strain: (a) simple extension; (b) simple shear

Herein, the Mooney-Rivlin model is used to simulate the elastic behaviour of the eight rubber compounds in the experimental tyre (i.e. the five rubber components and the rubber matrices of the carcass plies, bandages and breakers). The Mooney-Rivlin elastic constants C_1 and C_2 were calculated from the estimated tensile stress/strain relationships using a curve-fitting program based on the least squares method [89]. These elastic constants are shown in Table 4.3 where the rubber matrices of the carcass plies, and belt (bandages and breakers) are grouped as one compound referred to as the topping. This is acceptable since their mechanical properties are similar (see Table 4.2).

Rubber Components	Mooney-Rivlin Constants	
	C_1 [MPa]	C_2 [MPa]
Tread	0.07	0.32
Sidewalls	0.06	0.27
Liner	0.10	0.45
Apexes	0.38	1.80
Clinches	0.18	0.84
Topping	0.17	0.80

Table 4.3 Calculated Mooney-Rivlin elastic constants

The estimated stress/strain curve for the rubber tread compound subjected to simple extension and the corresponding Mooney-Rivlin curve derived from Equ. (4.5) are shown in Figure 4.7. Similar stress/strain curves can also be produced for the other rubber compounds. A favourable comparison is observed up to an engineering strain of

45 percent and in the most important region up to 10 percent strain, the correlation is excellent. The gradient of the Mooney-Rivlin curve at zero strain is similar to the estimated curve and, thus, the stress/strain relationship in compression is also likely to be accurately represented. The shear modulus in Equ. (4.6) was found to be 0.77 MPa. The elastic behaviour in simple shear has been shown in Chapter 3 (see Figures 3.8 and 3.10 to 3.15) to be particularly relevant to modelling tyre behaviour in the contact patch.

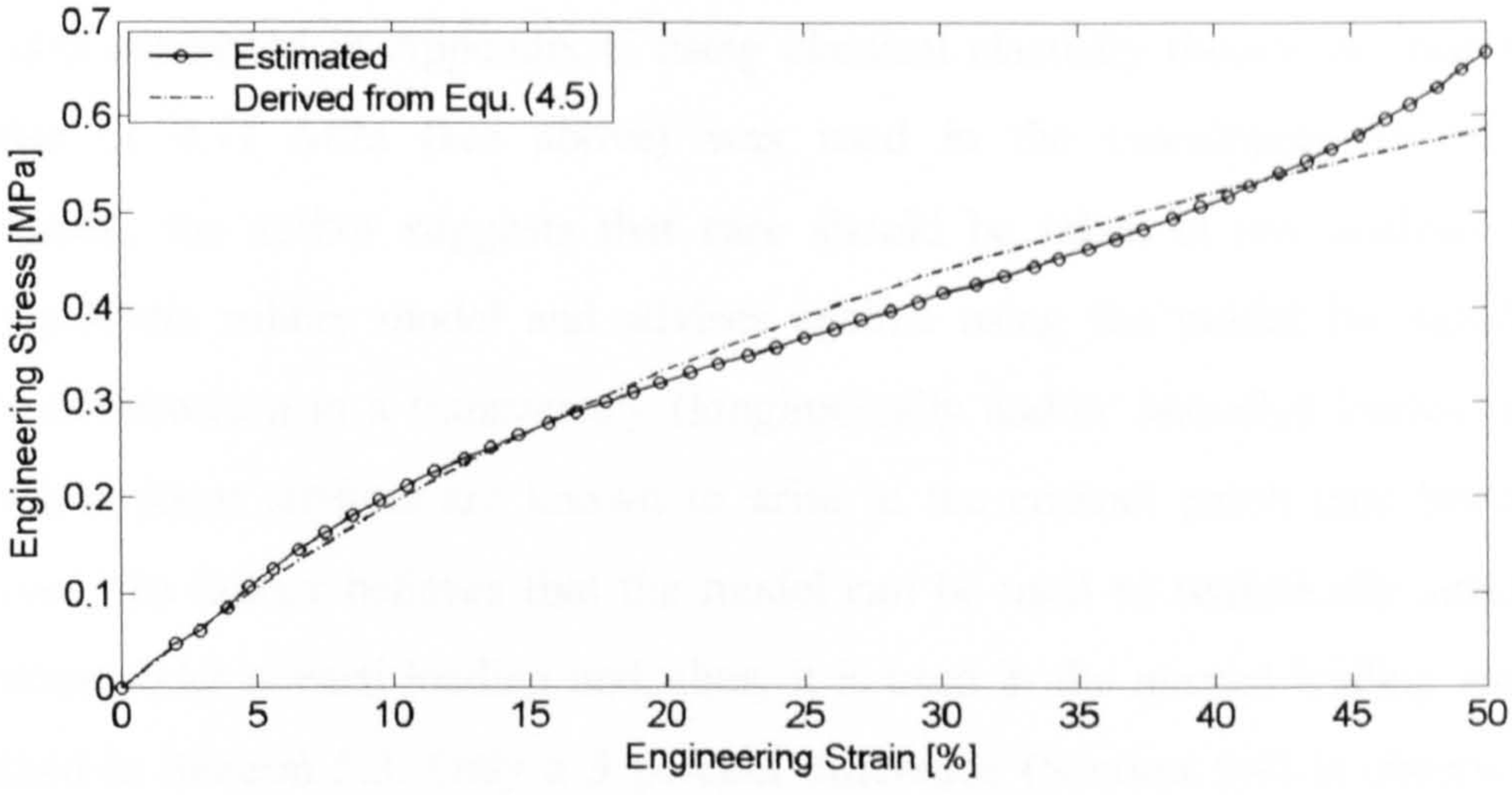

Figure 4.7 Comparison between the estimated stress/strain curve for the rubber tread compound in tension and that derived from the Mooney-Rivlin strain energy function

The Mooney-Rivlin expression in Equ. (4.2) can be represented in LS-DYNA [17] using either the incompressible Mooney-Rivlin rubber material model (model 27) or the Hyperviscoelastic rubber material model (model 77). The tyre FE analysts Kao and Muthukrishnan [57] have simulated the Mooney-Rivlin expression but do not specify the LS-DYNA material model used in their work. It is also not clear whether the Mooney-Rivlin or Hyperviscoelastic models are employed by C. Lee *et al.* [88]. Herein, to simulate a rolling tyre, the author prefers the Hypervisoelastic model and believes that, to control numerical instability, the actual model selection is important. This observation has been given support in private correspondence with Dunlop Tyres Ltd. FE analysts at Dunlop Tyres have used the Mooney-Rivlin model in tyre analyses and have found it to exhibit "some odd behaviour [90]". The material constitutive model appears not to accurately simulate the deformation of linear solid elements under shear deformation.

To verify the poor performance, an investigation was conducted and the main result is shown in Figure 4.8. In the figure, the 'tyre' is subjected to a 3 kN normal load followed by the imposition of a longitudinal load (acting in the negative *x*-direction). An unrealistic shear distortion is observed in the tread with the Mooney-Rivlin rubber model. This is shown in Figure 4.8(a) when the longitudinal load is 1 kN. As Figure 4.8(b) shows, the excessive localized tread distortion disappears when the Hypervisoelastic model is employed. A shear distortion of approximately 2.3 mm is shown to occur at a 2 kN longitudinal load. This value corresponds to the 1.8 mm distortion calculated in Appendix C using classical elasticity theory. A constant shear modulus of 0.77 MPa (see above) was used in the calculation. Based on this information, the author suggests that care should be taken in any analysis with the Mooney-Rivlin rubber model and advises against using the model for simulation of rubber deformation in a transversely (longitudinally and/or laterally) loaded or rolling tyre where shear stresses are known to arise in the contact patch (see Section 3.6). However, the author believes that the model can be used to realistically simulate tyre behaviour under normal loading and, thus, it is used in the normal loading simulations described in Section 5.3. Only a 3 percent difference (Section 5.4) is observed in the load-deflection behaviour using these two material models to simulate a load of 3 kN.

4.6 Reinforcements

The reinforcements of the carcass plies, bandages and breakers are represented in the stationary and rolling models using an orthotropic elastic material model. Single value elastic constants were calculated using volume fractions (see Equ. (4.1)) and the elastic constant data for the constituents shown in Table 4.2 by employing the Halpin-Tsai micromechanical equation [91]. This semi-empirical equation was originally derived for continuous fibre reinforced plastic composites. An alternative approach might be to use the Rule of Mixture equations which has been employed by FE analysts at Dunlop Tyres Ltd. but the Halpin-Tsai approach is preferred in this thesis because it is known to give more accuracy when determining the transverse moduli of a unidirectional lamina.

The Orthotropic Elastic material model (model 3) in LS-DYNA [17] requires the analyst to define the elastic constants in the element axes (*x*-, *y*-, *z*-), while the Halpin-Tsai equation calculates them in the cord axes (*1*-, *2*-, *3*-). The orientation of the cord axes

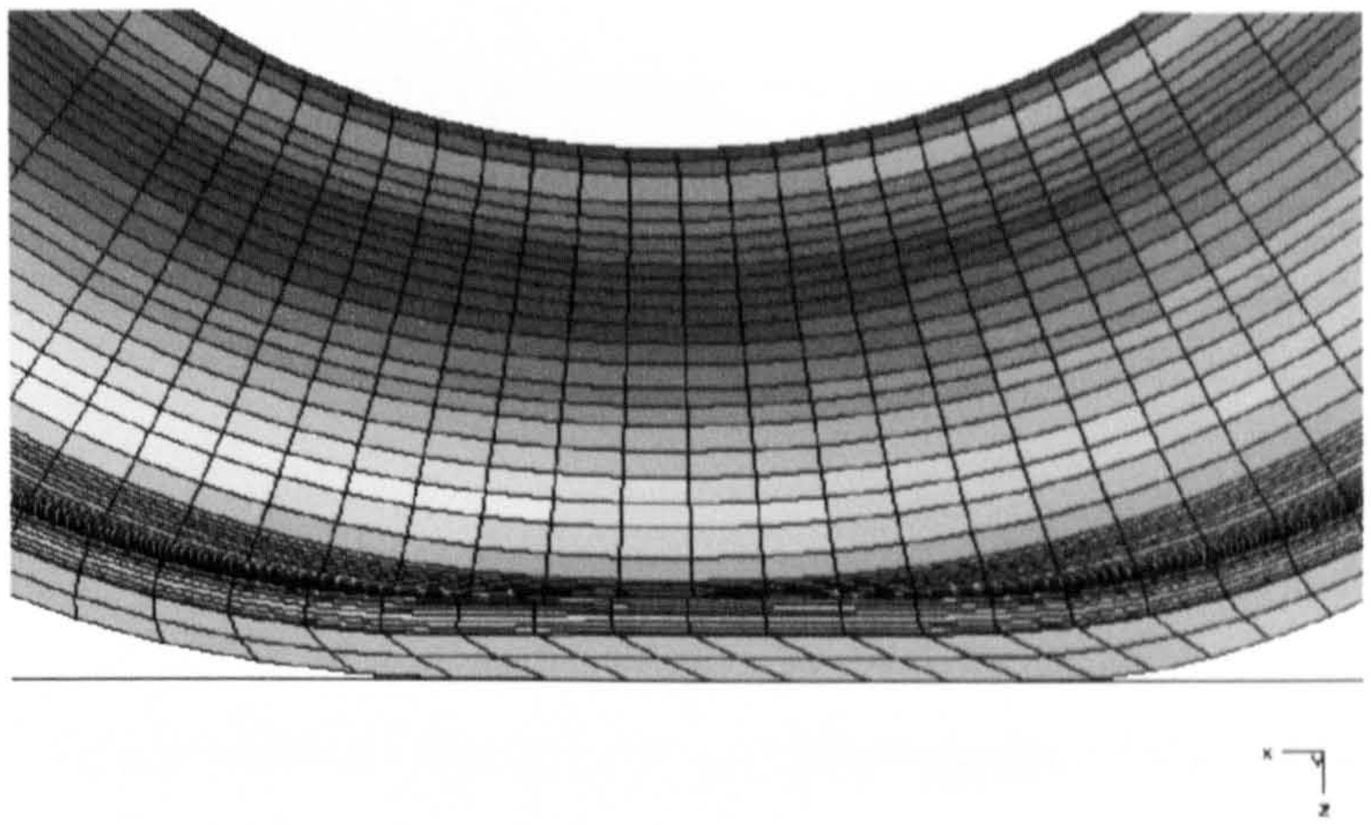

(a)

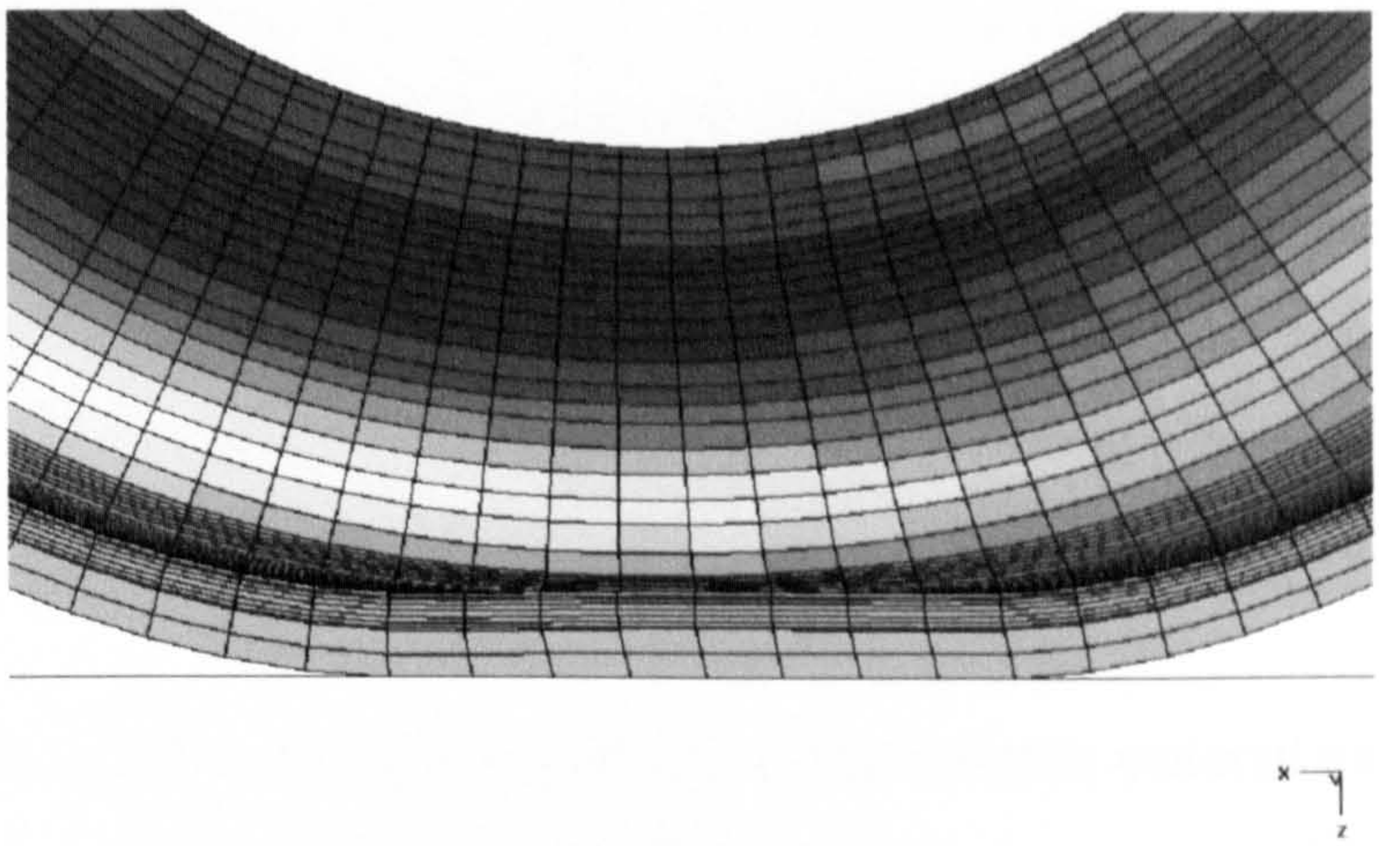

(b)

Figure 4.8 Shear distortion of linear solid elements in the contact region: (a) Mooney-Rivlin rubber model (LS-DYNA model 27); (b) Hyperviscoelastic model (model 77)

for the carcass plies and breakers differs from the element axes (see Figure 4.9) and, as a consequence, the elastic constants used as inputs need to be resolved. This complication can be avoided by using the Composite Failure material model (model 22) available in the code. This Composite Failure model simulates an orthotropic material with optional brittle failure. If the failure option is not used, orthotropic elastic behaviour is represented. The model allows the elastic constants to be defined in the cord axes instead of the element axes but the orientation of the cords also need to be defined (see Table 4.2). No noticeable difference was found when analyses were carried out using the Orthotropic Elastic and the Composite Failure material models and therefore the simpler approach using the Composite Failure model is preferred and used in this thesis.

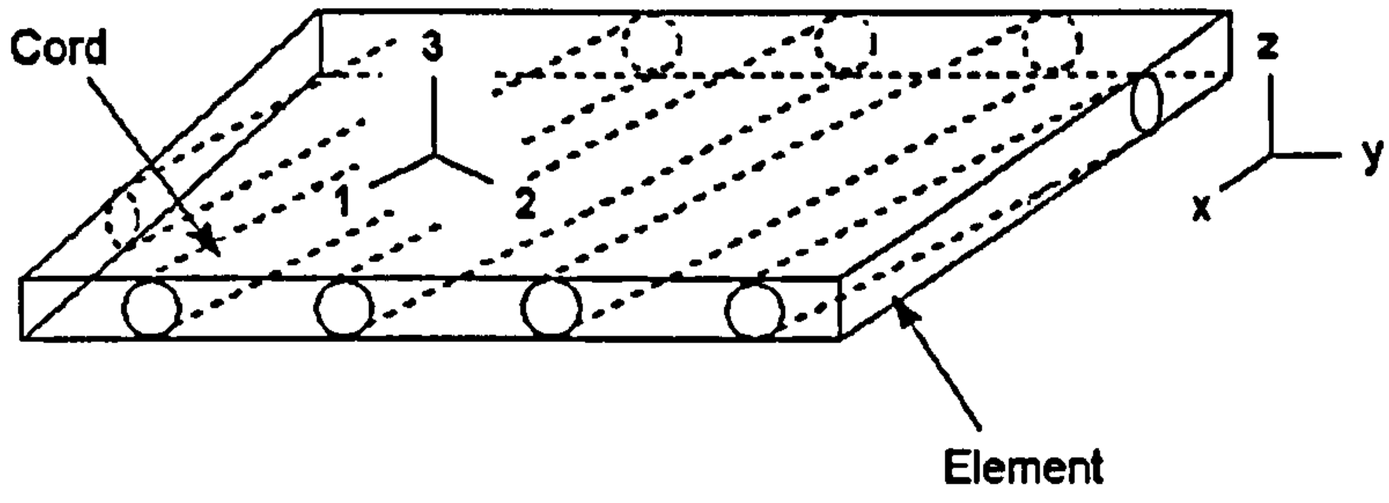

Figure 4.9 Element and cord axes in the reinforcements of the rubber composites

To determine the Halpin-Tsai constants, a single value elastic modulus of 3.16 MPa (corresponding to the 100 percent secant modulus) was assumed for the rubber matrix of the carcass plies, bandages and breakers (topping compound). Elastic moduli of 3.36 and 2.96 GPa (see Table 4.2) were assumed for the nylon cords in the carcass plies and bandages, respectively. A Poisson's ratio of 0.4 was used for the cords in both these components. For the steel cords in the breakers, the Young's modulus and Poisson's ratio were simply assumed to correspond to those of bulk steel (i.e. 200 GPa and 0.3).

The beads were simply represented using an isotropic elastic material model (model 1 in LS-DYNA [17]) with the elastic constants assumed to correspond to those of bulk steel. This simplification was again considered to be acceptable because the beads are a significant distance from the area of particular interest (as mentioned earlier).

4.7 Contact and Friction

There are two contact regions that need to be modelled: contact between the tyre and wheel; and contact between the tyre and 'ground' surface (i.e. the contact patch). The ground surface may be the glass plate used in the stationary experiments, or the flat bed and drum surfaces used in the rolling experiments (see Sections 3.3). Thus, the ground surface model is simulation dependent and is therefore not discussed in detail here, only salient features of the contact algorithms are considered relevant. The ground surface models are described in detail in relation to specific simulations in Chapters 5 and 6. It should be noted, however, that in each of the ground surface models, the contacting surface is assumed to be rigid (material model 20 in LS-DYNA [17]) and is modelled

using Belytschko-Lin-Tsay shell elements [82, 83]. This acceptable approximation simplifies the complex contact problem and hence reduces the computational time.

LS-DYNA [17] has numerous (>30) contact models incorporated in its code. These contact options are used, for example, to model contact of deformable bodies, single surface contact in deformable bodies, and deformable to rigid body contacts. They require the analyst to input numerous parameters (16 mandatory inputs are typically needed and further optional inputs can also be used) which influence the operation of the contact algorithms. The influence of many of these parameters has not been characterised and there is a lack of benchmark problems [17] to provide standardisation. Thus, contact modelling often relies on the experience and expertise of the FE analyst.

To simulate the tyre/wheel contact and the contact patch behaviour, versatile surface-to-surface contact models are used here. A surface-to-surface contact model allows compression to be carried but not tension, thereby allowing two bodies to be separate or in contact. Master nodes corresponding to the tyre/wheel contact are defined on the wheel and the contacting slave nodes on the tyre clinch (see Figures 3.1). The master nodes at the contact patch are defined on the 'ground' surface and the slave nodes on the 'tyre' tread. The master node nearest to each slave node is determined automatically by the code and the master segment (a 'segment' is defined to be a four-node element of the surface) attached to the master node is the first to be checked for contact. The process is repeated for all the relevant master nodes and slave segments. Thereafter, movement in the contact region may cause nodes to move from one segment to another.

The standard surface-to-surface option available in LS-DYNA [17] (contact type 3) tracks contact between two surfaces using 'mesh connectivity'. Instead of checking all segments for contact, only those segments attached to nodes of a previously contacted segment are checked. As a consequence, contact cannot be tracked across free edges. This standard option is suitable to model the contact between the tyre and the ground surface. It is, however, not suitable for modelling the tyre/wheel interaction because in this instance contact occurs across a free edge of the tyre. Thus, the automatic option (contact type a3) is required. This option checks for contact using a search method known as a 'bucket sort' which divides the three-dimensional space occupied by the contact surface into cubes (these cubes are referred to as buckets). The idea behind the

bucket sort is to perform some grouping of the nodes so that the sort operations need only calculate the distance of the nodes in the nearest groups. Nodes can contact any segment in the same bucket or an adjacent bucket. The bucket sort method is robust and between 100 to 1000 times faster than the old direct sort method employed in the code [17]. This sort method, however, is still an expensive part of the contact algorithm.

Sliding with closure and separation is analysed in LS-DYNA [17] by the Penalty stiffness method [92]. Once the contacting segments have been determine for each node, the amount of penetration of the slave node into the master segment is calculated and resisted by a penalty stiffness. For shell elements, the penalty stiffness (k) is given by

$$k = \frac{f_s A K}{d}, \tag{4.7}$$

where f_s is the penalty factor (default 0.1), A is the area of the contacted segment, K is the bulk modulus of the contacted element and d is the maximum diagonal of the shell. The maximum shell diagonal is shown in Figure 4.10. Equ. (4.7) is modified for a solid element by replacing $(1/d)$ with A/V^e, where V^e is the element's volume.

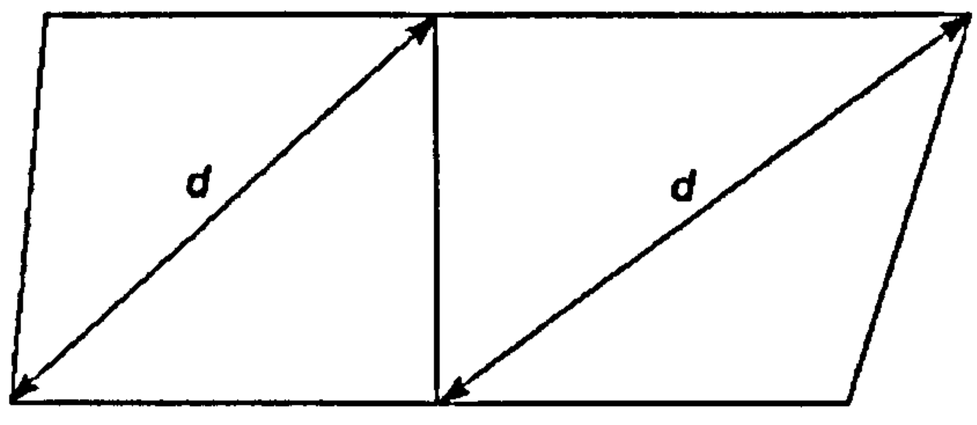

Figure 4.10 Maximum diagonal of a shell element

LS-DYNA [17] must calculate both the solid element penalty stiffness corresponding to the 'tyre' tread and clinches, and also the shell element penalty stiffness analogous with the steel wheel and ground surface models. These calculations are necessary because the code must factor both the master and slave stiffnesses for the contact algorithm.

It should be noted that a significant amount of unwarranted penetration can occur using the Penalty stiffness method. To avoid this, an optional SOFT flag is available in the surface-to-surface contact models. By setting the flag to 1 (i.e. on), the 'soft constraint'

contact formulation is used instead of the basic Penalty stiffness method. The soft constraint formulation is an advanced Penalty method where the maximum stable contact stiffness is chosen for each penetrating node. Thus, unwanted penetration is minimised. The approach is preferred by the author because in less complex rolling simulations (carried by FE analysts at Dunlop Tyres Ltd.), the basic Penalty stiffness method was found to cause contact problems. In these simulations, nodes on the perimeter of the 'tyre' tread were observed to penetrate the elements used to represent the 'ground' surface. The penetrating nodes became constrained on the opposite side of the defined tyre/ground contact and, as a consequence, the simulation became unstable.

Friction modelling in LS-DYNA [17] is based on the Coulomb formulation where it is assumed that no sliding occurs below a specific load level. The maximum friction force F_f that can be developed is μF_n (see Section 1.1), where F_n represents the force in the normal direction. A transverse force exceeding this maximum friction level causes sliding to occur. It should be noted, however, that the force necessary to cause sliding differs from that to maintain it and, as a consequence, a distinction is made between the static (peak) μ_p and the dynamic (sliding) μ_s coefficients of friction (Section 2.6). This transition is smoothed in the LS-DYNA code by an interpolation. This interpolation is

$$\mu = \mu_s + (\mu_p - \mu_s)\, e^{-d_c|v_{rel}|} \tag{4.8}$$

where d_c is a decay coefficient and v_{rel} is the relative velocity between the slave node and the master segment. A higher decay coefficient increases the decay rate of the coefficient of friction and a lower value reduces it. Since the frictional force is related to the coefficient of friction, the force necessary to maintain sliding is influenced by d_c.

The peak and sliding friction coefficients for a number of typical ground surfaces are presented in the literature (see Table 2.1), but to the author's knowledge no tyre/ground data is available in relation to the decay coefficient in Equ.(4.8). There is also very little information in relation to tyre/wheel interaction and its corresponding decay rate. It is known that FE analysts at Dunlop Tyres Ltd. typically use a decay coefficient of 0.5 and therefore this value is assumed by the author in this thesis. It has been used for all tyre/ground and tyre/wheel contacts herein. The peak and sliding friction coefficients

between the tyre and wheel have been estimated to be 0.3 and 0.1, respectively. Those at the contact patch are simulation dependent but, on the 'Safety Walk' surface used in the rolling experiments, are 1.2 and 1.0 (Section 3.7.3). The change in the tyre/ground friction coefficient on the this surface with relative velocity is shown in Figure 4.11.

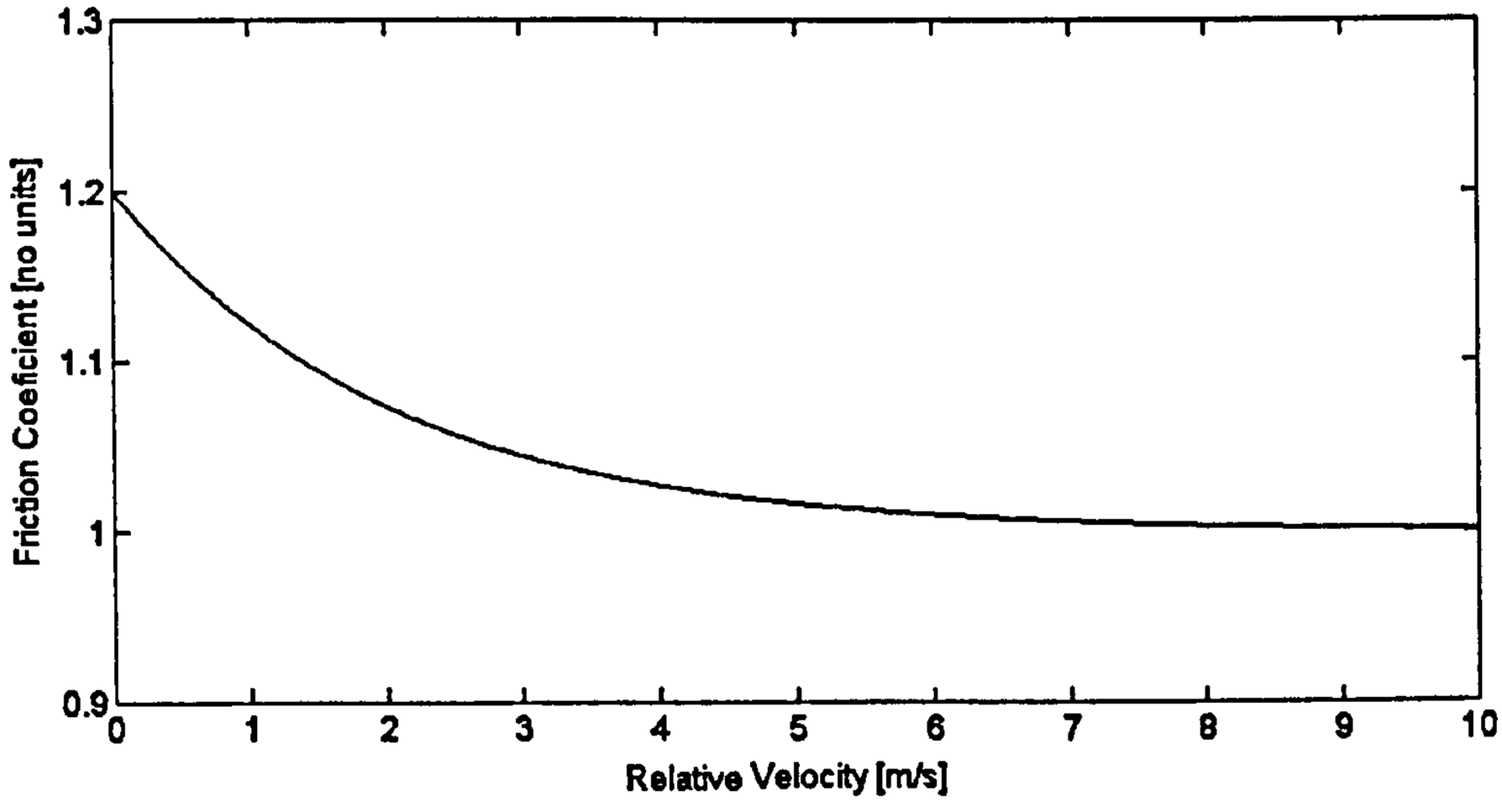

Figure 4.11 Simulated friction coefficient with relative velocity on a 'Safety Walk' surface

4.8 Summary

Two FE tyre models, developed to simulate the stationary and rolling behaviour of an automobile tyre have been described in detail. These models have been developed for simulations using the explicit FE software package LS-DYNA. The results from these analyses are shown in Chapters 5 and 6. The modelling methodology has been discussed and related to the author's experiences using the code. The 'tyre' has been represented as a composite material and the 'wheel' has been separately modelled. The interaction between the tyre and the wheel has been considered as an additional boundary condition. The chapter has addressed important aspects of the FE modelling, such as the mesh specification and the material descriptions, and the lack of experimental data needed to characterise the material properties of tyre rubber compounds has been highlighted. A simple method to estimate the elastic behaviour has then been presented. The method used to model the wheel fit and tyre/ground interaction has also been described.

Chapter 5 Simulation of Stationary (Non-Rolling) Tyre Behaviour

5.1 Introduction

The purpose of the Finite Element (FE) modelling work is to simulate rolling (dynamic) tyre behaviour at the microscopic level. However, to accurately predict dynamic tyre characteristics, it is clearly necessary to be able to simulate the less complex problem of stationary (non-rolling) tyre behaviour. Thus, this chapter addresses this important issue. Numerical results are presented that can be compared to those obtained in the stationary experiments (see Section 3.5) and to information available in the literature. These results are used to validate the stationary modelling methodology described in Chapter 4. A parametric study is then used to characterise the sensitivity of the numerical results to changes in the mesh density of the 'tyre' and contacting 'ground' surface, and to changes in the elastic properties of the tyre components. The development of a relevant and reliable modelling methodology is a major aspect of the work reported in this thesis.

5.2 Stationary Simulations

As discussed in Section 3.4.1, stationary experiments were conducted to determine the vertical tyre stiffness and the growth of the contact patch under normal load. In the present chapter, these experiments are simulated in a single LS-DYNA [17] analysis using the stationary model. This analysis is referred to here as the normal loading simulation. The inflation of the tyre, the wheel fit (interaction between the tyre and the wheel) and the normal loading of the tyre against the glass plate are considered. The 'tyre' deformation during the simulation is shown in Figure 5.1. Figure 5.1(a) shows the tyre cross-section at the start of the simulation and Figures 5.1(b) to 5.1(d) show the cross-section as the simulation evolves with time. In other stationary (non-rolling) simulations referred to as the longitudinal and lateral loading simulations, a 3 kN normal load was followed by the imposition of a longitudinal or lateral load. These simulations

were carried out to determine the longitudinal and lateral tyre stiffnesses, respectively. The stiffnesses are important to a tyre's tractive properties and cornering characteristics.

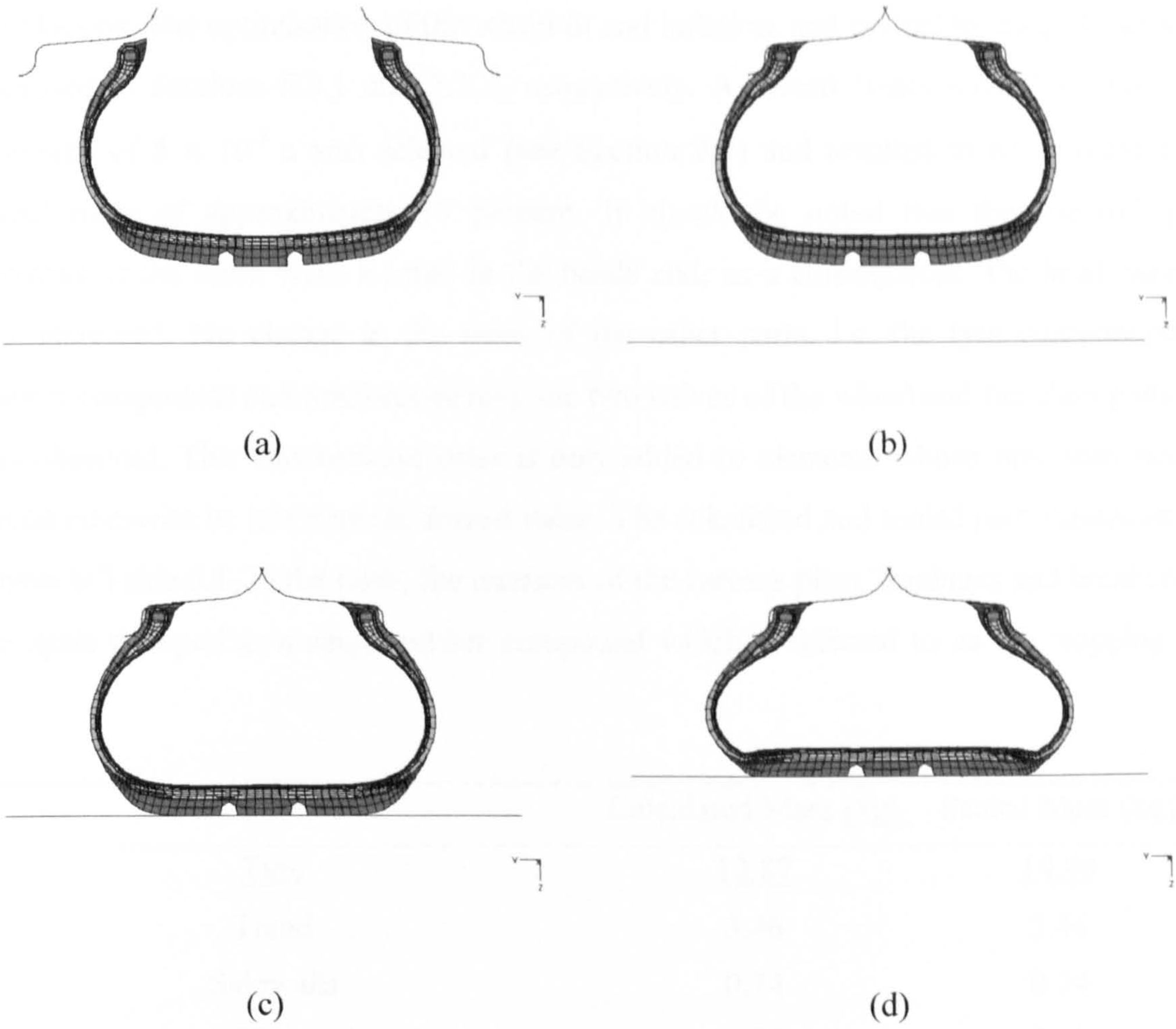

(a) (b)

(c) (d)

Figure 5.1 Deformation of the 'tyre' cross-section: (a) undeformed; (b) due to inflation pressure and wheel fit; (c) at a normal load of 1 kN; (d) at a normal load of 5 kN

5.3 Normal Loading Simulation

An initial test simulation was carried out over a 'real time' of 0.8 s with the time step size controlled by LS-DYNA [17]. This mesh dependent time step was 1.86×10^{-7} s and was governed by the solid elements in the beads local to the contact region (see Figure 4.1). The simulation time was found to be nearly 1200 h (50 days) based on the available computational resource, a Sun Ultra 60, 360 MHz workstation. This computational cost was considered intolerable for a quasi-static analysis and therefore modelling optimisation techniques [68] were employed to refine the analysis such that the most efficient use was made of the resource. As a consequence, the analysis time

was reduced to about 200 h, approximately one sixth of the initial simulation time.

The real time was halved by optimisation of the wheel fit and inflation, and normal loading phases, and the time step size was also 'forced' to minimise the number of calculations. The optimisation of the wheel fit and inflation, and normal loading phases is discussed in Sections 5.3.1 and 5.3.2, respectively. A forced 'mass scaled' minimum time step of 5×10^{-7} s was selected (see Section 2.9) and resulted in an increase in model mass of approximately 13 percent. It should be noted that the controlling elements of the mesh were located in the beads and, as a consequence, the bead mass was increased. No change in the mass of the other parts, i.e. the tyre components (rubber compounds and reinforcements), the two halves of the wheel and the glass plate, was observed. This was because mass is only added to elements whose time step size would otherwise be less than the forced value. The calculated and scaled part masses are shown in Table 5.1. In the table, the matrices of the carcass plies, bandages and breakers are again grouped as a single rubber compound which is referred to as the 'topping'.

Part	Calculated Mass [kg]	Scaled Mass [kg]
Tyre	12.87	14.99
Tread	3.46	3.46
Sidewalls	0.74	0.74
Liner	0.82	0.82
Apexes	0.36	0.36
Clinches	0.52	0.52
Beads	0.85	2.97
Topping	3.35	3.35
Reinforcements of carcass plies	1.17	1.17
Reinforcements of bandages	0.45	0.45
Reinforcements of breakers	1.15	1.15
Wheel	1.84	1.84
Glass Plate	1.18	1.18
	15.89	18.01

Table 5.1 Calculated and scaled part masses

Mass scaling (via modification to a material's density) is a very useful and simple method to increase the minimum time step of an analysis. However, it should be noted that a significant change in material density can influence the dynamic response of the model by increasing inertia forces through added mass and modifications to inertial properties, and the overall energy balance via changes in kinetic energy levels [68]. The analysis carried out here simulates the stationary experiments and, thus, a dynamic response does not exist. Similarly, a dynamic response is also not present in the longitudinal and lateral loading simulations (see Section 5.4) because the loading is quasi-static. The increase in the bead mass is therefore not important. It is postulated by the author that this increase in bead mass is also insignificant in the rolling tyre simulations presented in Chapter 6. This is because the beads are in contact with the wheel, at a significant distance from the area of particular interest, i.e. the contact patch.

To improve the model response, the tyre components were critically damped. The fundamental frequency of a typical passenger car tyre in isolation (and therefore of the tyre components) is approximately 40 Hz [35]. In LS-DYNA [17], damping can be applied at both the material and system levels. At a material level, damping is usually controlled by applying a factor proportional to the mass and/or stiffness term. This is commonly referred to as Rayleigh damping [68] and a different factor can be applied to each material. In the mass-proportional method, a retarding force is applied to each node proportional to its velocity, while in the stiffness method a restoring stress is applied at an elemental level based on the element strain and its constitutive properties. System damping is similar to material damping but on a global scale, i.e. the same damping factor must be applied to all materials. To the author's knowledge, no notable advantage is obtained by using one method over the other methods. Mass-proportional damping at a material level is employed herein because it is easily applied in the LS-DYNA code.

5.3.1 Wheel Fit and Inflation Phase

The wheel fit and tyre inflation (see Figure 5.1) were carried out simultaneously, initially over a period of 0.05 s. This real time is not representative of an actual situation but does not invalidate the analysis, since the transient results during the wheel fit and inflation phase are not relevant to the stationary experiments. Only the steady-state tyre deformation is important. Minimising the real time reduces the computational cost but,

at the extreme, may cause numerical instability, such as contact problems which are known to occur at high impact velocities. Thus, the initial real time was chosen conservatively to minimise simulation time while ensuring a stable solution. It was reduced to 0.03 s and the simulation was repeated without a discernible change in the steady-state deformation. A further reduction was found to cause numerical instability in the analysis. This is shown in Figure 5.2 with a real time of 0.01 s. In the figure, a high velocity impact occurs between the tyre and wheel, and a shock wave develops. This shock wave is transmitted through the structure and causes an unplanned termination of the simulation. This type of termination is usually referred to as an analysis 'crash'.

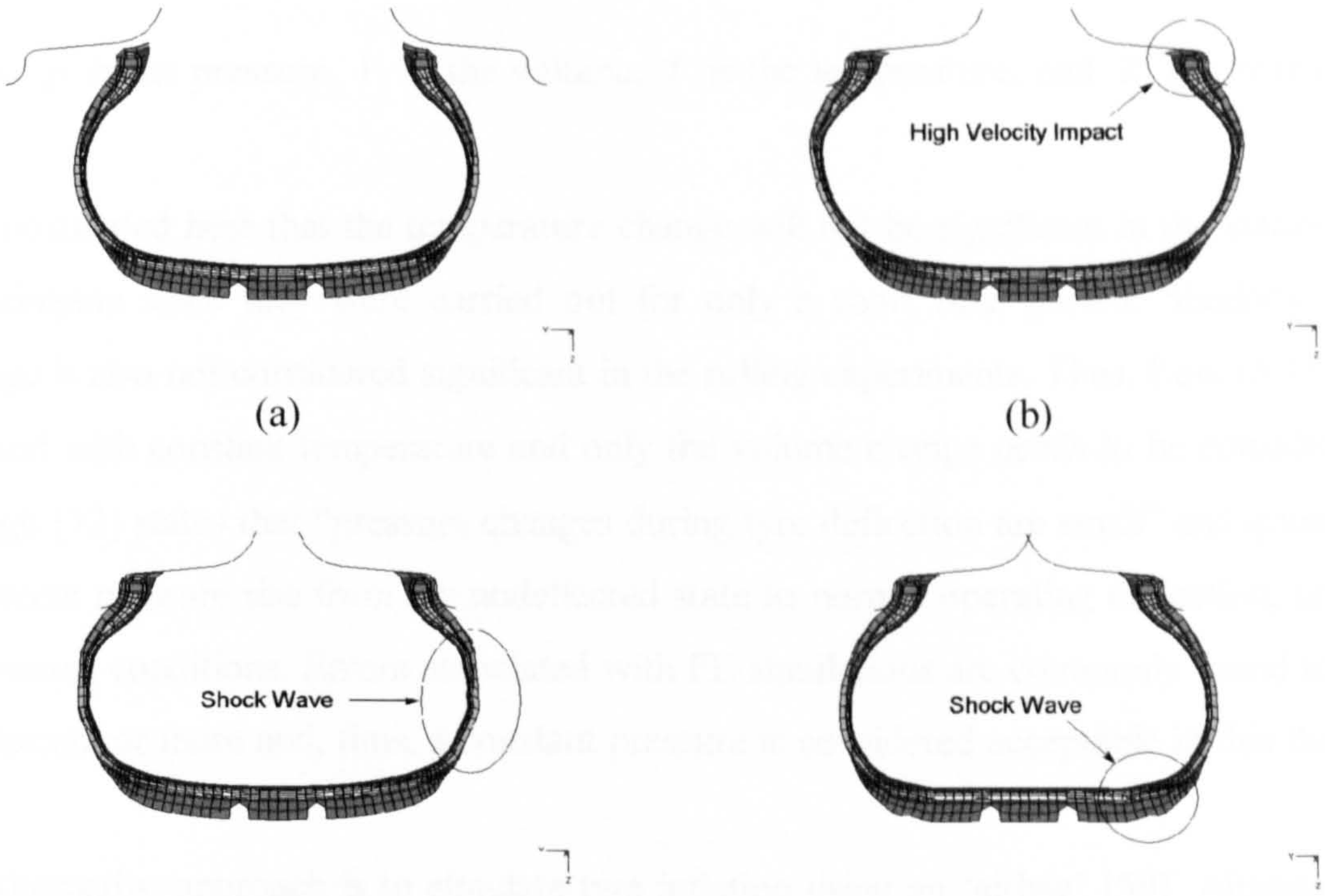

Figure 5.2 Deformation of 'tyre' cross-section at a high tyre/wheel impact velocity: (a) undeformed tyre ($t = 0.00\,\text{s}$); (b) tyre/wheel impact ($t = 6 \times 10^{-3}\,\text{s}$); (c) shock wave development ($t = 8 \times 10^{-3}\,\text{s}$); (d) shock wave transmission through structure ($t = 0.01\,\text{s}$)

A constant pressure of 200 kPa (see Section 3.4) was applied normal to the inner-face of the 'tyre' liner and the two halves of the 'wheel' were displaced laterally (in the y-direction) until the actual fit between the tyre and wheel was represented. One half of the wheel was displaced in the positive y-direction while the other was displaced in the

negative direction. The two halves were constrained in the longitudinal (x-) and vertical (z-) translations and in rotations about the x-, y- and z-axes via body constraints. They were merged to create a single part (referred to as the wheel) once the fit was achieved.

It should be noted that a constant inflation pressure is often assumed in tyre analysis [57, 61, 93] even though a slight change in the pressure is known to occur when a vehicle is running on the road [88]. This change is mainly due to tyre operating temperature variations and also deformation (air volume change), and for an ideal gas like air [94] is

$$\frac{pV}{T} = R \tag{5.1}$$

where p is the pressure, V is the volume, T is the temperature, and R is a constant.

It is postulated here that the temperature change will not be significant in the stationary experiments since they were carried out for only a short time period. Similarly, the change is also not considered significant in the rolling experiments. Thus, Equ. (5.1) can be used with constant temperature and only the volume change needs to be considered. Gough [72] states that "pressure changes during tyre deflection are small" and quotes a 2 percent pressure rise from the undeflected state to normal operating deflection, under isothermal conditions. Errors associated with FE simulations are commonly found to be 10 percent or more and, thus, a constant pressure is considered acceptable in this thesis.

An alternative approach is to simulate tyre inflation using an 'airbag' [59]. Airbags are represented in LS-DYNA [17] as an enclosed mesh of membrane elements. These elements define a 'control volume'. A mass flow rate for the inflation gas and a parameter to control the venting also need to be defined. In tyre analysis, the inflation gas is air and venting is usually set to zero. This assumes that there is no loss of inflation gas. Thermodynamic relationships (see Equ. (5.1)) are then used to determine the internal pressure in the control volume based on the mass and temperature of the inflation gas present and the volume enclosed. This internal pressure is then applied to the membrane elements causing the airbag to inflate. Thus, airbags can be used to simulate tyre inflation and the subsequent changes in the air volume, and the corresponding pressure change as the tyre deforms. Since the volume change is small (as

mentioned earlier), it is the author's opinion that this approach only adds an unnecessary complication to tyre analysis and therefore it is not used in the work reported herein.

5.3.2 Normal Loading Phase

After the 'tyre' was allowed to achieve a state of equilibrium, it was normally loaded. The glass plate model was displaced vertically until a normal load greater than 5 kN was applied to the tyre. The displacement was initially carried out at a rate of 0.05 m/s (over a real time of 0.6 s). This rate is significantly lower than that selected by others [88] in similar analyses but was conservatively chosen to ensure quasi-static loading, representative of the stationary experiments. The rate was increased and the simulation was repeated. The normal load exerted on the tyre was compared to the reaction at the wheel and at rates less than, or equal to, 0.125 m/s the load and reaction did not significantly deviate. At the maximum rate the reaction was 4.95 kN, being 1 percent lower than that applied. The kinetic energy was also checked at this rate and found to be negligible in the normal loading phase when compared to the total energy. Thus, at a displacement rate of 0.125 m/s, the loading could still be considered to be quasi-static.

It should be noted that the glass plate is represented by a 0.3×0.5 m horizontal surface coarsely modelled using 15 quadrilateral shell elements based on the Belytschko-Lin-Tsay shell elements [82, 83]. As mentioned in Section 4.7, the surface was taken to be rigid. The glass plate model is shown in Figure 5.3. Significant changes in the mesh density of the surface (up to 1500 elements have been used) were found not to noticeably affect the simulation results. No change in the predicted vertical tyre stiffness or contact patch dimensions (length and width) was observed with the more refined mesh. The peak μ_p and sliding μ_s coefficients of friction at the contact patch were estimated based on the values in Table 2.1 to be 0.3 and 0.2, respectively. However, it was considered unlikely that changing these values would significantly alter the simulation results. This was later confirmed in an investigation carried out to determine the sensitivity of the analysis to variations in the friction levels. No change in the results was found with variations in the peak and sliding friction coefficients between 0.15 and 1.2, and 0.1 and 1.0, respectively. These coefficients are considered to envelope the possible friction level between the tyre and the glass plate in the stationary experiments.

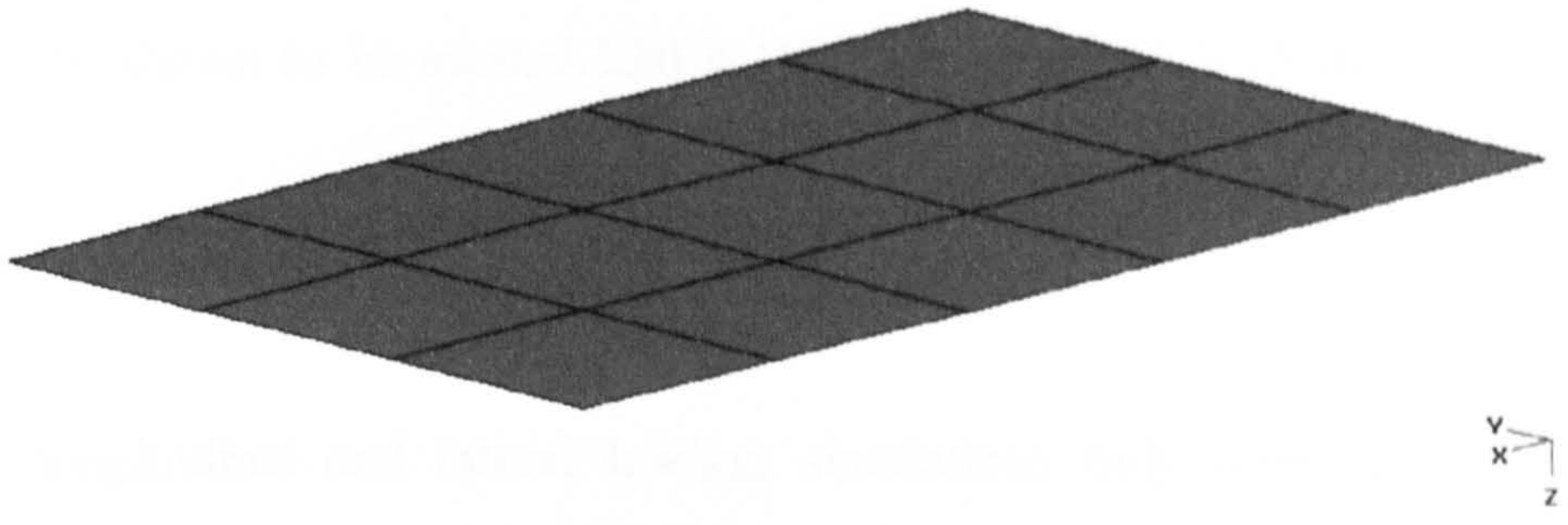

Figure 5.3 Three-dimensional glass plate model

5.4 Longitudinal and Lateral Loading Simulations

In the longitudinal and lateral loading simulations, consideration was given to a normal load of 3 kN followed by a subsequent quasi-static transverse (longitudinal or lateral) load. The normal load was selected based on the assumption that the weight of a typical saloon car is 12 kN (i.e. 3 kN per wheel). This load was exerted on the 'tyre' by displacing the glass plate model vertically. The displacement necessary to create the tyre load was calculated using the predicted quasi-static load-deflection characteristics obtained from the normal loading simulation. At the selected displacement, the normal load was 3.1 kN, about 3 percent too high. This was considered acceptable because as mentioned earlier, errors inherent in FE simulations are typically 10 percent or more.

5.4.1 Transverse Loading Phase

The 'tyre' structure was allowed to achieve a state of equilibrium and the glass plate model was displaced either longitudinally or laterally at a rate of 0.05 m/s until sliding was evident. Sliding was assumed to occur when an increase in the displacement of the plate did not result in a corresponding increase in either the longitudinal or lateral load. The point when sliding occurs is governed by the normal load and the peak coefficient of friction. Therefore to ensure an adequate amount of data prior to sliding, the peak coefficient was specified to be artificially high, i.e. 0.7. The longitudinal and lateral tyre stiffnesses were assumed to not be influenced by this friction coefficient. It should be noted that the longitudinal and lateral loads are developed by displacement of the glass plate and therefore the simulation time is dependent upon the load-deflection characteristics. A 10 mm displacement (0.2 s) corresponds to a computational time of

approximately 100 h. Thus, the simulation time for the longitudinal and lateral loading phases can be shown to be around 230 h (10 days) and 115 h (5 days), respectively.

5.4.2 Restart Files

Since the longitudinal and lateral loading simulations only represent a subsequent loading phase in addition to the wheel fit and inflation, and normal loading phases (see Section 5.3), restart files can be used to reduce the total computational time. A restart file is effectively a database that represents the complete description of a model at a time specified by the FE analyst. This method allows modifications to be made to a model without having to return to the initial stage of data initialisation. The simulation can be repeated from the restart time with the modifications included in subsequent time steps.

Two types of restart files are available in explicit software and these are referred to here as small and full-deck restart files. This terminology is commonly used by FE analysts. The small restart files are usually created more frequently than the full-deck restart files because they use less storage space. However, they are useful only when small changes need to be made to a model. An example is an increase in the real time of an analysis. A full-deck restart file is necessary when major changes are needed, such as the deletion or addition of parts of a model and/or the re-specification of loads. They are often created when an analysis is carried out in distinct loading phases. This is because a restart file created at the end of an analysis phase can be used as an input file for subsequent loading phases. A benefit is therefore achieved if a number of subsequent cases need to be assessed. In the normal loading simulation reported in Section 5.3, full-deck restarts can be created after the wheel fit and inflation phase, and when the normal load exerted on the tyre is 3 kN. To reduce computational cost, this later restart file could then be used as the input file for the longitudinal and lateral loading simulations. At the time the normal loading simulation was carried out (Nov. 2000), the author was not aware that restart files could be created in LS-DYNA [17] and, thus, they are not used in this thesis. The approach would have been used had the author been aware of the method.

5.5 Selection of Analysis Results

The selection of analysis results for output and their output frequency is an important

aspect of any explicit FE simulation. A careful selection avoids the unnecessary generation of large results files that contain superfluous data. These large data files cause an increase in computational cost and storage space. Thus, only analysis results needed to validate the modelling methodology in Chapter 4 have been created herein.

In LS-DYNA [17], analysis results can be output as field data (stresses, strains, displacements etc.) in binary or ASCII-format, or as X-Y data. The field data is typically used in this thesis for graphical animation (for example see Figure 5.1), and verification and debugging purposes, and the X-Y data is used for plotting key results (Figure 5.4). This method is recommended in the text book by Jacob and Goulding [68]. The X-Y data is stored electronically in ASCII-format and loaded into MATLAB [71] for analysis and visualisation. This is consistent with the method used to analyse the experimental data in Chapter 3. Here, the sampling frequency of the field data and X-Y data are 2×10^{-3} s and 5×10^{-4} s, respectively. These sampling frequencies were chosen to give an adequate data resolution while ensuring an efficient use of storage space. It should be noted that the X-Y data can be stored more efficiently than the field data. The field data and X-Y data at each sampling point are taken to be the instantaneous results at the end of the time step that coincides with the time output is desired [95].

5.6 Results and Discussion: Normal Loading Simulation

The load-deflection characteristics obtained from the normal loading simulation described in Section 5.3 are shown in Figure 5.4. Figure 5.5 shows the predicted contact patch dimensions (length and width). In the figures, the normal load is given in kN, and the deflection and contact patch dimensions are given in mm. To provide a meaningful comparison, the contact patch length and width are plotted on identical axes. The corresponding physical test data taken from Figures 3.6 and 3.7 is also included. The normal load was determined from the vertical contact force and the deflection from the vertical displacement of the 'glass-plate'. The contact patch dimension were calculated from the co-ordinates of the nodes on the perimeter of the tyre tread; assuming a symmetrical contact patch only a quarter of the tyre nodes were considered. These nodes were assumed to be in contact when their vertical co-ordinates corresponded to those of the nodes on the glass plate. Since linear solid elements were use to model the tyre tread it was assumed that the contact patch dimensions remain

constant between successive nodal contacts and, as a consequence, a 'staircase' plot is therefore produced. These nodal contacts are represented in Figure 5.5 by square points.

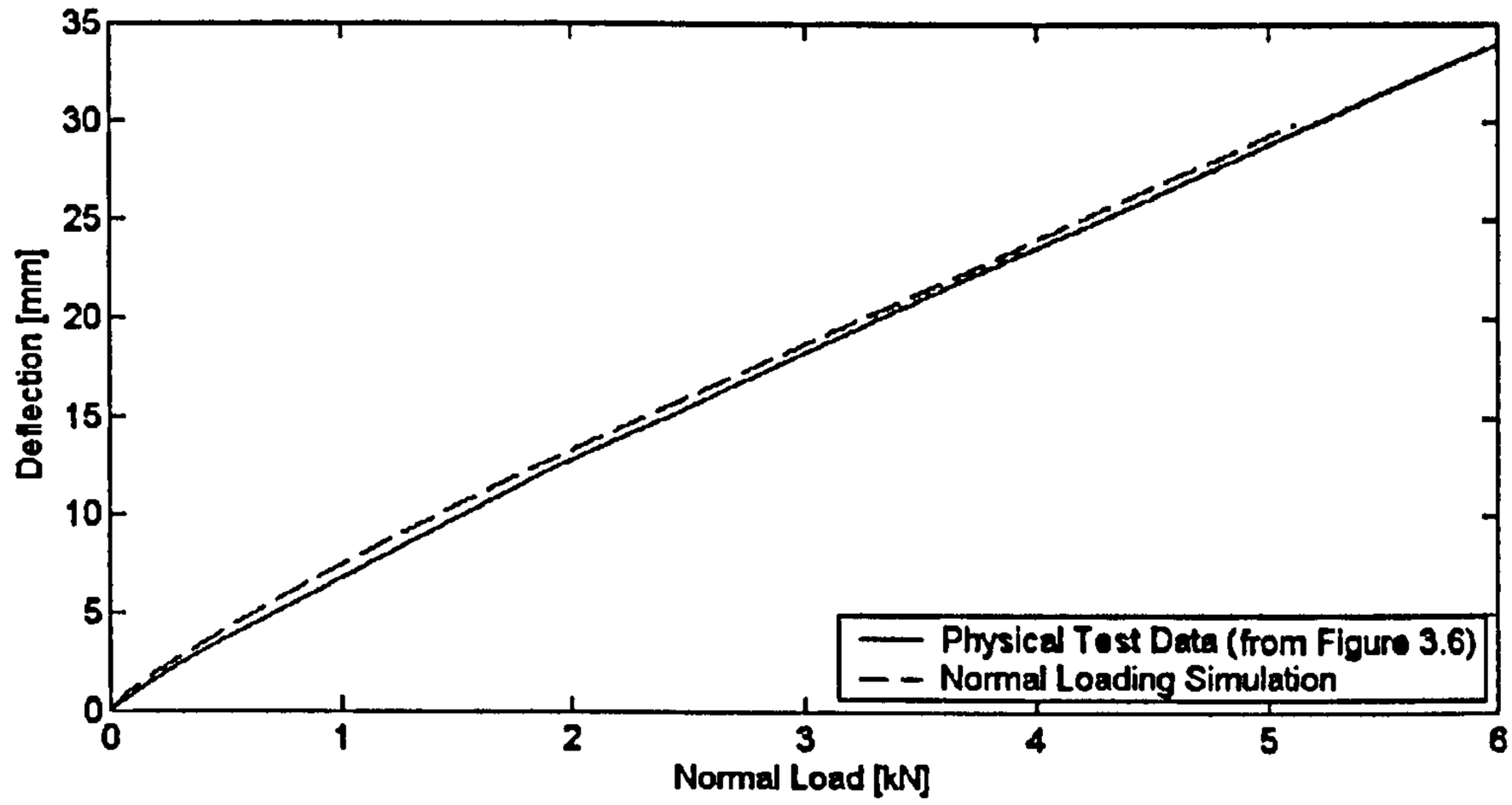

Figure 5.4 Normal load-deflection characteristics

The predicted load-deflection characteristics are shown in Figure 5.4 to be in excellent agreement with those determined from the stationary experiments. Both show a near linear relationship between load and deflection, and indicate the vertical tyre stiffness to be approximately 180 kN/m. Based on this information, it is postulated that global tyre behaviour is accurately represented using the modelling methodology described in Chapter 4. This is given further support by the results observed in the longitudinal and lateral loading simulations in Section 5.7. These simulations appear to give realistic longitudinal and lateral tyre stiffnesses. As will be discussed later, however, these stiffnesses have only been validated by typical tyre data and not by physical test data.

The numerical contact patch dimensions in Figure 5.5 yield a staircase plot. In reality, the growth of the contact patch is continuous and a trend-line (represented by closely spaced dots) is therefore also indicated. One approach would have been to draw the trend-line mid-way between the extreme values of the staircase plot. However, the author has chosen to represent the contact patch at the higher extreme. It is the author's opinion that refining the mesh will only displace the values at the lower extreme to the higher values; a coarser mesh will further reduce the lower values. The higher values, which correspond to the distinct points where node-to-surface contacts occur will

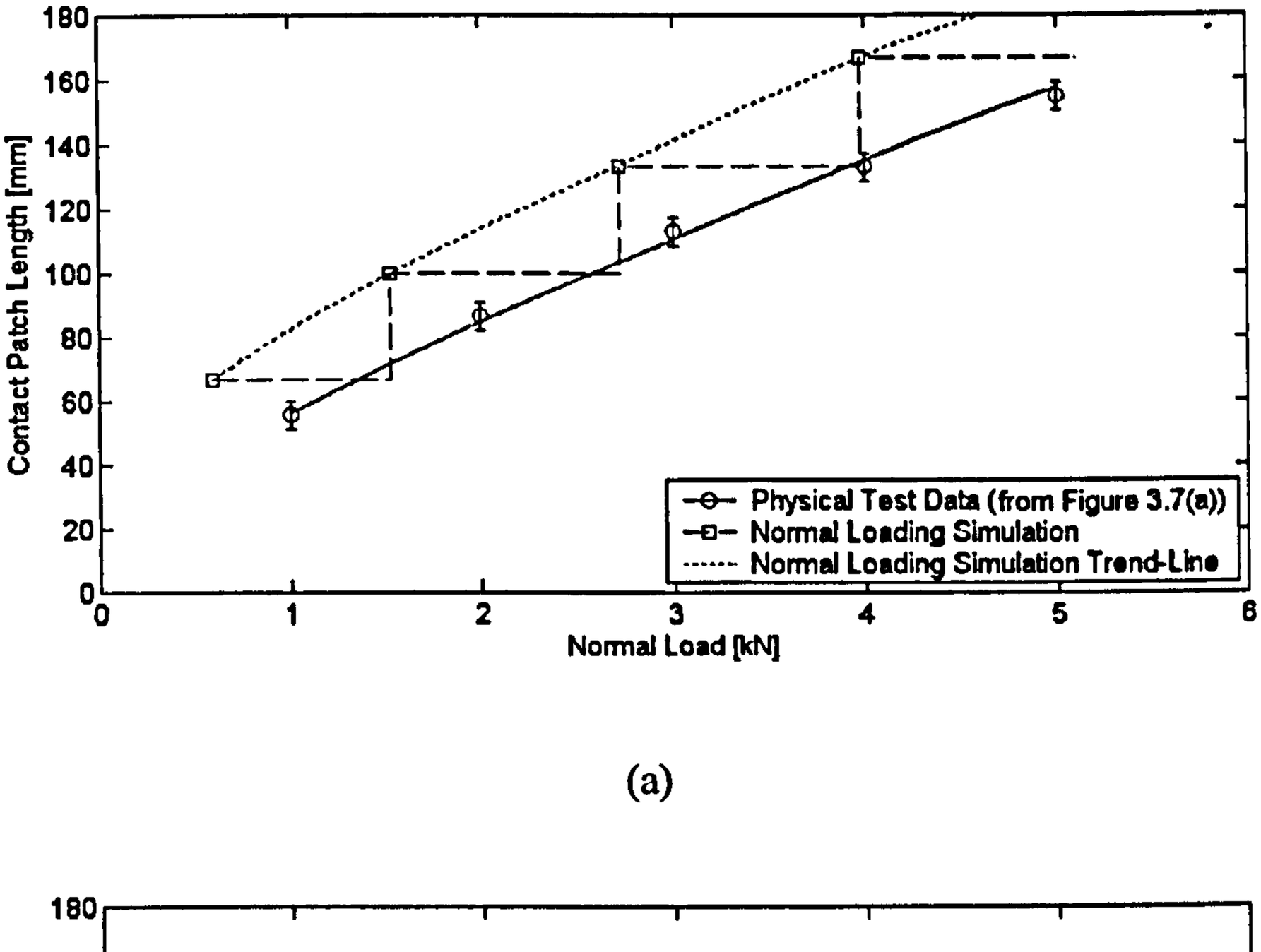

(a)

(b)

Figure 5.5 Tyre/ground contact patch dimension with normal load: (a) length; (b) width

remain unchanged. This behaviour is confirmed in Figure 5.6. To create the figure, the mesh density of the stationary model local to contact region was reduced in the circumferential direction and the simulation was repeated. No change was made to the mesh through the tyre cross-section and therefore a significant variation in the contact patch width was not expected. Thus, only the contact patch length is presented here.

In terms of the contact patch dimensions shown in Figure 5.5, a good trend-wise agreement is evident between the simulation results and those obtained in the stationary

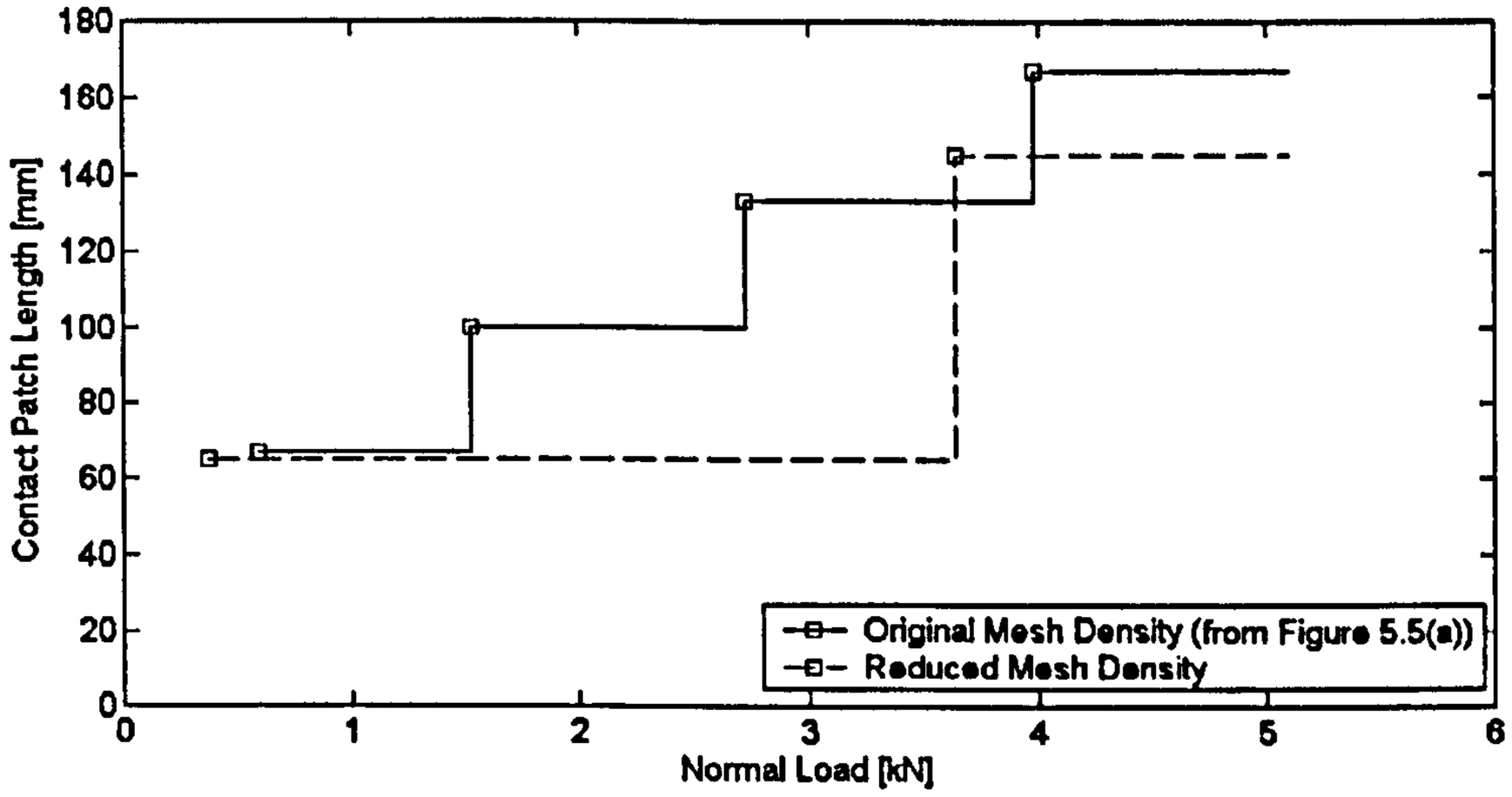

Figure 5.6 Simulated contact patch length with normal load and mesh density

experiments. Both sets of dimensions show a similar linear relationship between normal load and contact patch length, and non-linear relationship between load and contact patch width (for loads between 1 kN and 5 kN). Based on the assumed FE trend-line, however, the numerical contact patch length and width are typically 30 mm and 20 mm higher, respectively. To find out why the predicted contact patch dimensions differ from those obtained in the full-scale physical tests, a parametric study has been carried out.

5.6.1 Parametric Study

In the parametric study, the elastic constants of the tyre components, the mesh density of the tyre and glass plate models, and the contact algorithm were all identified as possible reasons why the contact patch dimensions differed. As mentioned earlier, changes in the mesh density of the tyre (see Figure 5.6) and glass plate (Section 5.3.2) do not significantly influence the contact length and width. Variations in the elastic constants of up to ±25 percent of the nominal values were also unable to account for the difference. This is clearly shown in Figure 5.7. In the figure, the physical test data is shown as a benchmark. To illustrate the fact that tyre behaviour under normal load is governed by the inflation pressure and not the tyre structure, the effects of an identical change in the pressure is also included in the contact patch length plot (Figure 5.7(a)).

By disregarding the elastic constants, and the mesh density of the tyre and glass plate models, it is postulated that the difference is related to the performance of the contact

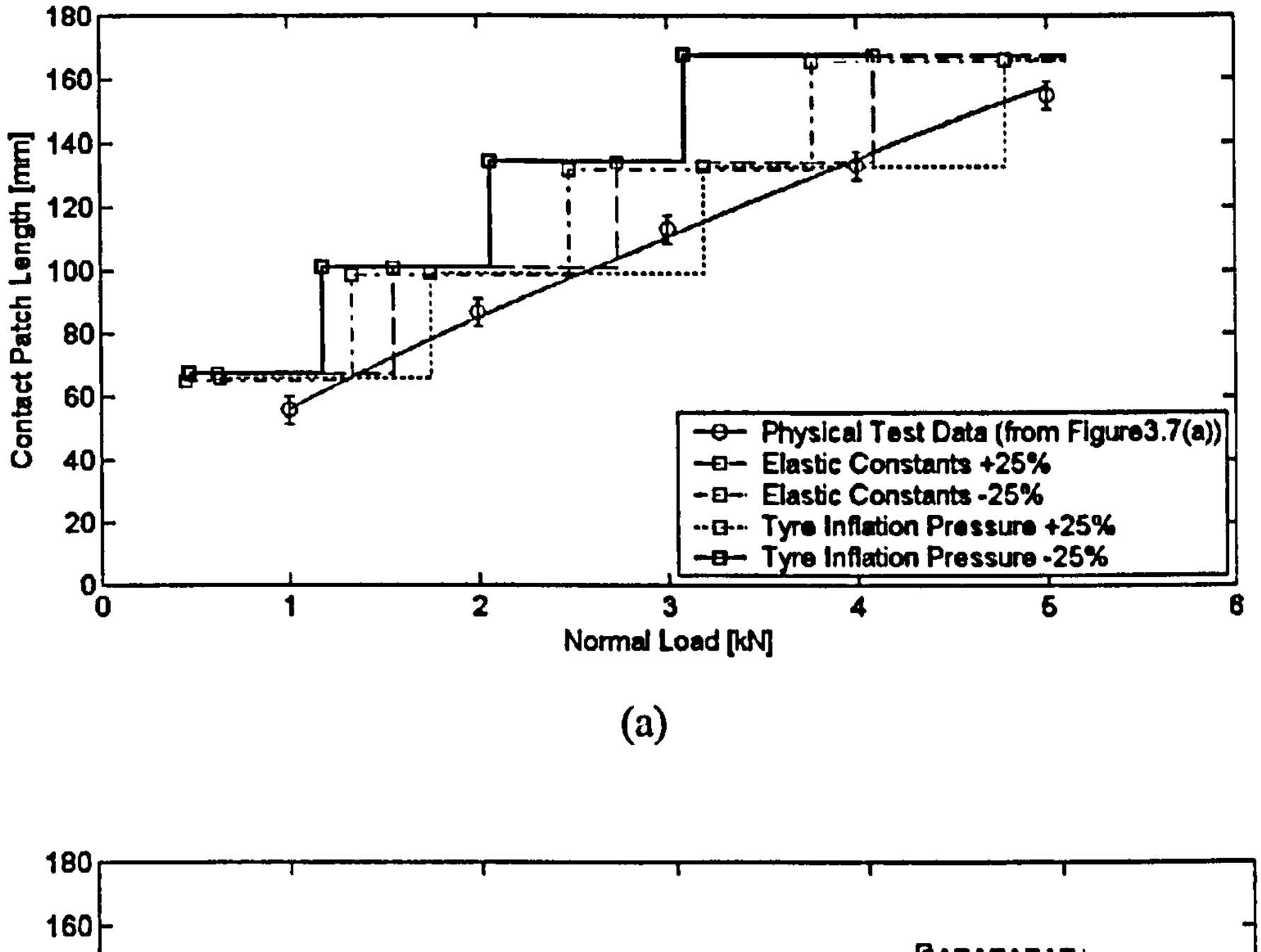

(a)

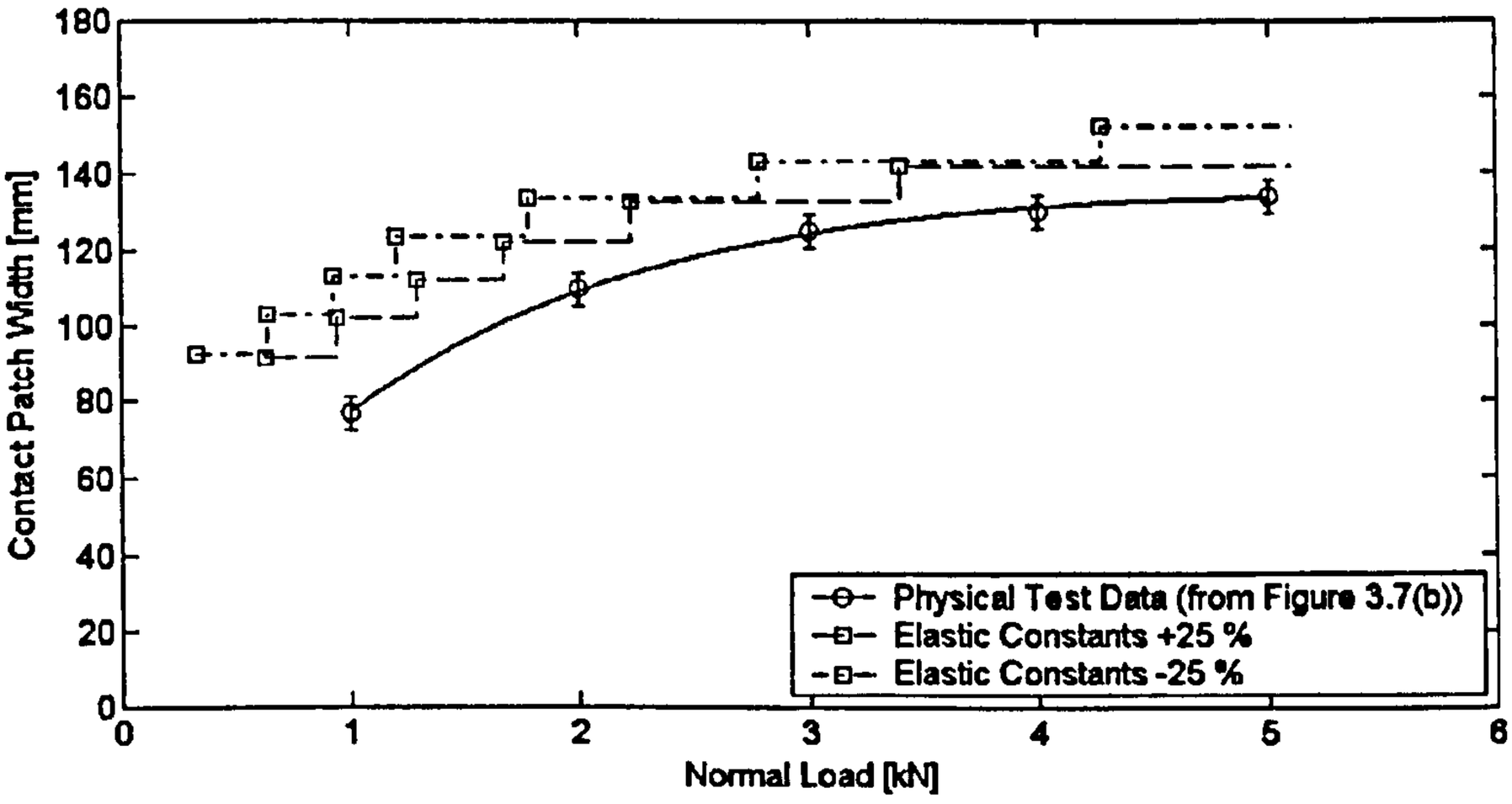

(b)

Figure 5.7 Tyre/ground contact patch dimensions with normal load at various 'tyre' component stiffnesses (elastic constants) and inflation pressures: (a) length; (b) width

algorithm. Numerous parameters influence the contact algorithm (16 mandatory and 14 optional inputs are needed in the standard surface-to-surface model) and therefore, to verify the author's opinion, it is necessary to characterise the effect of each of these. This is beyond the scope of the work reported here and, thus, this has not been possible. It should be noted, however, that a deficiency with the contact algorithm has been given support by way of private communication with a FE analyst at Ove Arup & Partners, the distributors of LS-DYNA [17] in the United Kingdom. Dr B. Walker [96] has strongly

indicated that a one-to-one correlation is unrealistic for such a complex non-linear contact problem and that a trend-wise agreement should be considered to be the norm.

5.6.2 Normal Pressure Distribution

The predicted normal pressure distributions in the contact patch at normal loads of 1, 3 and 5 kN are shown in Figure 5.8. These pressure distributions were calculated using nodal force data at the contacted tyre nodes; again only a quarter of the nodes were considered. An alternative and (in hindsight) more direct method is to use the nodal stress field data. This method can be shown to yield the same contact pressures but was not used here because as mentioned in Section 5.5, field data needs more storage space. At the time the analysis was carried out, this storage space was not available. At the centre of the contact patch, the longitudinal and lateral positions are 0 mm. It should be noted that the 'channels' evident across the contact patch (seen at a lateral position of ±20 mm) do not correspond precisely to the grooves of the tyre model shown in Figure 4.1. This is because the contact pressure at the very edge of the grooves was not considered. The channels are therefore wider than the grooves of the experimental tyre.

In Figure 5.8, a reduction in the normal pressure at the centre of the contact patch is seen to occur as the normal load increases. The simulation results therefore confirm the observation by Browne *et al.* [31] that the tyre centre 'buckles' upwards under increasing normal load. This phenomenon has previously been discussed in relation to the flat bed experiments (see Section 3.6.1). At the same time there is an increase in the contact patch size and the shape changes from an oval to a rectangular one (Figure 3.5). Thus, it is evident that the modelling methodology can be used to simulate the 'actual' contact deformations experienced in a stationary tyre. However, a one-to-one correlation in the normal pressures is not realised because, as discussed, the contact patch length and width (and therefore also area) differ from those obtained in the full-scale physical tests. This is clearly observed when the pressure distribution is compared to the rolling contact stresses at the lateral tyre centre, given in Chapter 3, and also those presented across the contact patch width, in work carried out by Dennehy [9].

It should be noted that a significant amount of 'noise' was evident in the nodal force data used to create Figure 5.8. This is shown for a node at the centre of the contact

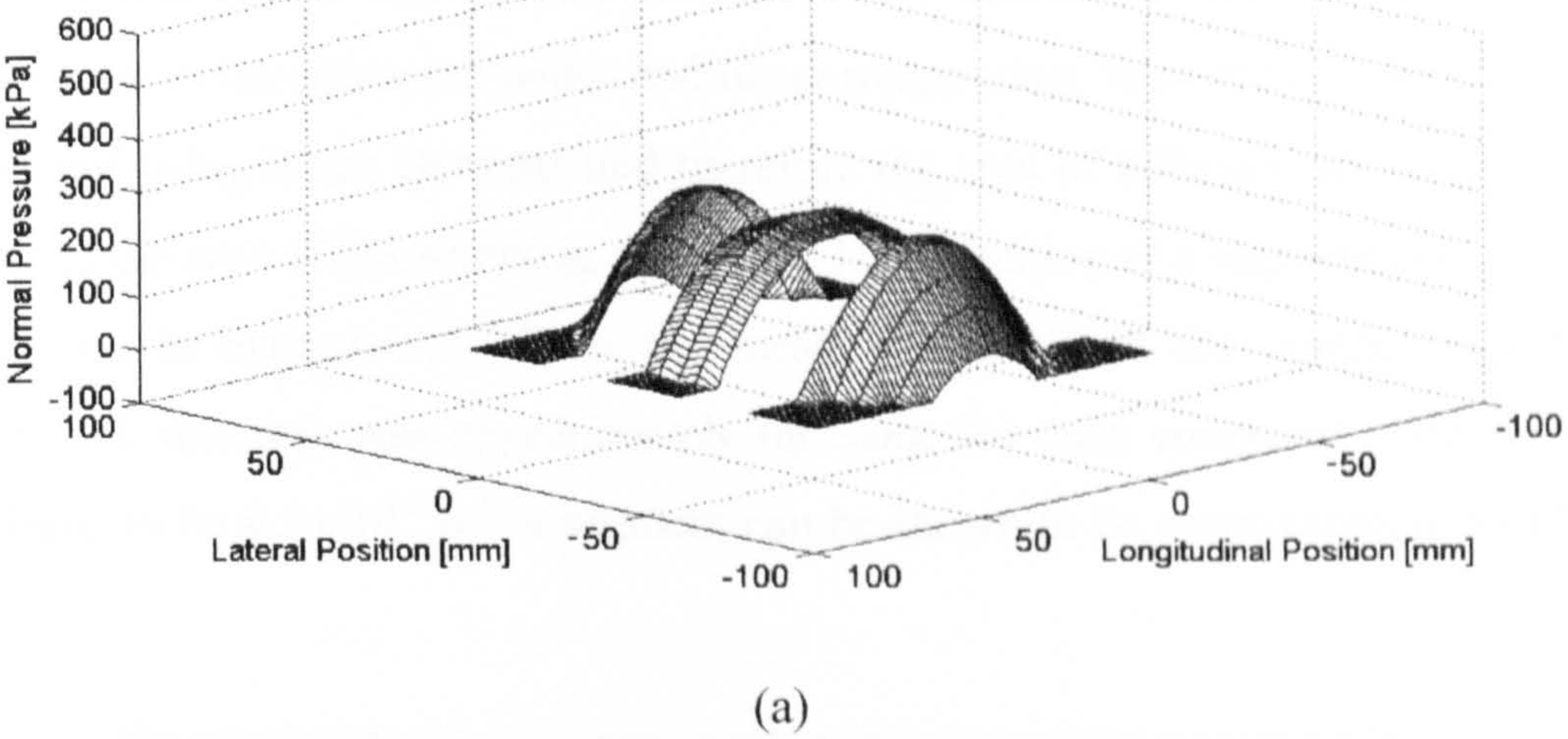

(a)

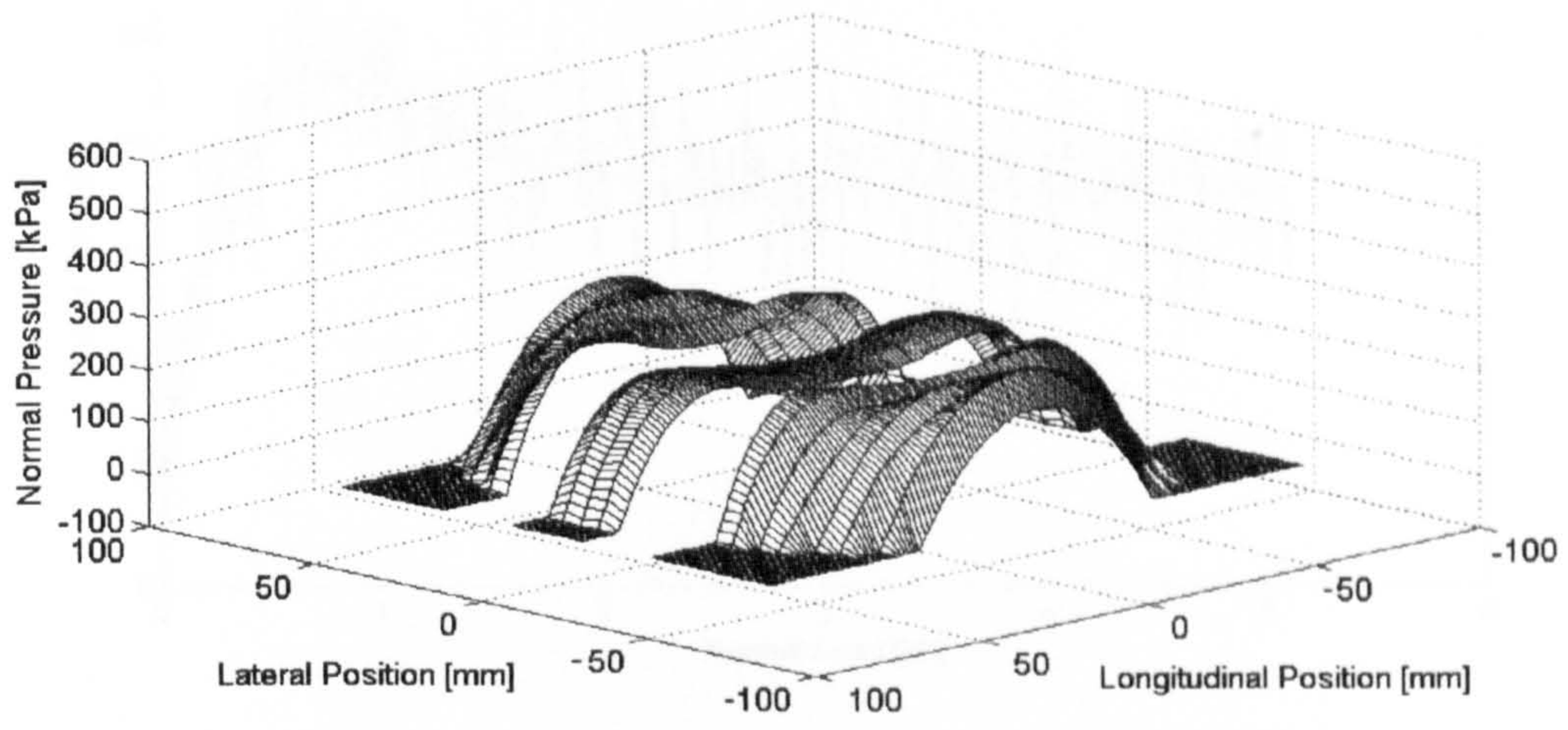

(b)

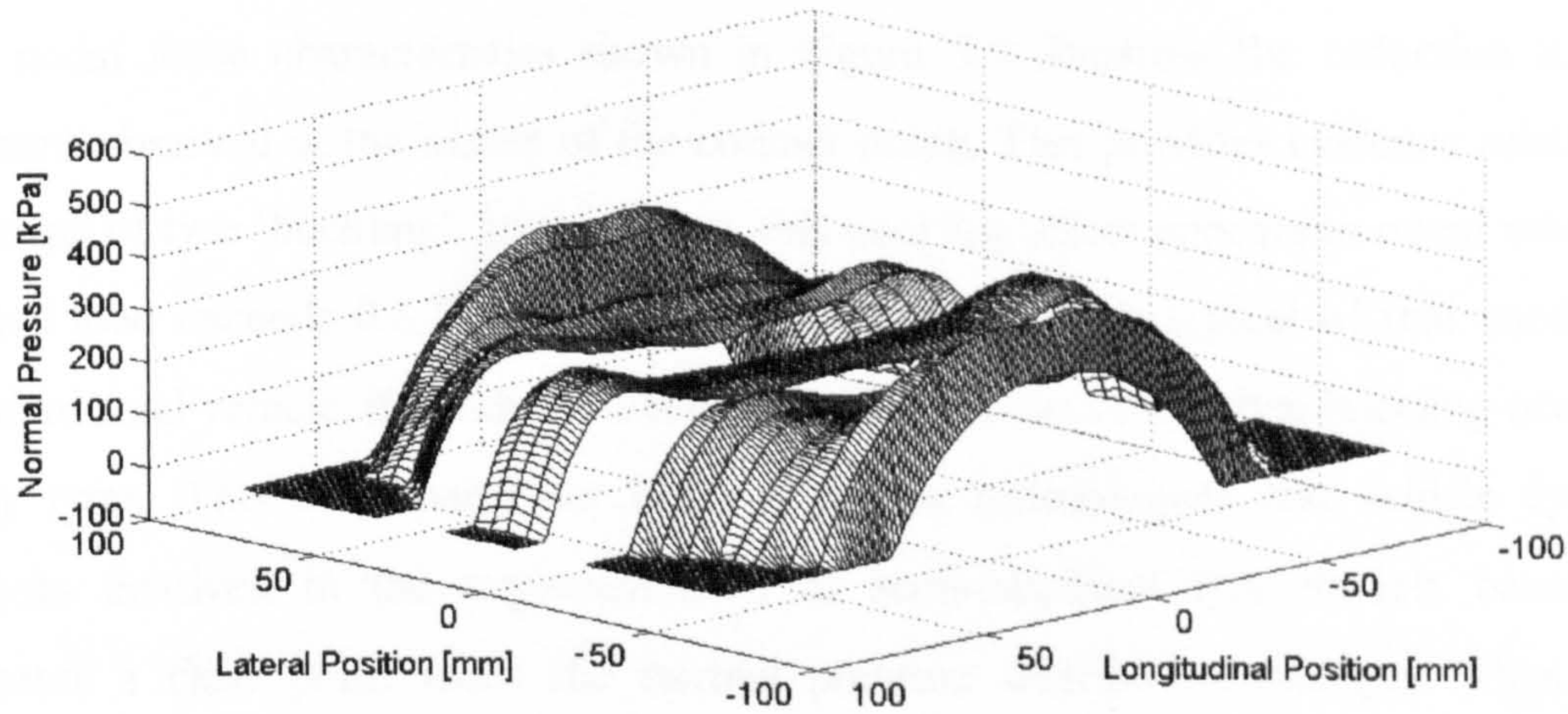

(c)

Figure 5.8 Simulated normal pressure distributions: (a) 1 kN; (b) 3 kN; (c) 5 kN

patch in Figure 5.9. In the figure, a smooth trend-line (represented by a bold line) is also indicated to illustrate the trend. Similar nodal force data can be presented for the other contacted tyre nodes. The normal pressures were calculated based on the smoothed nodal forces on the contacted nodes and the corresponding 'area of influence'. The tread is modelled using linear elements and therefore the area of influence was taken to be a quarter of the area of the adjoining segments. The definition of a segment has previously been given in Section 4.7. Since the mesh is uniform in the contact region (see Figure 4.1), this area was approximately the same for each contacted node. The area was found to be 8.5×10^{-5} m^2; a segment can be shown to be approximately 5×17 mm.

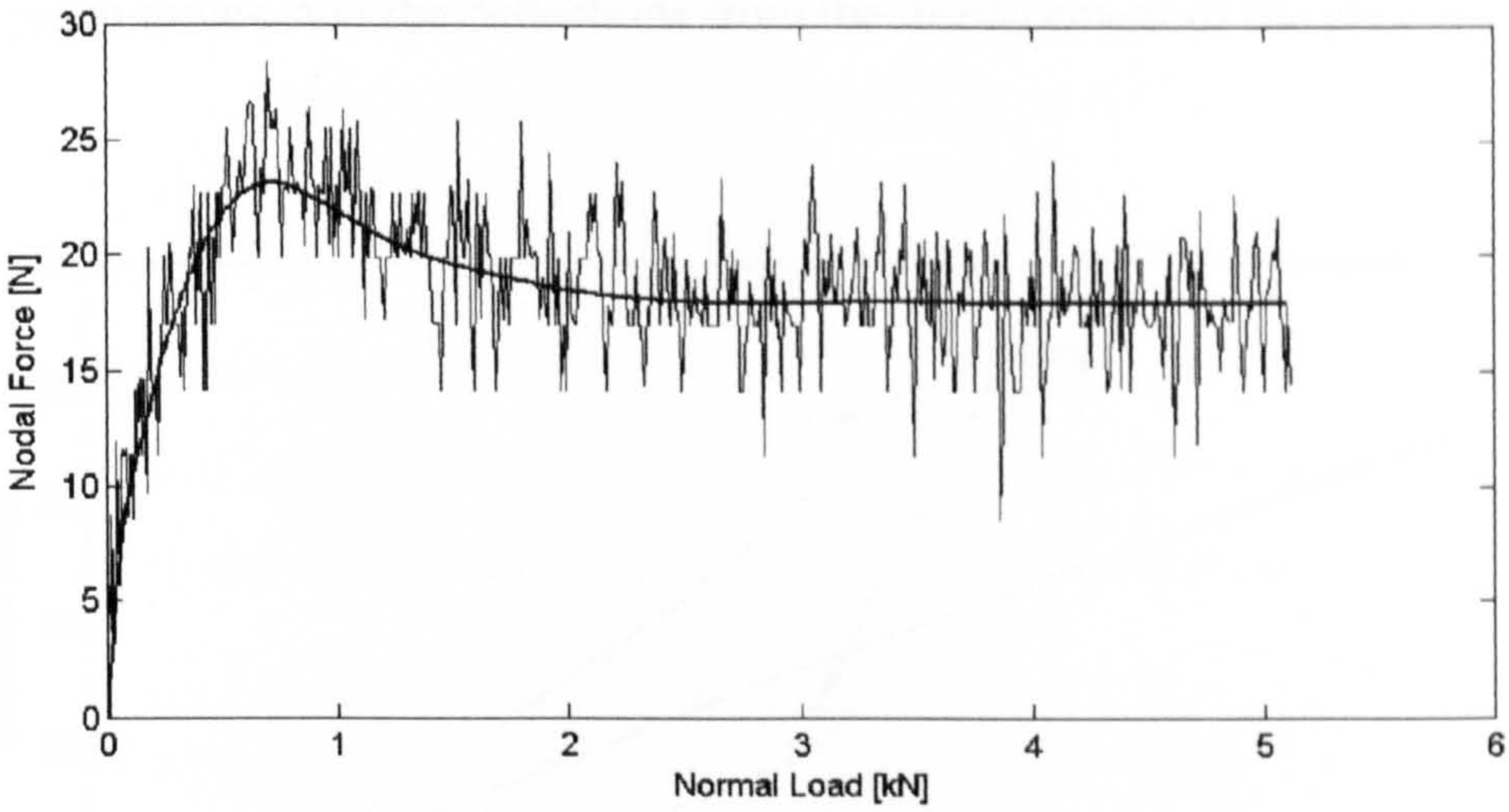

Figure 5.9 Contact force on a node at the centre of the contact patch with normal load

The nodal force characteristics shown in Figure 5.9 illustrate the reduction in load pressure observed at the centre of the contact patch. This provides evidence relating to the onset of tyre 'buckling'. In the figure, this buckling effect appears to occur when the normal load exceeds 0.8 kN. Since the tyre construction is typical of that used on a standard road vehicle, this value is likely to be representative of when buckling occurs in many tyres. This is of particular interest to tyre technologists and vehicle dynamic analysts involved in the implementation of semi-empirical tyre models because it indicates a clear point when the normal pressure distribution changes. Thus, it is suggested here that the parabolic normal pressure distribution sometimes assumed [41, 49] is only representative at low normal loads, e.g. to 1 kN. At slightly higher loads a uniform or trapezoidal distribution [33, 45] is better and, at typical operating loads (>2 kN), an alternative distribution which represents the tyre buckling effect is needed.

5.7 Results and Discussion: Longitudinal and Lateral Loading Simulations

The load-deflection characteristics obtained from the longitudinal and lateral loading simulations are shown in Figure 5.10. The loads are again given in kN and the deflections in mm. The normal load-deflection characteristics (see Figure 5.4) are also included in the figure to allow a simple visual comparison to be made between the normal, longitudinal and lateral tyre stiffnesses. These have been found to be approximately 180 kN/m, 200 kN/m and 100 kN/m, respectively. It should be noted that the longitudinal and lateral loads exerted on the 'tyre' were again determined from the contact patch forces, and the deflections from the displacement of the glass plate model.

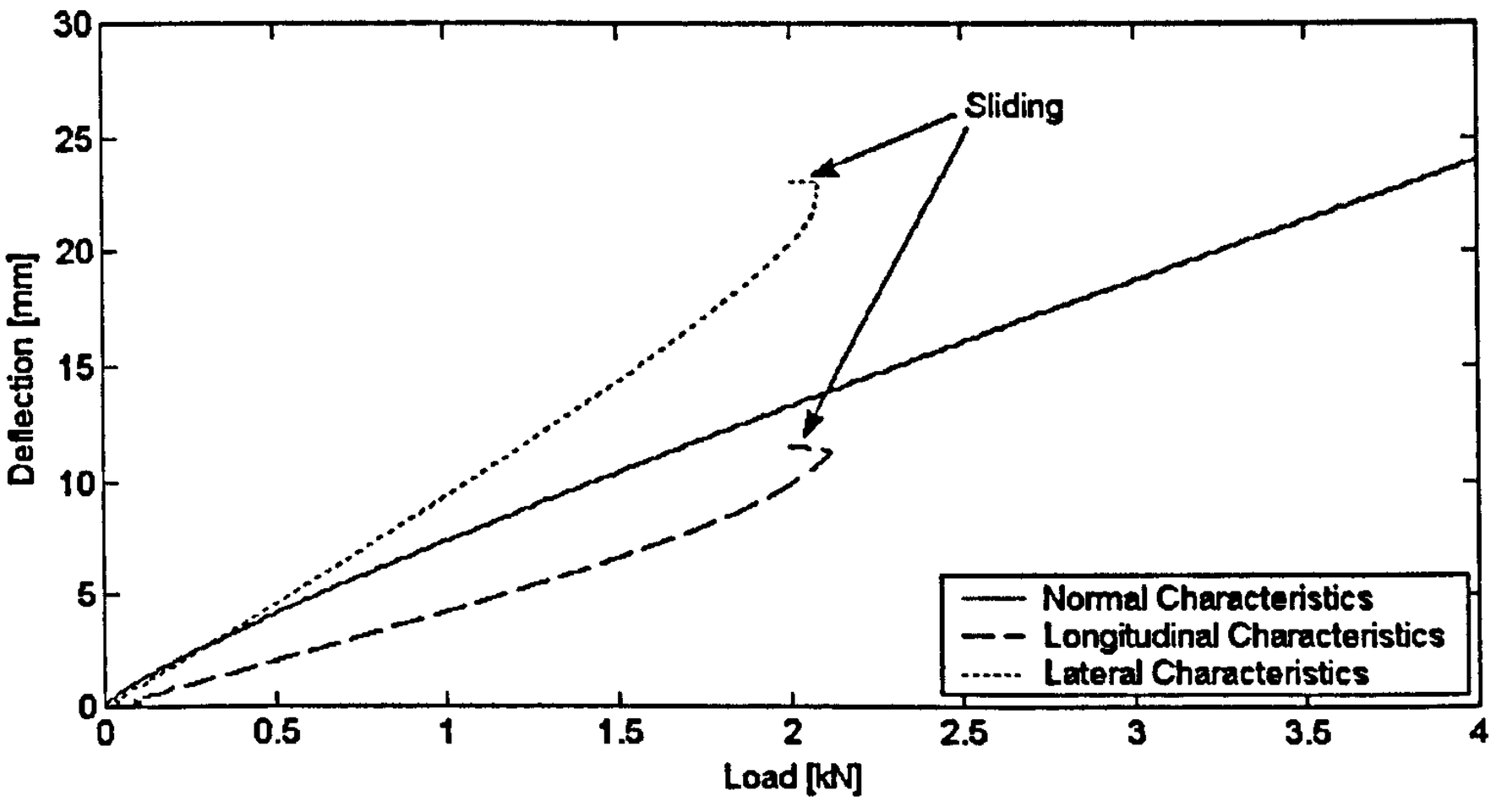

Figure 5.10 Simulated normal, longitudinal and lateral load-deflection characteristics

Due to the closure of the experimental facilities at Dunlop Tyres Limited, the author does not have longitudinal and lateral load-deflection measurements for the experimental tyre. As an alternative, however, Dunlop Tyres have provided longitudinal and lateral stiffness values for a similar 195/60 R15 tyre with an inflation pressure of 200 kPa [97]. These stiffnesses were 300 kN/m and 170 kN/m, respectively. It should be noted that although the tyres are of similar construction, these stiffness values are likely to be significantly higher than those for the experimental tyre. This is because sidewall deformations influence the longitudinal and lateral stiffnesses. These sidewall deformations are affected by the rubber properties and the tyre's aspect ratio (see

Section 2.3). The aspect ratio is different for the two tyres and therefore the stiffnesses are only useful as a guide. It is noted that for a 195/70 R15 tyre, the lateral stiffness is assumed in the work by Lee *et al.* [88] to be about 90 kN/m. Based on this information, it is postulated that the predicted longitudinal and lateral stiffness of 200 kN/m and 100 kN/m, respectively, are within the range expected. The simulations appear to give realistic longitudinal and lateral tyre stiffnesses which are necessary to simulate tyre behaviour during acceleration/braking, and cornering (slip and camber angle) conditions.

5.8 Summary

The structural behaviour of the experimental tyre during the stationary experiments (see Chapter 3) has been successfully simulated. Numerical results have been compared with a reasonable degree of success to experimental measurements. An excellent correlation was found for the normal load-deflection characteristics. Longitudinal and lateral load-deflection characteristics have also been analysed and these appear to give realistic tyre stiffnesses. These simulation results therefore suggest that the modelling methodology presented in Chapter 4 could be employed to accurately simulate global tyre behaviour.

The predicted contact patch dimensions (length and width) were found to give a good trend-wise agreement, but the contact patch length and width were typically 30 mm and 20 mm greater than the physical test data, respectively. As a consequence, the normal pressures in the contact patch were found to be lower than those expected. To determine the reason(s) for the difference, a parametric study has been carried out. Based on the results of the study and on information from Ove Arup & Partners, it appears that the difference is likely to be related to the contact algorithm inherent in the code. This suggests it is not straightforward to accurately predict the contact deformation, and corresponding internal transient stresses and strains in the tyre structure, in absolute terms. However, the good trend-wise agreement suggests that the modelling methodology should be capable of predicting internal transient responses which are, at least, related to the 'actual' contact patch deformations in a rolling tyre.

Chapter 6 Simulation of Rolling Tyre Behaviour

6.1 Introduction

It has already been mentioned that the aim of the Finite Element (FE) modelling work is to provide an initial investigation of the complex internal stresses and strains in a rolling tyre. Furthermore, it has been stated that the accuracy of any simulation is only as good as the FE program and the way in which it is employed. Stationary (non-rolling) tyre simulations have been carried out in Chapter 5, using a Sun Ultra 60, 360 MHz workstation. The computational time for simulating a tyre under normal loading (to 5 kN) was found to about 200 h. This time can be approximately halved utilising the current resource, a Sun Blade 1000, 750 MHz workstation. All simulations in the chapter were carried out using LS-DYNA [17] version 950d. This version was, at the time, the most up to date release. It should be noted that the current release is version 960. The stationary results suggest the modelling methodology is capable of predicting internal transient stresses and strains which are related to those in a rolling tyre. Thus, the rolling behaviour on a flat bed and a rolling drum (see Chapter 3) is considered here.

6.2 Computational Considerations

One full revolution of a rolling tyre is required at the desired speed (see Section 3.6). To simulate one revolution at a longitudinal tyre velocity corresponding to that in the flat bed experiments (0.18 km/h) would require a 'real time' in excess of 10 s. The computational cost for such a simulation is estimated to be greater than 12,000 h (500 days) using LS-DYNA version 950d with a 'forced' minimum time step of 5×10^{-7} s. This estimation is based on the current computational resource, a Sun Blade 1000. The computational time is doubled using the 'double precision' option now available in version 960 of the code. As will become clear later in this chapter, double precision is needed to successfully simulate a rolling tyre and the simulation time is therefore

obviously unacceptable. It was, however, recognised that a significantly reduction in the computational cost can be achieved by increasing the rolling tyre velocity. Consideration has been given here to a velocity of 20 km/h. This choice of speed was deemed acceptable based on the assumption that no discernible change occurs in the contact patch stress distributions up to a velocity of approximately 130 km/h [75]. Thus, the rolling simulations are carried out over a real time of approximately 1 s, about one tenth of the computational time originally estimated if the tyre velocity was only 0.18 km/h.

6.3 Rolling Simulations

The rolling model described in Chapter 4 is used to simulate tyre behaviour during free-rolling conditions on the flat bed and rolling drum surfaces. In the simulations, the wheel fit and inflation, the normal loading to 3 kN and the rolling of the tyre are represented.

6.3.1 Wheel Fit and Inflation, and Normal Loading Phases

The wheel fit and inflation phase was carried out in an identical manner to that in the normal loading simulation described in Section 5.3. The 'tyre' was then allowed to achieve a state of static equilibrium and the 'ground' surface was displaced vertically (in the *z*-direction) at a rate of approximately 0.4 m/s. This rate was chosen to minimise the simulation time while ensuring a stable solution. Contact problems, at high impact velocities, are known to occur with LS-DYNA [17] and these have been discussed in Section 5.3.1. The rate of 0.4 m/s is not representative of the rolling experiments and, as a consequence, it introduces a numerical dynamic effect into the normal loading phase. This does not invalidate the analysis because transient deformations during this phase are not relevant to the rolling simulation results, only the steady-state tyre deformation is important. To simulate the deformation, the surface displacement was again initially selected based on the quasi-static normal load-deflection characteristics shown in Figure 5.4. This has been discussed in Section 5.4. As will become clear later, it was necessary to modify this displacement to accurately simulate the deformation. The tyre was allowed to achieve a state of equilibrium after the specified displacement was reached.

The flat bed is represented by a 7.75 m long × 1.15 m wide horizontal surface coarsely modelled using 3,565 quadrilateral rigid shell elements. The mesh is uniform and the

elements are based on the Belytschko-Lin-Tsay shell element [82, 83]. Similarly, the 2.39 m diameter drum surface is modelled using 8,280 shell elements. The drum model is shown in Figure 6.1. It should be noted that this model is more than two times as refined circumferentially as the flat bed model is in the longitudinal (x-) direction. This is necessary to adequately represent the curvature of the drum using flat quadrilateral elements. Significant changes in the mesh density do not noticeably affect the stationary simulation results (see Section 5.3.2) and it is therefore acceptable here to assume that similar mesh density changes will also not significantly influence the rolling simulations.

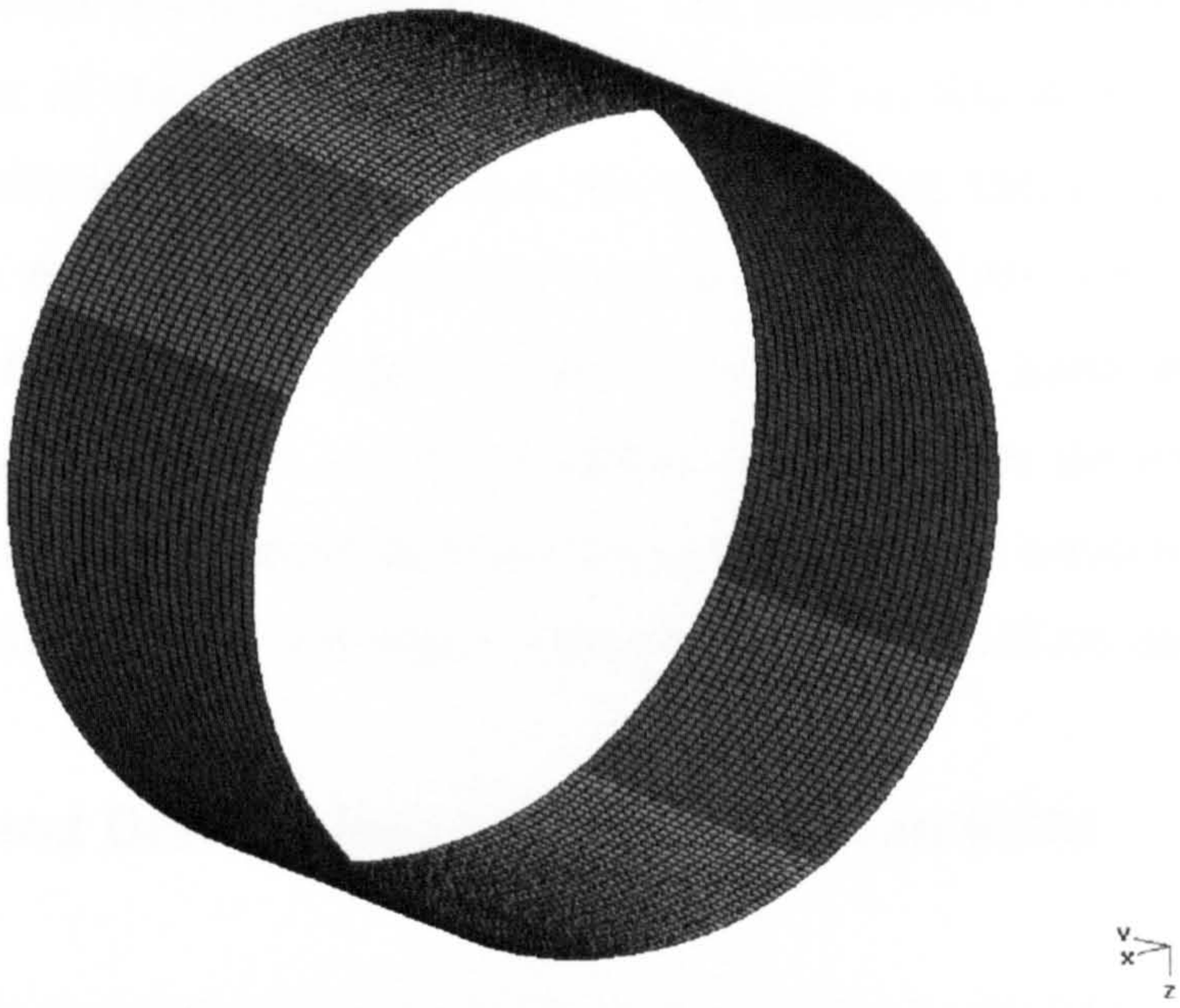

Figure 6.1 Three-dimensional drum surface model

6.3.2 Rolling Phase

To simulate the rolling action, the wheel rotational constraint about the y-axis is released and a velocity is then applied to the 'ground' surface. This is representative of the situation in the full-scale physical tests carried out on the flat bed and rolling drum machines, respectively. This velocity was applied in the longitudinal (x-) direction in the flat bed simulation. In the drum simulation, the drum was rotated about its centroid causing the contacting tyre to rotate. The velocity was increased linearly to the desired speed of 20 km/h over a real time of 0.4 s. This real time was chosen because excessive slip was found, by trial and error procedures, to occur at higher surface accelerations.

6.4 Tyre Damping

Mass-proportional damping has again been applied at a material level to optimise the model response in the wheel fit and inflation, and normal loading phases. This damping was removed prior to the rolling phase because retarding forces applied to each node are known to eliminate realistic transient responses. Appropriate damping levels are an area of constant debate and, like contact modelling, rely heavily on the experience and expertise of the FE analyst. Jacob and Goulding [68] have presented some representative viscous damping levels for selected structures but no recommendation is given for an automobile tyre (or similar structure). The recommended levels are typically less than 3 percent of the critical damping level. Based on this information, it was considered acceptable to discount damping in the rolling phase. This issue is discussed further in Section 6.5 where the damping level is linked to the rolling resistance characteristics. Rolling resistance has a constant but a relatively minor effect on the contact patch stress distributions and it is therefore postulated that the assumption to neglect damping does not invalidate the modelling methodology. To simulate tyre rolling resistance effects, further work is needed to characterise a more realistic damping level.

6.5 Results and Discussion: LS-DYNA version 950d

The flat bed and drum simulation were initially analysed using LS-DYNA version 950d. These analyses were found to experience numerical instabilities and in both cases a 'floating point exception' was found to occur. This numerical problem arises because real numbers are stored as words of finite length (i.e. fixed numbers of digits), usually referred to as either single or double precision with a word length of 32 bits and 64 bits, respectively. A floating point exception is said to occur when a number is too large or too small to be represented and, as a consequence, the analysis 'crashes'. This problem is known to occur in the code and has also been found by other FE analysts [98] but to the author's knowledge it has not previously been reported in relation to tyre analysis. The flat bed and drum simulations were carried out in July 2001 when only single precision was available. Double precision was not available until February 2002 with the current release (version 960) and, thus, a significant time period (almost 8 months) was spent by the author unsuccessfully trying to provide a modelling solution to a numerical instability problem inherent in the code. For example, various tyre acceleration rates

between 7 m/s^2 and 24 m/s^2 were tested. Based on this experience, it is the author's opinion that rolling tyre simulations using single precision are not to be attempted because the analysis is likely to crash before the required numerical results are available.

6.6 Results and Discussion: LS-DYNA version 960

The flat bed simulation was reanalysed using version 960 and the simulation time was found to be approximately 2,400 hours (100 days), double that needed for a single precision analysis. This penalty is deemed acceptable in terms of the project's aim but, for future analyses, the simulation time could be significantly reduced by model optimisation of the rolling phase. For example, the tyre acceleration could be increased by applying a rotational velocity to the wheel which corresponds to that given to the horizontal surface. This wheel rotational velocity could be removed once the desired speed is reached and the tyre would then be driven solely by the surface. Since the tyre acceleration is not relevant to the rolling simulations, such model optimisation would not invalidate the results. In a feasibility investigation carried out by the author, it was found that the desired speed could be reached in a real time of 0.1 s. This corresponds to a computational saving of about 720 h and thereby reduces the simulation time to 70 days.

After the tyre, travelling at 20 km/h, had rotated one full revolution, the contact patch behaviour was examined. The predicted contact stress distributions at the normal load of 3 kN are shown in Figure 6.2. Figure 6.3 shows a comparison between the stresses at the lateral tyre centre and those obtained in the flat bed experiments (again at 3 kN).

In Figure 6.2, the contact stresses are given in kPa, and the distance travelled by the tyre and the lateral tyre position are given in m and mm, respectively. The stress values are those obtained as a contacting node progresses through the contact patch and 17 nodes across the width are considered. The distance travelled in Figure 6.3 corresponds to that found in the flat bed simulation and not that found in the physical tests where the tyre travelled about 1.6 m. The physical test data is plotted on top of the simulation results for comparison purposes. In both figures, the numerical stresses were obtained directly from the nodal stress field data, not via the nodal force data, at an interval of 5×10^{-4} s. As explained in Section 5.6.2, this does not influence the simulation results. The stresses in the figures are those exerted on the tyre and not on the horizontal surface. The shear

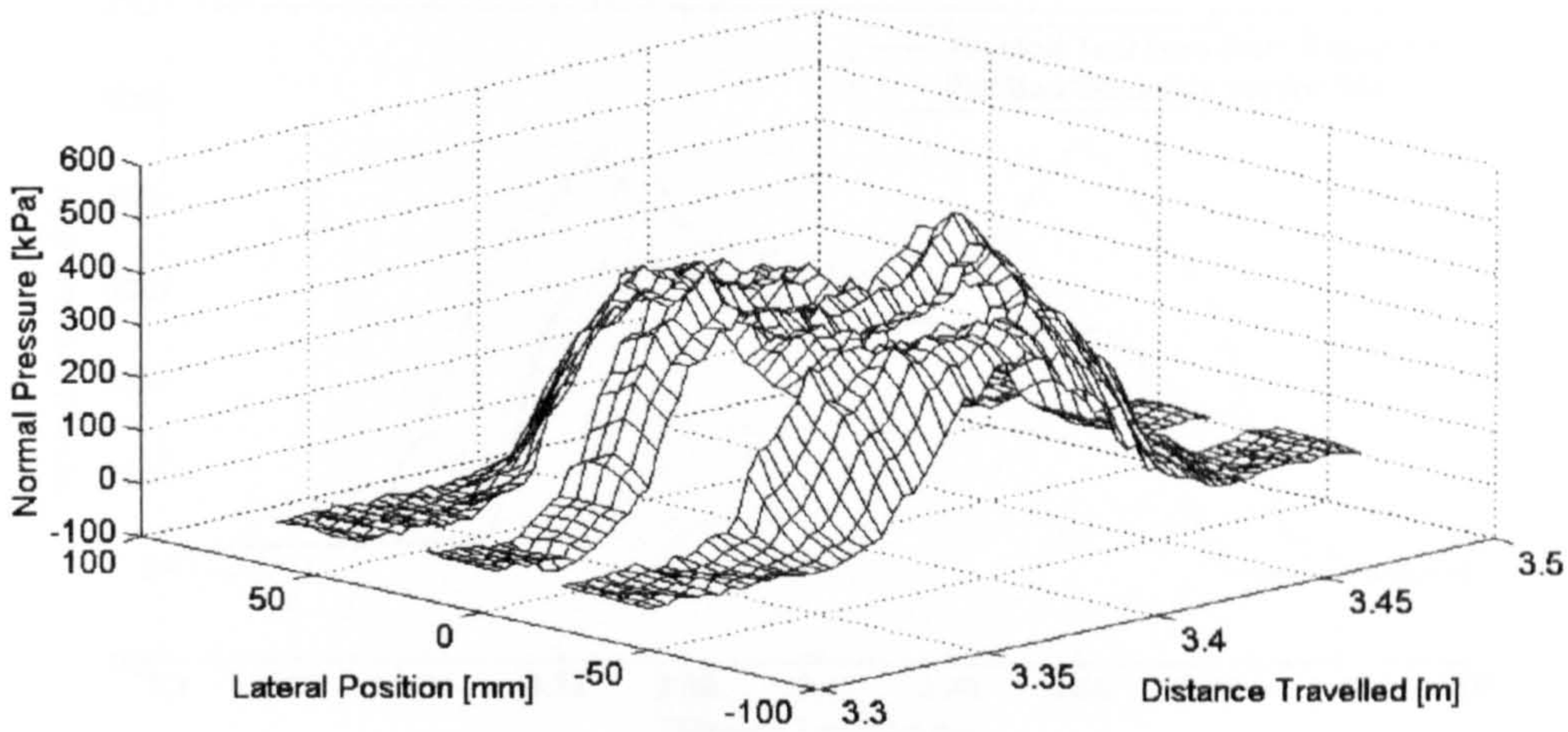

(a)

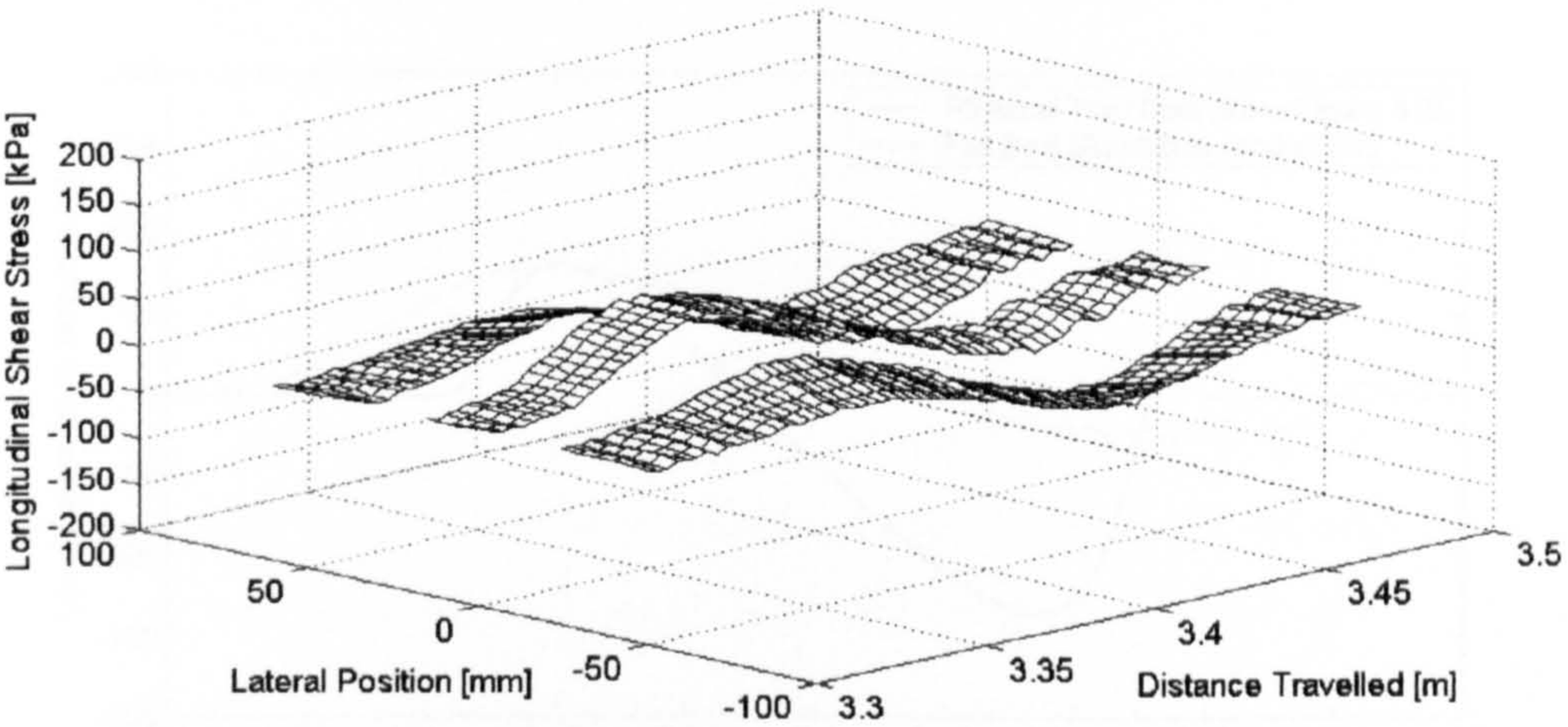

(b)

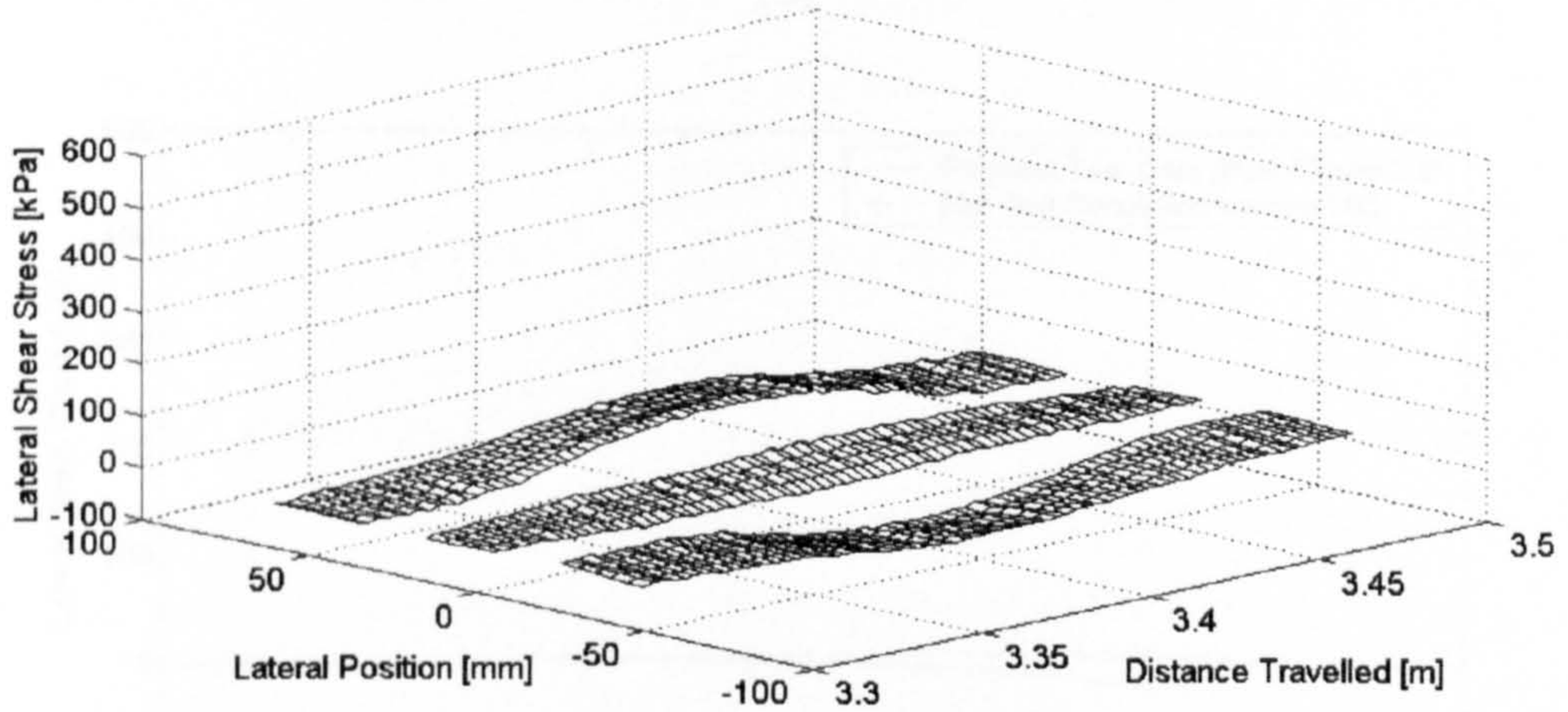

(c)

Figure 6.2 Simulated contact stress distributions at a normal load of 3 kN and a velocity of 20 km/h: (a) normal pressure; (b) longitudinal shear stress; (c) lateral shear stress

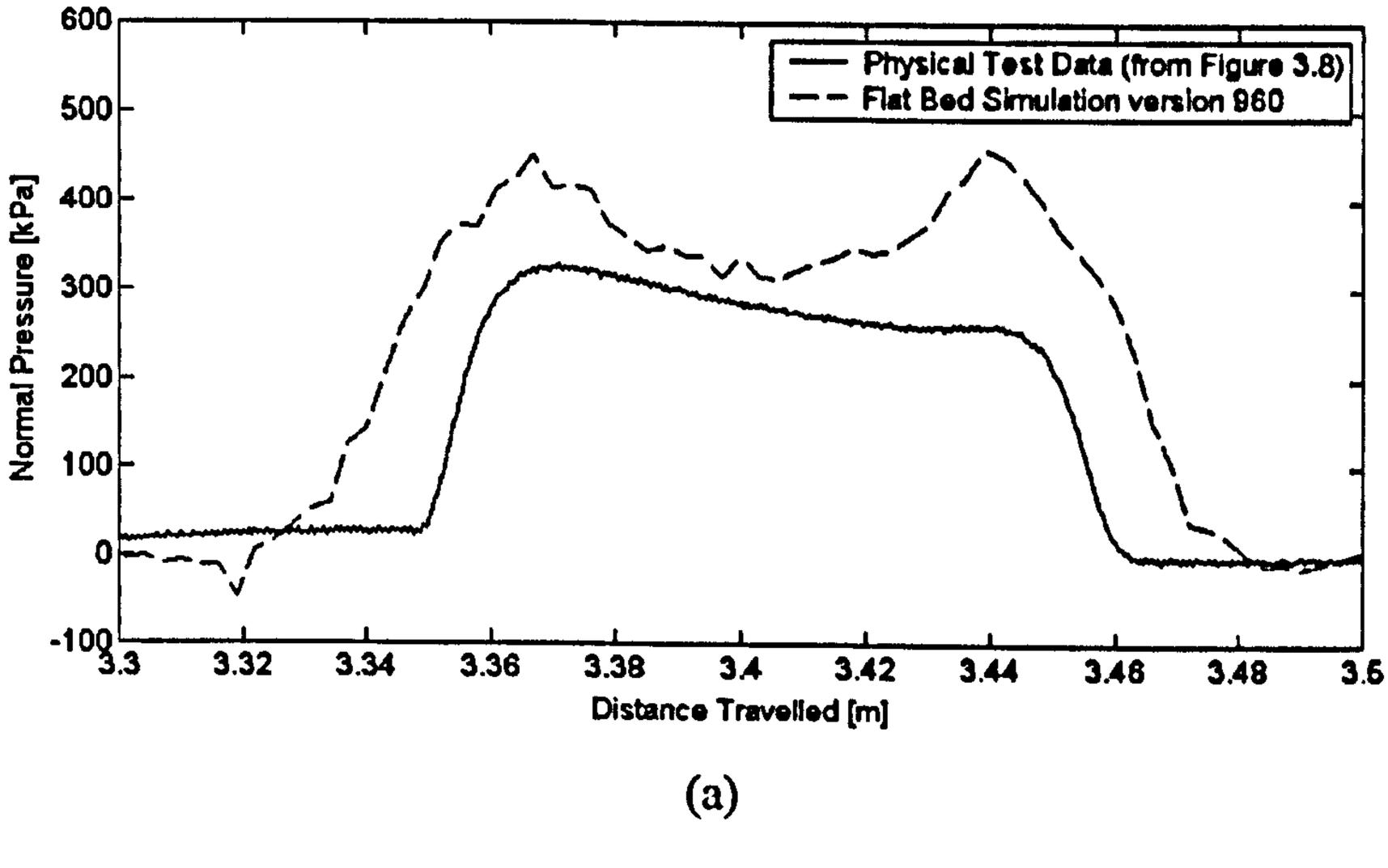

(a)

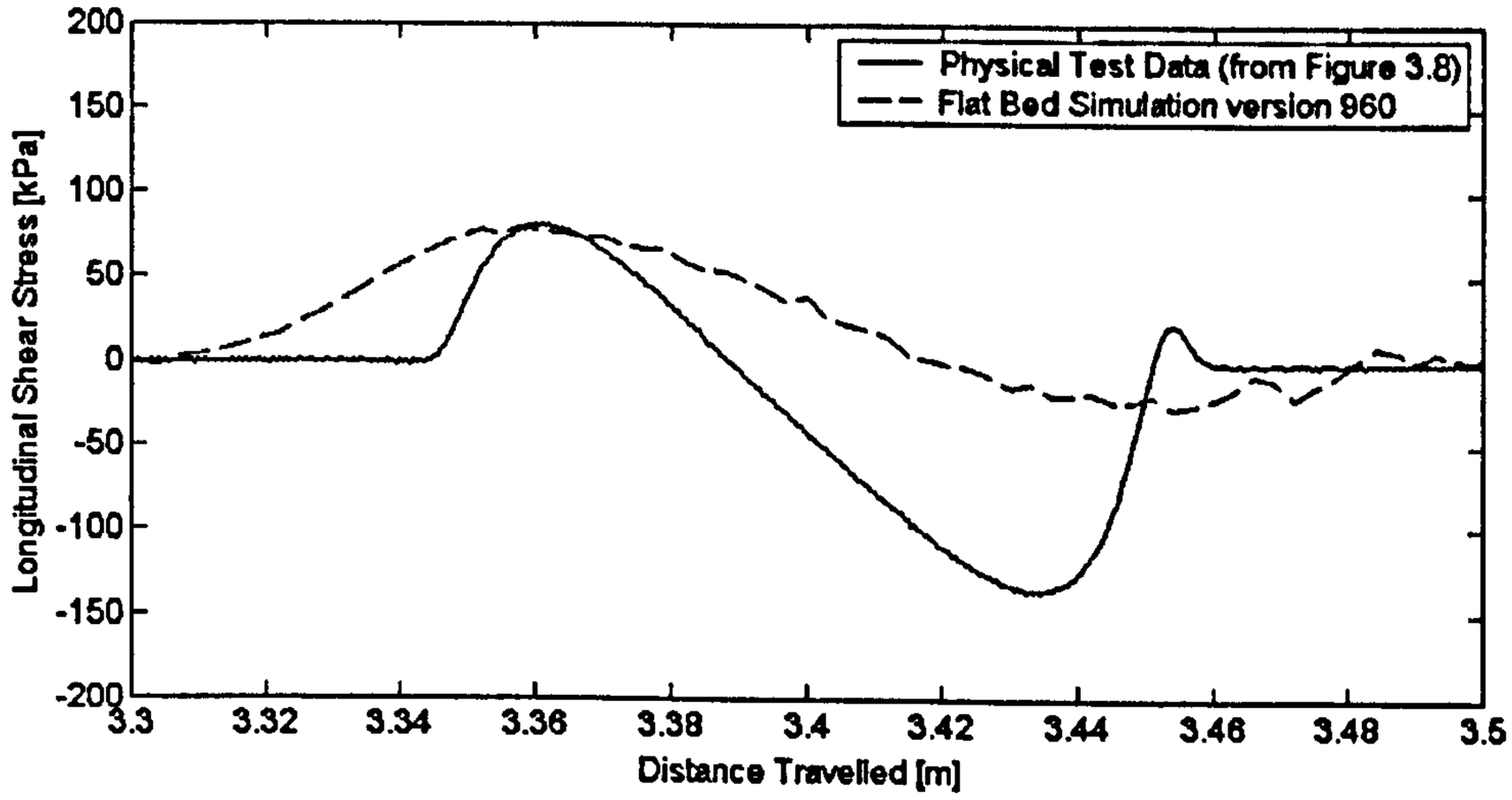

(b)

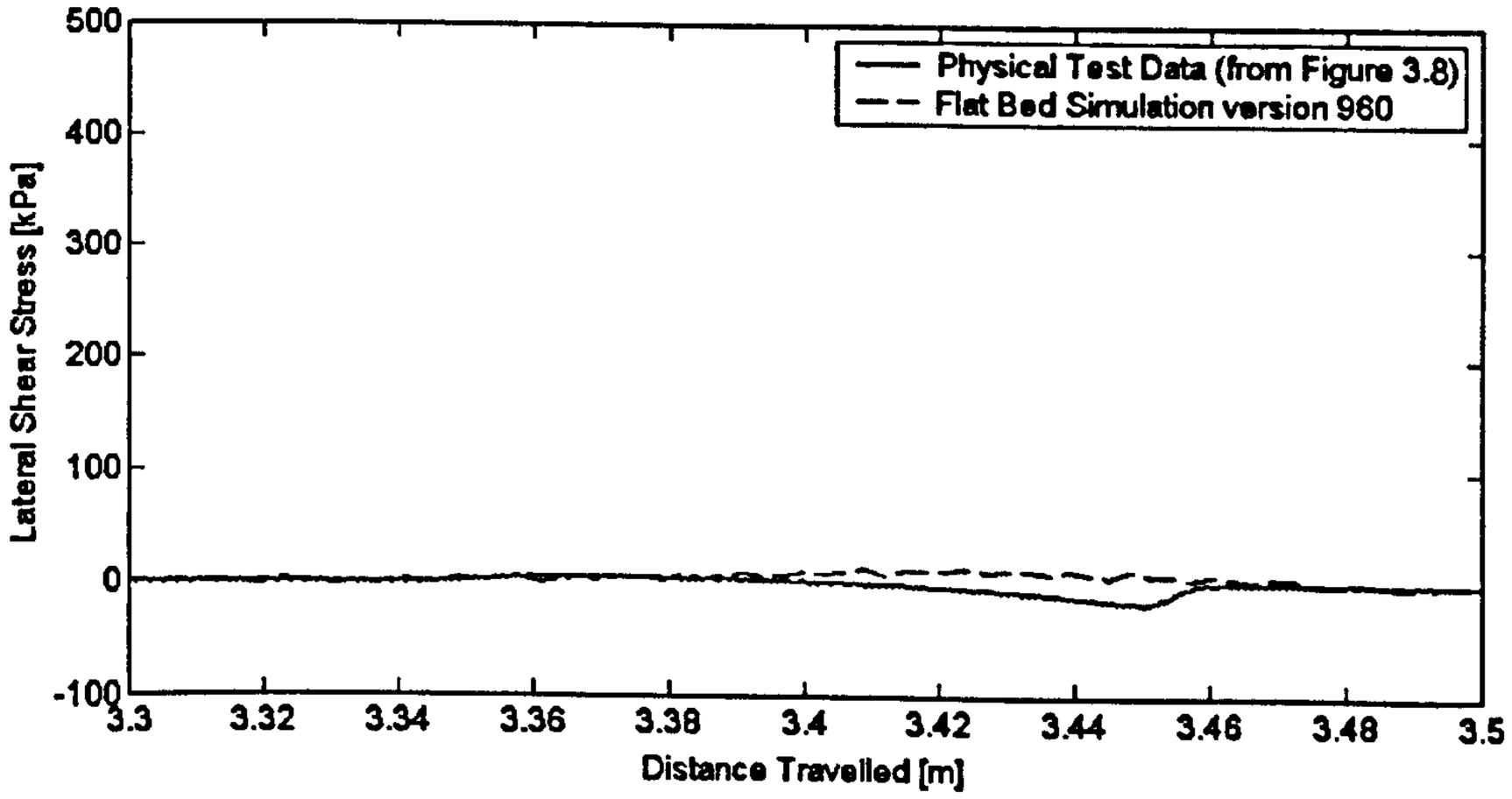

(c)

Figure 6.3 Contact stress distributions at the lateral centre of the tyre at a normal load of 3 kN: (a) normal pressure; (b) longitudinal shear stress; (c) lateral shear stress

stresses are therefore opposite in sense to the experimental measurements presented in Figures 3.8, and 3.10 to 3.15. The normal and shear contact stresses are plotted on similar axes to provide a simple meaningful comparison, and the length depicted in the plots is again 0.2 m. At the lateral centre of the tyre, the lateral coordinate is 0 mm.

The normal pressure exerted on the contacting nodes in Figures 6.2(a) tends to be high at the front of the contact patch, lowest at the centre and then high again at the rear. This characteristic is related to the 'buckling' effect of the tyre which has been discussed in Section 3.6.1. The pressures at the front are approximately the same as those at the rear suggesting that the rolling resistance effect is not simulated. This is also suggested by the longitudinal shear stress distribution in Figure 6.2(b). The author believes that the rolling resistance can be introduced into the numerical results by damping the tyre components. However, rolling resistance is a minor effect (typically about 50 N) and, thus, neglecting damping in the rolling phase is considered acceptable in this thesis.

At the lateral tyre centre (see Figure 6.3(a)), the maximum predicted pressure is found to be about 450 kPa and at the centre of the contact patch the pressure is 325 kPa. The corresponding normal pressure measurements obtained in the flat bed experiments are about 320 kPa and 275 kPa, respectively. The discrepancy in these numerical and measured values can be related to a difference in the pressure distributions across the width of the contact patch. Interestingly, the predicted pressure distribution also differs significantly from that experienced in the stationary (non-rolling) numerical results (at 3 kN) shown in Figure 5.8(b). This result is discussed further in Section 6.6 where the disparity is related to changes in the code between LS-DYNA version 950d and 960.

In Figures 6.3(b) and 6.3(c), the predicted longitudinal and lateral shear stresses at the lateral tyre centre are shown to exhibit similar characteristics to those observed in the flat bed experiments. The longitudinal shear stress follows a sinusoidal-style sweep as the contacting node progresses through the contact patch, and an excellent correlation is evident in the peak numerical and measured stresses at the front (≈80 kPa). In contrast to the physical test data, however, the predicted longitudinal shear stresses at the rear are significantly lower than those at the front, the peak value having a magnitude of about 30 kPa. Again this disparity can be related to a difference in the stress distribution across the width. Zero net longitudinal force is found in the rolling simulation because

the shear stresses predicted under the tyre shoulders are significantly greater at the rear of the contact patch than at the front. At a lateral tyre co-ordinate of ±55 mm, the peak stresses at the front and rear of the contact patch are 20 kPa and -50 kPa, respectively.

The lateral shear stresses across the width (see Figure 6.2(c)) exhibit similar characteristics to those observed in the experimental work by Dennehy [9] and DeBeer [23]. On one side of the tyre, positive lateral shear stresses are developed, whilst on the other side these stresses are negative. The stresses are about equal in magnitude and, as a consequence, the overall effect is a zero net lateral force. The lateral shear stresses at the lateral centre of the tyre are approximately zero. This is to be expected under free-rolling conditions because conicity and ply steer effects (Section 2.7.3) are negligible.

The numerical results show characteristics which are similar to those observed in the flat bed rolling experiments, and also mentioned in the literature [9, 31, 75]. The buckling effect in the normal pressure distribution and the sinusoidal-style style sweep in the longitudinal shear stress distribution are both evident. The lateral stress characteristics are also realistically simulated [9, 23]. Whilst the results are not a one-to-one correlation with the physical test data they again confirm the potential of the modelling methodology to predict contact deformations which are experienced by a rolling tyre.

6.7 Incompatibility between LS-DYNA version 950d and 960

The normal pressures in the contact patch shown in Figure 6.2(a) are significantly higher than those observed from the stationary (normal loading) simulation in Figure 5.8(b) using version 950d. This difference cannot be related to the 'real' physical behaviour of the tyre during the rolling mechanism and therefore must be related to changes in the coding. This was confirmed when the normal loading simulation was repeated using version 960. The normal load-deflection characteristics and contact patch dimensions (length and width) are shown in Figures 6.4 and 6.5, respectively. To provide a simple visual comparison, the simulation results obtained using version 950d (see Figures 5.4 and 5.5) and the physical test data (Figures 3.6 and 3.7) are also included in the plots. To discount the possibility that the rolling tyre simulation results were influenced by the analysis precision, both single and double precision analyses were carried out with version 960. Precision can affect the results through truncation of real numbers, or

round off-errors in repeated numerical calculations. No discernible change was found here between the two precisions. The differences shown in Figure 6.4 and 6.5 between the two versions are therefore due to algorithm changes in the LS-DYNA [17] coding.

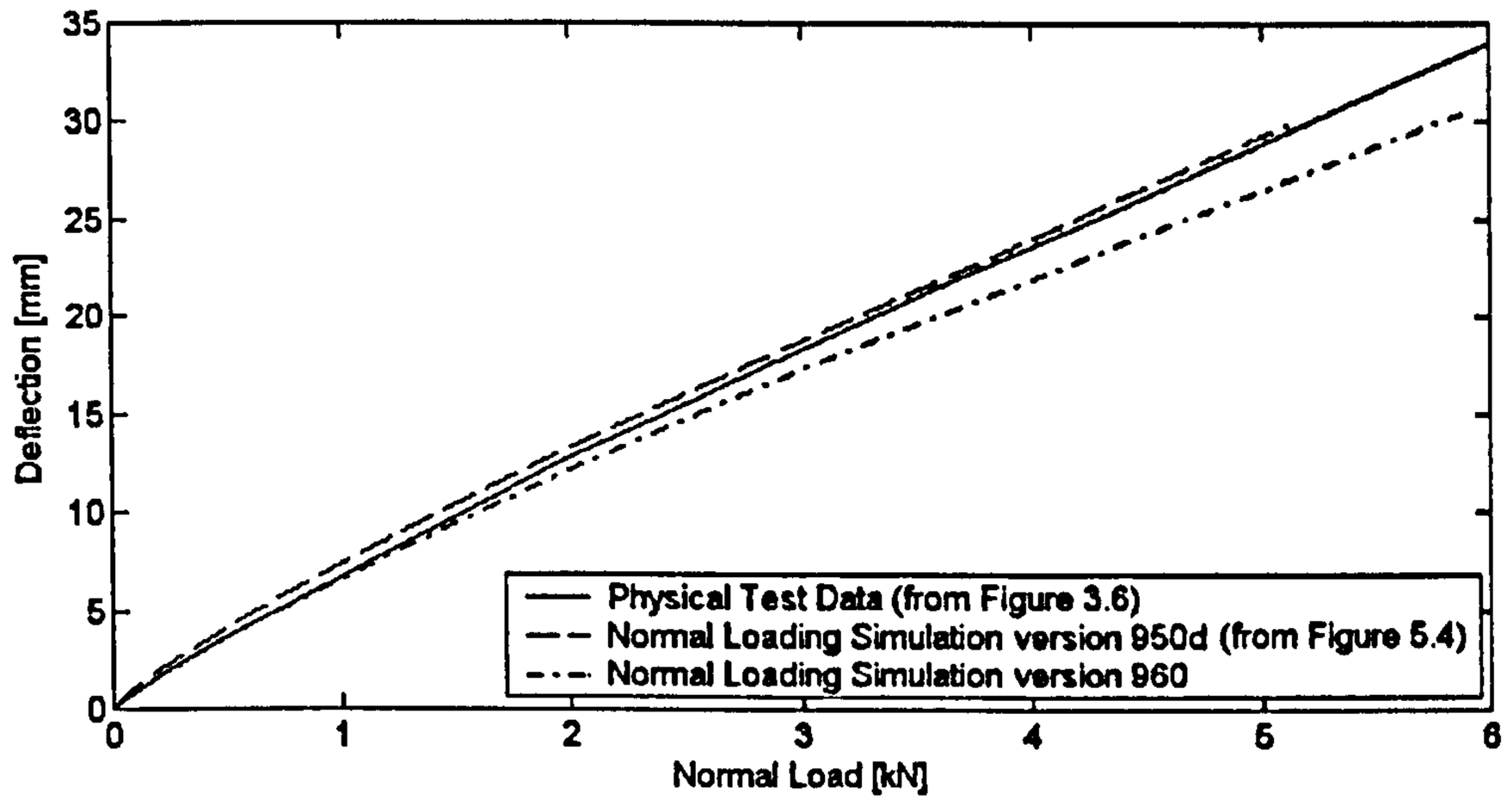

Figure 6.4 Normal load-deflection characteristics

The load-deflection characteristics shown in Figure 6.4 are seen to differ using the two different versions of the code. Version 960 again gives a linear relationship between normal load and deflection but the correlation with the physical test data is now not as good as observed with version 950d. The new predicted vertical tyre stiffness is approximately 200 kN/m. This stiffness is 11 percent higher than that obtained using version 950d and that measured in the stationary experiments. It is, however, within the error limits usually expected for FE simulations and is therefore considered acceptable.

The contact patch area is more accurately represented using version 960 (see Figure 6.5). The contact dimensions (length and width) again show a good trend-wise agreement with the physical test data but the difference in the width dimension has significantly reduced. Based on the distinct points when the node-to-surface contacts occur (represented by the square points), the predicted width from version 950d is typically reduced by approximately 15 mm. The contact patch length remains approximately the same to a load of 4 kN, i.e. typically 30 mm greater than the physical test data and, as a consequence, the contact patch area is reduced. This reduction in contact patch area correlates to the increase in the normal pressures using version 960.

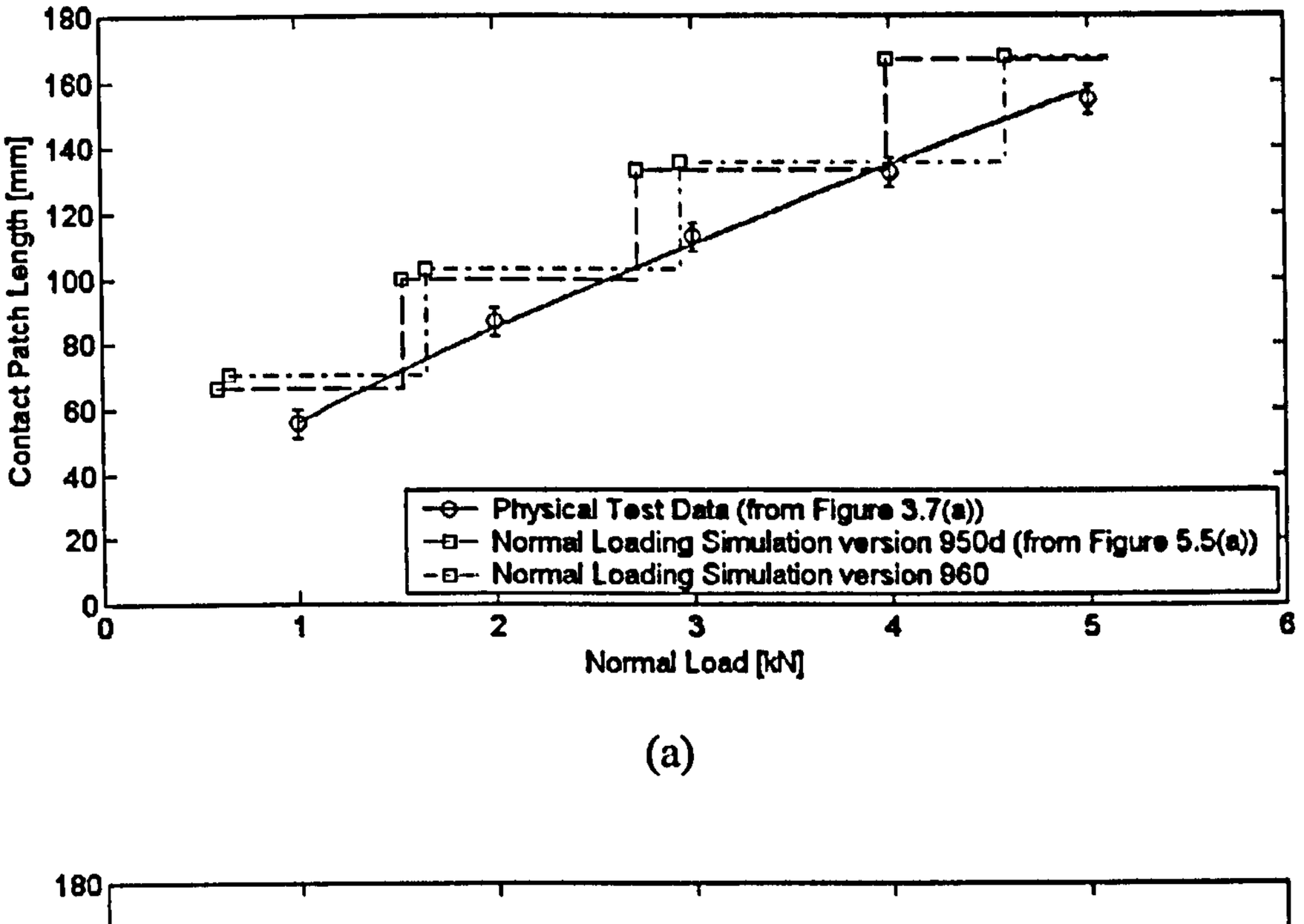

(a)

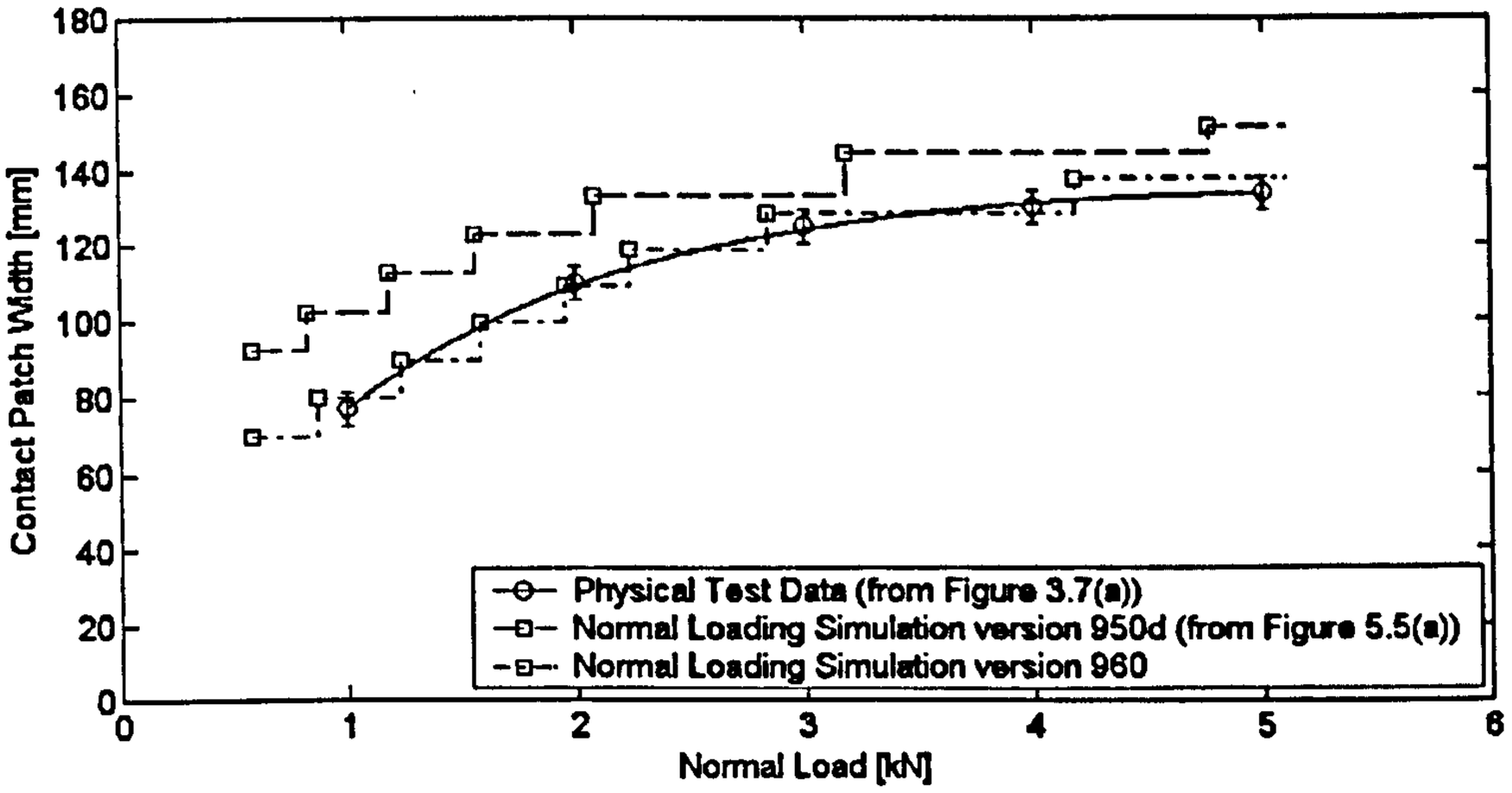

(b)

Figure 6.5 Tyre/ground contact patch dimension with normal load: (a) length; (b) width

It should be noted that as LS-DYNA [17] develops, 'bugs' found in the code are removed. A number of problems with version 950d have been identified by others [99] and changes have been made to the two subsequent releases, i.e. versions 950e and 960. These changes, as well as new additional features, are summarised in the Update and Release Notes [100, 101]. The changes are numerous (>100 bugs were removed from version 950d prior to releasing 950e) and the differences shown in Figures 6.3 and 6.4 are unlikely to be related to any one specific modification. Possible causes range from changes in element formulations to the performance of the contact algorithm. Analysis results can also differ from machine to machine [99]. Research plays a major role in FE

software development and this thesis has identified some problems with version 950d. For example, the performance of the incompressible Mooney-Rivlin rubber material model (material model 27) under shear deformation. This problem is not mentioned in the subsequent Update and Release Notes [100, 101] and must therefore remain an issue for the code developers. The problem is beyond the scope of the work reported herein.

It is the author's opinion that the difference in the results from the two versions does not undermine the earlier model validation work when only version 950d was available. These numerical results, shown in Figures 6.3 and 6.4, only reemphasize the difficulty in predicting tyre behaviour local to the contact patch. A good trend-wise agreement in the contact patch dimensions (length and width) is still observed and because the contact patch width is more accurately represented, it is likely that, the internal transient responses in the tyre will be more accurately predicted. Thus, the author believes an improved understanding of the transient tyre stresses and strains local to the contact patch can still be achieved via numerical simulation using version 960. The results also suggests that a FE analyst should demonstrate extreme caution before using results obtained from different versions of the same code to validate a modelling methodology.

6.8 Internal Stresses and Strains

In Section 1.3 it was stated that to support the development of in-tyre sensor system technologies, it is necessary to gain a greater understanding of the internal transient stresses and strains in a rolling tyre. These are important because they can be used to determine the most appropriate location for an in-tyre sensor (or sensors) and the dynamic relationship (transfer function) between the sensor outputs and the contact patch stresses. It should be noted, however, that the location of a sensor will be influenced by its performance in terms of strain range and cyclic endurance, as well as tyre operating temperature. The cyclic endurance is a function of the strain level [102].

A number of technologies are potentially available for in-situ measurement of transient elastic deformations in rolling tyres. There are a number of advantages and disadvantages with each potential method, and a significant amount of development work is needed before any solution becomes practical. Some of these technologies are detailed in the work by Tomka *et al.* [103], and include surface acoustic wave (SAW)

electroactive materials and magnetoactive soft magnetic materials. This work has focused on one of the key potential sensor technologies and this has resulted in the development of a magnetic field insensitive stress sensor based on amorphous magnetic materials [104]. This sensor technology is likely to be attractive in the measurement of the longitudinal, and lateral stresses at, or near to, the contact patch. Displacement sensors such as those developed by Darmstadt University [13, 14] are likely to better suited to the measurement of vertical stresses due to changes in the tyre thickness.

To provide an improved understanding of internal behaviour in a rolling tyre, the vertical σ_z, longitudinal σ_x, and lateral stresses σ_y and strains (ε_z, ε_x and ε_y) from the flat bed simulation (using version 960) are shown in Figures 6.7 and 6.8, and 6.10 to 6.13. These results provide information which could be used to identify the best location for in-tyre sensors. The stresses and strains at six nodal positions local to the contact patch are considered. Figure 6.6 shows that the selected six nodes are located at three different lateral coordinates, i.e. at the lateral centre of the tyre, and at +30 and +55 mm from the centre. The height positions are 5 mm and 10 mm from the contacting horizontal surface. Nodal positions 1, 3 and 5 are in the tread, half-way between the contact patch and belt (bandages and breakers), while those at positions 2, 4 and 6 are situated at the interface between the tread and bandages. The internal behaviour at other positions can easily be obtained, and the stresses and strains are approximately symmetrical about the lateral tyre centre. Thus, the values at a lateral position of -30 mm and -55 mm are approximated by those shown here at +30 mm and +55 mm. In the figures, the stresses and strains were again obtained directly from the nodal stress field data and were taken as the nodes progress through the contact region at a sampling frequency of 5×10^{-4} s.

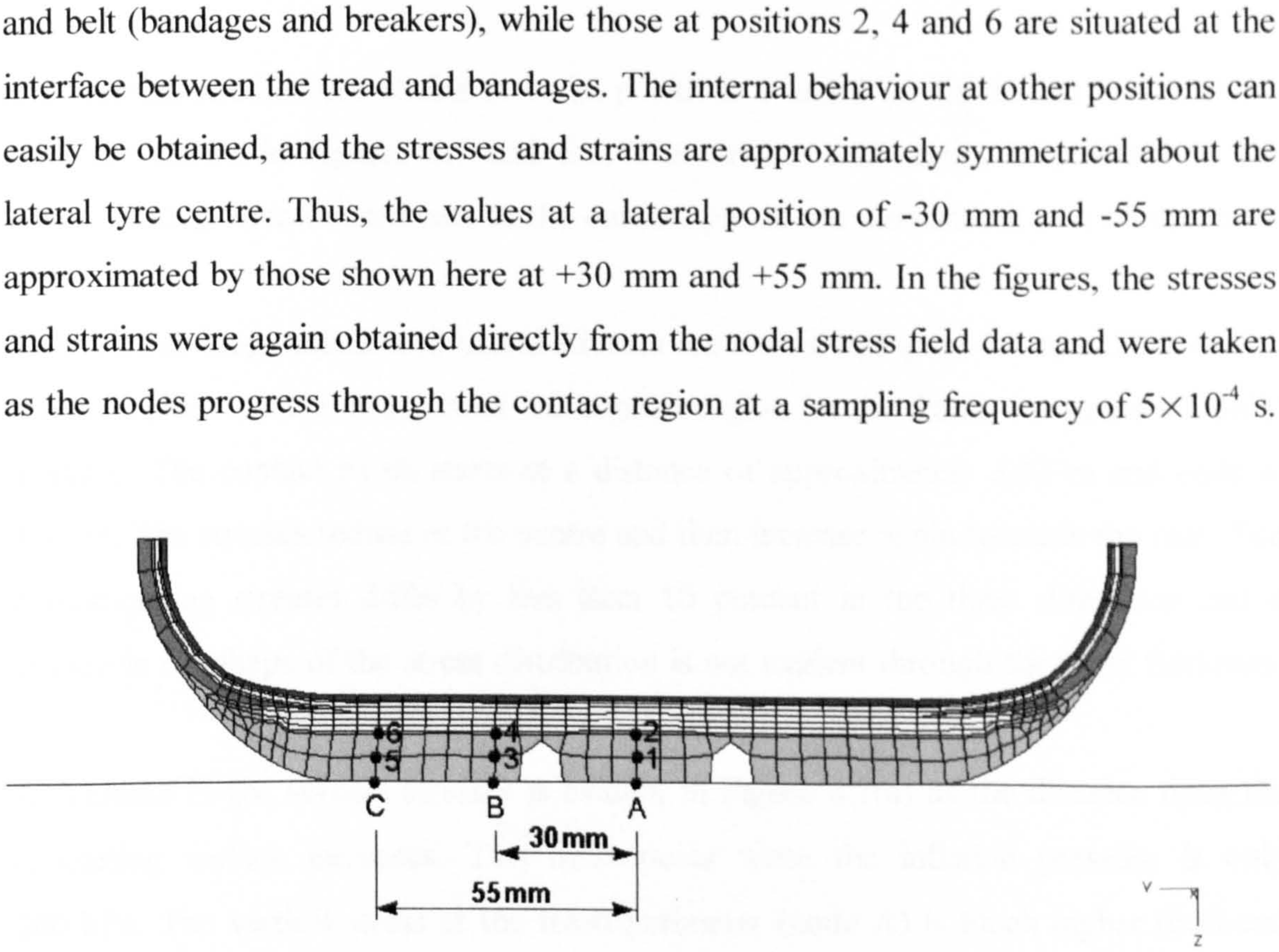

Figure 6.6 Nodal positions local to the contact patch

Typically, strain gauges measure ranges between ±2 percent, and the cyclic endurance is ±2000 micro-strain for between 10^5 and 10^8 cycles [102]. A tyre is commonly used over approximately 50,000 km (>25 × 10^6 revolutions/cycles) under acceleration/braking and cornering conditions, and sometimes in misuse situations [59]. These conditions are likely to increase the internal stresses and strains observed in the tyre structure beyond the values observed under free-rolling conditions. The strains may be experienced over short time periods of less than 1/200th s and at temperatures in excess of 100 °C. These values were estimated based on a linear velocity of 100 km/h and a contact patch length of 0.1 m. They should be considered by the tyre technologist when choosing a position for an in-tyre sensor package. Furthermore, it should be noted that the strains experienced by a sensor will be influenced by its mechanical properties. The relatively stiff sensor will cause a redistribution of stresses and strains in the surrounding rubber. Thus, the stresses and strains presented herein are useful as a initial guide to the location of an in-tyre sensor (or sensors). To determine the outputs with specific types of sensor, the simulation must be repeated with the sensor package represented in the tyre model.

6.8.1 At the Lateral Tyre Centre

The internal stresses and strains at nodal positions 1 and 2 (at the lateral centre of the tyre) are shown in Figures 6.7 and 6.8. The stresses and strains at position A, the corresponding lateral coordinate in the contact patch, are also shown as a comparison.

The vertical, longitudinal, and lateral stresses are shown in Figure 6.7 to exhibit similar characteristics. As the nodes enter the contact region (at the front) the stresses rapidly increase. The contact patch starts at a distance of approximately 3.33 m and ends at 3.47 m. The stresses reduce at the centre and then increase again towards the rear. The corresponding stresses differ by less than 10 percent in the three directions and a change in the shape of the stress distribution is not evident through the tread thickness.

A decrease in the vertical stresses is evident in Figure 6.7(a) as the distance from the contacting surface increases. This must occur since the inflation pressure is only 200 kPa. The vertical stress at the tread perimeter (node A) is much higher (between 300 kPa and 450 kPa). Through the tyre thickness, the stress reduces from the value at node A to the inflation pressure at the inner-face of the liner. The stress reduction is

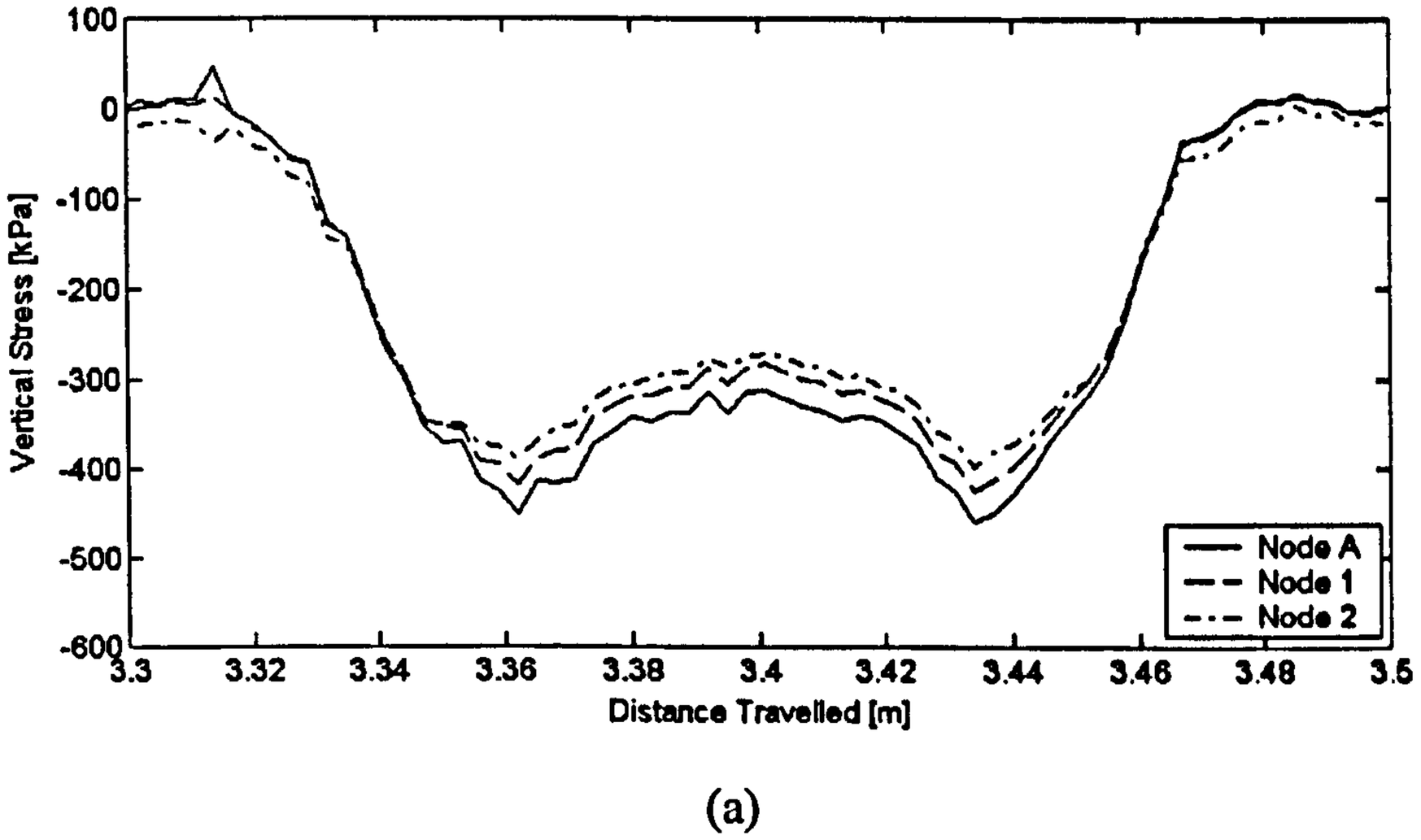

(a)

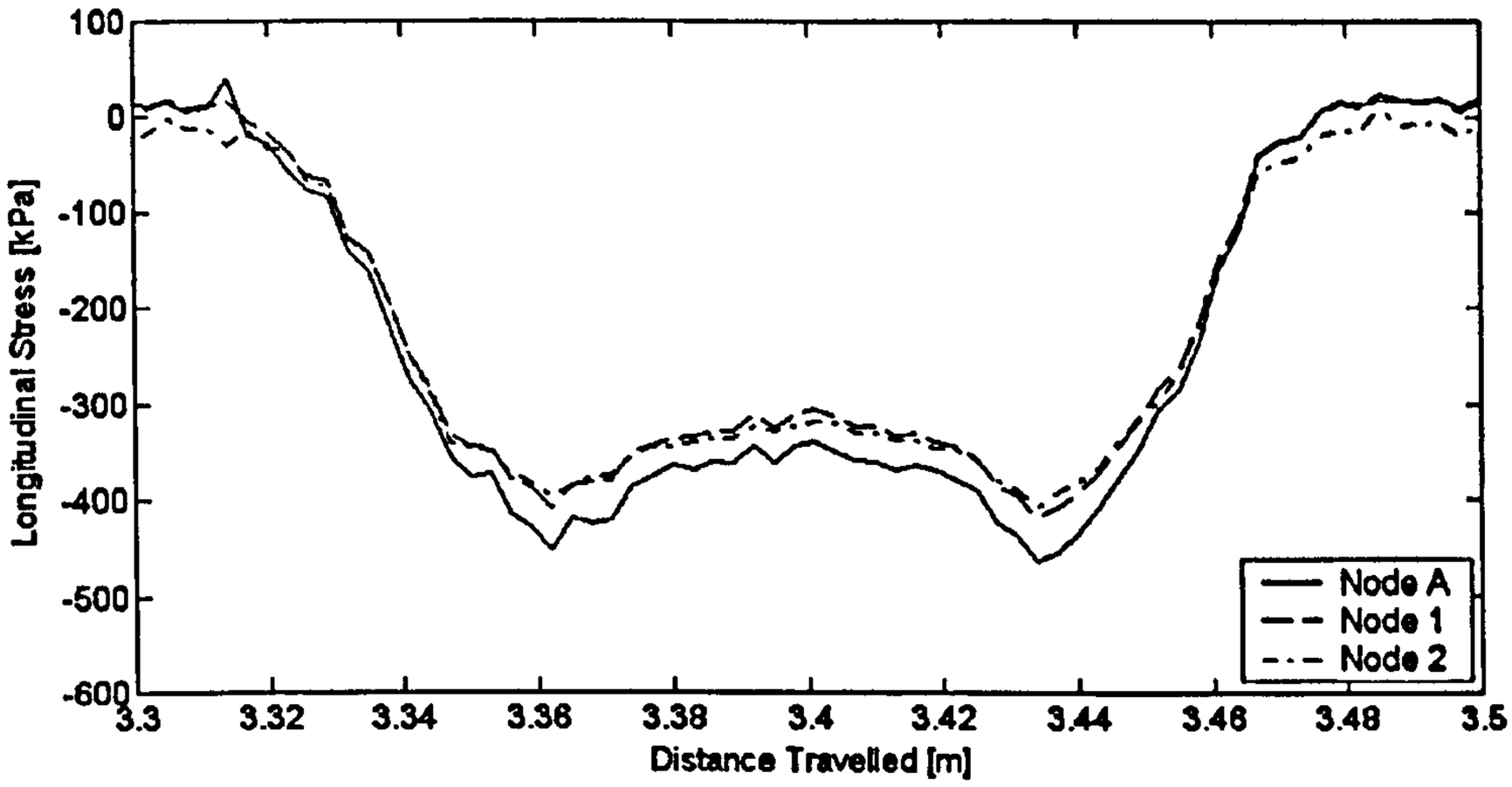

(b)

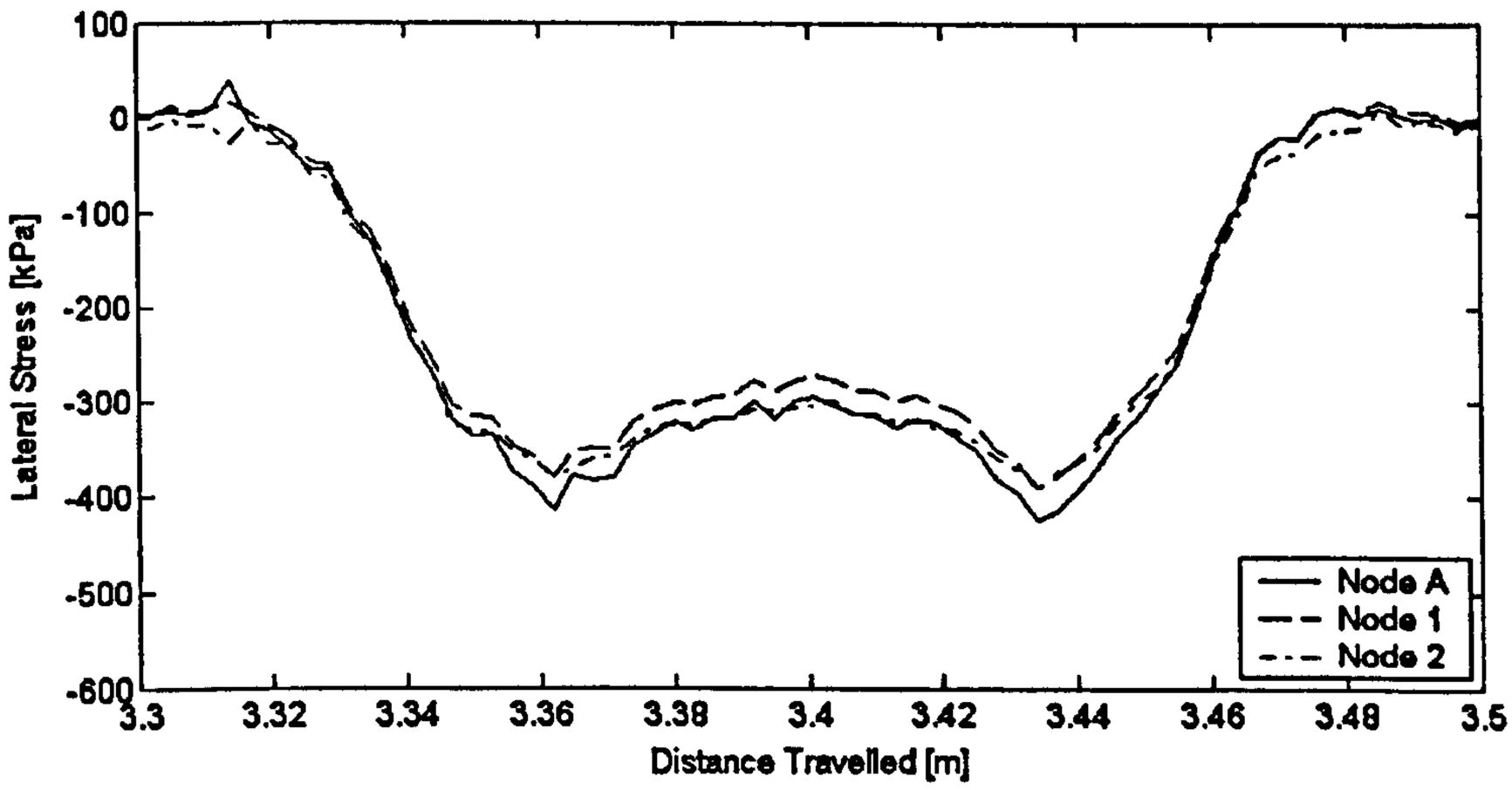

(c)

Figure 6.7 Simulated internal stress distributions at the lateral centre of the tyre with a normal load of 3 kN and a velocity of 20 km/h: (a) vertical; (b) longitudinal; (c) lateral

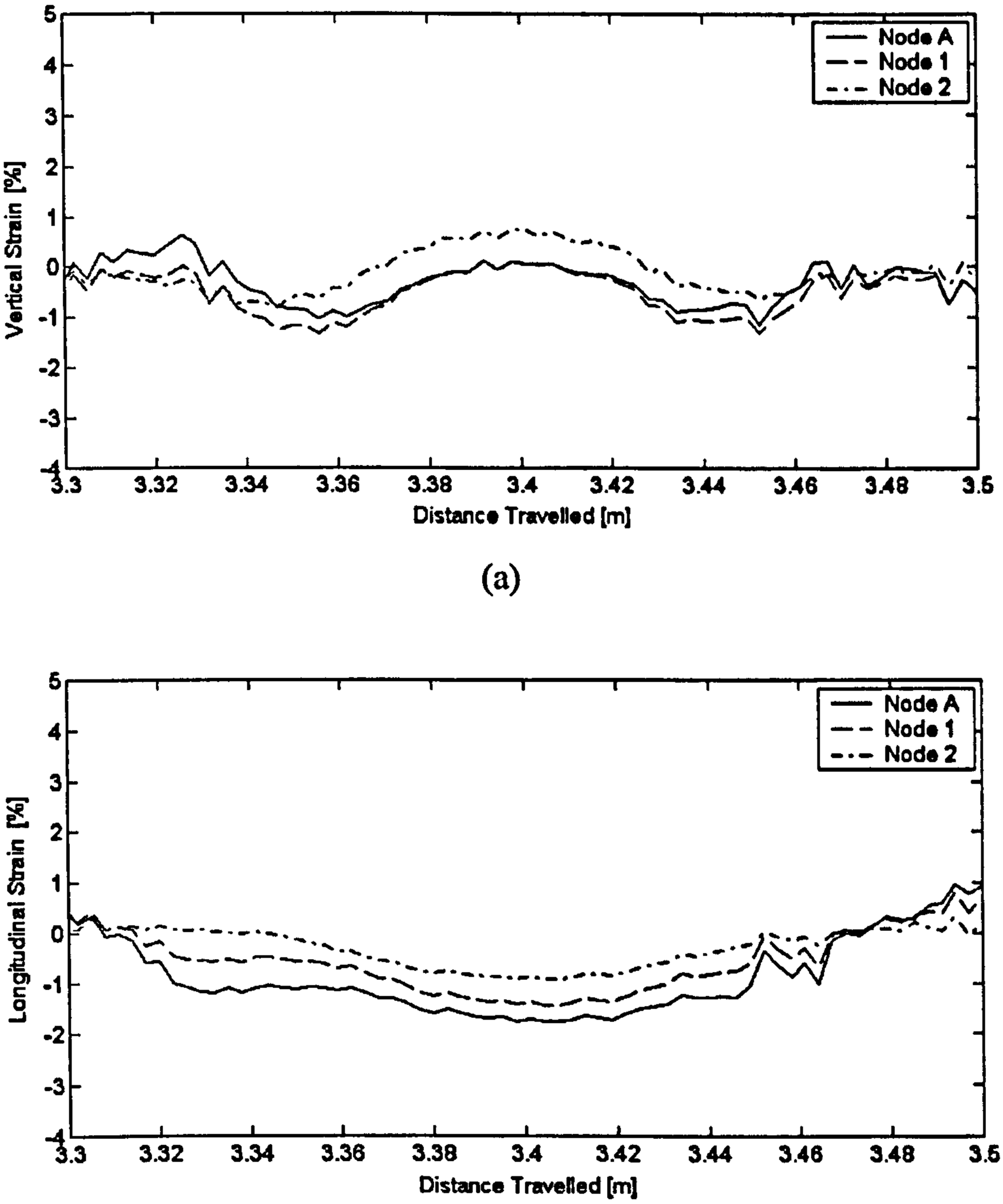

(a)

(b)

(c)

Figure 6.8 Simulated internal strain distributions at the lateral centre of the tyre with a normal load of 3 kN and a velocity of 20 km/h: (a) vertical; (b) longitudinal; (c) lateral

approximately linear, and is 20 kPa every 5 mm of tread depth. Beyond the interface between the tread and bandages, however, there must be a change in the distribution as the pressure at the inner-face of the liner is uniform. This change is shown in Figure 6.9.

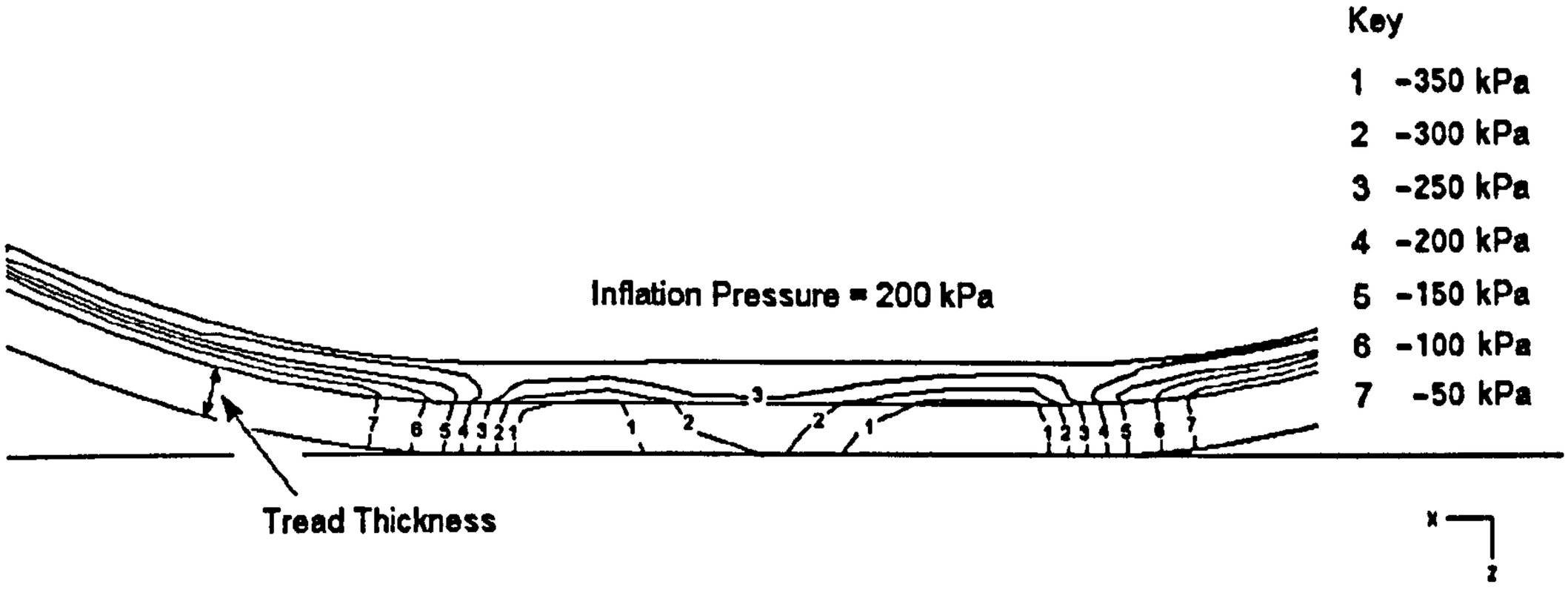

Figure 6.9 Cross-sectional vertical stress distribution at the lateral tyre centre

The linear reduction through the tread does not occur with the longitudinal and lateral stress distributions shown in Figures 6.7(b) and 6.7(c). No logical trend can be identified as the distance from the contacting surface increases. A reduction of approximately 25 kPa is evident in the longitudinal stresses from node A to node 1 and node 1 to 2, while the typical reductions in the lateral stresses are 20 kPa and 0 kPa. It is postulated that the internal longitudinal and lateral stresses at nodes 1 and 2 are influenced by the behaviour of the adjoining belt. This influence is more significant at node 2 because it is situated at the interface between the tread and belt. Since the cords in the breakers are orientated at an angle of ±20 degrees to the tyre circumference, the overlapping layers stretch causing the rubber matrix to flex. This local flexing action is transmitted to the rubber tread via the bandages and diminishes as the distance from the breakers increases.

In Figure 6.8, the direct strains at the lateral tyre centre are shown to be less than 2 percent for the flat bed simulation. The magnitude (and variation) of these strains tends to reduce through the tread thickness. At node 1, the strains range is approximately 1.4 percent in the vertical direction, and 2.2 and 1.5 percent in the longitudinal and lateral directions, respectively. The corresponding strain ranges at node 2 are 1.5, 1.2 and 0.5 percent. The reduction through the tread is to be expected as the reinforcing cords in the belt stiffen the tyre and, thus, reduce the local deformation.

6.8.2 At +30 mm and +55 mm from the Lateral Tyre Centre

The internal stresses and strains at the two positions +30 mm (nodes 3 and 4) and +55 mm (nodes 5 and 6) from the lateral tyre centre are shown in Figures 6.10 and 6.11, and 6.12 and 6.13, respectively. The stresses and strains at positions B and C, the corresponding lateral coordinates in the contact patch, are also shown as a comparison.

In Figures 6.10 and 6.12, the three stresses are shown to exhibit similar characteristics to those at the lateral tyre centre (see Figure 6.7) as the distance from the surface increases. The stress distributions obviously differ because the contact stresses are not the same across the width of the contact patch. The vertical stress distributions again suggest a linear reduction through the thickness of the tread. At +30 mm and +55 mm from the lateral centre, the reduction is about 45 kPa and 10 kPa every 5 mm, respectively. Again a logical trend cannot be identified in the longitudinal and lateral stresses. From node B to node 3 and from node 3 to node 4, the longitudinal stresses reduce by approximately 45 kPa and 10 kPa, respectively. The lateral stresses reduce by 15 kPa and 20 kPa. The reduction in the longitudinal stresses from node C to nodes 5 and 6 is typically 20 kPa, and those in the lateral stresses are 20 kPa and 0 kPa. As mentioned earlier, this behaviour is influenced by the action of the belt, primarily the cords in the breakers.

The direct strains (at nodes 3 to 6) are shown in Figures 6.11 and 6.13 to vary between +5 and -4 percent. The strain ranges at nodes 3 and 4 are 1.7, 1.8 and 2.0 percent, and 0.8, 1.1 and 0.8 percent in the vertical, longitudinal and lateral directions, respectively. At nodes 5 and 6 these ranges are 3.1, 1.5 and 2.0 percent, and 2.0, 0.7 and 1.6 percent. The simulated strain characteristics at nodal positions 1 to 6 are given in Tables 6.1.

The numerical results suggest that an in-tyre sensor package will experience high strain variations even under free-rolling conditions. These strain ranges coupled with the cyclic endurance and temperature requirements raise questions about the survivability of in-tyre sensors. Further work is needed to fully characterise the internal stresses and strains in a rolling tyre under typical driving scenarios, such as acceleration/braking and cornering (slip and camber angle) conditions, and in specific sensors embedded in the tyre. The work presented here has suggested that magnitude of the internal strains tend to reduce through the tread depth since the reinforcing cords of the bandages and

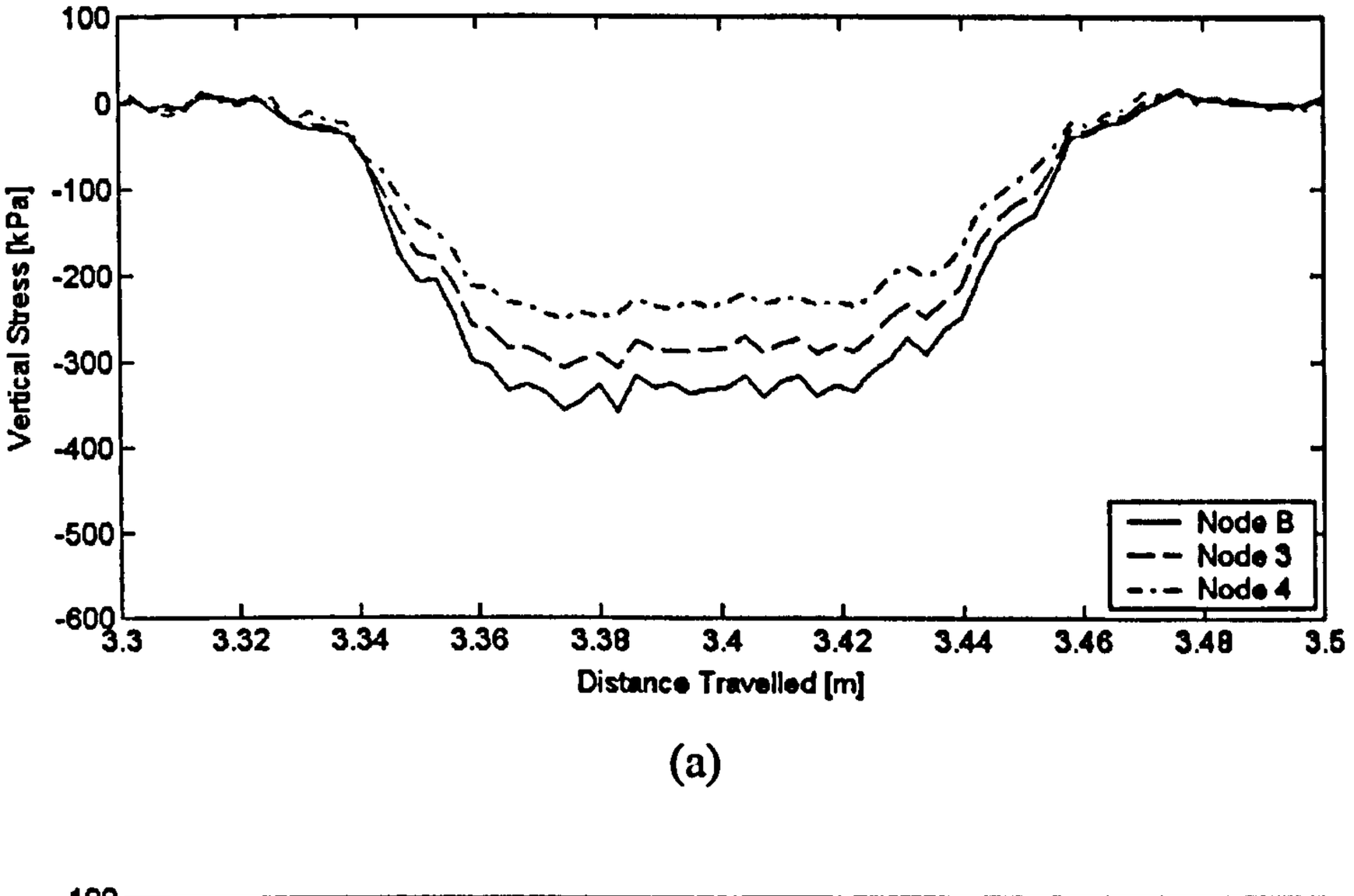

(a)

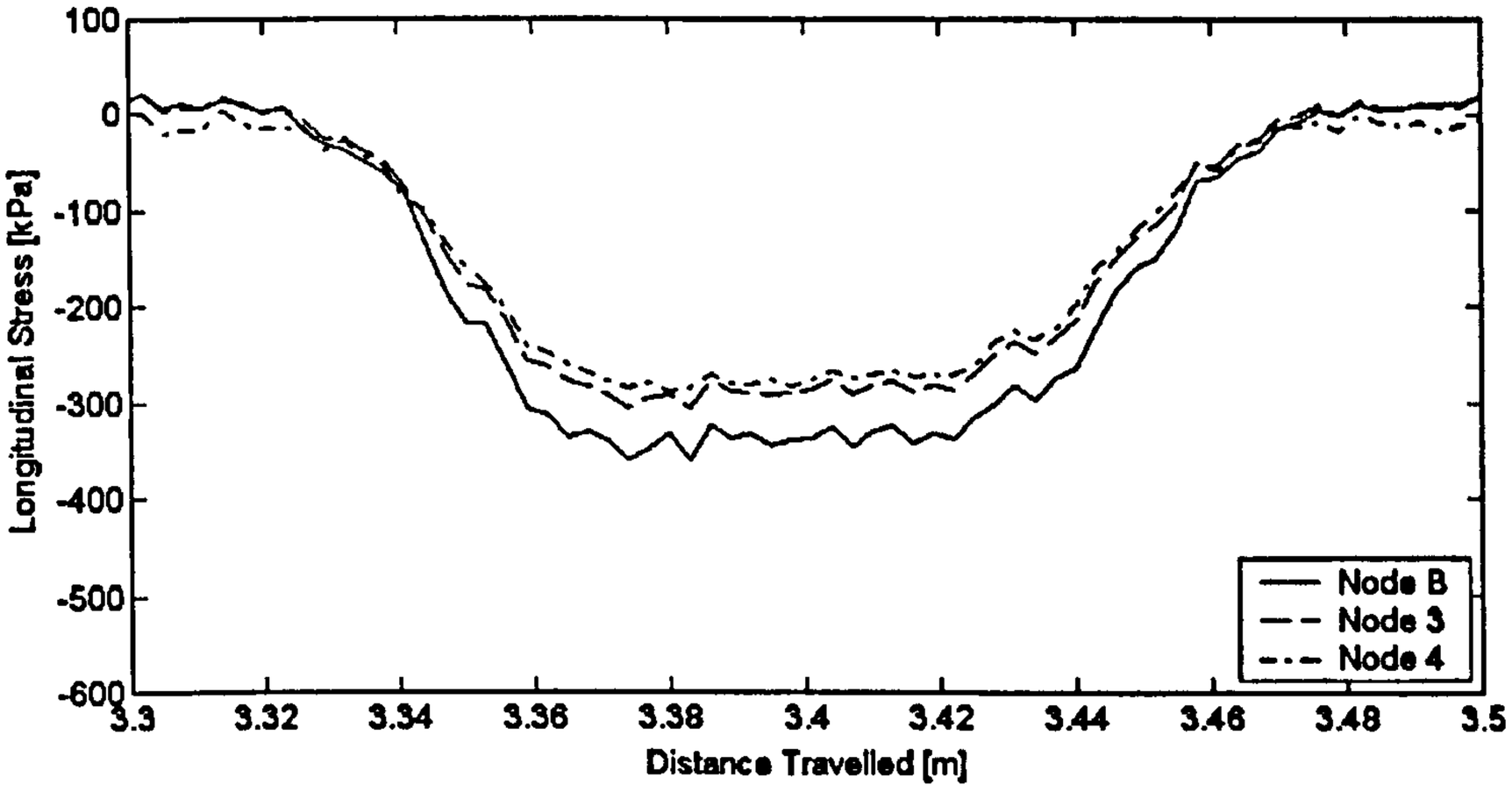

(b)

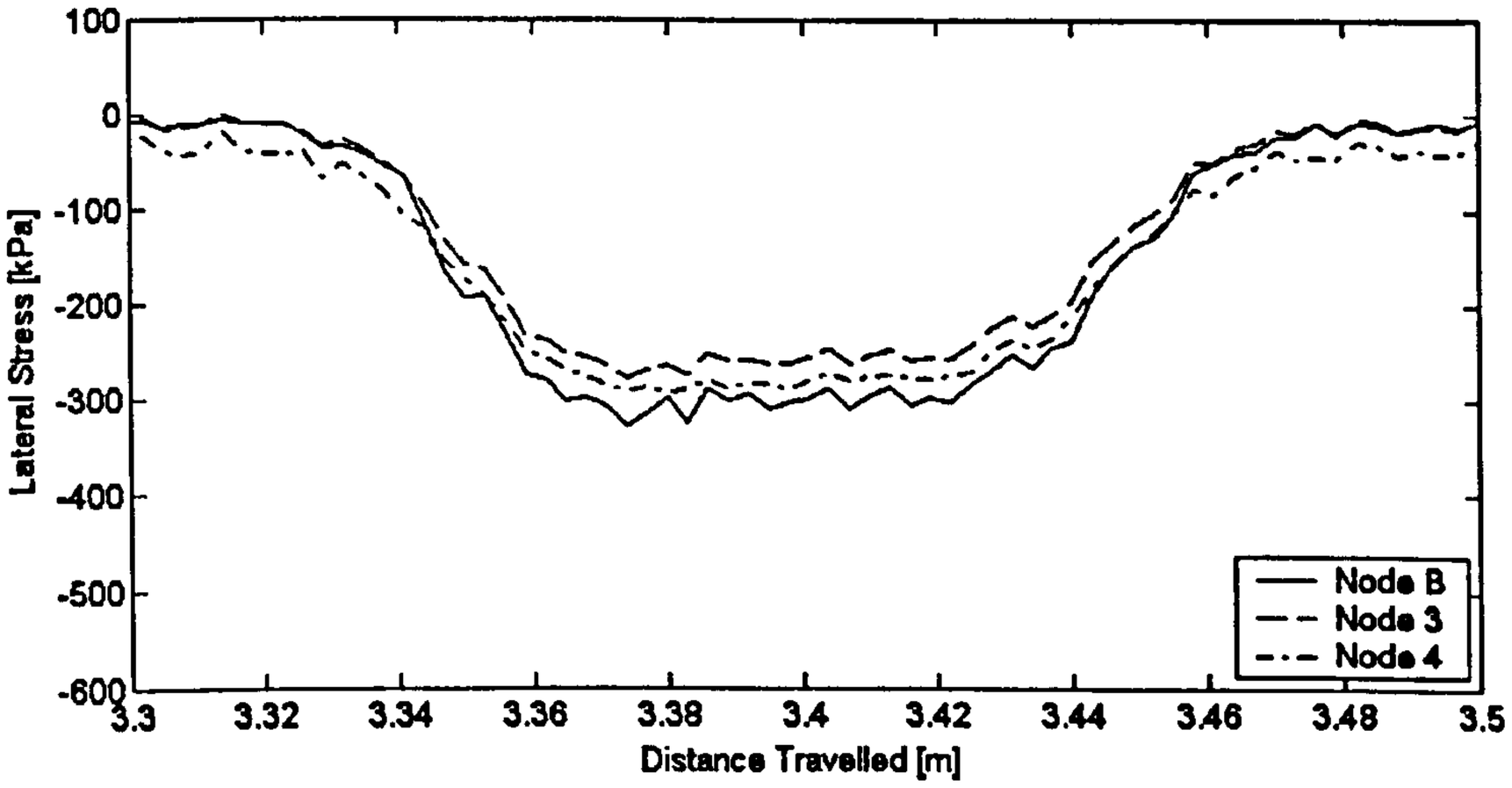

(c)

Figure 6.10 Simulated internal stress distributions at lateral coordinate of +30 mm with a normal load of 3 kN and a velocity of 20 km/h: (a) vertical; (b) longitudinal; (c) lateral

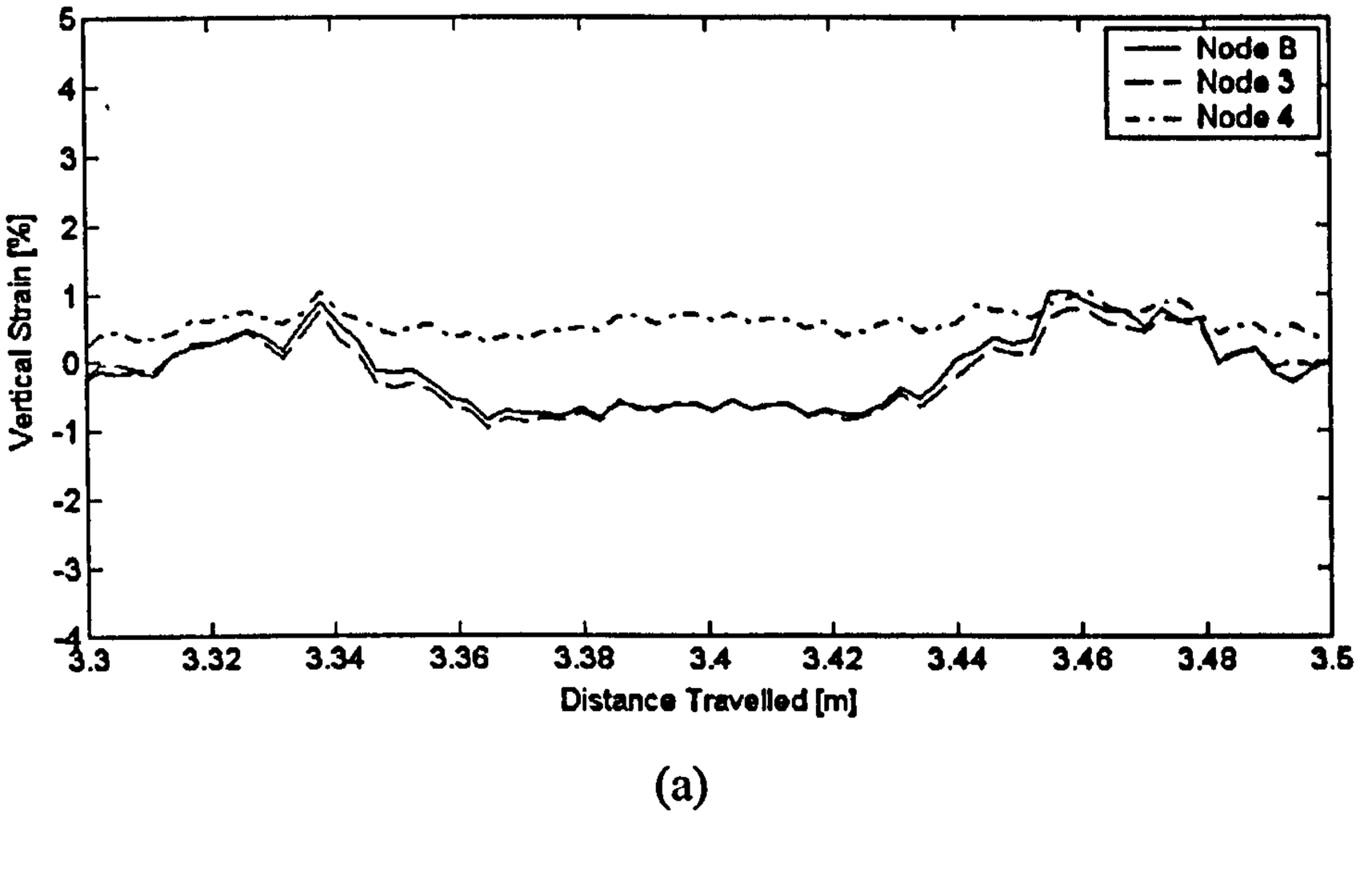

(a)

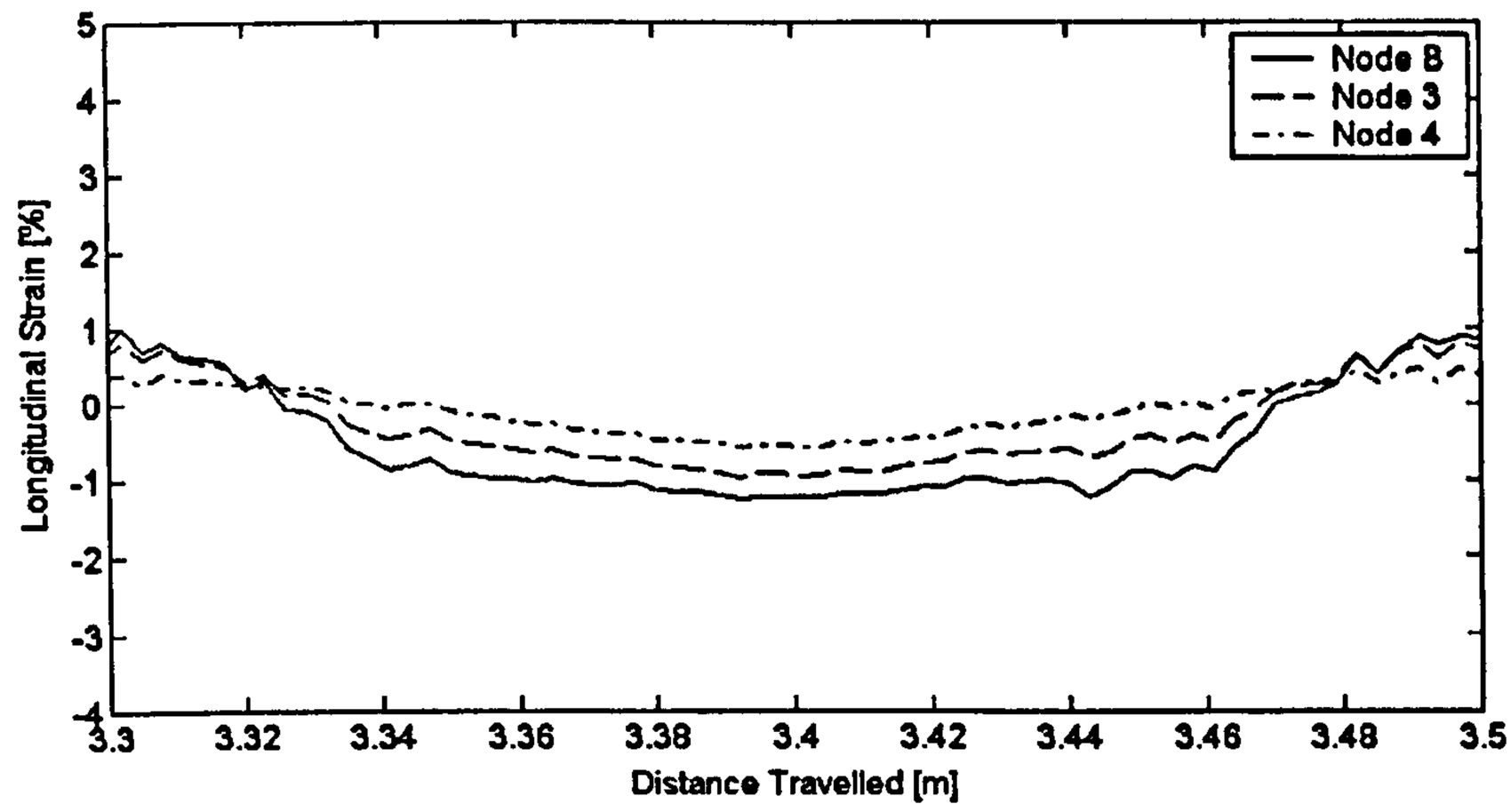

(b)

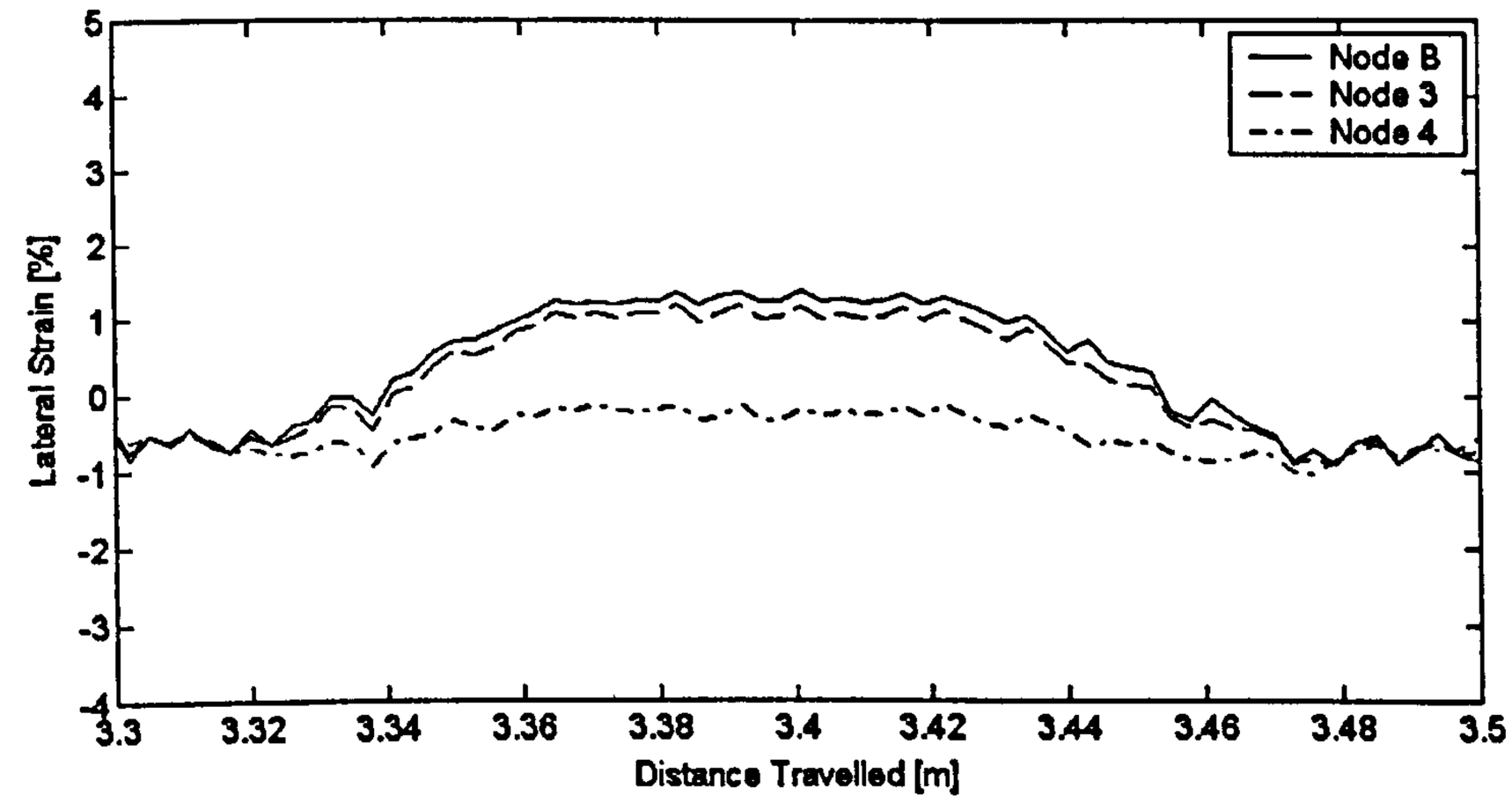

(c)

Figure 6.11 Simulated internal strain distributions at lateral coordinate of +30 mm with a normal load of 3 kN and a velocity of 20 km/h: (a) vertical; (b) longitudinal; (c) lateral

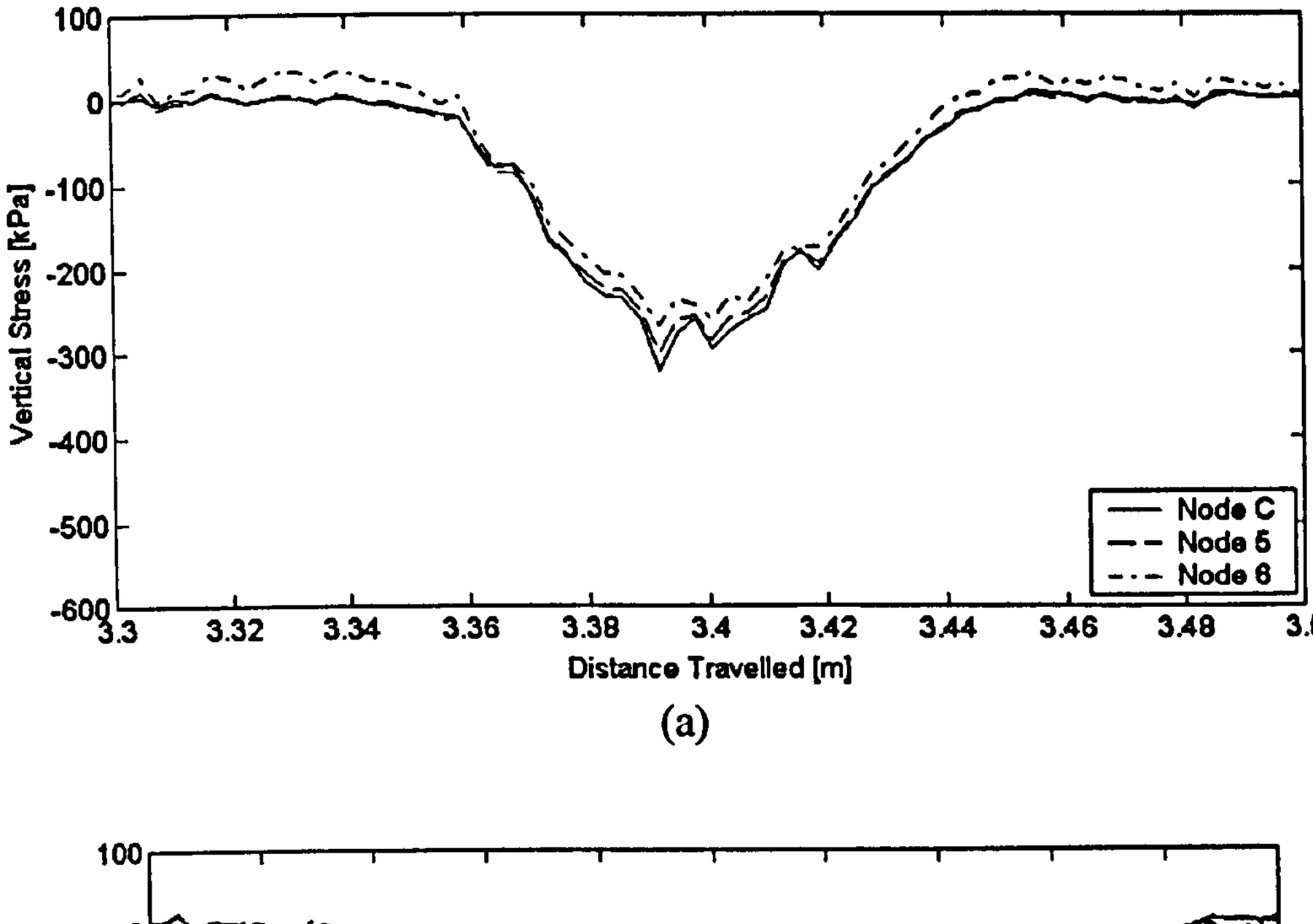

(a)

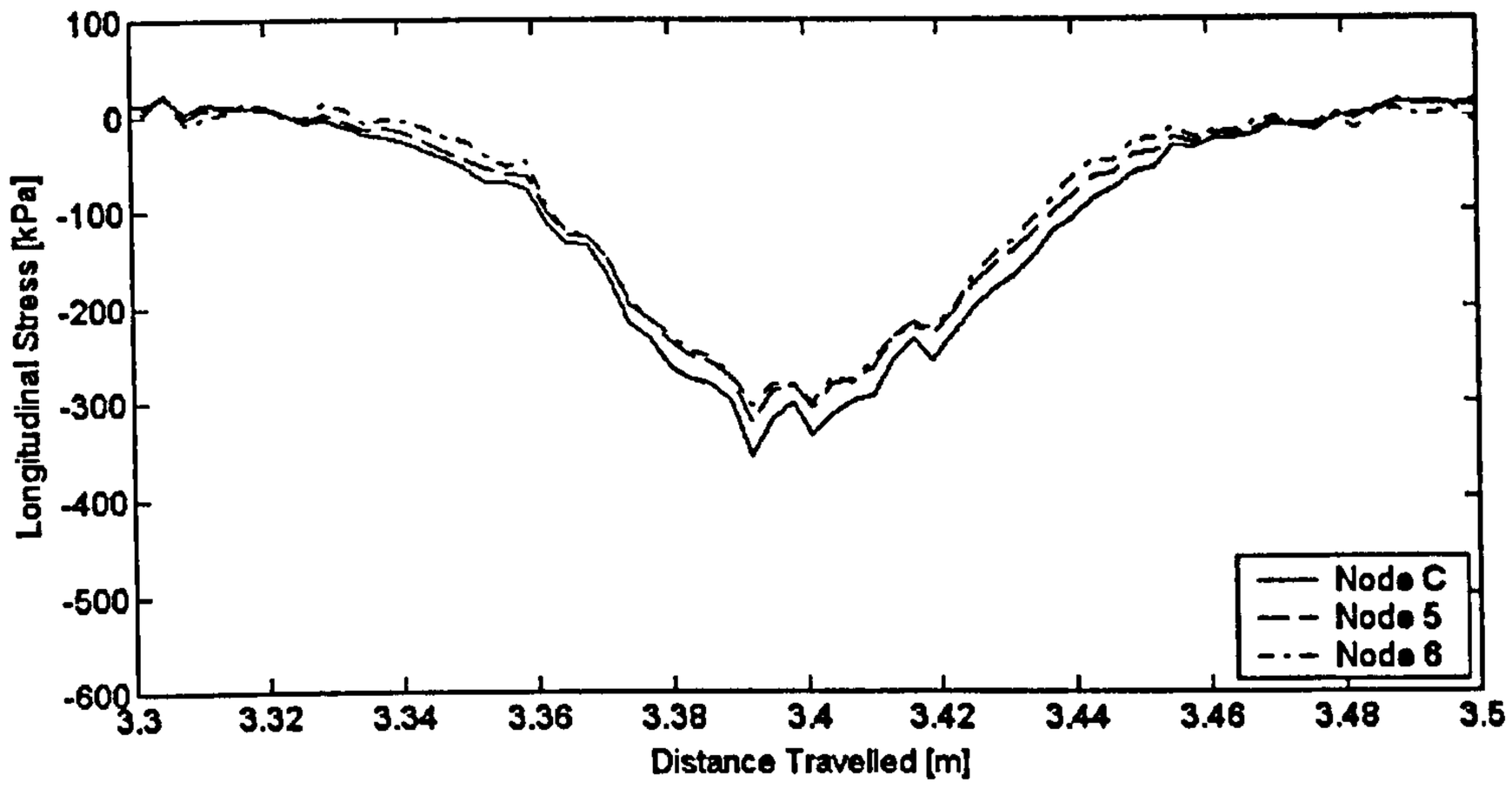

(b)

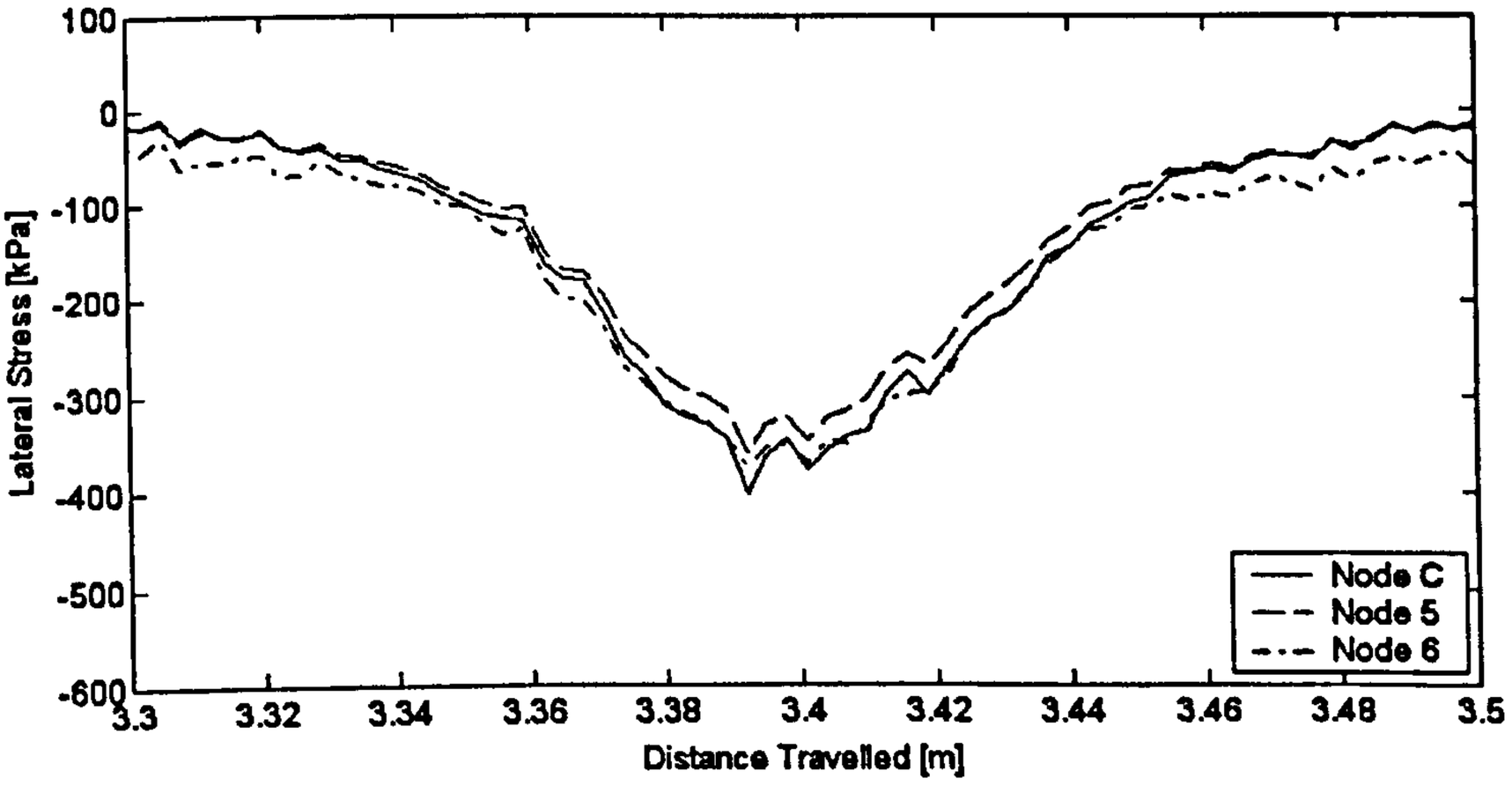

(c)

Figure 6.12 Simulated internal stress distributions at lateral coordinate of +55 mm with a normal load of 3 kN and a velocity of 20 km/h: (a) vertical; (b) longitudinal; (c) lateral

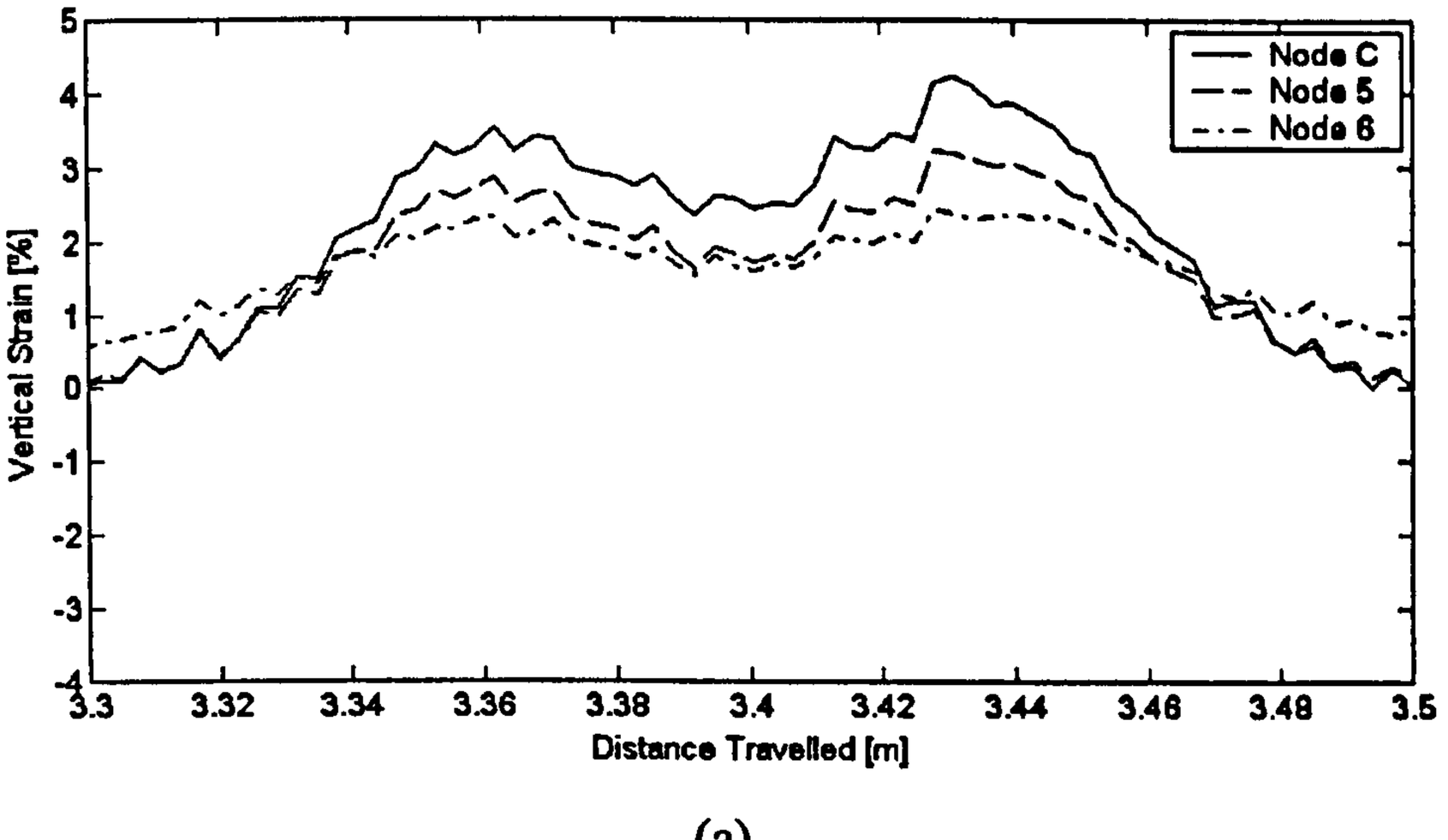

(a)

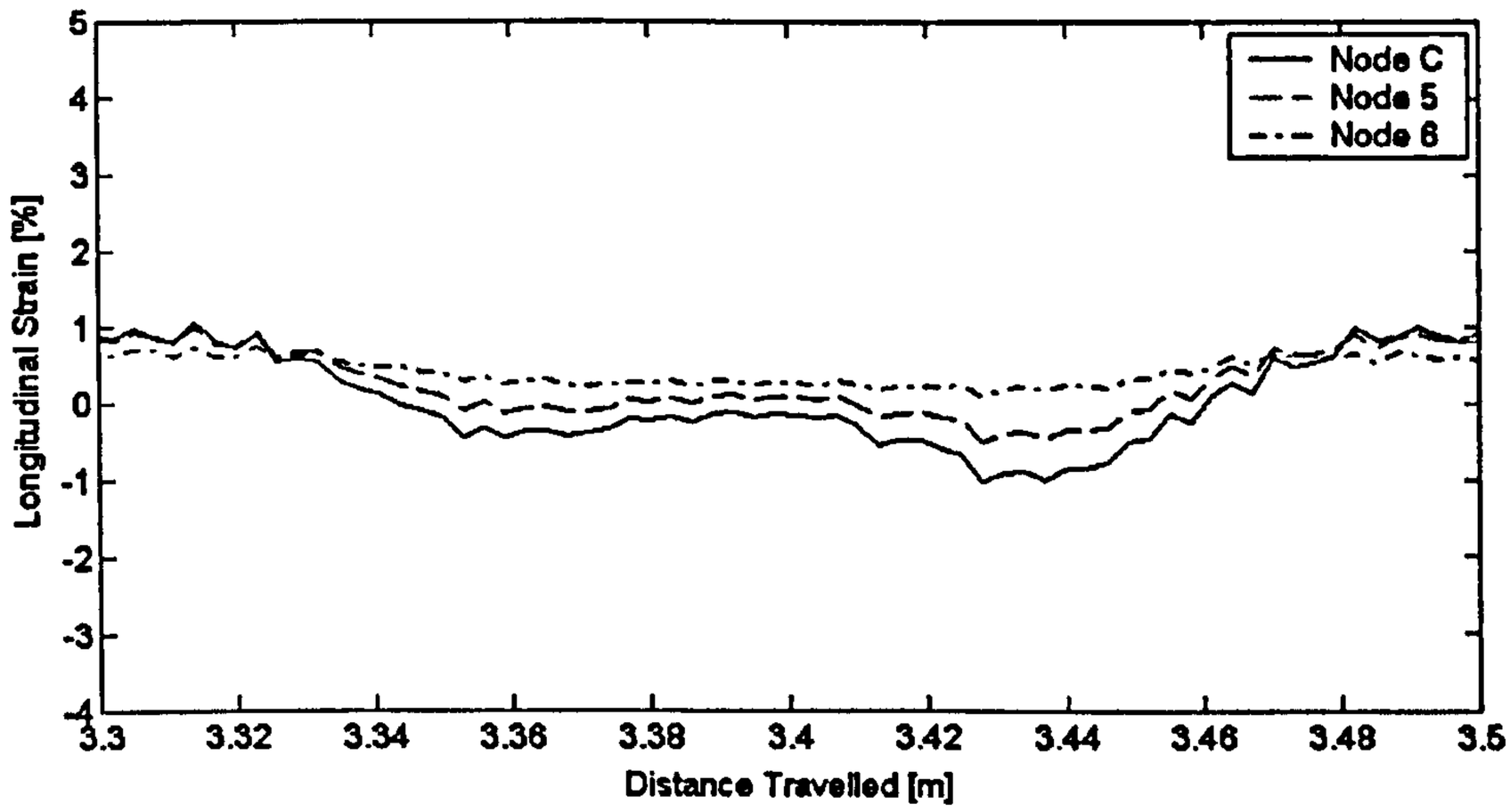

(b)

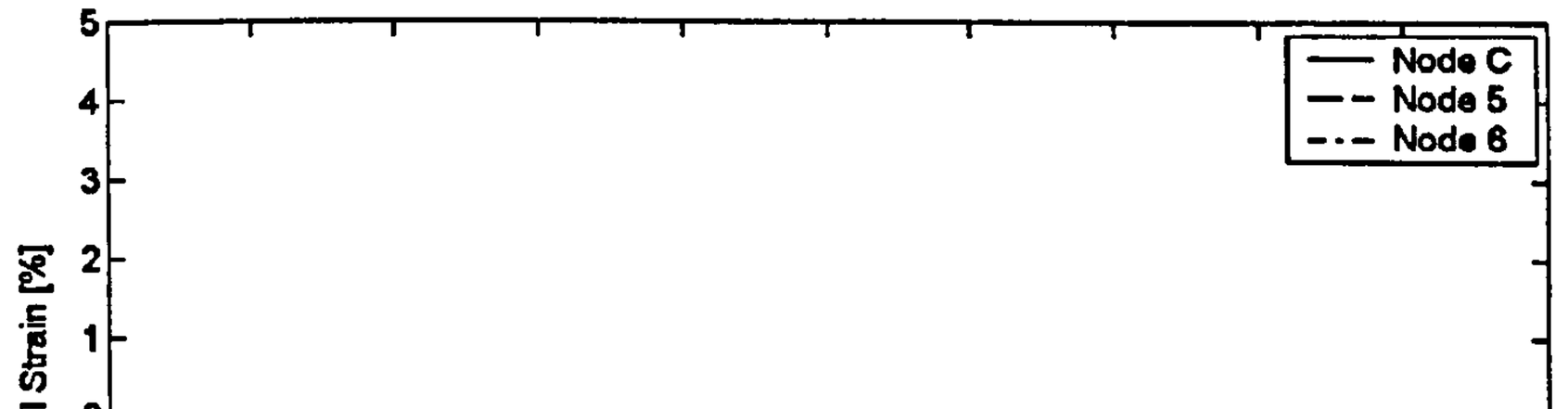

(c)

Figure 6.13 Simulated internal strain distributions at lateral coordinate of +55 mm with a normal load of 3 kN and a velocity of 20 km/h: (a) vertical; (b) longitudinal; (c) lateral

Node Number	Strain Ranges (Max/Min) [%]			Height Position [mm]
	Vertical	Longitudinal	Lateral	
1	0.1/-1.3	0.7/-1.5	1.3/-0.2	5
2	0.7/-0.8	0.3/-0.9	0.7/0.2	10
3	0.8/-0.9	0.8/-1.0	1.2/-0.8	5
4	1.0/0.2	0.5/-0.6	-0.1/-0.9	10
5	3.2/0.1	1.0/-0.5	-1.0/-3.0	5
6	2.5/0.5	0.8/0.1	-1.0/-2.6	10

Table 6.1 Simulated internal strain ranges

breakers stiffen the local region. The results also suggest that the strains are higher near the tyre shoulders. Based on this information, it is postulated that consideration should be given to positioning in-tyre sensors near to, or in, the belt. By doing so, the author believes the strains experienced by in-tyre sensors could be within acceptable levels.

6.9 Summary

Rolling tyre experiments on the flat bed and rolling drum machines (see Chapter 3) have been simulated using LS-DYNA version 950d. These were found to experience numerical instabilities which have been related to imperfections inherent in the code. The flat bed simulation was successfully repeated using the current release, version 960. Inconsistencies were highlighted in simulation results observed using the two versions and these have been investigated. Based on the results it has been concluded that these inconsistencies do not undermine the earlier model validation work carried out using version 950d. The contact stresses obtained using the current release have been compared with a reasonable degree of success to those found in full-scale physical tests. The internal stresses and strains in the tyre structure have then been extracted at selected positions local to the contacting surface. By doing so, the chapter provides valuable information to the tyre engineer wishing to develop robust in-tyre sensors. The results suggest that the most appropriate position for in-tyre sensors is near to, or in the belt.

Chapter 7 Review, Conclusions and Recommendations for Further Work

The automobile tyre is often considered to be a simple and reliable component of a vehicle. A closer inspection, however, shows that the tyre is subjected to severe stresses and deformation whose quantities must be determined in order to accurately predict tyre behaviour. The aim of this thesis was to provide an initial investigation into the internal stresses and strains in a rolling tyre via numerical simulation. An understanding of internal tyre behaviour is essential to aid the development of 'smart' tyre technologies. Tyres play a crucial role in the support of vehicle dynamics and the integration of in-tyre sensors could allow the contact patch stresses to be monitored in each tyre under motion. Thus, the tyre could become a key sensor in future vehicle control technology.

7.1 Thesis Review

The thesis is broadly categorised into three main areas: a review of the relevant tyre research literature; an experimental investigation into the contact patch behaviour of an automobile tyre; and a Finite Element (FE) modelling investigation using LS-DYNA.

The review of the literature carried out in Chapters 1 and 2 set the background to the work, and also highlighted the lack of knowledge on contact patch stress distributions and the absence of existing models to simulate this behaviour. Chapter 3 described physical tests conducted on an experimental automobile tyre. The results have provided a better understanding of the physical behaviour of tyres in the contact patch. The measurements also provided a valuable source of data that can be used to validate the modelling methodology. Finally, and most crucially, Chapters 4 to 6 describe the investigation of macroscopic tyre behaviour via numerical simulation. The two LS-DYNA models described in Chapter 4 were developed to simulate the stationary (non-rolling) and rolling behaviour of the experimental tyre. Results from the models are presented in Chapters 5 and 6, and have been validated against the physical test data.

The internal stresses and strains in the tyre under free-rolling conditions (at 20 km/h) were characterised at several positions in the tread region. These numerical results have been discussed in context with the development of in-tyre sensor system technologics.

7.2 Experimental Investigation

Full-scale physical tests have been performed to characterise the behaviour of the stationary tyre under normal load, and the rolling tyre behaviour under free-rolling and cornering (slip and camber angle) conditions. The rolling experiments were carried out on flat bed and drum surfaces. The load-deflection characteristics and the contact patch dimensions of the experimental tyre have been discussed, and a reasonably complete picture is presented on how the normal and shear contact stresses might change under driving conditions. A comparison between the stress measurements obtained on the two surfaces has also been given. No similar comparison is reported in the literature and the investigation therefore provides unique measurements in relation to the interfacial stresses experienced by a rolling tyre on two geometrically different ground surfaces.

The normal and shear contact stress distributions exhibit distinct characteristics. The normal pressure at the front of the contact patch is higher than at the rear and, thus, the distribution is not symmetrical about the lateral axis. This is because a longitudinal force, usually referred to as the rolling resistance, exists at the tyre/ground interface. The maximum pressure on the flat bed exceeds the inflation pressure (200 kPa) by a factor of about 1.6, and a tyre 'buckling' effect is also evident at the centre of the contact area.

A sinusoidal-style sweep is observed in the longitudinal shear stress distribution. This is because there is a change in radius at the perimeter of the tyre tread. The rolling resistance is evident in this distribution as a difference in the magnitude of the maximum positive and negative stresses. The lateral shear stresses are shown to increase approximately linearly through the contact patch under slip angle conditions. At 2 degrees slip angle, the maximum stress was found to be 290 kPa on the horizontal surface (just below the maximum normal pressure measurement (320 kPa)). The magnitude of the lateral shear stresses at the same camber angle are significantly lower (<200 kPa) since the camber stiffness of the tyre is less than the cornering stiffness.

Normal pressures at the tyre/drum interface are higher than those experienced on the flat bed. The maximum value exceeds the inflation pressure by a factor between 1.75 and 2.25. This indicates the contact patch on the drum surface is smaller than on the horizontal surface. The longitudinal and lateral shear stresses are similar under free-rolling and camber angle conditions. Under slip angle conditions, the contact stresses on the drum surface differ considerably from those observed on the flat bed. The maximum pressure is much higher and the contact patch length (at the lateral tyre centre) increases with slip angle. This phenomenon has not previously been identified and no explanation is currently at hand. The lateral shear stresses on the drum surface are also higher. At 1 degree slip angle, the difference in the maximum shear stress is greater than three times.

7.3 Modelling and Simulation

The advanced FE models, developed to simulate macroscopic tyre behaviour, represent the structure as a rubber and reinforced rubber composite. Two-dimensional membrane elements have been used to model the fibre and steel reinforcements, and three-dimensional solid elements to represent the thick rubber sections. The behaviour of the reinforcements was simulated using the Halpin-Tsai equation and the rubber was modelled based on the Mooney-Rivlin strain energy function. The models have been developed for simulation using LS-DYNA and the model descriptions were created using HyperMesh. The models represent a distinct improvement from those described in the literature which have tended to be developed to simulate global tyre behaviour.

The rubber industry characterises the elastic behaviour of a compound based on the secant modulus. This method, combined with the reluctance of tyre manufacturers to release property data for their preferred compounds, had meant that material stress/strain data for rubber components was not easy to obtain. This issue has been addressed herein and a simple method has been developed to characterise the elastic constants of rubber materials used in a tyre. The method is based on the secant modulus of the rubber and on the stress/strain data for a typical tyre compound. It is validated by the numerical results and, as a consequence, is of particular interest to FE tyre analysts.

Other model simplifications, such as the assumptions that the elastic constants of the

reinforcing cords in the steel breakers (and also those of the beads) correspond to those of bulk steel, have been implemented because this mechanical property data was not available. Furthermore, the inflation pressure has been assumed to remain constant during typical tyre deflections. Tyre analysis is much more complex if inflation pressure variations due to volume changes are introduced. These simplifications have only a small influence on the numerical results and, thus, do not adversely effect the simulations.

The stationary (non-rolling) behaviour of the experimental tyre was successfully simulated. The normal load-deflection characteristics and the contact patch dimensions have been compared with a reasonable degree of success to those obtained in the full-scale physical tests. Consideration was given to the inflation of the tyre, the wheel fit and the normal loading of the tyre. Simulation results were also presented when a subsequent longitudinal or lateral load was applied. The longitudinal and lateral tyre stiffnesses appear to be realistically represented. The contact patch dimensions gave a good trend-wise agreement, but the length and width were found to be greater than the experimental measurements. A parametric study was carried out and this disparity is related to a deficiency in the performance of the contact algorithm. It is therefore observed that it far from straightforward to accurately predict contact patch behaviour and the internal stresses and strains in absolute terms. However, the good trend-wise agreement does suggest that the modelling methodology is capable of predicting internal responses which are related to the 'actual' tyre deformations at the contact patch.

To simulate the rolling tyre behaviour on flat bed and drum surfaces, in addition to developing modelling methodology to inflate the tyre, fit it to the wheel and apply the normal loading, it was necessary to consider accelerating the tyre to reach a desired constant velocity. Despite consideration of these salient modelling features, numerical instabilities were found to occur. These instabilities have been related to imperfections inherent in version 950d of the code. This version was, at the time (July 2001), the most up to date release. The current release is version 960 and it does not contain many of the imperfections in the earlier version. Thus, the flat bed simulation was repeated using the current release. The predicted contact patch stresses under free-rolling conditions have been presented and these are shown to exhibit similar characteristics to those evident in the experimental data. The internal stresses and strains have then been characterised at a several positions in the tread region. These stresses and strains are useful as an initial

guide to the location of in-tyre sensors. The 'actual' deformations experienced by a sensor will be influenced by its mechanical properties. The numerical results suggest that the tread could experience high strain ranges (>3 percent) even under free-rolling conditions. Such high ranges, coupled with the cyclic endurance and temperature requirements, raise questions about the survivability of in-tyre sensors. Furthermore, the simulation results suggest that consideration should initially be given to positioning the sensors near to, or in, the belt. The internal strain ranges can be more than halved as the distance form the contacting surface increases (and that from the stiff belt reduces).

7.4 Recommendations for Further Work

Attention has been drawn to the fact that there appears to be a lack of knowledge about tyre behaviour in the contact patch and therefore the internal stresses and strains in a rolling tyre. The research work presented in this thesis is therefore novel in nature and, hence, offers significant scope for further investigation. It is hoped that the models developed herein, together with the comprehensive experimental work, can be used to improve understanding of tyre behaviour and its relationship to vehicle dynamics.

The aim of the thesis was to provide an initial investigation of the internal stresses and strains in an automobile tyre via numerical simulation. This has been achieved for a tyre on a horizontal surface at a speed of 20 km/h under free-rolling conditions. Further simulations of rolling tyre behaviour have not been possible in this thesis due to the limitations in the available computational resource and also time constraints. The next logical step is to investigate the internal stresses and strains under typical driving conditions, i.e. at various normal loads, speeds, slip and camber angles and slip ratios, and on different surfaces. Such an investigation is needed to fully characterise the internal stress field in a tyre structure. This information would further aid the tyre engineer wishing to develop in-tyre sensors for monitoring tyre behaviour. The work could also progress to the investigation of stresses and strain experienced by specific in-tyre sensors. This would require the mechanical property data of the sensor package.

The contact and friction models employed herein have addressed the macroscopic characteristics at the tyre/ground and tyre/wheel interfaces via the Coulomb formulation. Since the main reason for the difference between the simulation results and those

observed experimentally is the performance of the contact algorithm used in the code, the issue of contact modelling is an obvious area for further consideration. The microscopic asperities in the ground surface have not been considered herein but may be important in the simulation of rolling resistance. Rolling resistance is known to be higher on rough than on smooth surfaces. Also important to the numerical rolling resistance characteristics is the assumed damping level. Damping was acceptably neglected in this thesis because rolling resistance effects are small (typically less than 50 N). Further work could be used to determine appropriate damping levels for simulating rolling resistance.

The experimental work presented in this thesis has addressed the lack of knowledge of contact patch behaviour for free-rolling and cornering (slip and camber) conditions. These studies could be extended to include acceleration/braking characteristics and also larger data ranges, and cross-contact patch measurements. This could be achieved via experimental measurements (or using the FE models). This thesis has considered small slip and camber angles, but these do not envelop the possible ranges experienced. Furthermore, the influence of speed on the contact stresses needs greater consideration.

Other obvious areas for future work are the simulation of rolling tyres on deformable surfaces such as mud, sand and snow, and the delamination effects of tyres. To simulate tyre behaviour on deformable surfaces would simply require a more detailed representation of the ground surface while the delamination effects could easily be incorporated into the current models. The interface between the adjoining components, and between the rubber matrix and reinforcements, could be modelled as separate contacts, with the nodes tied to the adjacent surface until a failure criterion was reached.

Finally, this rolling tyre study has been limited to the investigation of tyre behaviour under experimental situations represented in the laboratory. These simulation have not been influenced by tyre temperature variations because the tyre rolling experiments were carried out for only a short time period. This is a major consideration for tyres operating in 'real' driving conditions and, thus, must be considered as an area for further work.

References

1. *Road Accident Statistics*, Department of the Environment, Transport and the Regions, Great Britain, 1998.
2. W. Walton, 'The Potential Scope for the Application of Pollution Permits to Reducing Car Ownership in the UK - Some Preliminary Thoughts,' *Transport Policy*, Elsevier Science Inc., April 1997, Vol. 4, No. 2, pp. 115-122.
3. A. Dickerson, J. Peirson, R. Vickerman, 'Road Accidents and Traffic Flows: An Econometric Investigation,' *Economica*, Blackwell Publishing, February 2000, Vol. 67, No. 265, pp. 101-121.
4. *Vehicle Technology*, Department of the Environment, Transport and the Regions, Great Britain, 2002.
5. *Tomorrow's Roads: Safer for Everyone*, Department of Transport, Local Government and the Regions, Great Britain, 2002.
6. A. R. Williams and M. Evans, 'Tyre Technology: Future Developments,' *Materials World*, December 1995, pp. 588-591.
7. B. Castle, 'The Coming Revolution,' *Tire Technology International*, UK & International Press, March 2002, pp. 16-19.
8. T. D. Gillespie, *Fundamentals of Vehicle Dynamics*, Society of Automotive Engineers Inc., 1992.
9. D. J. Dennehy, *Drive-by-Tyre: Investigating the Feasibility of Improving Vehicle Dynamics Control by Measurements made at the Tyre/Ground Interface*, MSc Thesis, University of Warwick, United Kingdom, 2002.
10. W. F. Milliken and D. L. Milliken, *Race Car Vehicle Dynamics*, Society of Automotive Engineers Inc., 1995.
11. W. R. Pasterkamp and H. B. Pacejka, 'The Tyre as a Sensor to Estimate Friction,' *Vehicle System Dynamics*, Vol. 27, 1997, pp.409-422.
12. W. R. Pasterkamp, 'Tires as Sensors,' *Tire Technology International*, UK & International Press, June 1999, pp. 33-35.

13. T. Bachmann and B. Breuer, 'Research at the Tire to Road Interface at Darmstadt University,' *Progress in Rubber and Plastics Technology*, Vol. 12, 1996, pp. 153-173.
14. V. Bachmann, M. Fach and B. Breuer, 'Future Car-Tires as Provider of Information for Vehicle Systems to Enhance Primary Safety,' Society of Automotive Engineers Inc., *SAE Paper 981944*, 1998, pp. 1878-1884.
15. T. Becherer, 'Brain of the Road,' *Tire Science and Technology*, UK & International Press, December 1998, pp. 23-26.
16. F. Dollinger, 'Sensors reveal the Secrets of Car Tires,' *Physics World*, January 2001, pp. 22.
17. J. O. Hallquist, *LS-DYNA Theoretical Manual*, Livermore Software Technology Corporation, 1998.
18. J. W. Wong, *Theory of Ground Vehicles*, Third Edition, John Wiley & Sons Inc., 2001.
19. V. E. Gough, 'Structure of the Tire', *Mechanics of Pneumatic Tires*, S. K. Clarke ed., US Department of Transportation, DOT-HS-805-952, Washington D.C., USA, 1981, pp. 203-249.
20. *Vehicle Dynamics Terminology*, SAE J670e, Society of Automotive Engineers Inc., 1978.
21. W. E. Meyer and H. W. Kummer, 'Mechanism of Force Transmission Between Tire and Road,' Society of Automotive Engineers Inc., *Paper 620407(490A)*, 1962, pp.325-336.
22. D. L. Nordeen and A. D. Cortese, 'Force and Moment Characteristics of Rolling Tires,' Society of Automotive Engineers Inc., *SAE Transactions*, Vol. 72, 1964, pp. 325-336.
23. M. DeBeer, 'Paving the Way,' *Tyre Technology International 2000*, UK & International Press, 2000, pp. 30-36.
24. J. D. Walter and F. S. Conant, 'Energy Losses in Tires,' *Tire Science and Technology*, Vol. 2, 1974, pp. 235-260.
25. S. K. Clarke, R. N. Dodge, R. J. Ganter and J. R. Luchini, 'Rolling Resistance of Pneumatic Tires,' Interim Report No. DOT-TSC-OST-74-33, US Department of Transportation, Washington D.C., USA, 1975.
26. J. D. Hunt, J. D. Walter and J. L. Hall, 'The Effect of Tread Polymer Variations on Radial Tire Rolling Resistance,' *Tire Rolling Losses and Fuel Economy - An*

R & D Planning Workshop, Society of Automotive Engineer, Special Publication P-74, 1977, pp. 161-168.

27. L. W. DeRadd,' The Influence of Road Surface Texture on Tire Rolling Resistance,' *Tire Rolling Losses and Fuel Economy - An R & D Planning Workshop*, Society of Automotive Engineers Inc., Special Publication P-74, 1977, pp. 143-149.
28. B. L. Collier and J. L. Warchol, 'The Effect of Inflation Pressure on Bias, Bias-Belted and Radial Tire Performance,' Society of Automotive Engineers Inc., *SAE Paper 800087*, 1980, pp. 552-563.
29. V. I. Novopol'skii and E. F. Nepomnyashchii, The Interaction of a Motor Vehicle Tyre Tread with the Road Surface,' D. I. James ed., Palmerton Publishing Co., New York.
30. G. Bode, 'Krafte und Bewegungen unter rollenden Lastwagenreifen,' *A. T. Z*, Vol. 64, No. 10, 1962, pp. 300-306.
31. A. Browne, K. C. Ludema and S. K. Clarke, 'Contact Between Tyre and Roadway,' *Mechanics of Pneumatic Tires*, S. K. Clarke ed., US Department of Transportation, DOT-HS-805-952, Washington D.C., USA, 1981, pp. 249-364
32. H. B. Pacejka and R. S. Sharp, 'Shear Force Development by Pneumatic Tyres in Steady State Conditions: A Review of Modelling Aspects,' *Vehicle System Dynamics*, Vol. 20, 1991, pp. 121-176.
33. H. Dugoff, P. S. Fancher and L. Segel, 'An Analysis of Tire Traction Properties and their Influence on Vehicle Dynamic Performance,' *SAE Paper 7003077*, 1970, pp. 1219-1243.
34. E. Bakker, L. Nyborg and H. B. Pacejka, 'Tire Modelling for use in Vehcile Dynamics Studies,' Society of Automotive Engineers Inc., *SAE Paper 870421*, 1987, pp. 101-113.
35. J. R. Ellis, *Vehicle Handling Dynamics*, Mechanical Engineering Publications, 1994.
36. R. D. Ervin, *The State of Knowledge Relating Tire Design to those Traction Properties which may Influence Vehicle Safety*, The University of Michigan Transport Research Institute, USA, Report No. UH-HSRI-78-31, 1978.
37. H. Dugoff and B. J. Brown, 'Measurement of Tire Shear Forces,' *SAE Paper 700092*, 1970, pp. 316-324.

38. V. E. Gough, 'Practical Tyre Research,' Society of Automotive Engineers Inc., *SAE Transactions*, Vol. 64, 1956, pp. 310-318.

39. S. A. Lippmann and K. L. Oblizajek, 'The Distribution of Stress Between Tread and the Road for Freely Rolling Tires,' Society of Automotive Engineers Inc., *SAE Paper 740072*, 1974, pp. 339-369.

40. J. S. Loeb, D. A. Guenther, H. H. Chen and J. R. Ellis, 'Lateral Stiffness, Cornering Stiffness and Relaxation Length of the Pneumatic Tire,' *SAE Paper 900129*, 1990, pp. 147-155.

41. P. W. A. Zegelaar, *The Dynamic Response of Tyres to Brake Torque Variations and Road Unevennesses*, Delft University of Technology, Netherlands, 1998.

42. T. W. Chu, *Eigenstructure Analysis of Automobile Steering Dynamics with Application to Robust Four-Wheel-Steering Control*, University of Warwick, UK, 2001.

43. L. Segel, 'The Mechanics of Heavy-Duty Truck Tires and Truck Combinations,' Engineering Summer Conferences, University of Michigan, Ann Arbor, USA, 1998.

44. M. V. Blundell, 'The Modelling and Simulation of Vehicle Handling Part 3: Tyre Modelling,' *Journal of Multi-Body Dynamics*, Vol. 214, No. 1, 2000, pp. 1-32.

45. J. E. Bernard, L. Segel and R. E. Wild, 'Tire Shear Force Generation During Combined Steering and Braking Maneuvers,' Society of Automotive Engineers Inc., *SAE Paper 770852*, 1977, pp.2953-2969.

46. P. S. Fancher and Z. Bareket, 'Including Roadway and Tread Factors in a Semi-Empirical Model of Truck Tyres,' *Vehicle System Dynamics*, Vol. 21, No. Supplement, 1991, pp. 92-107.

47. H. B. Pacejka and E. Bakker, 'The Magic Formula Tyre Model,' *Vehicle System Dynamics*, Vol. 21, No. Supplement, 1991, pp. 1-18.

48. H. B. Pacejka and I. J. M. Basselink, 'Magic Formula Tyre Model with Transient Properties,' *Vehicle System Dynamics*, Vol. 27, No. Supplement, 1997, pp. 234-249.

49. H. Sakai, 'Study on Cornering Properties of Tire and Vehicle,' *Tire Science Technology*, Vol. 18, No. 3, 1990, pp. 136-169.

50. J. J. M. van Oosten and E. Bakker, 'Determination of Magic Formula Tyre Parameters,' *Vehicle System Dynamics*, Vol. 21, No. Supplement, 1991, pp. 19-29.

51. D. J. Schuring, W. Peiz and M. G. Pottinger, 'The BNPS Model - An automated Implementation of the "Magic Formula" Concept,' Society of Automotive Engineers Inc., *SAE Paper 931909*, pp. 1-11.

52. M. Durand and E. Jankovich, 'Nonapplicability of Linear Finite Element Programs to the Stress Analysis of Tires,' *Nastran Users Experiences Second Colloquium*, Langley Research Centre, USA, 1972.

53. R. H. Kennedy, H. P. Patel and M. S. McMinn, 'Radial Truck Tire Inflation Analysis - Theory and Experiment,' *Rubber Chemistry and Technology*, Vol. 54, 1981, pp. 751-766.

54. M. J. Trinko, 'Ply and Rubber Stress and Contact Forces for a Loaded Radial Tire,' *Tire Science and Technology*, Vol. 11, Nos. 1-4, 1984, pp. 20-38.

55. G. Laging and H. Rothert, 'Numerical Results of Tire-Test Drum Interaction,' *Tire Science and Technology*, Vol. 14, No. 3, 1986, pp. 160-175.

56. M. Hashimoto, H. Yoshinaga, H. Yoshikawa, N. Morikawa, T. Uekusa and S. Asai, 'Three-Dimensional Finite Element Analysis of Loaded Tires,' *NEC Research and Development*, Vol. 35, No. 4, 1994, pp. 477-487.

57. B. G. Koa and M. Muthukrishnan, 'Tire Transient Analysis with an Explicit Finite Element Program,' *Tire Science and Technology*, Vol. 25, No. 4, 1997, pp. 230-244.

58. A. Kamoulakas and B. G. Koa, 'Transient Dynamics of a Tire Rolling over Small Obstacles - A Finite Element Approach with Pam-Shock,' *Tire Science and Technology*, Vol. 26, No. 2, 1998, pp. 84-108.

59. R. Hanley, 'Impact Model,' *Tire Technology International 2000*, UK & International Press, 2000, pp. 24-28.

60. M. Koishi, K. Kabe and M. Shiratori, 'Tire Cornering Simulation using an Explicit Finite Element Analysis Code,' *Tire Science and Technology*, Vol. 26, No. 2, pp. 109-119.

61. H. Rothert and R. Gall, 'On the Three Dimensional Computation of Steel-Belted Tires,' *Tire Science and Technology*, Vol. 14, No. 2, 1986, pp. 116-124.

62. J. T. Mottram and C. T. Shaw, *Using Finite Elements in Mechanical Design*, McGraw-Hill, 1996.

63. R. A. Ridha, 'Analysis of Pressurised Composite Shells Deflected Against Rigid Flat Surfaces,' *Symposium of Applications of Computer Methods in Engineering*, Vol. II, 1977, pp. 1075-1083.

64. R. Gall, F. Tabaddor and D. Robbins, 'Some Notes on the Finite Element Analysis of Tires,' *Tire Science and Technology*, Vol. 23, No. 3, 1995, pp. 175-188.

65. A. A. Becker, *Understanding Non-Linear Finite Element Analysis Through Illustrative Benchmarks*, NAFEMS Ltd., 2001.

66. M. A. Crisfield, *Non-Linear Finite Element Analysis of Solids and Structures*, John Wiley & Sons Ltd., 1991.

67. R. D. Jones and M. D. Kemp, 'An Overview of Explicit Finite Element Technology in Industry,' *Benchmark*, NAFEMS Ltd., October 1999, pp. 8-12.

68. P. Jacob and L. Goulding, *An Explicit Finite Element Primer*, NAFEMS Ltd., 2002.

69. T. Belytschko, W. K. Liu and B. Moran, *Nonlinear Finite Elements for Continua and Structures*, John Wiley & Sons Ltd., 2000.

70. D. J. Dennehy, R. P. Jones and J. T. Mottram, 'Foresight Vehicle: Drive by Tyre,' Society of Automotive Engineers Inc., *SAE 2002 World Congress*, Paper 2002-01-1872, Arlington, Virginia, USA, June 2002.

71. MATLAB version 5.3, The MathWorks Inc. (http://www.mathworks.com)

72. V. E. Gough, 'Tyres and Air Suspension,' *Advances in Automobile Engineering*, G. H. Tidbury ed., Pergamon Press, 1963, pp.59-91.

73. S. P. Timoshenko and J. N. Goodier, *Theory of Elasticity*, Third Edition, McGraw-Hill Book Company, 1982.

74. D. J. Dennehy, R. P. Jones and K. Hardy, 'Experimental Investigation of the Tyre/Ground Contact Patch Behaviour of an Automobile Tyre,' *IoM International Rubber Conference*, Birmingham, United Kingdom, June 2001, pp. 102-117.

75. N. Seitz and A. W. Hussman, 'Forces and Displacements in Contact Area of Free Rolling Tires,' Society of Automotive Engineers Inc., *SAE Paper 710626*, 1971, pp. 2323-2329.

76. S. A. Lippmann, 'Effects of Tire Structure and Operating Conditions on the Distribution of Stress Between the Tread and Road,' *The Tire Pavement Interface*, M. G. Pottinger and T. J. Yager ed., ASTM Special Technical Publication 929, 1985, pp. 91-109.

77. HyperMesh version 4.0, Altair Engineering, 2001. (http://www.altair.com/)

78. H. Kaga, K. Okamoto and Y. Tozawa, 'Stress Analysis of a Tire Under Vertical Load by a Finite Element Method,' *Tire Science and Technology*, Vol. 5, No. 2, 1977, pp. 102-118.

79. N. T. Tseng, R. G. Pelle, J. P. Chang and T. C. Warholic, 'Finite Element Simulation of Destructive Tire Testing,' *Tire Science and Technology*, Vol. 19, No. 1, 1991, pp. 2-22.

80. L. O. Faria, J. T. Oden, B. Yavari, W. W. Tworzydlo, J. M. Bass, E. B. Becker, 'Tire Modelling by Finite Elements,' *Tire Science and Technology*, Vol. 20, No. 1, 1992, pp. 33-56.

81. T. Dutton, Ove Arup & Partners, Private communication, December 2002.

82. T. Belytschko and C. S. Tsay, 'Explicit Algorithms for Nonlinear Dynamics of Shells,' *ASME*, AMD-Vol. 48, 1981, pp. 209-231.

83. T. Belytschko, J. Lin and C. S. Tsay, 'Explicit Algorithms for Nonlinear Dynamics of Shells,' *Computer Methods in Applied Mechanics and Engineering*, Vol. 42, 1984, pp. 225-251.

84. A. Lewis, 'Who's Blaming Whom?,' *Tire Technology International*, UK & International Press, June 2001, pp. 28-31.

85. R. N. Datta and F. A. A. Ingham, 'Improved Dynamic Properties in Truck and Off-the-Road Tyres,' *IoM International Rubber Conference*, Birmingham, United Kingdom, June 2001, pp. 484-495.

86. R. L. G. Treloar, *The Physics of Rubber Elasticity*, Third Edition, Clarendon Press, 1975.

87. S. Jerrams, 'An Introduction to the Physical Properties of Rubber,' Materials Failure Analysis (module 305PMS) course notes, Coventry University, 1999.

88. C. Lee, J. W. Kim, J. O. Hallquist, Y. Zhang and A. D. Farahani, 'Validation of a FEA Tire Model for Vehicle Dynamic Analysis and Full Vehicle Real Time Proving Ground Simulations,' *SAE Paper 971100*, 1997, pp. 1-8.

89. E. Kreyszig, *Advanced Engineering Mathematics*, Eighth edition, John Wiley & Sons Inc., 1999.

90. N. Nock, Dunlop Tyres Limited, Private Communication, January 2002.

91. D. Hull and T. W. Clyne, *An Introduction to Composite Materials*, Second Edition, Cambridge University Press, 1996.

92. A. Konter, *How to - Undertake a Contact and Friction Analysis*, NAFEMS Ltd., 2000.

93. T. M. Kenny, R. A. Stechschulte, 'Application of Finite Element analysis in Tire Design,' *Tire Science and Technology*, Vol. 16, No. 2, 1988, pp. 96-117.

94. D. H. Bacon and R. C. Stephens, *Mechanical Technology*, Second Edition, Butterworth-Heinemann Ltd., 1990.

95. T. Dutton, Ove Arup & Partners, Private Communication, June 2002.

96. B. Walker, Ove Arup & Partners, Private Communication, July 2001.

97. K. Hardy, Dunlop Tyres Limited, Private Communication, December 2000.

98. J. M. Kennedy, KBS2 Inc., Private Communication, February 2002.

99. T. Dutton, Ove Arup & Partners, Private Communication, October 2002.

100. *Version 8.1 Update and Release Notes*, Ove Arup & Partners, May 2001.

101. *Version 8.2 Update and Release Notes*, Ove Arup & Partners, February 2002.

102. *Student Manual for Strain Gage Technology*, Measurement Group Inc., 1991.

103. G. J. Tomka, S. Eaton, J. Milne, W. HALL, R. P. Jones and J. T. Mottram, 'Foresight Vehicle: Smarter Tires using Advance Sensors For Improved Safety', Society of Automotive Engineers Inc., *SAE 2002 World Congress*, Paper 2002-01-1871, Arlington, Virginia, USA, June 2002.

104. G. J. Tomka, J. Milne, J. Gore, M. Maylin, P. T. Squire and S. Atalay, 'Properties and Applications of Soft Magnetic Materials,' *UK Magnetics Society Meeting*, May 2001.

Appendix A Cross-Coupling Effects in the Longitudinal and Lateral Shear Stresses

In the rolling tyre experiments (see Chapter 3), the shear stresses exerted on the ground surface were measured in the transducer axes (X-, Y-) and not the tyre axes (x-, y-). As discussed in Section 3.6.2, applying a slip angle changes the orientation of the tyre axes relative to the transducer axes and a cross-coupling effect occurs. This is shown in Figure A.1. Thus, the longitudinal τ_{xz} and lateral τ_{xy} shear stresses need to be resolved.

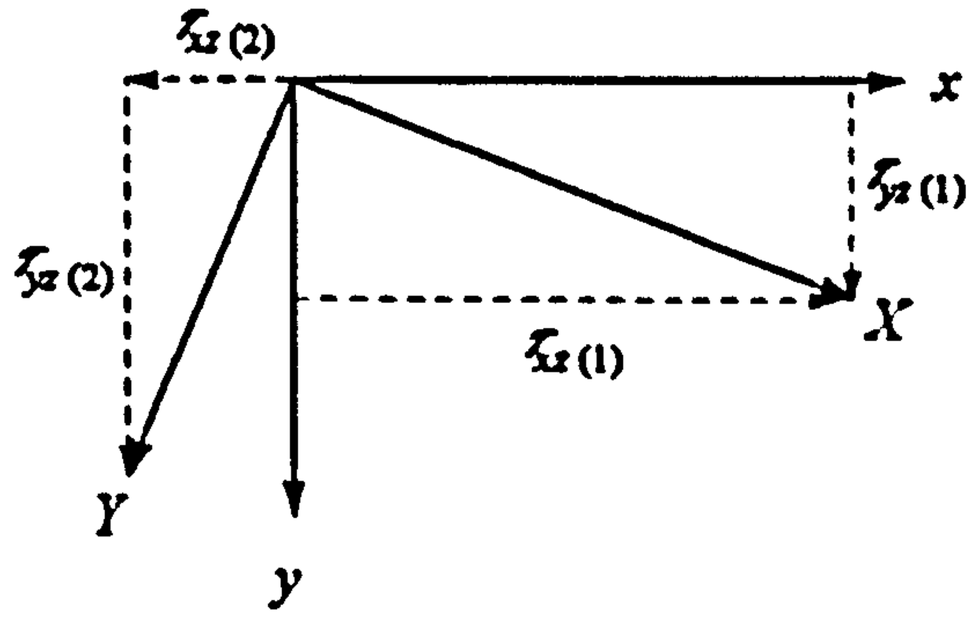

Figure A.1 Longitudinal and lateral shear stress cross-coupling

The shear stress measurement in the X-axis (τ_{XZ}) can be resolved into the longitudinal and lateral shear stress components $\tau_{xz(1)}$ and $\tau_{yz(1)}$. These components are given by

$$\tau_{xz(1)} = \tau_{XZ}\cos(\alpha) \tag{A.1}$$

and

$$\tau_{yz(1)} = \tau_{XZ}\sin(\alpha) \tag{A.2}$$

Similarly, the shear stress measurement in the Y-axis (τ_{YZ}) can also be resolved into the longitudinal and lateral components $\tau_{xz(2)}$ and $\tau_{yz(2)}$. These components are given by

$$\tau_{xz(2)} = \tau_{YZ}\sin(\alpha) \tag{A.3}$$

and

$$\tau_{yz(2)} = \tau_{YZ}\cos(\alpha) \tag{A.4}$$

The total longitudinal shear stress is obtained from Equ. (A.1) and (A.3), and is given by

$$\tau_{xz} = \tau_{xz(1)} - \tau_{xz(2)} = \tau_{XZ}\cos(\alpha) - \tau_{YZ}\sin(\alpha) \tag{A.5}$$

Similarly, the total lateral shear stress obtained from Equ. (A.2) and (A.4) is given by

$$\tau_{yz} = \tau_{xz(1)} + \tau_{yz(2)} = \tau_{XZ}\sin(\alpha) + \tau_{YZ}\cos(\alpha) \tag{A.6}$$

At small slip angles such as those considered in this thesis (≤ 2 degrees on the flat bed tyre testing machine), it should be noted that $\cos(\alpha) \approx 1$ and $\sin(\alpha) \approx 0$. Thus, an acceptable approximation of the longitudinal and lateral shear stresses is obtained via

$$\tau_{xz} = \tau_{XZ} \tag{A.7}$$

and

$$\tau_{yz} = \tau_{YZ} \tag{A.8}$$

Appendix B Stress/Strain Data for a Typical Rubber Tyre Compound in Simple Extension

The stress/strain data provided by Dunlop Tyres Limited for a typical 'unknown' rubber tyre compound subjected to simple extension is given here (see Section 4.4). The secant modulus at 100 percent strain was also provided and was 3.19 MPa. These stress/strain measurements were obtained in accordance with BS 903: Part A2: 1995 (ISO 37: 1994).

Engineering Strain [%]	Engineering Stress [MPa]	Engineering Strain [%]	Engineering Stress [MPa]
0.0	0.00	26.1	0.96
2.0	0.12	27.1	0.99
2.9	0.16	28.2	1.01
3.9	0.22	29.2	1.04
4.7	0.27	30.1	1.06
5.6	0.32	31.3	1.08
6.5	0.37	32.3	1.11
7.5	0.42	33.4	1.13
8.5	0.46	34.3	1.16
9.5	0.50	35.4	1.18
10.5	0.54	36.4	1.21
11.5	0.58	37.4	1.23
12.6	0.61	38.5	1.26
13.6	0.64	39.5	1.29
14.6	0.68	40.5	1.32
15.7	0.71	41.3	1.34
16.7	0.74	42.4	1.38
17.8	0.77	43.4	1.41
18.8	0.79	44.3	1.44
19.8	0.82	45.3	1.48
20.9	0.84	46.3	1.52
21.9	0.87	47.2	1.56
23.0	0.89	48.2	1.60
24.0	0.92	49.1	1.65
25.0	0.94	50.0	1.70

Table B.1 Stress/strain data for a typical rubber tyre compound in simple extension

Appendix C Shear Distortion of the Tyre Tread in the Contact Patch

The poor performance of the Mooney-Rivlin model (model 27) in the LS-DYNA code [17] is discussed in Section 4.5. Excessive localised shear distortion in the tyre tread is observed under longitudinal loading. This excessive distortion disappears when the Hyperviscoelastic model (model 77) is used and, thus, the author recommends this model to simulate a transversely (longitudinal and/or lateral) loaded or rolling tyre. To aid validation of the performance of the Hyperviscoelastic model, a simple hand calculation is performed here using classical elasticity theory. It is based on the assumption that the tyre's belt is rigid since its stiffness is several orders of magnitude greater than that of the rubber tread. This simple model is shown in Figure C.1. The assumption is used in semi-empirical tyre models, such as the brush model [33, 45, 46].

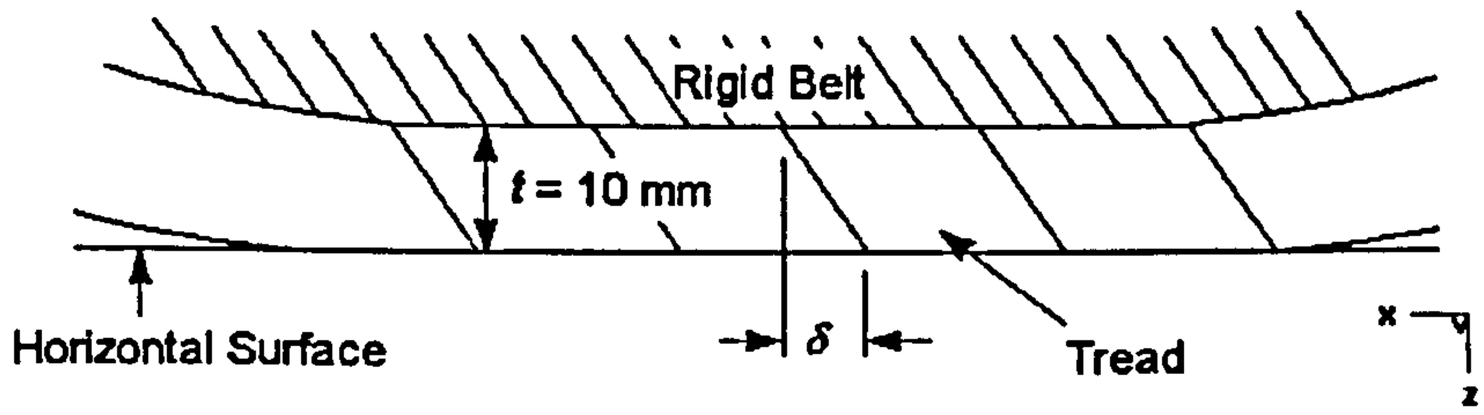

Figure C.1 Simple model of experimental tyre under longitudinal loading

For the particular case of simple shear, rubber exhibits a linear stress/strain relationship (see Equ. (4.6)). This relationship is characterised by the shear modulus G, given by

$$G = \frac{\tau_{xz}}{\gamma_{xz}} \tag{C.1}$$

where τ_{xz} is the shear stress and γ_{xz} is the shear strain. The average shear stress over the contact patch is F_x / A, where F_x is the applied longitudinal force and A is the area.

Assuming the shear modulus of the tread is 0.77 MPa, the longitudinal force is 2 kN, and the contact patch length and width are 115 mm and 122 mm, γ_{xz} can be estimated to be approximately 18 percent using Equ.(C.1). The shear distortion δ is then given by

$$\delta = \gamma_{xz} \times d \tag{C.2}$$

where d is the depth of the tread and, thus, the distortion is estimated to be 1.8 mm. This value corresponds to the 2.3 mm obtained in the advanced FE simulation using the same modulus and longitudinal force. It should be noted, however, that the contact patch length and width used were those obtained in the stationary experiments discussed in Section 3.4.1. The calculated shear distortion increases to approximately 2.6 mm if the simulated contact patch dimensions (length and width) from Figure 5.5 are utilised.